



# CLIQ

A new quench protection technology  
for superconducting magnets

*Emmanuele Ravaioli*



# CLIQ

A new quench protection technology  
for superconducting magnets

Dissertation graduation committee:

Chairman: Prof. dr. ir. H.J.W.M. Hilgenkamp, University of Twente  
Supervisor: Prof. dr. ir. H.H.J. ten Kate, University of Twente  
Assistant supervisor: Dr. ir. A.P. Verweij, CERN, Geneva, Switzerland  
Referee: Dr. M.M.J. Dhallé, University of Twente  
Members: Prof. dr. ir. H.J.M. ter Brake, University of Twente  
Prof. dr. ing. B. van Eijk, NIKHEF, Amsterdam  
Prof. dr. N.J. Lopes Cardozo, Eindhoven University of Technology  
Prof. dr. L. Rossi, University of Milan, Italy  
Dr. ir. H. Wormeester, University of Twente

The research described in this thesis was carried out at  
CERN, Geneva, Switzerland.

Cover by Emmanuele Ravaoli, with help from his friends, his family, and JT.  
At the top, magnetic field generated with a Crossed-Layers CLIQ configuration  
applied to a quadrupole magnet for the High Luminosity LHC.  
At the bottom, experimental data showing the first CLIQ discharge, measured at  
the CERN cryogenic laboratory on February 8, 2013.

CLIQ

Emmanuele Ravaoli

Ph.D. thesis, University of Twente, The Netherlands

ISBN 978-90-365-3908-1

Printed by Ipskamp Drukkers, Enschede, the Netherlands

© Emmanuele Ravaoli, Enschede, 2015.



# CLIQ

A new quench protection technology  
for superconducting magnets

DISSERTATION

to obtain  
the degree of doctor at the University of Twente,  
on the authority of the rector magnificus,  
prof. dr. H. Brinksma,  
on account of the decision of the graduation committee,  
to be publicly defended  
on Friday the 19<sup>th</sup> of June 2015 at 16.45

by

**Emmanuele Ravaioli**

born on the 22<sup>nd</sup> of September 1984  
in Bologna, Italy

This dissertation has been approved by:

Promotor: prof. dr. ir. H.H.J. ten Kate

*Alla mia famiglia,  
che porto sempre nel mio cuore,  
anche quando sono lontano,  
in ogni sfida e in ogni gioia.*

*Raffaella,  
mi amor,  
una vita intera non basta  
per scoprire se sei  
più bella, più dolce, o più divertente...  
...ma farò del mio meglio!*



# Preface

Many people asked me where the idea of CLIQ came from.

I consider the CLIQ (Coupling-Loss Induced Quench) project as an excellent example of successful collaboration between various groups at CERN, namely the TE-MPE, TE-MSc, and PH-ADO groups.

A few months before the beginning of my doctorate, Glyn Kirby (TE-MSc) wondered whether it was possible to utilize AC losses to protect a superconducting magnet. Vladimir Datskov (TE-MSc) pointed him to two papers dated 1979 and 1996 (see references [87] and [88] at the end of the thesis). Together they went to my supervisor Arjan Verweij (TE-MPE), who proposed me to explore the concept and assess its applicability. Quite soon, I proposed a crucial modification, the addition of the reverse diode, that greatly improved the design and made it applicable to most types of magnets. Simulation results were clearly showing that this new technique could be used for a very effective quench protection system.

The first CLIQ units were produced by the TE-MSc group with limited budget and manpower. My professor Herman ten Kate (PH-ADO) supported the concept from the start, and proposed to try it as soon as possible on a superconducting coil. The first CLIQ discharges were performed on the 8th of February 2013 on a small test solenoid at the CERN cryogenic laboratory, with the help of Alexey Dudarev (PH-ADO).

The test results were so convincing and the concept so innovative that we proposed to patent the method a few months after the first test under the name *AC-Current Induced Quench Protection System*.

Herman and Arjan suggested that a catchy name for the invention was mandatory, and the best I came up with was CLIQ.

It soon became clear that CLIQ would be the topic of my PhD dissertation and I devoted most of my time and energy at developing CLIQ's theoretical background, simulating its application on magnets with very different characteristics, optimizing its performance, and testing the technology on various superconducting magnets. These R&D efforts culminated in the first CLIQ discharges on a full-size LHC magnet, just a few weeks before the publication of this thesis.



# Acknowledgements

I am extremely grateful to Arjan Verweij. Anyone who works with him knows his clever opinions on most topics and deep knowledge of superconducting magnets. I also had the opportunity to know him as my supervisor, and I appreciated the perfect balance he established between mentoring and letting me work autonomously.

I feel very lucky and honoured, for being promoted by Herman ten Kate, whose constant support and positive and constructive criticism pushed me to improve myself and to target ambitious goals.

I take this opportunity to express gratitude to the co-inventors of the CLIQ system, Glyn Kirby and Vladimir Datskov, who were essential for the start of the project.

I extend my gratitude to colleagues working in other CERN sections, whose contributions were important to CLIQ's successful development: Alexey Dudarev during the first campaigns of CLIQ tests at the CERN cryogenic laboratory; Hugo Bajas, Marta Bajko, Vincent Desbiolles, Jerome Feuvrier, Christian Giloux, and Gerard Willering (special thanks for translating in Dutch the summary of the thesis) during the experimental campaigns at the CERN magnet test facility; François-Olivier Pincot during the manufacture of the first CLIQ units; Knud Dahlerup-Petersen and Felix Rodriguez-Mateos during the design of the second generation of CLIQ units.

I thank Bernhard Auchmann for the interesting discussions about modeling, in particular when developing the theory of the LEDET model.

I am also grateful for the help of the technical students who contributed to the simulations and tests during the various phases of the CLIQ project: Jonas Blomberg Ghini, Michał Maciejewski and Kevin Sperin.

Many thanks to the colleagues with whom I shared most of my coffee breaks. They made working at CERN an even more pleasant and interesting experience: Andrea, Carlo (special thanks for the template of the thesis), Daniel, Domenico, Ernesto, Giancarlo, Giordana, Giuseppe, Lucio (special thanks for the help with the cover of the thesis) and Mario.

Voglio anche ringraziare e abbracciare la mia famiglia e JT, che hanno sopportato la mia mancanza e il mio nervosismo in questo periodo speciale della mia vita, e hanno condiviso lo sbrilluccichio nei miei occhi nei momenti più emozionanti.





# List of publications

- [1] E. Ravaoli, K. Dahlerup-Petersen, F. Formenti, V. Montabonnet, M. Pojer, R. Schmidt, A. Siemko, M.S. Camillocci, J. Steckert, H. Thiesen, and A.P. Verweij, *Impact of the Voltage Transients After a Fast Power Abort on the Quench Detection System in the LHC Main Dipole Chain*, IEEE Transactions on Applied Superconductivity, vol. 22, no. 3, June 2012, doi: 10.1109/TASC.2012.2183572.
- [2] E. Ravaoli, K. Dahlerup-Petersen, F. Formenti, J. Steckert, H. Thiesen, and A.P. Verweij, *Modeling of the Voltage Waves in the LHC Main Dipole Circuits*, IEEE Transactions on Applied Superconductivity, vol. 22, no. 3, June 2012, doi: 10.1109/TASC.2011.2176306.
- [3] E. Ravaoli, B. Auchmann, and A.P. Verweij, *Fast method to quantify the collective magnetization in superconducting magnets*, IEEE Transactions on Applied Superconductivity, vol. 23, no. 3, June 2013, doi: 10.1109/TASC.2012.2227649.
- [4] E. Ravaoli, A.P. Verweij, and H.H.J. ten Kate, *Unbalanced Impedance of the Aperture Coils of Some LHC Main Dipole Magnets*, IEEE Transactions on Applied Superconductivity, vol. 23, no. 3, June 2013, doi: 10.1109/TASC.2012.2227650.
- [5] *AC-Current Induced Quench Protection System*, EP13174323.9, priority date: 28 June 2013.
- [6] E. Ravaoli, V.I. Datskov, C. Giloux, G. Kirby, H.H.J. ten Kate, and A.P. Verweij, *New, Coupling Loss Induced, Quench Protection System for Superconducting Accelerator Magnets*, IEEE Transactions on Applied Superconductivity, vol. 24, no. 3, June 2014, doi: 10.1109/TASC.2013.2281223.
- [7] E. Ravaoli, V.I. Datskov, A.V. Dudarev, G. Kirby, K.A. Sperin, H.H.J. ten Kate, and A.P. Verweij, *First Experience with the New Coupling-Loss Induced Quench System*, Cryogenics, 2014, Vol. 60, pp. 33-43, <http://dx.doi.org/10.1016/j.cryogenics.2014.01.008>.
- [8] E. Ravaoli, V.I. Datskov, G. Kirby, H.H.J. ten Kate, and A.P. Verweij, *A New Hybrid Protection System for High-Field Superconducting Magnets*,

---

Superconductor Science and Technology, 2014, Vol. 27 (4), 044023, doi:10.1088/0953-2048/27/4/044023.

- [9] E. Ravaioli, V.I. Datskov, V. Desbiolles, J. Feuvrier, G. Kirby, M. Maciejewski, K.A. Sperin, H.H.J. ten Kate, A.P. Verweij, and G. Willering, *Towards an optimized Coupling-Loss Induced Quench protection system (CLIQ) for quadrupole magnets*, Physics Procedia, to be published in 2015.
- [10] E. Ravaioli, H. Bajas, V.I. Datskov, V. Desbiolles, J. Feuvrier, G. Kirby, M. Maciejewski, G. Sabbi, H.H.J. ten Kate, and A.P. Verweij, *Protecting a Full-Scale Nb<sub>3</sub>Sn Magnet with CLIQ, the New Coupling-Loss Induced Quench System*, IEEE Transactions on Applied Superconductivity, vol. 25, no. 3, June 2015, doi: 10.1109/TASC.2014.2364892.
- [11] E. Ravaioli, H. Bajas, V.I. Datskov, J. Blomberg Ghini, G. Kirby, M. Maciejewski, H.H.J. ten Kate, A.P. Verweij, and G. Willering, *First implementation of the CLIQ quench protection system on a full-scale LHC matching quadrupole magnet*, IEEE Transactions on Applied Superconductivity, to be published in 2015.
- [12] E. Ravaioli, V.I. Datskov, G. Kirby, M. Maciejewski, H.H.J. ten Kate, and A.P. Verweij, *Advanced Quench Protection for the Nb<sub>3</sub>Sn Quadrupoles for the High Luminosity LHC*, IEEE Transactions on Applied Superconductivity, to be published in 2015.
- [13] E. Ravaioli, B. Auchmann, M. Maciejewski, H.H.J. ten Kate, and A.P. Verweij, *Lumped-Element Dynamic Electro-Thermal model of a superconducting magnet*, Cryogenics, to be published in 2015.
- [14] E. Ravaioli, V.I. Datskov, G. Kirby, M. Maciejewski, H.H.J. ten Kate, A.P. Verweij, and G. Willering, *First implementation of the CLIQ quench protection system on a 14 m long full-scale LHC dipole magnet*, IEEE Transactions on Applied Superconductivity, to be published in 2015.
- [15] E. Ravaioli, V.I. Datskov, J. Blomberg Ghini, G. Kirby, M. Maciejewski, G. Sabbi, H.H.J. ten Kate, and A.P. Verweij, *Quench protection of a 16 T block-coil dipole magnet for a 100 TeV Hadron Collider using CLIQ*, IEEE Transactions on Applied Superconductivity, to be published in 2015.
- [16] E. Ravaioli, V.I. Datskov, G. Kirby, M. Maciejewski, H.H.J. ten Kate, and A.P. Verweij, *CLIQ-based quench protection of a chain of high-field superconducting magnets*, IEEE Transactions on Applied Superconductivity, to be published in 2015.

# Contents

<b>Preface</b>	<b>I</b>
<b>Acknowledgements</b>	<b>III</b>
<b>List of publications</b>	<b>V</b>
<b>1 Introduction</b>	<b>1</b>
1.1 Superconducting magnets . . . . .	1
1.2 Quench . . . . .	5
1.3 Protection . . . . .	6
1.3.1 Self-protection . . . . .	8
1.3.2 By-pass elements . . . . .	9
1.3.3 Coupled secondary coil . . . . .	10
1.3.4 Energy-extraction system . . . . .	11
1.3.5 Active heating . . . . .	12
1.4 Quench heaters . . . . .	15
1.5 New CLIQ technology . . . . .	17
<b>2 Coupling-Loss Induced Quench</b>	<b>21</b>
2.1 Electrical circuit . . . . .	21
2.2 Governing equations . . . . .	23
2.3 Advantages . . . . .	30
2.4 Disadvantages . . . . .	31
2.5 Characteristic example of a CLIQ discharge . . . . .	32
2.6 Conclusion . . . . .	41
<b>3 Optimization of the CLIQ discharge circuit</b>	<b>43</b>
3.1 CLIQ effectiveness, $\Psi$ . . . . .	43
3.2 Multi-CLIQ . . . . .	46
3.3 Optimum discharge circuit for various magnet geometries . . . . .	51
3.3.1 One-layer $\cos\theta$ dipole . . . . .	51
3.3.2 Two-layer $\cos\theta$ dipole . . . . .	52
3.3.3 Two-layer $\cos\theta$ quadrupole . . . . .	56
3.3.4 Block-coil dipole . . . . .	62
3.3.5 Solenoid . . . . .	63

3.3.6	Pancake coil . . . . .	68
3.3.7	Chain of uncoupled magnets . . . . .	70
3.4	Conclusion . . . . .	72
<b>4</b>	<b>Lumped-Element Dynamic Electro-Thermal model</b>	<b>75</b>
4.1	Dynamic electro-thermal model . . . . .	75
4.1.1	Lumped-element modeling . . . . .	76
4.1.2	LEDET in a nutshell . . . . .	76
4.2	Electrical sub-network . . . . .	80
4.3	Thermal sub-network . . . . .	80
4.4	Coupling-current sub-networks . . . . .	85
4.4.1	Equivalent IFCC loops . . . . .	85
4.4.2	Equivalent ISCC loops . . . . .	91
4.4.3	Extension to other coupling-current mechanisms . . . . .	96
4.5	Conclusion . . . . .	97
<b>5</b>	<b>CLIQ-based protection of existing magnets</b>	<b>99</b>
5.1	Design . . . . .	99
5.2	Implementation . . . . .	101
5.2.1	Unit . . . . .	102
5.2.2	Terminals . . . . .	103
5.2.3	Redundancy . . . . .	104
5.3	Cases analyzed . . . . .	106
5.3.1	Case 1: Nb <sub>3</sub> Sn quadrupole model magnet . . . . .	107
5.3.2	Case 2: Nb-Ti quadrupole model magnet . . . . .	110
5.3.3	Case 3: ten-layer solenoid . . . . .	111
5.4	Conclusion . . . . .	119
<b>6</b>	<b>CLIQ using an external excitation coil</b>	<b>121</b>
6.1	Design of the excitation coil . . . . .	121
6.1.1	Position . . . . .	122
6.1.2	Geometry . . . . .	123
6.1.3	Subdivision . . . . .	124
6.2	Advantages and disadvantages . . . . .	126
6.3	First experience using an external excitation coil . . . . .	127
6.4	Excitation coil for a full-scale 11 T dipole magnet . . . . .	129
6.5	Conclusion . . . . .	136
<b>7</b>	<b>CLIQ-integrated magnet design</b>	<b>137</b>
7.1	Design strategy . . . . .	137
7.2	Optimization of the superconductor . . . . .	138
7.2.1	Filament twist-pitch and resistivity of the matrix . . . . .	138
7.2.2	Performance of a multi-pitch cable . . . . .	143
7.2.3	Strand twist-pitch and cross-contact resistance . . . . .	145
7.2.4	Fraction of superconductor and stabilizer . . . . .	147
7.3	Optimization of the magnet design . . . . .	149
7.3.1	Number of coil turns . . . . .	149

7.3.2	Electrical order of coil sections . . . . .	155
7.3.3	Intra-layer terminals . . . . .	156
7.3.4	Electrical and mechanical improvements . . . . .	156
7.4	High-temperature superconducting magnets . . . . .	157
7.5	Conclusion . . . . .	158
<b>8</b>	<b>CLIQ integrated in a chain of superconducting magnets</b>	<b>161</b>
8.1	Protection of a chain of magnets . . . . .	161
8.2	Integration of CLIQ in the chain . . . . .	162
8.3	CLIQ in the LHC chain of dipole magnets . . . . .	163
8.3.1	LHC chain of dipole magnets . . . . .	163
8.3.2	Electro-dynamic model of an LHC dipole magnet . . . . .	164
8.3.3	Electrical transients in the chain of dipole magnets . . . . .	165
8.3.4	CLIQ configuration for the LHC main dipole magnet . . . . .	168
8.3.5	Simulation of a CLIQ in the LHC chain of dipole magnets . . . . .	170
8.4	CLIQ in a chain of 16 T dipole magnets . . . . .	173
8.5	Conclusion . . . . .	176
<b>9</b>	<b>Conclusion</b>	<b>177</b>
	CLIQ . . . . .	177
	CLIQ effectiveness, $\Psi$ . . . . .	179
	LEDET model . . . . .	179
	Protection of existing magnets . . . . .	180
	CLIQ using an external excitation coil . . . . .	180
	Protection of future magnets . . . . .	181
	Outlook . . . . .	181
	<b>References</b>	<b>183</b>
	<b>Summary</b>	<b>199</b>
	<b>Samenvatting (Summary in Dutch)</b>	<b>203</b>



# Chapter 1

## Introduction

*The scope of this thesis is characterizing a novel and powerful method for the protection of superconducting magnets called CLIQ, the Coupling-Loss Induced Quench protection system. CLIQ is an active system relying on heat generated by coupling loss in superconducting wires to transfer quickly and homogeneously the winding pack to the normal state. Its fast energy-deposition mechanism and its simple and robust electrical design can make it the best option for an effective and reliable protection of high magnetic field, high energy density, large scale superconducting magnets.*

### 1.1 Superconducting magnets

The vanishing electrical resistance and the capacity to generate magnetic fields far beyond those of saturated iron and in large volumes are the main motivations to use superconductor technology in magnets [1, 2].

Superconducting materials exhibit the superconducting state if their temperature  $T$  [K], applied magnetic field  $B$  [T], and current density  $J_{sc}$  [ $\text{Am}^{-2}$ ] are below certain critical values, which are interdependent and constitute the critical surface [3–6]. The maximum temperature and magnetic field allowing superconductivity,  $T_c(B=0)$  [K] and  $B_{c2}(T=0)$  [T], are defined as the critical temperature and upper critical field, respectively. As an example, figure 1.1 shows the critical current density of  $\text{Nb}_3\text{Sn}$  as a function of temperature and magnetic field:  $T_c(B=0)=18$  K and  $B_{c2}(T=0)=29$  T. Conventionally, superconducting materials exhibiting a critical temperature lower than 30 K are called low-temperature superconductors.

Most superconducting magnets are composed of low-temperature superconductors operating in cryogenic baths of liquid helium at temperatures between 1.8 and 4.5 K. Due to the shape of their critical surfaces, the maximum magnetic field attainable in magnets using Nb-Ti and  $\text{Nb}_3\text{Sn}$  superconductors at a temperature of 4.2 K is

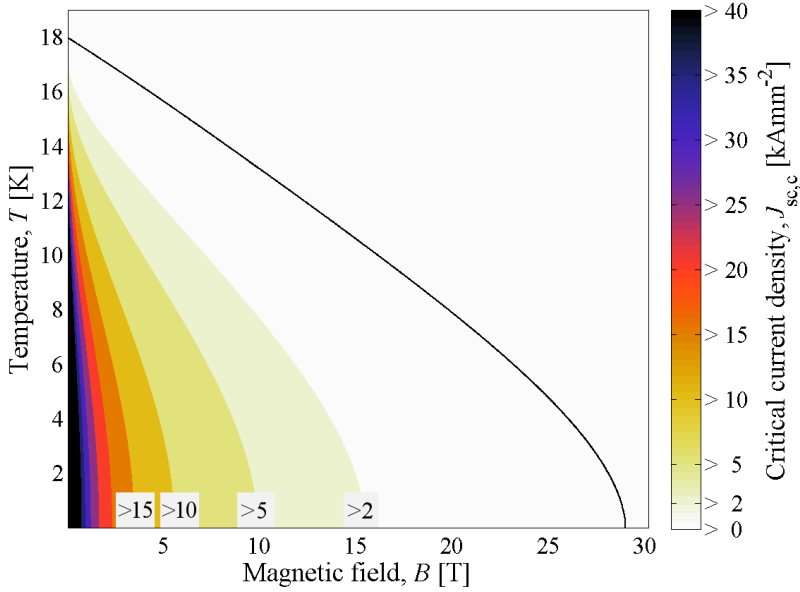


Figure 1.1. Critical surface of Nb<sub>3</sub>Sn. Critical current density as a function of the superconductor temperature and applied magnetic field.

around 9 and 18 T, respectively. The design of hybrid magnets combining coils made of low and high temperature superconductors (BiSrCaCuO, YBaCuO) is currently under study with the ambition to reach peak stationary magnetic fields of some 35 T and beyond [7].

When in the normal state, superconducting materials used in magnets have an electrical resistivity three orders of magnitude higher than metals employed as electrical conductors at room temperature, such as copper and aluminium. For this reason, the superconductor is commonly embedded in a matrix of low-resistivity material. When the superconductor is in the normal state, the stabilizer provides a low resistance path for the transport current, hence reducing the local ohmic loss. Moreover, the stabilizer provides a heat conduction path to remove heat from the superconductor with a much lower thermal conductivity.

In order to avoid flux jumps and reduce magnetic-field errors, the superconductor is shaped as thin filaments in the order of a few to a few tens of micrometer [1, 8]. Examples of the cross-section of round wires and a tape of various types of superconductor are shown in figure 1.2 [9]. The superconducting filaments are embedded in a matrix of low electrical-resistivity material, usually copper. It is possible to manufacture round wires comprising filaments with diameter in the order of a few micrometer, or tens of micrometer, as shown in figures 1.2a-c. Superconducting filaments are usually not present in the wire inner core to allow filament transposition. For obvious manufacturing reasons a thin layer of copper is also present around the filament bundle.

In order to decrease the local ohmic loss in the case of a transition to the normal



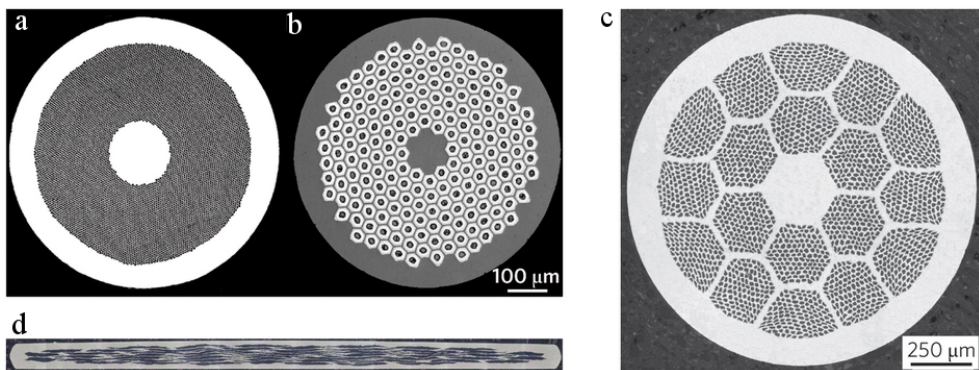


Figure 1.2. Examples of cross-sections of round wires and tape made of various types of superconductor. a. Wire made of Nb-Ti filaments embedded in a copper stabilizer. b. Wire comprising Nb<sub>3</sub>Sn filaments. c. Wire with Bi<sub>2</sub>Sr<sub>2</sub>Ca<sub>1</sub>Cu<sub>2</sub>O<sub>x</sub> filaments in Ag matrix. d. Tape with Bi<sub>2</sub>Sr<sub>2</sub>Ca<sub>2</sub>Cu<sub>3</sub>O<sub>x</sub> filaments, sized 0.2×4 mm<sup>2</sup>. Figures reproduced from: a-b, d. [10], © 2001 NPG; c. Courtesy of J. Jiang of National High Magnetic Field Laboratory, and the wire manufactured by Oxford Superconducting Technology. Reprinted by permission from Macmillan Publishers Ltd: Nature Materials [9], copyright 2014.



Figure 1.3. Cross-sections of the conductor used in ATLAS barrel toroid. On the left is the full conductor, sized 12×57 mm<sup>2</sup>, in the middle a detail of the cable and the bonding between Al and Cu, and on the right the Nb-Ti/Cu strand of 1.33 mm diameter [12].

state, and to drastically reduce the heat generation in the conductor when in the normal state, additional low-resistivity material can be added to the wire cross-section, acting as heat sink. This is the case, for example, with the wire-in-channel, using extra copper, whose stabilizer to superconductor ratio are typically increased by one order of magnitude, or with the ATLAS conductor using pure Al, see figure 1.3 [12].

To achieve higher transport currents, multiple wires can be cabled. When part of a cable, wires are called strands. Various cable types have been proposed and used in superconducting magnets, such as Rutherford cables [3,8], Roebel cables [13], nuclotron cables [14], and cable-in-conduit conductors [15]. The most commonly used cable type in accelerator magnets is the Rutherford cable, due to a very high packing factor and good stacking possibilities (figures 1.4a-b).

Superconductors used in magnets are routinely subject to magnetic-field changes, which introduce transitory loss - often referred to as AC loss in the case of periodic operation, or ramp loss following a magnet charge or discharge. This transitory loss is related to various phenomena:

- inter-filament coupling loss (IFCL): loss generated in the matrix of wires/strands

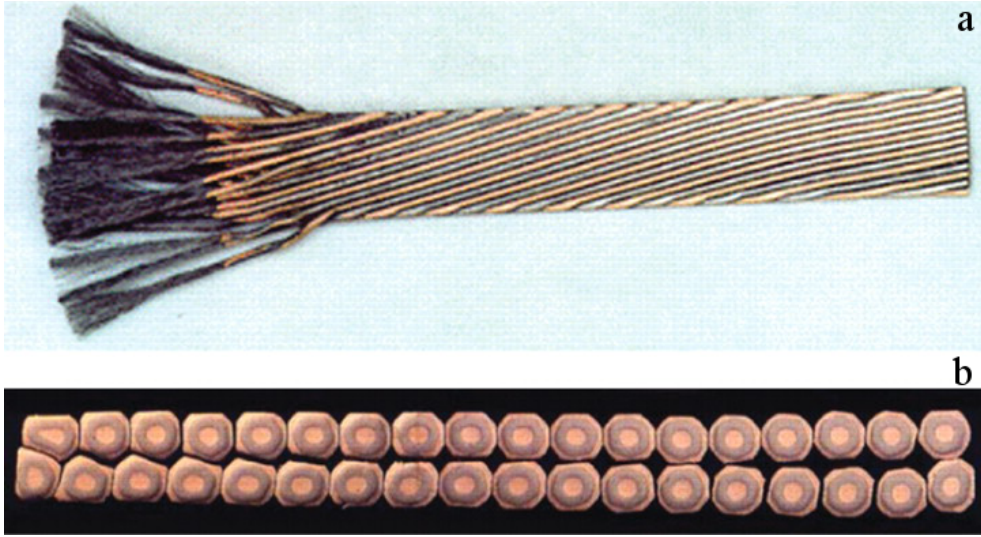


Figure 1.4. Example of a Nb-Ti Rutherford cable used in the LHC main dipole magnets [8, 11]. a. View from the top. b. Cross-section, sized  $1.48 \times 15.10 \text{ mm}^2$ .

due to coupling currents forced to flow between superconducting filaments forming open loops where magnetic field can penetrate causing circulating currents (sections 2.2 and 4.4.1), [3, 16–18];

- inter-strand coupling loss (ISCL): loss generated at the contact points between superconducting strands of a cable due to coupling currents between strands, again due to the open loops between strands (section 4.4.2), [18];
- hysteresis loss in the superconducting filaments (often called magnetization loss): loss generated due to a change in the magnetic-field distribution in the superconducting filaments [3];
- eddy currents loss: loss generated by induced currents flowing in normal conducting material in contact with the superconductor, such as added stabilizing material;
- ferromagnetic loss: loss generated by hysteretic behaviour of ferromagnetic non-superconducting material of a wire;
- mechanical loss: loss generated due to conductor movements caused by the Lorentz force.

To limit the development of inter-filament coupling loss, the superconducting filaments are twisted with a certain twist-pitch. Analogously, to limit inter-strand coupling loss, strands composing a cable are twisted as well. For achieving uniform current density in the cable cross-section, strands are fully transposed, so that every strand changes position with every other strand along the length of the cable.

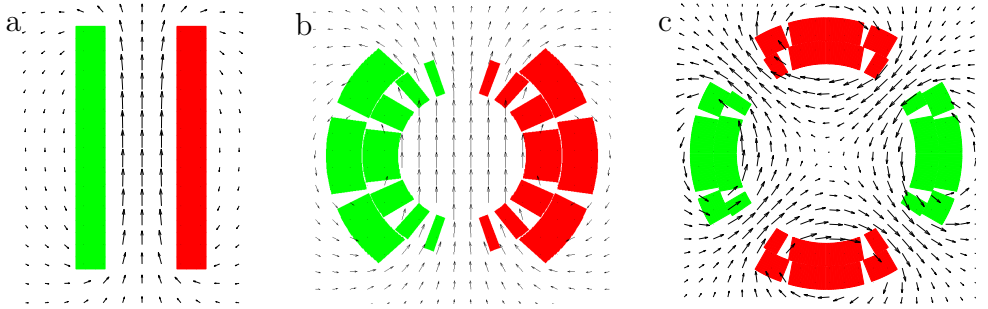


Figure 1.5. Examples of the cross-section of various coils. Colors indicate the polarity of the transport current. Arrows indicate the direction of the generated magnetic field. a. Solenoid. b. Dipole. c. Quadrupole.

Superconducting wires or cables are repeatedly wound to form coils of chosen geometry, which are used for magnetic resonance imaging, particle accelerators and detectors, and other research or applications requiring high magnetic field. A homogeneous unidirectional magnetic field can be generated in a cylindrical volume by means of a solenoidal coil, obtained by circularly winding the conductor. The resulting cross-section is shown in figure 1.5a. This coil geometry is often used in particle detection, magnetic resonance imaging, and laboratory magnets, where highly uniform magnetic fields are required.

High-energy physics studies the interaction of elementary particles by means of particle accelerators and colliders. These large-scale machines are composed of various circuits of different magnets [19–25]. Synchrotron accelerators, featuring a circular track with RF cavities to accelerate bunches of particles, rely on multipole magnets. Dipole magnets (figure 1.5b) are required to bend the particle beam and maintain it in its circular trajectory; quadrupole magnets (figure 1.5c) are needed to focus and defocus the beam; whereas higher-order multipole magnets are used to correct magnetic-field errors introduced by the non-ideal former magnets. The particle collision energy depends on the radius of the accelerator  $R$  [km] and on the strength of the magnetic field generated by its dipole magnets  $B_d$  [T], following  $E \approx 0.3RB_d$  [TeV]. Thus, it is of high interest to design magnets achieving high magnetic field in order to enhance the collision energy while limiting the size of the particle accelerator. Furthermore, since they are usually installed in confined underground areas, the requirement of high compactness is important for accelerator magnets.

## 1.2 Quench

A quench [3, 26–29] is the sudden and irreversible transition of a superconductor to the normal state, occurring when local conditions in terms of temperature, magnetic field, or current density do not allow to continue the superconducting state. Since the heat capacity of all materials is very low at low temperature, even minor perturbations of the order of  $\mu\text{Jmm}^{-3}$  are sufficient to initiate a transition to the normal state. The occurrence of a quench is thus part of the normal operation of a superconducting

magnet. Numerous disturbances occurring in superconducting magnets can lead to a quench such as flux jumps, mechanical events (conductor movement, cracking of epoxy resin), electro-magnetic transients (hysteretic loss, coupling loss, eddy current loss), heat loads (radiation, beam loss), heat leaks, or even loss of primary services like power cuts, loss of coolant, or loss of insulation vacuum [30,31]. These perturbations are characterized by differences of several orders of magnitude in energy density and time-scale.

Superconducting magnets operate at high magnetic field and can store high magnetic energy, thus the damage potential by overheating is significant. Furthermore, their operating current densities are high, hence when in the normal state joule heating will increase the temperature in the coils very quickly. The consequences of a quench, to be carefully considered during the magnet design, include [29,32]:

- hot-spot temperature increase in the coil, usually the position in the conductor where the quench started, which can degrade or damage the coil insulation or even the conductor itself. There is no unanimous opinion about the maximum temperature allowable in a superconducting coil after a quench. A conservative limit is 100 K [33,34], and usually room temperature is considered in the case the energy density is very high. Some experiments on short model Nb<sub>3</sub>Sn magnets showed no degradation up to a temperature of 400 K [35]. The temperature where the conductor insulation undergoes a phase transition can be considered a hard limit. For Nb<sub>3</sub>Sn magnets, also the softening temperature of the impregnation constitutes a hard limit [35];
- temperature gradients between coil sections transferred to the normal state at different times and hence subject to different ohmic loss, which can introduce high local thermal stress and structural failure. In particular, the insulation usually undergoes higher temperature gradients and has low shear strength;
- high voltage induced within the coil and between coil and ground resulting from the inhomogeneous transition of the winding pack to the normal state, which can cause short circuits and arcing;
- pressure increase caused by the cryogen blow-off, which can cause a high mechanical load on the cryostat or other components;
- flow of blown helium, which can cause rupture of voltage taps and instrumentation wires;
- forces caused by thermal and electromagnetic loads during a magnet discharge transient, especially in the case of inductively coupled systems.

## 1.3 Protection

During and after a quench, part of the magnetic energy stored in the magnet, varying from a minimal fraction to its totality, is converted into heat deposited in the winding pack. One of the primary concerns of magnet design is assuring that the temperature

reached in the coil hot-spot at the end of the discharge is maintained below the allowable limit. A conservative estimation of the coil hot-spot temperature can be obtained from the equation of local heat balance [29, 36, 38, 55]. In the adiabatic approximation, the increase of the conductor temperature  $T$  [K] is determined by the local ohmic loss,

$$\bar{c}(T)A \frac{\partial T}{\partial t} = \rho_{\text{st}}(T, B) \frac{I^2}{f_{\text{st}}A}, \quad [\text{Wm}^{-1}] \quad (1.1)$$

where  $\bar{c}$  [ $\text{JK}^{-1}\text{m}^{-3}$ ] is the volumetric specific heat, weighted over the fractions of the materials composing the conductor,  $A$  [ $\text{m}^2$ ] is the conductor cross-section,  $\rho_{\text{st}}$  [ $\Omega\text{m}$ ] is the electrical resistivity of the stabilizer material,  $f_{\text{st}}$  is its fraction in the conductor, and  $I$  [A] is the magnet transport current. Rearranging the terms of equation 1.1 and integrating it over time after the start of the quench ( $t=0$ ), yields:

$$f_{\text{st}} \int_{T_0}^{T_{\text{max}}} \frac{\bar{c}(T)}{\rho_{\text{st}}(T, B)} dT = \int_0^\infty J^2 dt, \quad [\text{A}^2\text{sm}^{-4}] \quad (1.2)$$

with  $T_0$  [K] and  $T_{\text{max}}$  [K] the temperatures at the beginning and at the end of the discharge, respectively, and  $J$  [ $\text{Am}^{-2}$ ] the current density in the entire conductor. A function  $\Gamma(T_{\text{max}})$  [ $\text{A}^2\text{sm}^{-4}$ ] can be conveniently defined as the left-hand side of equation 1.2, which is solely dependent on the conductor materials and the fraction of stabilizer. The  $\Gamma$  function can be approximated by a simple power-law expression [3, 29]. Copper is the material showing the highest value of the  $\Gamma$  function, allowing design values in the range of 5 to 20  $10^{16} f_{\text{st}} [\text{A}^2\text{sm}^{-4}]$  [36].

On the contrary, the right-hand side of equation 1.2 is determined by the operating current density  $J_0$  [ $\text{Am}^{-2}$ ] and the response of the magnet circuit and protection system:

$$\Gamma(T_{\text{max}}) = \int_0^\infty J^2 dt = J_0^2 \int_0^\infty \left\{ \exp \left[ -t \left( \frac{R_C(t) + R_w}{L_M} \right) \right] \right\}^2 dt, \quad [\text{A}^2\text{sm}^{-4}] \quad (1.3)$$

where  $L_M$  [H] is the magnet self-inductance,  $R_C$  [ $\Omega$ ] the electrical resistance of the normal zone in the coil, and  $R_w$  [ $\Omega$ ] the electrical resistance of the warm parts of the circuit.

This equation shows that, for a given magnet self-inductance and operating current density, the coil hot-spot temperature can be maintained below a certain value by either a sufficiently high coil resistance, or a sufficiently high warm resistance, or a combination of both. The most common methods for protecting superconducting magnets can be classified according to two characteristics:

- Discharge mechanism: protection systems can rely on partly extracting the magnet energy and dissipating it outside the coil (external energy discharge, high  $R_w$ ), or on uniformly spreading in the winding pack the stored energy by forcing a transition to the normal state of a large fraction of the coil (internal energy discharge, high  $R_C$ ).
- Passive/active systems: active protection systems require an external trigger to be activated, such as an electronic signal generated after the detection of a quench. Passive protection systems are activated by the occurrence of the quench itself.

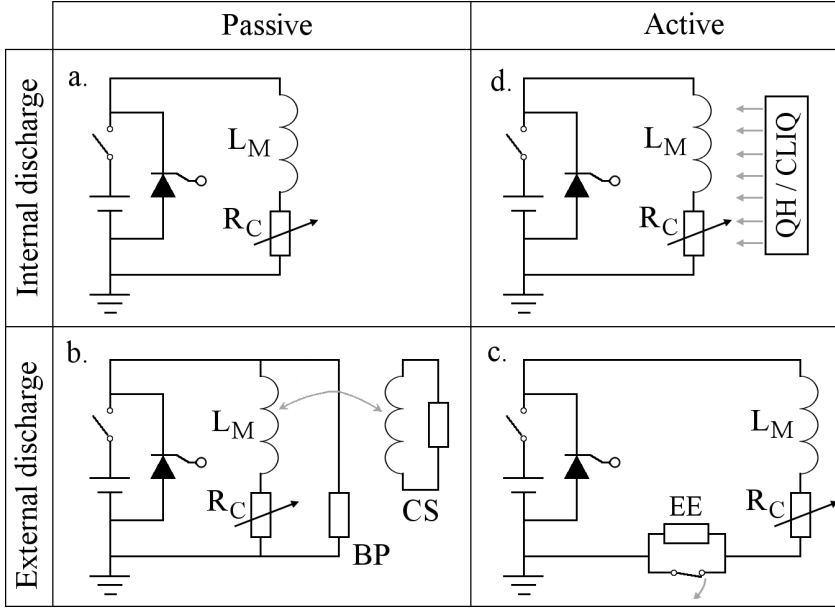


Figure 1.6. Classification and schematic representation of the most common quench protection methods. a. Self-protection. b. By-pass elements (BP); coupled secondary coil (CS). c. Energy extraction (EE). d. Active heating (quench heaters, CLIQ).

This classification results in four possible categories of quench protection methods as summarized in figure 1.6. As explained in the rest of the chapter, the choice of the protection strategy is based on the advantages and limitations of each method and driven by the constraints imposed by the magnet design [27, 36–38].

### 1.3.1 Self-protection

Completely passive protection (figure 1.6a) is the simplest, most reliable, and least expensive magnet protection method, because it does not employ additional equipment and does not rely on active triggering which may fail.

Once a transition to the normal state occurs, local ohmic heat is generated in the coil hot-spot. The normal zone then propagates to other sections of the coil by means of thermal conduction in the direction of the transport current through the conductor, and to other coil turns across insulation layers. If this process is sufficiently fast, the electrical resistance developed in the normal zone can cause a discharge of the magnet transport current before the temperature of the coil hot-spot exceeds safe limits. In this condition, most of the magnetic energy stored in the magnet is deposited in the winding pack during the discharge.

A superconducting coil can be designed so as to guarantee that the local ohmic heat in a normal zone is smaller than the heat extraction to the cryogen bath, and hence the superconductor switches back to the superconducting state after a quench. Such cryo-stabilized coils characteristically require a stabilizer-to-superconductor

ratio between 10 and 20 [39], which results in coils with low current density and very large dimensions usually incompatible with the requirements of many practical applications, in particular accelerator magnets.

Past studies [40–42] investigating the passive normal zone propagation and the resulting internal coil temperatures and voltages in solenoids and multipole magnets have shown that the maximum operating current-density  $J_{\text{st},0}$  [ $\text{Am}^{-2}$ ] allowable in a self-protected coil is ultimately limited by the magnetic energy stored in the coil  $E_{\text{M}}$  [J],  $J_{\text{st},0} < c_{\text{sp}}/\sqrt{E_{\text{M}}}$ , with  $c_{\text{sp}}$  [ $\text{Am}^{-2}\text{J}^{-0.5}$ ] a characteristic design constant [43,44]. In practice, completely passive self-protection is limited to small coils with low stored energy and low stabilizer current-density.

### 1.3.2 By-pass elements

Another passive protection method consists in installing one or multiple by-pass elements across the coil to protect (figure 1.6b). Valid by-pass elements include resistors, single diodes, back-to-back diodes, or more complex protection schemes composed of combinations of these [36]. In the case of a quench, the electrical resistance developed in the coil normal zone forces part of the magnet transport current through the by-pass branch, thus dissipating part of the magnet energy in the by-pass element, thereby also limiting the voltage across the branch.

The advantage of this protection solution is the passivity of the system as it does not rely on quench detection or other electronics, but only on the unavoidable rise of electrical resistance in the normal zone. However, the presence of the by-pass branch affects the normal operation of the magnet. In fact, if a by-pass resistor is mounted across the coil, a leakage current flows through the resistor when the magnet current is increased or decreased. The design value of its resistance is a compromise between the need to provide an effective alternative path in the case of a quench, calling for a lower resistance, and the need to reduce the operational loss which constitutes a significant cryogenic load, calling for higher resistance. If a diode is installed across the coil, the leakage current is reduced to nil during normal operation, but the maximum operating current-change  $dI_{\text{M}}/dt$  [ $\text{As}^{-1}$ ] is limited by the diode forward voltage  $U_{\text{d}}$  [V]. For a magnet with self-inductance  $L_{\text{M}}$  [H],  $(dI_{\text{M}}/dt)_{\text{max}} \leq U_{\text{d}}/L_{\text{M}}$ .

A protection system based on by-pass diodes is relatively insensitive to the initiation of a quench. In fact, no current is diverted from the coil until the normal zone develops a voltage larger than the diode forward voltage, which is usually in the range 1 to 10 V. For a quench during a down-ramp phase, the conduction of the diode is further delayed by the inductive voltage across the coil.

Quench protection based on by-pass elements is a good solution for superconducting magnets characterized by low to medium stabilizer current-densities, due to its reliability and its low cost compared to active protection systems. In various cases, it is convenient to increase the fraction of stabilizer in the coil conductor in order to apply this low-performing but less expensive method [45].

By-pass protection elements can also be used to subdivide a coil into multiple sections [36]. As an example, the implementation of a protection system comprising four by-pass resistors across identical individual coil sections is schematized in figure 1.7a. In the case of a quench in one section, the resistance of its normal

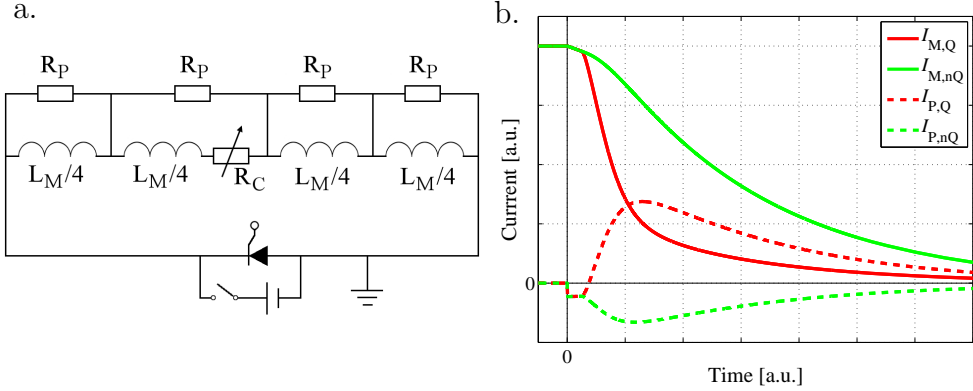


Figure 1.7. Magnet protection by means of four by-pass resistors across individual coil sections. a. Electrical scheme. b. Qualitative time evolution of the currents in the system.

zone diverts a part  $I_{P,Q}$  [A] of the current to the by-pass resistor mounted across it as shown in figure 1.7b. The current in the coil section where the quench developed  $I_{M,Q}$  [A] is rapidly discharged, thus limiting the energy-deposition in the coil hot-spot. The current  $I_{M,nQ}$  [A] flowing in the coil sections still in the superconducting state decreases with a longer time constant, and the negative inductive voltage across them drives a negative current  $I_{P,nQ}$  [A] through their respective by-pass resistors. Since at the end of the discharge only one of the sections is in the normal state, thermal stress due to the highly inhomogeneous coil temperature arises which is potentially harmful to the magnet. As explained in section 1.3.5, this can be avoided by implementing active systems forcing a more uniform transition of the coil to the normal state.

In addition, series-powered magnets forming a superconducting chain can be by-passed by individual elements, thus avoiding depositing the energy stored in all magnets of the circuit into the only coil in the normal state. Each coil of the chain can be protected by active systems relying on external [45–47] or internal energy discharge [52, 53].

### 1.3.3 Coupled secondary coil

Another passive protection system relying on partly discharging the magnet stored energy externally to its coil is the installation of a secondary coil magnetically coupled to the main coil (CS, see figure 1.6.b). When the main coil is subject to a current-change, a current is induced in the coupled coil. This effect reduces the magnet differential self-inductance, hence causing a faster discharge of the transport current after a transition to the normal state. Part of the energy stored in the magnet is not dissipated in the main coil, but in the secondary-coil windings due to ohmic heat generation. If the resistance of the secondary coil is in close contact with the superconducting coil, ohmic heat is generated therein and transferred to the conductor via thermal diffusion, hence causing a faster transition of the superconductor to the normal state.

The effectiveness of this method depends on the strength of the coupling between



the main and the secondary coils, which is roughly proportional to the number of their turns. Thus, effective secondary coils need to be of relatively large dimensions, incompatible with requirements of many applications. Moreover, a stronger coupling also induces a higher current through the secondary-coil windings during normal operation, unless it is disconnected, resulting in transitory loss which constitutes a significant cryogenic load.

### 1.3.4 Energy-extraction system

The relatively slow response of passive protection systems make them incompatible with the very fast energy discharge required to protect large but compact superconducting coils with high current density and stored energy. Thus, active systems have to be employed which detect the occurrence of a quench, switch off the circuit power source, and promptly force the discharge of the magnet stored energy. The total time required to activate an active quench protection system,  $t_{\text{QD}}$  [s], can be regarded as the sum of the times required to detect a quench,  $t_{\text{d}}$  [s], to validate the detection,  $t_{\text{v}}$  [s], and to trigger the protection system,  $t_{\text{t}}$  [s].

An active protection system relying on an external energy discharge is called an energy-extraction system (EE, see figure 1.6c). Upon quench detection, a switch is activated to divert the circuit current to a resistor  $R_{\text{EE}}$  [ $\Omega$ ], in which part of the magnet energy is deposited. In first approximation, the coil self-inductance and the energy-extraction resistance can be considered constant during the discharge. Under these assumptions, the magnet transport current decays exponentially with time constant  $\tau_{\text{EE}} = L_{\text{M}}/R_{\text{EE}}$  [s]. The maximum fraction of energy that can be extracted for a given system can be evaluated with the method described in [54].

In the case of an energy-extraction system, a conservative approach consists in assuming that the electrical resistance of the normal zone is much smaller than the energy-extraction resistor, i.e.  $R_{\text{w}} + R_{\text{C}} \approx R_{\text{EE}}$ . Under this assumption, equation 1.3 can be written as

$$\Gamma(T_{\text{max}}) = \int_0^\infty J^2 dt = J_0^2 \left( t_{\text{d}} + t_{\text{v}} + t_{\text{t}} + \frac{\tau_{\text{EE}}}{2} \right) = \Gamma_{\text{QD}} + \Gamma_{\text{EE}}, \quad [\text{A}^2\text{sm}^{-4}] \quad (1.4)$$

and two distinct contributions are identified:  $\Gamma_{\text{QD}}$  [ $\text{A}^2\text{sm}^{-4}$ ], depending on the initial quench propagation, the sensitivity of the quench detection system, the validation time, and the rapidity of the triggering of the energy-extraction switch; and  $\Gamma_{\text{EE}}$  [ $\text{A}^2\text{sm}^{-4}$ ], depending on the discharge time constant.

The discharge time constant can be expressed as:

$$\tau_{\text{EE}} = \frac{L_{\text{M}}}{R_{\text{EE}}} = \frac{L_{\text{M}} I_0}{U_{\text{EE}}}, \quad [\text{s}] \quad (1.5)$$

where  $I_0$  [A] is the initial operating current and  $U_{\text{EE}}$  [V] is the maximum operating voltage across the energy-extraction resistor.

Combining equations 1.2-1.5 shows that, in order to maintain the hot-spot temperature below a certain level  $T_{\text{max}}$ , the operating stabilizer current-density cannot

exceed the limit:

$$J_0 < \left[ \frac{\Gamma(T_{\max})}{\left(t_d + t_v + t_t + \frac{\tau_{EE}}{2}\right)} \right]^{0.5} = \left[ \frac{\Gamma(T_{\max})}{\left(t_{QD} + \frac{L_M I_0}{2U_{EE}}\right)} \right]^{0.5} \cdot [\text{Am}^{-2}] \quad (1.6)$$

This relation leads to the conclusion that the hot-spot temperature in a coil protected by an energy-extraction system can be reduced by:

- using materials with a large  $\Gamma$  function, i.e. with high volumetric heat capacity and low resistivity;
- increasing the fraction of stabilizer  $f_{st}$ , with the undesirable effect of increasing the size of the conductor;
- detecting the quench rapidly, hence reducing  $t_{QD}$ ;
- increasing the operating voltage of the energy-extraction  $U_{EE}$ ;
- decreasing the product  $L_M I_0$ , either by reducing the coil dimensions or the number of coil turns. As an example, a coil composed of half as many turns has a self-inductance four times smaller, but generates a similar peak magnetic field operating at a current only two times higher, i.e. the product  $L_M I_0$  is halved.

### 1.3.5 Active heating

The constant pursuit of higher magnetic performance reaching higher magnetic field and higher current density [56–59] calls for an equivalent effort in developing effective protection systems capable of quickly discharging the energy stored in the magnet. High current-density, compact, long superconducting coils can be protected by an energy-extraction system only allowing very high voltages to ground, which are presently incompatible with safety and practical requirements of most laboratories. Furthermore, the cost of energy-extraction systems for large-scale applications is significant.

An alternative quench protection strategy is required based on actively transferring the superconductor to the normal state, hence forcing the discharge of the magnet stored energy with the electrical resistance developed in the coil itself (figure 1.6d). With respect to an external energy-discharge system, active transfer of the superconductor to the normal state also offers a more uniform profile of the voltages and stress within the coil due to the distribution of inductive and resistive components over the conductor length.

As mentioned in section 1.1, the superconducting state is maintained only when the superconductor temperature, applied magnetic field, and current density are below critical values. Thus, an active transition of the superconductor can be forced by increasing one, or more, of these properties. The most common active internal-discharge systems are based only on the heating of the superconductor. In fact, it is usually difficult to rapidly change the local magnetic field in the superconductor, due to the high self-field generated by the coil and the development of induced magnetic fields opposing to any magnetic field-change. Also, a protection

system introducing a pulse in the coil current to increase it above its critical limit is either ineffective at low current levels, or largely over-dimensioned at high current levels. In fact, the superconductor critical current-density significantly increases at low applied magnetic fields, hence when the magnet is operated at low current a very high over-current is required to transfer the coil to the normal state. Whilst this strategy was recently tested to protect a small-scale high-temperature superconducting coil [48], usually its implementation is limited to fault-limiter or power switch applications [49–51].

Nowadays highest performance superconducting magnets are protected by active systems relying on active heating of the conductor. A protection scheme frequently adopted comprises active-heating units and a by-pass element protecting each coil. This solution reduces the problem of the protection of the entire superconducting chain to the more manageable task of protecting individual shunted coils. An energy-extraction system can be added to avoid dissipating the energy of the coils still in the superconducting state in the by-pass element of the quenched coil [52, 53, 60–62].

If spread uniformly across the winding pack, the magnet energy is well below the amount required to damage the conductor by overheating. For instance, consider that the integral of the volumetric specific heat from 1.9 to 300 K for common insulated superconducting cables is in the order of  $0.5 \text{ Jmm}^{-3}$ , whereas present and near-future accelerator magnets are composed with cables with energy densities in the range 0.05 to  $0.1 \text{ Jmm}^{-3}$  [38]. Achieving a fast and homogeneous distribution of the energy in the coil is very challenging because of the high power which has to be delivered to the superconductor in order to force its transition to the normal state. As a simple example, consider that to turn to the normal state in 10 ms a volume of  $0.1 \text{ m}^3$  of superconductor, roughly corresponding to the coil of an accelerator magnet, one would need about 250 kW of power, to be delivered uniformly, safely, and reliably to an object with a size of several meters. Furthermore, due to magneto-resistivity the initial inhomogeneous magnetic-field profile in the coil results in non-uniform ohmic heating even if the entire winding pack is transferred to the normal state simultaneously.

Defining more realistic limits for an active internal energy discharge system requires knowledge of the time evolution of the electrical resistance developed in the coil normal zone,  $R_C [\Omega]$ , which depends on the effectiveness of the protection system, quench propagation, and material properties. A simplified approach can be followed to estimate limits of an internal energy discharge [3, 29, 38]. In the case of an internal energy discharge system, the resistance of the warm parts of the circuit are negligible as compared to the coil internal resistance. Thus, the adiabatic heat balance shown in equation 1.3 reads

$$\Gamma(T_{\max}) = \int_0^\infty J^2 dt = J_0^2 \left\{ t_{\text{QD}} + \int_{t_{\text{QD}}}^\infty \left[ \exp\left(-\frac{R_C(t)}{L_M} t\right) \right]^2 dt \right\}. \quad [\text{A}^2 \text{sm}^{-4}] \quad (1.7)$$

Let us consider a protection system capable of initiating a simultaneous transition to the normal state of the entire winding pack in a time  $t_Q$  [s]; assume the magnet current does not change before this transition occurs ( $t < t_{\text{QD}} + t_Q$ ); and define  $\Gamma_D [\text{A}^2 \text{sm}^{-4}]$  as the quench load during the discharge ( $t > t_{\text{QD}} + t_Q$ ). The resulting transient is qualitatively illustrated in figure 1.8.

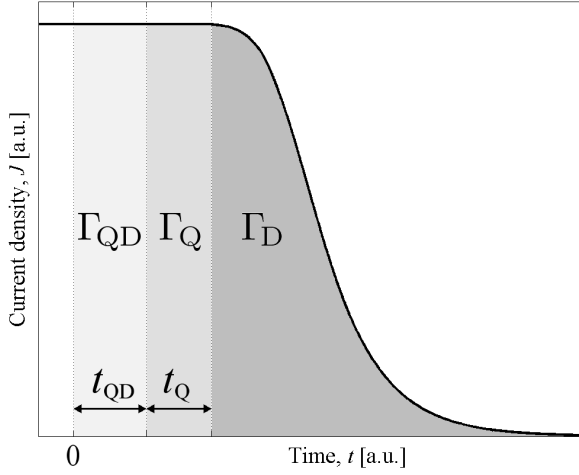


Figure 1.8. Qualitative representation of the phases of the protection of a coil with an internal discharge system.  $t=0$ : Start of the quench.  $t=t_{\text{QD}}$ : The quench is detected, the detection is validated, the protection system is triggered.  $t=t_{\text{QD}}+t_{\text{Q}}$ : The protection system transfers the entire coil to the normal state.

While this approach does not represent the real behavior of a superconducting magnet, it allows a qualitative subdivision of the contributions to the quench load. In fact, one can rewrite equation 1.7 as

$$\Gamma(T_{\text{max}}) = J_0^2(t_{\text{QD}} + t_{\text{Q}}) + \Gamma_{\text{D}} = \Gamma_{\text{QD}} + \Gamma_{\text{Q}} + \Gamma_{\text{D}}, \quad [\text{A}^2\text{sm}^{-4}] \quad (1.8)$$

and three contributions are identified:

- $\Gamma_{\text{QD}}$ , depending on the initial quench propagation, the sensitivity of the quench detection system, the validation time, and the rapidity of the protection-system triggering;
- $\Gamma_{\text{Q}}$ , depending on the effectiveness of the protection system, normal zone propagation throughout the coil, and the heat generated by loss in the superconductor due to the current change during the discharge, also called quench-back effect [63–65]. Note that in this simplified model this last contribution is strictly zero since the current does not change in the time period from  $t_{\text{QD}}$  to  $t_{\text{Q}}$ ;
- $\Gamma_{\text{D}}$ , depending on the coil geometry, conductor parameters, and material properties.

All contributions have a non-linear dependence on the operating current density. For a given quench detection system and coil design, the time  $t_{\text{Q}}$  has the meaning of maximum time margin for transferring the entire coil to the normal state without exceeding a temperature  $T_{\text{max}}$  in the coil hot-spot at the end of the discharge [38]:

$$t_{\text{Q}}(T_{\text{max}}) = \frac{\Gamma(T_{\text{max}}) - \Gamma_{\text{QD}} - \Gamma_{\text{D}}}{J_0^2} = \frac{\Gamma(T_{\text{max}}) - \Gamma_{\text{D}}}{J_0^2} - t_{\text{QD}}. \quad [\text{s}] \quad (1.9)$$

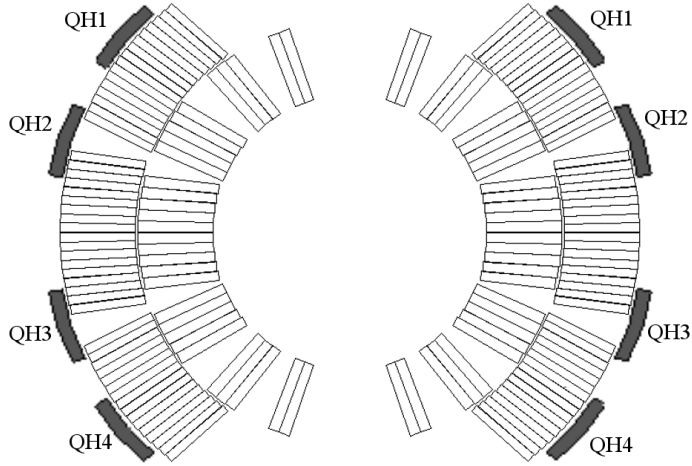


Figure 1.9. Implementation of a quench-heater system on one aperture of the LHC main dipole magnet. Coil cross-section including four quench-heater circuits (QH1-QH4), attached to the outer layer, each acting on half a pole. Note that the thickness of the quench-heater strips is intentionally inflated.

Coils composed of conductor with lower fraction of stabilizer and operating at higher current densities show lower time margins.

## 1.4 Quench heaters

Conventional active internal-discharge systems rely on quench heaters (QH), for example, consisting of stainless steel strips with thickness of a few tens of micrometer glued between two layers of polyimide electrical insulation foil, and attached to the insulation layer of the coil to protect. As an example, figure 1.9 shows the coil cross-section of one aperture of the LHC main dipole magnet, including four quench-heater circuits glued to the outer layer of the coil, each acting on half a pole [23, 52, 53, 66–69].

The terminals of each quench-heater strip are connected to a capacitor bank with capacitance  $C_{QH}$  [F] charged at a voltage  $U_{QH,0}$  [V]. Upon quench detection, the energy stored in the capacitor bank is discharged in the strips, which heat up by ohmic loss and transfer the energy to the coil through thermal diffusion across the thin insulation layer. Neglecting the dependence of the strip electrical resistance  $R_{QH}$  [ $\Omega$ ] on the temperature, the voltage across the strip  $U_{QH}$  [V] decays exponentially with time constant  $\tau_{QH}=R_{QH}C_{QH}$  [s]. The ohmic loss generated in the strip is  $P_{QH}=U_{QH}^2/R_{QH}$  [W].

To concentrate the energy deposition and to reduce the resistance of the strips, heat is deposited in resistive heating stations, well distributed along the direction of the conductor. Once the superconductor in correspondence to the heating stations is transferred to the normal state, the local ohmic loss causes heat propagation

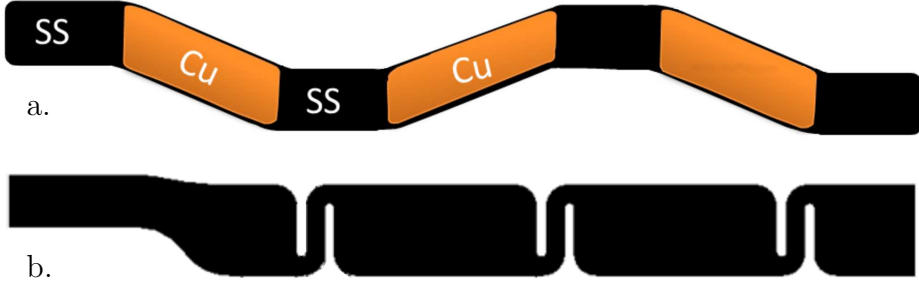


Figure 1.10. Schematic representation of quench-heater strips with periodic heating stations. a. Strips partly copper-plated (SS: Stainless steel; Cu: Copper). b. Strips with varying width along the conductor. Courtesy of T. Salmi of Tampere University of Technology.

and thus propagation of the normal zone in the direction of the transport current up to the next heating station. Effective heating stations can be achieved by partially plating the steel quench-heater strips with copper (figure 1.10a) [66–68], or by manufacturing quench-heater strips with varying width along the conductor direction (figure 1.10b) [70]. Such more complex geometries can be studied with recently developed codes [71, 72].

The thickness of the insulation layer between the quench-heater strips and the coil is a key parameter of a quench-heater system, and is chosen as a compromise between maximizing the heat diffusion calling for thinner layers, and reducing the risk of electrical breakdown calling for thicker layers [73].

Contrarily to an energy-extraction system, a protection system based on quench heaters is mostly independent on the magnet length, since both the coil self-inductance and resistance when in the normal state are proportional to the magnet length. In such systems, the only ingredients depending on the magnet length are quench-back effects [63–65] and the time required to fully propagate the normal zones longitudinally. However, both are not key design features and do not significantly affect the quench-heater performance.

The main limitations of the quench-heater technology are twofold. The first limitation is constituted by the difficulty of using them to transfer the entire winding pack to the normal state in a sufficiently short time. The values of the time margin defined in equation 1.9 are in the range of 50 to 200 ms for the most recent accelerator coils based on Nb-Ti. New-generation Nb<sub>3</sub>Sn accelerator magnets, however, have time margins in the range of 10 to 50 ms and require even more effective protection systems [38].

The so-called quench-heater delay indicates the time between the quench-heater triggering and the initiation of the normal zone in the high magnetic-field areas of the coil. Typical values recently measured on the Nb<sub>3</sub>Sn model magnets for the High Luminosity LHC [78] are in the range 10 to 30 ms at 80% of the short-sample current for the 12 T quadrupole magnet [79] and 11 T dipole [80, 81], in good agreement with simulation predictions [71, 72]. However, the quench-heater delay refers to the very start of the induced normal zone, whereas the time margin refers to the transfer

to the normal state of the entire winding pack, and the difference between these two values is significant. In fact, if the quench-heater strips do not touch all coil turns, the normal zones have to propagate to adjacent turns through thermal diffusion across insulation layers, with a typical delay of about 10 ms per turn [38]. Moreover, most designs for multipole coils include two or more layers of turns, with quench heaters attached to the turns of the outer layer only. The normal zone propagation from the outer to the inner layer of the coil requires additional 30 to 50 ms [81]. Finally, since the heat is deposited in separated heating stations, the entire length of the coil is not transferred to the normal state simultaneously, but after a delay depending on the propagation velocity. As an example, for a longitudinal normal zone propagation velocity of  $20 \text{ ms}^{-1}$  and a distance between heating stations of 100 mm, the entire length of a turn is transferred to the normal state 2.5 ms after the normal zones start in the points heated by the stations.

In order to improve the effectiveness of a quench-heater system, additional strips can be glued to the inner layer of the coil, or between the two layers [38]. However, both methods have disadvantages. Quench heaters are relatively easy to attach to the inner layer during the coil potting, but they are not supported and are prone to detachment with a consequent reduction of their effectiveness [82]. Also, quench heaters constitute a barrier to the heat removal. Interlayer quench heaters applied to  $\text{Nb}_3\text{Sn}$  multi-layer coils undergoing a heat treatment at the same time are an option only if they are designed to withstand the same heat treatment. A reliable and redundant system including inner or interlayer quench heaters is indeed challenging. In conclusion, if the protection of the coil requires time margins less than about 50 ms, it is very challenging to design effective quench-heater systems [38].

The second fundamental disadvantage of a quench-heaters based protection system is the delicate electrical design making the manufacturing costly and reliability a significant concern. Given the thin insulation layer between the strips and the coil required for effective heat transfer, quench heaters may cause electrical shorts, may get damaged by overheating, and suffer from repetitive operation due to Lorentz forces and to stress and strain during thermal cycles [74,75]. Quench-heater failure is one of the main causes of rejection of high-field accelerator magnets. For example, 11 out of 30 cases of rejection of LHC main dipole magnets were related to quench heaters [74]. Of the 15 dipole magnets replaced during the LHC long shutdown in 2013 and 2014, 5 had quench-heater related issues [76,77].

## 1.5 New CLIQ technology

The CLIQ (Coupling-Loss Induced Quench) technology relies on the generation of high coupling loss in the superconductor, an effective mechanism, which causes deposition of heat inside the conductor itself where it is most needed to initiate a transition to the normal state. This method is by principle much faster than conventional quench heaters, which rely on heat diffusion for the propagation of normal zones.

Characteristically, a CLIQ-based protection system can turn to the normal state the entire winding pack of a full-scale high magnetic-field magnet in 10 to 40 ms,

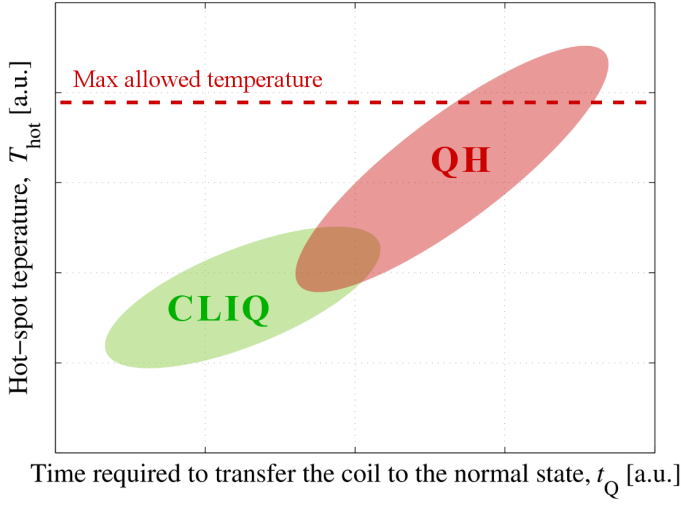


Figure 1.11. Hot-spot temperature after a quench in high magnetic field magnets, as a function of the time required to transfer the coil to the normal state. Qualitative comparison between the performance of conventional quench-heater systems and of the new CLIQ system.

presently out of reach with quench-heaters systems. A qualitative comparison between the performance of the two methods is shown in figure 1.11. CLIQ's superior heating mechanism allows reducing significantly the hot-spot temperature, as will be shown in detail in the following chapters.

In addition, CLIQ offers a significantly easier and more robust electrical design. The power deposition is achieved with an external system, not severely interfering with the coil winding technology, and easy to install and to replace in the case of damage. This constitutes a definite advantage of CLIQ over quench heaters, which are fragile, prone to electrical breakdown, and difficult to install to cover a large fraction of the coil surface. CLIQ is therefore a very promising technology for existing and future high magnetic field magnets.

The description of the electro-magnetic and thermal transient occurring in a superconducting coil after triggering CLIQ presented in this thesis constitutes a complete reference for the implementation of this new technology (chapter 2). Methods for optimizing the effectiveness of a CLIQ system are discussed for the magnet geometries adopted in the majority of nowadays superconducting magnets (chapter 3). A new technique to model the coupling loss in superconductors and their effect on the magnet's dynamics based on equivalent lumped-elements, is developed in order to reproduce the CLIQ behavior and assess its performance on future magnets (chapter 4).

First experiments have shown that CLIQ can be successfully implemented for protecting existing magnets of different geometries and made of various superconductors, dimensions, cables and strand parameters (chapter 5). A promising variant of the CLIQ method using an external excitation coil is tested on a small-scale



coil (chapter 6).

More ambitiously, the application of CLIQ may influence the design of future superconducting magnets. In fact, including CLIQ in the magnet design from the start can lead to better performing, safer, more compact, and more cost-effective magnets. This new generation of CLIQ-optimized coils will fully exploit the potential of the technology by implementing various modifications to the magnet design (chapter 7). The integration of a CLIQ protection system in the electrical circuit including chains of superconducting magnets is considered feasible and various test cases are proposed (chapter 8).

In conclusion, the new CLIQ technology is rapidly reaching maturity and causes a drastic change in the design and protection of superconducting magnets. In the next years it will be likely applied in particle accelerator magnets, where highest quench performance is required to assure their protection. Due to its robust electrical design enhancing the system safety, CLIQ has the potential to replace the conventional technology relying on thermal diffusion by internal quench heaters usually applied in high-field magnets.



## Chapter 2

# Coupling-Loss Induced Quench

*CLIQ (Coupling-Loss Induced Quench) is a new method for the protection of superconducting magnets. It relies on a capacitive discharge that introduces a few short periods of oscillation in the magnet transport current. The resulting fast change of the local magnetic field in the coil windings introduces high inter-filament and inter-strand coupling losses, which, in turn, cause the heating of the superconductor and a fast transfer of voluminous sections of the coil to the normal state. This intra-wire heating process is by principle much faster than thermal diffusion from an external heater to the superconductor. Furthermore, CLIQ relies on a system with simple, robust, reliable components, minimizing the risk of electrical breakdown and interference with the coil manufacture.*

### 2.1 Electrical circuit

The electrical scheme of a protection system based on the CLIQ method is shown in figure 2.1 [83–86]. It is composed of a capacitor bank  $C$  with capacitance  $C$  [F], a floating voltage supply  $S$ , two additional resistive current leads  $C_{L1}$  and  $C_{L2}$  connecting the system to the magnet, a thyristor  $TH$ , and a reverse diode  $D$ . A similar protection scheme was proposed in [87, 88], but is now improved with the addition of the reverse diode [86]. This new diode drastically improves the method as explained later. The leads  $C_{L1}$  and  $C_{L2}$  are dimensioned to carry only pulsed currents, therefore they typically have a cross-section of a few square millimeter. The capacitor bank is charged by  $S$  with a voltage  $U_0$  [V]. Upon quench detection, the thyristor is activated resulting in an oscillating current  $I_C$  [A] to be introduced in the coil sections. Part of this current flows through coil section  $L_A$ , whereas the remainder flows through

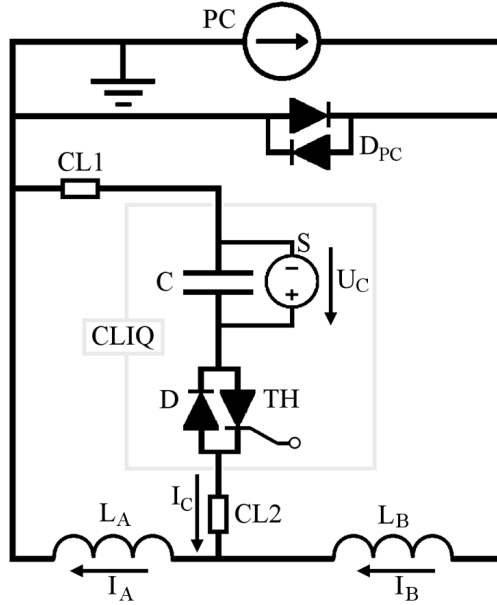


Figure 2.1. Electrical scheme of the protection system based on the Coupling-Loss Induced Quench (CLIQ) method in its simplest version.

coil section  $L_B$  in reverse direction. The presence of the reverse diode essentially allows continuous oscillations in  $I_C$ , which results in significant increase of the energy deposited by CLIQ. Note that another reverse diode  $D_{PC}$  is connected across the main power converter PC to protect it against a reverse current flow ( $I_B < 0$ ) in the case of a CLIQ discharge at low current.

In figure 2.2 the results of a typical CLIQ discharge are presented [89]. One 28.2 mF, 500 V CLIQ unit is connected to the midpoint of a 120 mm aperture  $Nb_3Sn$  quadrupole model magnet developed by the US LARP collaboration for the high luminosity LHC [79, 90–94]. At  $t=0$  the magnet is at the nominal current of  $I_0=14.6$  kA. An oscillating 2 kA, 26 Hz current  $I_C$  is introduced by the CLIQ unit. The resulting oscillation of the transport current in the two branches of the magnet is sufficient to start a transition to the normal state of the entire coil winding pack in less than 10 ms. Thus, a large electrical resistance  $R_C$  [ $\Omega$ ] is developed in the resistive zone of the coil resulting in a quick discharge of the magnet. In addition, the figure shows the same electro-thermal transient simulated with the model later presented in chapter 4 [95]. The simulated currents  $I_A$ ,  $I_B$  and  $I_C$ , and coil resistance  $R_C$  are in very good agreement with the measured curves.

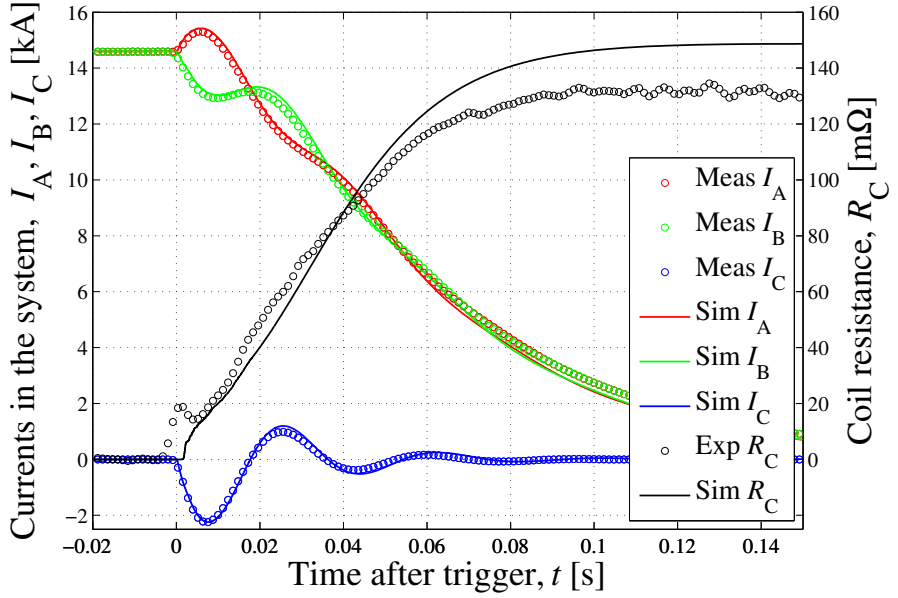


Figure 2.2. A characteristic coil discharge by a CLIQ transient. Measured currents  $I_C$  and  $I_B$ , calculated current  $I_A = I_B - I_C$  versus time, after triggering CLIQ at  $t=0$ . Experimental effective coil resistance  $R_C$ , versus time. Simulated  $I_A$ ,  $I_B$ ,  $I_C$ , and  $R_C$ .

## 2.2 Governing equations

The time evolution of the electrical transients during and after a CLIQ discharge can be analyzed by applying Kirchhoff's voltage and current laws to the schematic shown in figure 2.1. The following system describes the system behavior:

$$\begin{cases} (L_A + M_{AB})\dot{I}_A + (L_B + M_{AB})\dot{I}_B + R_{C,A}I_A + R_{C,B}I_B + U_D = 0 & [\text{V}] \\ U_C = L_A\dot{I}_A + M_{AB}\dot{I}_B + R_{C,A}I_A + (R_{cb} + R_{CL1} + R_{CL2})I_C + U_{TH} & [\text{V}] \\ I_A = I_B + I_C & [\text{A}] \\ I_C = -C\dot{U}_C & [\text{A}] \end{cases} \quad (2.1)$$

with the following initial conditions:

$$\begin{cases} I_A(0) = I_B(0) = I_0 & [\text{A}] \\ I_C(0) = \dot{U}_C(0) = 0 & [\text{A}] \\ U_C(0) = U_0 & [\text{V}] \end{cases} \quad (2.2)$$

where  $I_A$  and  $I_B$  [A] are the currents flowing in  $L_A$  and  $L_B$ ,  $L_A$  and  $L_B$  [H] the self-inductances of  $L_A$  and  $L_B$ ,  $M_{AB}$  [H] their mutual inductance,  $R_{C,A}$  and  $R_{C,B}$  [ $\Omega$ ]

the electrical resistances of the normal-zones developed therein,  $U_D$  [V] the voltage drop across the diode  $D_{PC}$ ,  $U_C$  [V] the voltage across the capacitor  $C$ ,  $R_{cb}$  [ $\Omega$ ] the equivalent series resistance of the capacitor bank,  $R_{CL1}$  and  $R_{CL2}$  [ $\Omega$ ] the resistances of  $C_{L1}$  and  $C_{L2}$ ,  $U_{TH}$  [V] the voltage drop across the thyristor  $TH$ , and  $I_0$  [A] the initial magnet transport current. At the moment of the discharge, it can be assumed that nearly the entire coil is in the superconducting state, i.e.  $R_{C,A} \approx R_{C,B} \approx 0$ ; moreover, the voltage drop across the diode  $D$  is usually small as compared to the charging voltage,  $U_D \ll U_0$ , and can be neglected. Under these assumptions, the system described by 2.1 is reduced to a series RLC circuit,

$$\ddot{I}_C + \frac{R_{eq}}{L_{eq}} \dot{I}_C + \frac{1}{L_{eq}C} I_C = 0, \quad [As^{-2}] \quad (2.3)$$

characterized by the capacitance of the CLIQ capacitor bank, the equivalent circuit resistance  $R_{eq} = R_{cb} + R_{CL1} + R_{CL2} + U_{TH}/I_C$  [ $\Omega$ ], and the equivalent inductance of the magnet circuit:

$$L_{eq} = \frac{L_A L_B - M_{AB}^2}{L_A + L_B + M_{AB}}, \quad [H] \quad (2.4)$$

which corresponds to the impedance of two parallel opposing inductors. In reality the values of  $L_A$ ,  $L_B$ , and  $M_{AB}$  change somewhat with the frequency due to dynamic effects related to coupling currents, which change the amount of magnetic flux linked to the superconducting coil [84, 95], as further explained in chapter 4. Equation 2.3 can be rewritten as

$$\ddot{I}_C + 2\alpha \dot{I}_C + \omega_0^2 I_C = 0, \quad [As^{-2}] \quad (2.5)$$

where an angular frequency  $\omega_0 = 1/\sqrt{L_{eq}C}$  [ $rad\ s^{-1}$ ] and an attenuation  $\alpha = R_{eq}/(2L_{eq})$  [ $rad\ s^{-1}$ ] are defined. The solution of this second-order differential equation, well known in the literature [96, 97], depends on the value of the damping factor  $\zeta = \alpha/\omega_0$ . If  $\zeta < 1$  the system response is under-damped and the time evolution of  $I_C$  is a damped sinusoidal oscillation with angular frequency  $\omega = \sqrt{\omega_0^2 - \alpha^2}$  [ $rad\ s^{-1}$ ]. For  $\zeta > 1$ , the system response is over-damped and  $I_C$  decays without oscillating. In a CLIQ circuit  $R_{eq}$ , corresponding to the resistance of the warm parts of the system, is very small, hence, the under-damp condition  $\zeta < 1$ , i.e.  $R_{eq} < \sqrt{L_{eq}/C}$ , is usually verified. For the same reason,  $\alpha \ll \omega_0$  and therefore  $\omega \approx \omega_0$ . Thus, the voltage  $U_C$  and the current  $I_C$  are equal to:

$$U_C(t) = U_0 \exp(-\alpha t) \left[ \cos(\omega t) + \frac{\alpha}{\omega} \sin(\omega t) \right], \quad [V] \quad (2.6)$$

and

$$I_C(t) = -C \frac{dU_C(t)}{dt} = CU_0 \frac{\omega^2 + \alpha^2}{\omega} \exp(-\alpha t) \sin(\omega t). \quad [A] \quad (2.7)$$

With an initial transport current  $I_0$  [A], the currents in the two branches of the circuit are:

$$I_A(t) = I_0 + \frac{L_B + M_{AB}}{L_A + L_B + M_{AB}} I_C = I_0 + f_{g,A} I_C, \quad [A] \quad (2.8)$$

and

$$I_B(t) = I_0 - \frac{L_A + M_{AB}}{L_A + L_B + M_{AB}} I_C = I_0 + f_{g,B} I_C, \quad [A] \quad (2.9)$$

where the non-dimensional parameters  $f_{g,A}$  and  $f_{g,B}$  are purely geometric if the self- and mutual inductances are constant. They always have opposite sign, and in the case of symmetric discharge circuits  $f_{g,A} = -f_{g,B}$ .

The local magnetic field inside the coil is determined by the currents  $I_A$  and  $I_B$ . Let  $x$  and  $y$  be two directions perpendicular to the transport-current direction. The generated magnetic field along  $x$  and  $y$  in each superconducting strand is a linear function of the transport currents in  $L_A$  and  $L_B$ , hence

$$\begin{aligned} B_{a,x} &= (f_{x,A} + f_{x,B}) I_0 + (f_{g,A} f_{x,A} + f_{g,B} f_{x,B}) I_C \\ &= B_{a,x,0} + f_{\text{CLIQ},x} I_C, \end{aligned} \quad [\text{T}] \quad (2.10)$$

and

$$\begin{aligned} B_{a,y} &= (f_{y,A} + f_{y,B}) I_0 + (f_{g,A} f_{y,A} + f_{g,B} f_{y,B}) I_C \\ &= B_{a,y,0} + f_{\text{CLIQ},y} I_C, \end{aligned} \quad [\text{T}] \quad (2.11)$$

where  $B_{a,x,0}$  and  $B_{a,y,0}$  [T] are the components of the initial magnetic field in the  $x$  and  $y$  directions, respectively. The magnetic parameters  $f_{x,A}$ ,  $f_{x,B}$ ,  $f_{y,A}$ , and  $f_{y,B}$  [ $\text{TA}^{-1}$ ] can be calculated for each strand by means of dedicated software, such as ROXIE [98] and SOLENO [99]. They are purely geometric apart from second-order non-linear effects such as iron-yoke saturation and self-fields. The parameters  $f_{\text{CLIQ},x}$  and  $f_{\text{CLIQ},y}$  [ $\text{TA}^{-1}$ ] characterize the behavior of the CLIQ system. In fact, they relate the current change introduced by CLIQ to the resulting applied magnetic-field change in the two directions,

$$\frac{dB_{a,x}}{dt} = f_{\text{CLIQ},x} \frac{dI_C}{dt}, \quad [\text{Ts}^{-1}] \quad (2.12)$$

and

$$\frac{dB_{a,y}}{dt} = f_{\text{CLIQ},y} \frac{dI_C}{dt}. \quad [\text{Ts}^{-1}] \quad (2.13)$$

The absolute applied magnetic-field change can be calculated as

$$\frac{dB_a}{dt} = \sqrt{\left(\frac{dB_{a,x}}{dt}\right)^2 + \left(\frac{dB_{a,y}}{dt}\right)^2} = f_{\text{CLIQ}} \frac{dI_C}{dt}, \quad [\text{Ts}^{-1}] \quad (2.14)$$

with  $f_{\text{CLIQ}} = \sqrt{f_{\text{CLIQ},x}^2 + f_{\text{CLIQ},y}^2}$  [ $\text{TA}^{-1}$ ]. An example of the variation of this parameter in the strands of a quadrupole coil is presented in section 2.5. Methods for maximizing  $f_{\text{CLIQ}}$  by changing the configuration of the discharge circuit will be discussed in chapter 3.

The presence of a magnetic-field change in a superconductor introduces transitory loss related to various phenomena, as explained in section 1.1. Among these effects, the inter-filament coupling loss is the most effective and reliable mechanism for CLIQ application. Many filaments are present in practically all nowadays superconductors with the exception of monofilament wires which are not used in magnets of any significant size. Instead, many conductors are single multifilamentary wires, hence no inter-strand coupling loss can be generated in these by principle. Furthermore, the parameters determining the inter-filament coupling loss, namely the filament

twist-pitch and the effective transverse resistivity of the matrix (equation 2.24), are usually rather uniform along the practical superconductor. As shown later in this section, the effective magnetic-field change generated in the strands by introducing an oscillation in the magnet transport current with a frequency in the range of 10 to 100 Hz is usually small, due to the presence of an induced magnetic field which opposes to the change. Thus, during a CLIQ discharge the contribution of hysteresis loss is limited as compared to inter-filament coupling loss. Most superconductors used in particle accelerator, detector, and magnetic resonance imaging magnets are composed of strands with parameters in a rather restricted range. For common strand parameters, the inter-filament coupling loss develops fast enough to allow a substantial heat generation in the superconductor in the first tens of milliseconds after triggering CLIQ. For this reason, it is convenient to assume that a CLIQ-based protection system must primarily rely on inter-filament coupling loss as the loss-generation mechanism. The presence of transitory loss related to other effects improves the overall system performance; hence, considering only the contribution of inter-filament coupling loss constitutes a conservative assumption.

As shown in section 4.4.1, the effects of a local magnetic-field change in each direction can be studied separately and then superposed. Combining equations 2.7 and 2.12 yields an explicit expression for the applied magnetic-field change in the  $x$  direction,

$$\frac{dB_{a,x}}{dt} = f_{\text{CLIQ},x} C U_0 \frac{\omega^2 + \alpha^2}{\omega} \exp(-\alpha t) [\omega \cos(\omega t) - \alpha \sin(\omega t)]. \quad [\text{Ts}^{-1}] \quad (2.15)$$

When a superconducting wire is subjected to an applied magnetic-field change in the  $x$  direction  $dB_{a,x}/dt$ , an induced magnetic field  $B_{\text{if},x}$  [T] is generated in the opposite direction due to inter-filament coupling currents (IFCC) [3, 16, 18]. Thus, the total local magnetic-field change is:

$$\frac{dB_{t,x}}{dt} = \frac{dB_{a,x}}{dt} + \frac{dB_{\text{if},x}}{dt}. \quad [\text{Ts}^{-1}] \quad (2.16)$$

As it will be shown in detail in section 4.4.1, the magnetic field induced by the inter-filament coupling currents is related to the variation of the total magnetic field,

$$B_{\text{if},x} = -\tau_{\text{if},x} \frac{dB_{t,x}}{dt}, \quad [\text{T}] \quad (2.17)$$

where  $\tau_{\text{if},x}$  [s] is the characteristic time constant of the inter-filament coupling currents,

$$\tau_{\text{if},x} = \frac{\mu_0}{2} \left( \frac{l_f}{2\pi} \right)^2 \frac{1}{\rho_{\text{eff},x}} = \frac{\mu_0}{2} \beta_{\text{if},x}, \quad [\text{s}] \quad (2.18)$$

with  $l_f$  [m] the filament twist-pitch,  $\rho_{\text{eff},x}$  [ $\Omega\text{m}$ ] the effective transverse resistivity of the strand matrix in the  $x$  direction,  $\mu_0 = 4\pi 10^{-7} \text{ TmA}^{-1}$  the magnetic permeability of vacuum, and  $\beta_{\text{if},x} = (l_f/2\pi)^2 / \rho_{\text{eff},x}$  [ $\text{m}\Omega^{-1}$ ]. The effective transverse resistivity depends on the absolute magnetic field in the matrix due to magneto-resistivity effects,

$$\rho_{\text{eff},x} = \rho_m f_{\text{eff},x} = (c_0 + c_1 B_t) f_{\text{eff},x}, \quad [\Omega\text{m}] \quad (2.19)$$



where  $\rho_m$  [ $\Omega\text{m}$ ] is the electrical resistivity of the matrix material,  $c_0$  [ $\Omega\text{m}$ ] and  $c_1$  [ $\Omega\text{mT}^{-1}$ ] are opportune parameters depending on the residual resistivity ratio (RRR) and magneto-resistivity of the material used as matrix, and usually known from the literature [100], and  $f_{\text{eff},x}$  is a parameter depending on the fraction of superconductor in the matrix, on the interface resistance between the filaments and the matrix, and on the position of the filaments in the strand cross-section [101–103]. In the most general case the effective resistivity in the  $x$  and  $y$  directions may differ ( $\rho_{\text{eff},x} \neq \rho_{\text{eff},y}$ ); hence, the time constants of the coupling currents in the two directions can be different as well ( $\tau_{\text{if},x} \neq \tau_{\text{if},y}$ ).

In the case of a strand with a fraction of superconductor  $f_{\text{sc}}$ , whose superconducting filaments are uniformly distributed in a matrix of a single material, it is found that the value of the effective parameter  $f_{\text{eff}} = f_{\text{eff},x} = f_{\text{eff},y}$  is

$$f_{\text{eff}} = \frac{1 - f_{\text{sc}}}{1 + f_{\text{sc}}}, \quad \text{or} \quad f_{\text{eff}} = \frac{1 + f_{\text{sc}}}{1 - f_{\text{sc}}}, \quad (2.20)$$

in the case the superconducting filaments do or do not contribute to the transverse conduction, respectively [18, 101–103]. The former case occurs for large interface resistance between the filaments and the matrix; whereas the latter occurs if the interface resistance is small. Furthermore, if the strand contains an internal core and/or an external shell of stabilizer, the value of the effective transverse resistivity needs to be corrected to take into account the currents developed in the non-uniform strand geometry [104], as explained later in this section.

By substituting equation 2.15 in the set of equations constituted by 2.16 and 2.17, with initial conditions

$$\begin{cases} B_{a,x}(0) = B_{a,x,0}, \\ B_{if,x}(0) = 0, \end{cases} \quad [\text{T}] \quad (2.21)$$

one obtains the expression of the total magnetic-field change introduced by a CLIQ discharge,

$$\begin{aligned} \frac{dB_{t,x}}{dt} &= f_{\text{CLIQ},x} C U_0 \frac{\omega^2 + \alpha^2}{\omega_n [\omega_n^2 + (1 - \alpha_n)^2]}. \\ \{ \exp(-\alpha t) [\omega_n \cos(\omega t) + (\omega_n^2 + \alpha_n^2 - \alpha_n) \sin(\omega t)] - \omega_n \exp(-t/\tau_{\text{if},x}) \}, \end{aligned} \quad [\text{Ts}^{-1}] \quad (2.22)$$

where  $\omega_n = \omega \tau_{\text{if},x}$  and  $\alpha_n = \alpha \tau_{\text{if},x}$  are the angular frequency and attenuation, respectively, normalized to  $1/\tau_{\text{if},x}$  (note that the suffix "if,x" is dropped only for the sake of simplicity). Large values of  $\omega_n$  and  $\alpha_n$  indicate that the variation of applied magnetic-field occurs in a time scale much smaller than the characteristic time constant of the inter-filament coupling currents; in this case, the total magnetic-field change is very limited. On the contrary, for  $\omega_n \approx \alpha_n \approx 0$  the development of coupling currents can be considered instantaneous as compared to the magnetic-field changes, hence  $dB_{t,x}/dt \approx dB_{a,x}/dt$ .

The inter-filament coupling currents flowing in the resistive matrix generate local inter-filament coupling loss. As later explained in section 4.4.1, the loss per unit

volume introduced in the strand by an oscillating magnetic field in  $x$  direction is [18]

$$\begin{aligned} P_{\text{if},x}''' &= \left( \frac{l_f}{2\pi} \right)^2 \frac{1}{\rho_{\text{eff},x}} \left( \frac{dB_{t,x}}{dt} \right)^2 \\ &= \beta_{\text{if},x} \left( \frac{dB_{t,x}}{dt} \right)^2. \end{aligned} \quad [\text{Wm}^{-3}] \quad (2.23)$$

The strand is simultaneously subject to a magnetic-field change in the  $y$  direction, hence a similar inter-filament coupling loss  $P_{\text{if},y}'''$  [ $\text{Wm}^{-3}$ ] develops due to coupling currents in  $y$  direction. This inter-filament coupling loss can be analyzed following the same process illustrated in equations 2.15-2.23. Thus, the total loss per unit volume is expressed as

$$\begin{aligned} P_{\text{if}}''' &= P_{\text{if},x}''' + P_{\text{if},y}''' \\ &= \left( \frac{l_f}{2\pi} \right)^2 \frac{1}{\rho_{\text{eff},x}} \left( \frac{dB_{t,x}}{dt} \right)^2 + \left( \frac{l_f}{2\pi} \right)^2 \frac{1}{\rho_{\text{eff},y}} \left( \frac{dB_{t,y}}{dt} \right)^2 \\ &= \beta_{\text{if},x} \left( \frac{dB_{t,x}}{dt} \right)^2 + \beta_{\text{if},y} \left( \frac{dB_{t,y}}{dt} \right)^2 \\ &= \frac{2}{\mu_0} \left[ \tau_{\text{if},x} \left( \frac{dB_{t,x}}{dt} \right)^2 + \tau_{\text{if},y} \left( \frac{dB_{t,y}}{dt} \right)^2 \right]. \end{aligned} \quad [\text{Wm}^{-3}] \quad (2.24)$$

The total heat per unit volume deposited in the strand during a CLIQ discharge can be calculated by integrating over time equation 2.24. Section 2.5 shows an example of the numerical calculation of such an integral for various CLIQ and strand parameters.

In the case of strands whose superconducting filaments are uniformly positioned in the strand cross-section, and neglecting the effect of the magnetic-field direction, the effective transverse resistivities in the  $x$  and  $y$  directions are equal (i.e.  $\beta_{\text{if},x} = \beta_{\text{if},y} = \beta_{\text{if}}$ ) and equation 2.24 reduces to

$$\begin{aligned} P_{\text{if}}''' &= \beta_{\text{if}} \left[ \left( \frac{dB_{t,x}}{dt} \right)^2 + \left( \frac{dB_{t,y}}{dt} \right)^2 \right] \\ &= \beta_{\text{if}} \left( \frac{dB_t}{dt} \right)^2 \\ &= \left( \frac{l_f}{2\pi} \right)^2 \frac{1}{\rho_{\text{eff}}} \left( \frac{dB_t}{dt} \right)^2. \end{aligned} \quad [\text{Wm}^{-3}] \quad (2.25)$$

Note that under this assumption the time constants of the inter-filament coupling currents developed in the two directions are also equal,  $\tau_{\text{if},x} = \tau_{\text{if},y} = \tau_{\text{if}}$ . Equation 2.25 is analogous to the classical formulations of inter-filament coupling loss [3, 18].

Strands used in nowadays superconducting magnets often include a bundle of superconducting filaments embedded in a matrix, plus an inner core and/or an outer shell of stabilizer. As an example, consider the strand shown in figure 2.3a, used in the cable of the outer layer of the LHC main dipole magnets [23]. When such a

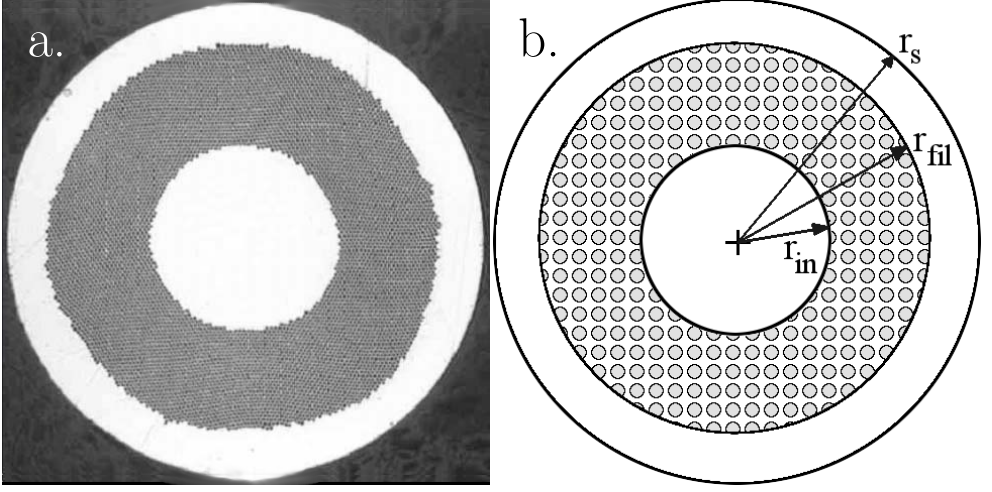


Figure 2.3. Cross-section of the strand used in the cable of the outer layer of the LHC main dipole magnets [23]. a. Photography. b. Schematic representation.

strand is exposed to a magnetic-field change, different inter-filament coupling loss is generated in the volume of the inner stabilizer core ( $0 < r < r_{\text{in}}$ , see figure 2.3b), of the annular ring where the superconducting filaments are located ( $r_{\text{in}} < r < r_{\text{fil}}$ ), and in the outer stabilizer shell ( $r_{\text{fil}} < r < r_{\text{s}}$ ). Following the treatise presented in [104, 105], these three loss contributions, per unit volume of strand, are

$$P_{\text{in}}''' = \left( \frac{l_f}{2\pi} \right)^2 \frac{1}{\rho_m} \frac{r_{\text{in}}^2}{r_s^2} \left( \frac{dB_t}{dt} \right)^2, \quad [\text{Wm}^{-3}] \quad (2.26)$$

$$P_{\text{fil}}''' = \left( \frac{l_f}{2\pi} \right)^2 \frac{1}{\rho_{\text{eff,fil}}} \left( \frac{r_{\text{fil}}^2 - r_{\text{in}}^2}{r_s^2} \right) \left( \frac{dB_t}{dt} \right)^2, \quad [\text{Wm}^{-3}] \quad (2.27)$$

$$P_{\text{out}}''' = \left( \frac{l_f}{2\pi} \right)^2 \frac{1}{\rho_m} \left( \frac{r_s^2 - r_{\text{fil}}^2}{r_s^2 + r_{\text{fil}}^2} \right) \left( \frac{dB_t}{dt} \right)^2, \quad [\text{Wm}^{-3}] \quad (2.28)$$

where  $\rho_{\text{eff,fil}}$  [ $\Omega\text{m}$ ] is the effective transverse resistivity in the region occupied by the bundle of filaments. Its value is comprised in the range between the two extremes defined in equation 2.20.

Thus, equation 2.25 can still be used for the calculation of the power per unit volume of strand generated by inter-filament coupling loss, if the value of  $f_{\text{eff}}$  is corrected as follows:

$$f_{\text{eff}} = \frac{\rho_{\text{eff}}}{\rho_m} = \left[ \frac{r_{\text{in}}^2}{r_s^2} + \frac{1}{\rho_{\text{eff,fil}}} \left( \frac{r_{\text{fil}}^2 - r_{\text{in}}^2}{r_s^2} \right) + \left( \frac{r_s^2 - r_{\text{fil}}^2}{r_s^2 + r_{\text{fil}}^2} \right) \right]^{-1}. \quad (2.29)$$

The description of the transient following a CLIQ discharge is concluded with the analysis of the system evolution once the oscillations introduced by CLIQ are

completely damped, i.e.  $I_C \approx 0$ . During this transient, system 2.1 can be reduced to:

$$\begin{cases} I_A \approx I_B \approx I_M & [\text{A}] \\ (L_A + L_B + 2M_{AB})\dot{I}_A + (R_{C,A} + R_{C,B})I_A + U_D = 0. & [\text{V}] \end{cases} \quad (2.30)$$

Neglecting the limited voltage drop across the diode  $U_D$  during this transient, the magnet current is discharged following the relation:

$$\frac{dI_A}{dt} = \frac{dI_M}{dt} = -\frac{L_A + L_B + 2M_{AB}}{R_{C,A} + R_{C,B}}I_A = -\frac{L_M}{R_C}I_A = -\frac{I_A}{\tau_d}, \quad [\text{As}^{-1}] \quad (2.31)$$

where  $\tau_d$  [s] generally decreases during the discharge due to the increase of the electrical resistance of the normal zone in the coil windings following a quench.

## 2.3 Advantages

CLIQ is a new solution for the protection of superconducting magnets. With respect to conventional systems based on quench heaters, the main advantages of a CLIQ-based system are twofold. Firstly, it allows a faster and more effective energy deposition in the coil winding pack, which assures a quicker and more homogeneous quench initiation. Secondly, it features a simpler and more robust electrical design which results in a lower failure rate and an easier repair.

Its effective heating mechanism is a consequence of the generation of heat by coupling loss directly in the matrix of the superconducting strands, hence within the conductor insulation layer. On the contrary, conventional quench heaters rely on thermal diffusion across insulation layers, an inherently slower process.

Furthermore, the energy deposition in the strands is homogeneous along the conductor as long as the magnetic-field change is uniform, because the properties of superconducting strands show usually small longitudinal variation and hence the coupling loss is uniformly generated in the conductor. Quench heaters, instead, are usually size limited and generate only local heat in spot-like locations. Thus, CLIQ can transfer voluminous regions of the coil windings to the normal state in a short time. For this reason, CLIQ is especially well-suited for the protection of coils characterized by low normal zone propagation velocities.

As a result of the quick and uniform quench initiation achieved by CLIQ, the energy stored in the magnet is distributed rather uniformly in the winding pack. Furthermore, the fast development of the normal-zone resistance causes a quick discharge of the magnet current. Thus, the temperature reached in the coil hot-spot after a quench can be significantly decreased.

Moreover, CLIQ, being an external system, does not interfere with the coil winding technology. Quench-heater strips, on the other hand, need to be attached to the coil through thin insulation layers. This is considered a delicate and cumbersome process, in particular when quench heaters are attached to the inner layer of a coil, or between its layers. Once installed, the quench heaters are integral part of the coil windings and cannot be easily repaired nor replaced. Their insulation layer needs to be very thin,

in the order of a few tens of micrometer, in order to allow a sufficiently fast thermal diffusion. For this reason, they are prone to electrical shorts and burn-through. On the contrary, CLIQ is composed of simple and robust elements. Apart from the current-introducing leads, the system is located outside the cryostat where it is easily accessible and repairable. The CLIQ terminals are usually situated at the coil ends where in the case of damage they can be accessed relatively easily.

The CLIQ technology can be effectively applied to magnets with a wide range of coil geometries and strand types, and its installation work is rather straightforward. Thus, it can be implemented as an easy repair option on magnets with damaged quench heaters, hence avoiding costly and time-consuming repair work. It can be added to any magnet provided an additional current lead can be connected somewhere halfway between the standard coil terminals. Note that cost and dimensions of a CLIQ unit are fairly comparable with a conventional quench-heater unit.

The CLIQ technology already achieved a good level of maturity. In the last years it was successfully applied to various existing magnets of different geometry (quadrupole, dipole, solenoid), type of superconductor (Nb-Ti, Nb<sub>3</sub>Sn), and size (from small laboratory test magnets to full-scale magnets) [83–85, 89, 106–108]. Although none of these magnets was specifically optimized for CLIQ, the performance in terms of quench initiation and resulting hot-spot temperature was always very good. An even better performance can be expected if CLIQ is integrated in the magnet design from the start, allowing an optimum positioning of the current-introducing taps for maximizing the heat generation.

Eventually, it is possible that the superior protection offered by CLIQ may allow designing future magnets with reduced stabilizer-superconductor ratio, resulting in high current-density, more compact, cost-effective magnets, as explained in chapter 7.

## 2.4 Disadvantages

Since CLIQ introduces a magnetic-field change everywhere in the coil cross-section and along the magnet length, it generates coupling loss in the entire winding pack. This fast and simultaneous heat generation everywhere in the coil is the key ingredient to achieve highest performance using CLIQ. When a magnet is operated at low current, for example during the early stage of charging, the energy density in the coil is low and consequently the enthalpy margin to initiate a transition to the normal state significantly higher. In this low-current condition, a protection system depositing its initial energy in separate, well-distributed heating stations can be more effective than CLIQ, which deposits its energy more uniformly and thus requires larger initial stored energy to transfer to the normal state a similar volume of superconductor. However, in general protection at low current is not critical and CLIQ is able to perform even when less efficient than local heaters under these conditions.

The effectiveness of a CLIQ system is highly depending on the equivalent inductance of its discharge circuit, which is proportional to the coil length. Thus, the performance observed while testing short model magnets cannot be directly extended to the case of full-size magnets.

The installation and operation of a CLIQ-based protection system present various

aspects which need to be carefully considered during its design. First, since the terminals of a CLIQ unit are in direct contact with the conductor, the occurrence of a short circuit in the unit would have critical consequences, including the transfer of energy from the magnet circuit to the CLIQ system. For this reason, every action has to be taken to lower the probability of a full short circuit across the unit, even in the event of a short circuit in one of its elements. This is achieved, for instance, by implementing self-healing film capacitors and by including a fuse in series with the charging power supply.

The presence of extra direct electrical connections to the magnet circuit through the CLIQ terminals poses two potential issues. The oscillations of the magnet transport current provoked by CLIQ propagate to the main circuit and appropriate protection elements have to be installed across circuit elements (see for example the diode  $D_{PC}$  in figure 2.1). Relatively high voltages to ground and between coil sections are introduced in locations where they are otherwise not present; thus, an increase of the thickness of the layer-to-layer insulation or an improvement of its quality may be needed.

Naturally, the terminals connecting the CLIQ unit to the magnet represent the most critical element of the system. Since pulsed mechanical forces are expected due to the interaction between the oscillating currents and the background magnetic field, adequate mechanical support has to be guaranteed to the terminals, including robust and secure connection (for example soldering in combination with secure bolting and reinforcement).

Another important aspect is the presence of pulsed mechanical stresses caused by the unbalanced oscillating currents in the different coil sections. Whilst these stresses are usually of limited entity as compared to the overall mechanical stress due to the magnetic field of the coil, they have to be analyzed case by case.

Finally, the extra CLIQ leads constitute additional heat conducting paths between the coil and room temperature, resulting in a slightly increased cryogenic load. However, the leads only carry high current for a short time, hence their cross-section can be small and the extra cryogenic load acceptable.

## 2.5 Characteristic example of a CLIQ discharge

As explained in section 2.2, the electro-magnetic transient following a CLIQ discharge depends on three main categories of parameters:

- CLIQ unit parameters: charging voltage  $U_0$ ; capacitance of the capacitor bank  $C$ ; equivalent resistance of the discharge circuit  $R_{eq}$ ;
- magnet geometry parameters: equivalent inductance of the discharge circuit  $L_{eq}$ ; geometric factors  $f_{g,A}$ ,  $f_{g,B}$ ; magnetic parameters  $f_{x,A}$ ,  $f_{x,B}$ ,  $f_{y,A}$ ,  $f_{y,B}$ , for each strand;
- strand parameters: filament twist-pitch  $l_f$ ; effective transverse resistivity of the matrix  $\rho_{eff,x}$ ,  $\rho_{eff,y}$ , for each strand.

In this section a sample calculation is presented of the current change, magnet-field changes, and inter-filament coupling loss introduced by CLIQ. The example is based

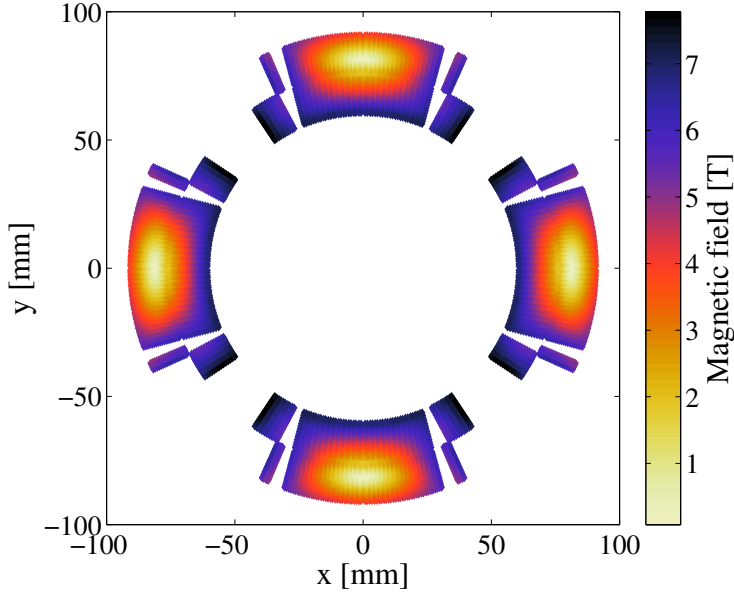


Figure 2.4. Calculated initial magnetic field  $B_{a,0}$  in the quadrupole coil cross-section ( $I_0=12.6$  kA).

on the geometry of a Nb-Ti quadrupole accelerator magnet composed of four blocks of windings in two layers [83, 106, 109, 110].

Let P1-P4 be the four magnet poles, ordered counter-clockwise. The poles are connected in series, following the order P1-P3-P4-P2. Thus, when a CLIQ unit is connected to the midpoint of the magnet, the sections  $L_A$  and  $L_B$  shown in figure 2.1 are composed of P1-P3 and P2-P4, respectively. The equivalent inductance of the CLIQ discharge circuit is calculated using equation 2.4;  $L_A=L_B=2.7$  mH and  $M_{AB}=1.5$  mH yield  $L_{eq}=0.57$  mH. Since the discharge circuit is symmetric, the geometrical parameters introduced in equations 2.8-2.9 are simply  $f_{g,A}=-f_{g,B}=1/2$ . The equivalent resistance of the discharge circuit is conservatively assumed  $R_{eq}=50$  m $\Omega$ . The filament twist-pitch  $l_f$  is 15 mm. Finally, the effective transverse resistivity of the matrix of the copper stabilizer is calculated with equation 2.19, assuming  $f_{eff,x}=f_{eff,y}=1$  and experimental parameters  $c_0=1.7 \cdot 10^{-10}$   $\Omega\text{m}$  and  $c_1=4.2 \cdot 10^{-11}$   $\Omega\text{mT}^{-1}$ .

Figure 2.4 shows the initial magnetic field distribution  $B_{a,0}$  in the quadrupole coil cross-section, assuming an initial current of  $I_0=12.6$  kA, corresponding to the magnet nominal current. The enthalpy per unit volume  $W_q'''$  [ $\text{Jm}^{-3}$ ] required to initiate a transition to the normal state, shown in figure 2.5, is calculated based on this magnetic-field distribution, an initial homogeneous temperature of  $T_0=1.9$  K, and the physical properties of the conductor [109, 110]. At this current level it ranges between  $50 \mu\text{Jmm}^{-3}$  in the high-field inner layer and  $220 \mu\text{Jmm}^{-3}$  in the low-field, mid-plane outer region. Note that about 90% of this enthalpy is due to the heat capacity of superfluid helium which fills the voids in the cable and accounts for about

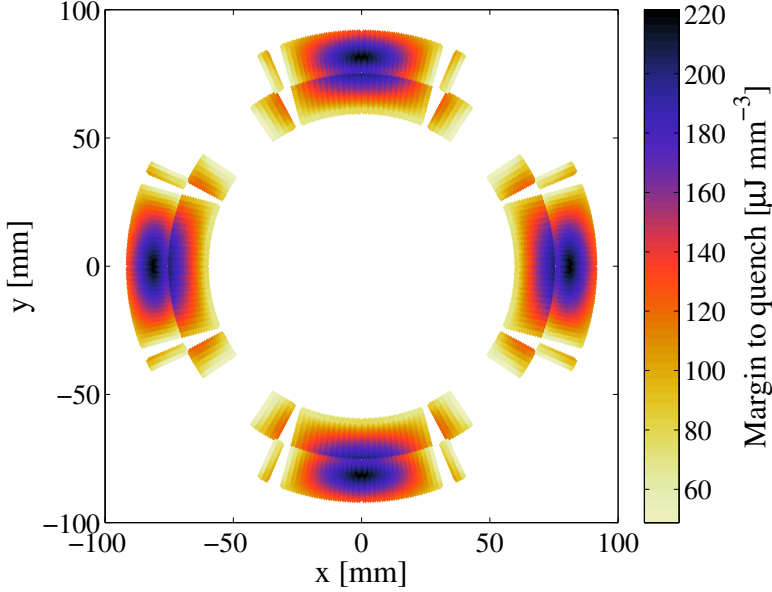


Figure 2.5. Calculated enthalpy per unit volume  $W_q'''$  required to initiate a transition to the normal state in the quadrupole coil cross-section ( $I_0=12.6$  kA).

5% of its volume.

For a given magnet and positioning of the CLIQ terminals, the electrical transient after triggering depends on the characteristic parameters of the unit. Figure 2.6 shows the effect of the charging voltage and capacitance of the capacitor bank on the current  $I_C$  introduced in the magnet. According to equation 2.7, the introduced current is proportional to the charging voltage. Its peak value, reached after a quarter of oscillation, is

$$I_{C,\text{peak}} = I_C \left( t = \frac{\pi}{2\omega} \right) = CU_0 \frac{\omega^2 + \alpha^2}{\omega} \exp \left( -\frac{\pi\alpha}{2\omega} \right), \quad [\text{A}] \quad (2.32)$$

which for  $\alpha \ll \omega$  reduces to  $I_{C,\text{peak}} \approx U_0 \sqrt{C/L_{\text{eq}}}$ . Hence, for a given coil the peak discharged current is roughly proportional to the square root of the capacitance of the CLIQ capacitor bank.

The initial current change is a key parameter for CLIQ performance. By differentiating equation 2.7, one obtains

$$\frac{dI_C}{dt}(0) = CU_0 (\omega^2 + \alpha^2), \quad [\text{A}] \quad (2.33)$$

which for  $\alpha \ll \omega$  reduces to  $dI_C/dt(0) \approx U_0/L_{\text{eq}}$ . As an example, in figure 2.6 one can observe that the initial rate of change of the introduced current doubles for a doubled CLIQ charging voltage but is unchanged for a doubled value of the CLIQ capacitance.



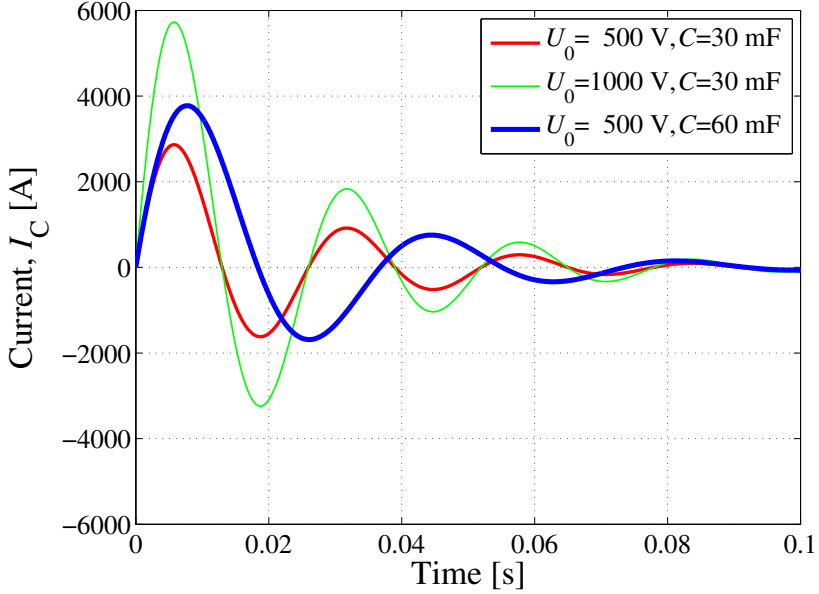


Figure 2.6. Calculated current discharged by CLIQ,  $I_C$  for varying  $U_0$  and  $C$ .

For a given coil and CLIQ configuration the time period of the system oscillations is only depending on the capacitance of the CLIQ unit,  $t_\omega = 2\pi\sqrt{L_{eq}C}$  [s].

The charging voltage and capacitance of the CLIQ capacitor bank determine the total energy stored in the CLIQ unit,  $E_{CLIQ} = 0.5CU_0^2$  [J].

The absolute magnetic-field change generated in each strand of the coil is proportional to the introduced current and to the characteristic parameters  $f_{CLIQ}$  introduced equation 2.14. These parameters depend on the coil geometry, the electrical order of its sections (poles, layers), and the positioning of the CLIQ terminals. Figure 2.7 shows the distribution of  $f_{CLIQ}$  in the coil cross-section. The four regions at the edge between each pole with high value of  $f_{CLIQ}$  are developed due to the superposition of the magnetic fields generated by adjacent poles. In fact, each pole generates a magnetic field with opposite direction in its coil and in the coil of the adjacent poles. Remember that in this example due to the electrical order of the four poles the same current-change is introduced in the pair of poles P1-P3 and P2-P4. In chapter 3 it is thoroughly described how to maximize  $f_{CLIQ}$  by changing the configuration of the CLIQ discharge circuit.

The heat per unit volume deposited in the superconductor by inter-filament coupling loss  $W_{if}'''$  [ $Jm^{-3}$ ] can be calculated by numerically integrating over time equation 2.24 for each strand. Figure 2.8 shows an example of such a calculation. The distribution of the energy per unit volume deposited in the first 50 ms after triggering CLIQ is plotted for the case  $U_0=500$  V,  $C=50$  mF, and  $l_f=15$  mm. As expected, the inter-filament coupling loss profile is primarily dependent on the value of  $f_{CLIQ}$ . A large part of the loss is deposited in the four mid-plane regions.

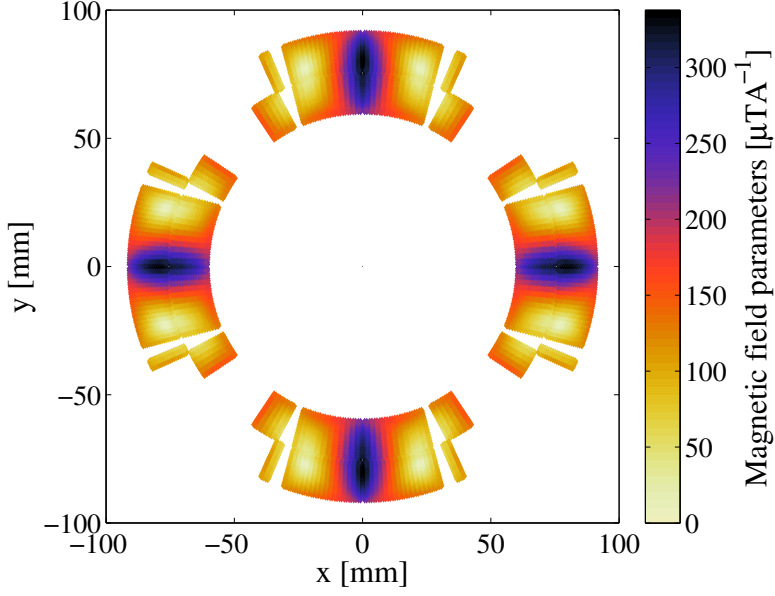


Figure 2.7. Calculated distribution of the parameter  $f_{\text{CLIQ}}$  in the quadrupole coil cross-section.

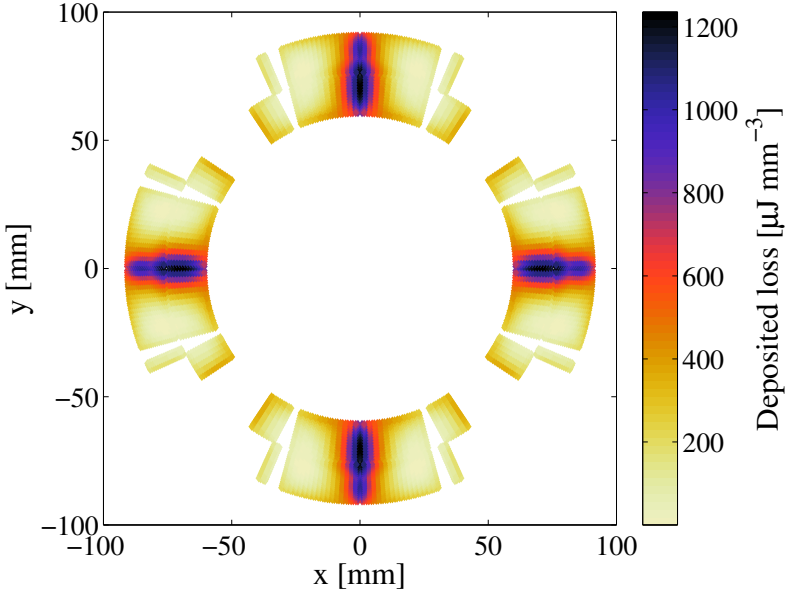


Figure 2.8. Calculated distribution of the inter-filament coupling loss per unit volume  $W'''_{\text{if}}$  deposited during the first 50 ms after triggering CLIQ ( $U_0=500$  V,  $C=50$  mF,  $l_t=15$  mm).

Given the very efficient heat diffusion between adjacent strands of the same cable, occurring in a time scale shorter than 1 ms [113,114], the assumption of homogeneous temperature of the strands of the same cable during a CLIQ discharge is satisfactory. It can therefore be assumed that the strands in a cable are transferred to the normal state simultaneously. Due to the transposition of the cable strands, each strand occupies the highest magnetic-field position within the cable cross-section twice every strand twist-pitch length. Thus, the relevant quantity to assess the initiation of a coupling-loss induced normal zone is the average loss deposition in the strands of each cable,  $W'''_{\text{if,c,ave}}$  [ $\text{Jm}^{-3}$ ], as compared to the energy required to increase the temperature of the conductor up to the current-sharing temperature of the strand with the lowest margin to normal state in the cable cross-section,  $W'''_{\text{q,c,min}}$  [ $\text{Jm}^{-3}$ ]. A conservative approach consists in considering that also the cable insulation layers and eventual resin or helium in the cable are in perfect thermal contact with the strands. Following this assumption, the energy per unit volume required to initiate a transition to the normal state is considerably higher.

By comparing the average coupling loss per unit volume generated by CLIQ in each cable to the specific enthalpy required to initiate a normal zone shown in figure 2.5, it can be concluded that the amount of energy deposited by CLIQ is largely sufficient to transfer large areas of the winding pack to the normal state in a very short time. Figure 2.9 shows the time required to transfer to the normal state each superconducting cable with the energy deposited by CLIQ, i.e. the time when  $W'''_{\text{if,c,ave}} > W'''_{\text{q,c,min}}$ . The strands located in the mid-plane of the magnet are transferred to the normal state in about 3 ms, and about half of the entire winding pack in less than 10 ms. After 30 ms only 10 to 15% of the conductor is still in the superconducting state. Note that the loss generation, and hence the heat-deposition profile, is uniform along the straight part of the coil.

The presented calculation is valid for given values of transverse resistivity and filament twist-pitch. However, the total magnetic-field change and resulting inter-filament coupling loss in the strands strongly depend on the characteristic time constant of the inter-filament coupling currents  $\tau_{\text{if}}$  [s] introduced in equation 2.18, which is proportional to the square of the filament twist-pitch. Figure 2.10 shows the calculated magnetic-field change in the  $x$  direction introduced in a selected strand located in the mid-plane region of the inner layer of the magnet, for different values of filament twist-pitch. The time constant for the selected strand is 1.5, 13.7, and 124 ms for a filament twist-pitch of 5, 15, and 45 mm, respectively.

Note that the applied magnetic-field change  $dB_{\text{a,x}}/dt$  is independent on the filament twist-pitch; its initial value is  $dB_{\text{a,x}}/dt(0) \approx f_{\text{CLIQ,x}} U_0 / L_{\text{eq}}$  for  $\alpha \ll \omega$ . Instead, the initial value of the total magnetic-field change  $dB_{\text{t,x}}/dt$  is always zero due to the presence of the magnetic-field change induced by the coupling currents which opposes to an instantaneous variation of the magnetic field.

The evolution of  $dB_{\text{t,x}}/dt$  depends on the inter-filament coupling current time-constant which characterizes the time required to reach a constant value of total magnetic-field change, i.e.  $dB_{\text{if,x}}/dt=0$ . As described by equation 2.22, if the coupling time-constant is much smaller than the typical period of oscillation of the magnetic field, the total magnetic-field change closely follows the applied magnetic-field change,  $dB_{\text{t,x}}/dt \approx dB_{\text{a,x}}/dt$ ; this behavior is observed for the case

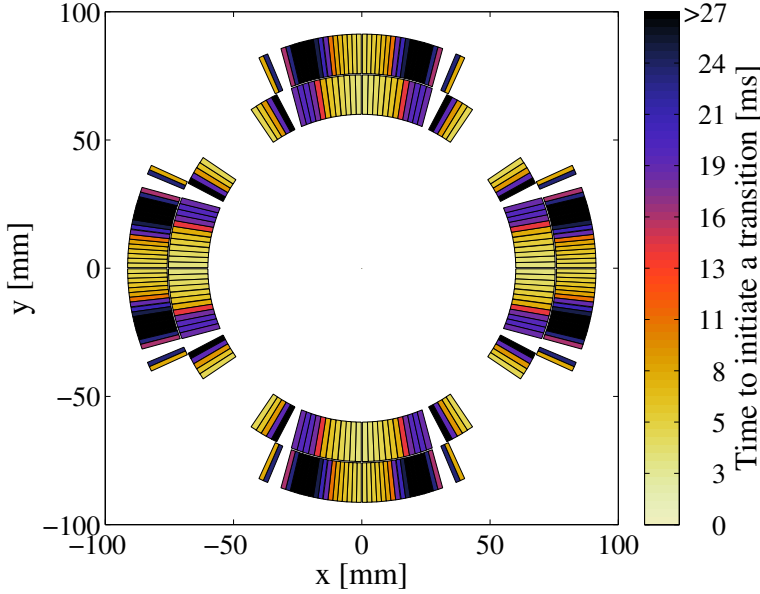


Figure 2.9. Calculated time required to initiate a transition to the normal state in each superconducting cable ( $I_0=12.6$  kA,  $U_0=500$  V,  $C=50$  mF,  $l_f=15$  mm).

$l_f=5$  mm shown in figure 2.10. On the contrary, for values of the time constant in the same range of the oscillation period or larger, the introduced total magnetic-field change is significantly reduced. As an example, in the presented case the peak value of  $dB_{t,x}/dt$  is reduced to about 31 and 4% of the peak applied magnetic-field change for a filament twist-pitch of 15 and 45 mm, respectively.

The inter-filament coupling loss generated for the same magnetic-field change is also proportional to the coupling-currents time constant, as shown in equation 2.24. Thus, in strands characterized by a larger time constant more inter-filament coupling loss is generated, but more slowly. Figure 2.11 shows the deposited loss calculated for the three cases previously introduced. The loss generated in the first 50 ms after triggering CLIQ is increased by 19% for a filament twist-pitch of 15 instead of 5 mm, because the reduction of magnetic-field change is compensated by the higher coupling-loss per rate of change of total magnetic field.

Note that the oscillation frequency of the applied magnetic field is the same in the entire magnet, but each of its strands is characterized by a different time constant due to magneto-resistivity effects. For this reason, and due to the complex relation between inter-filament coupling loss and its characteristic time-constant, the value of filament twist-pitch which maximizes the deposited loss in the entire winding pack is not easily found analytically. A convenient approach consists in computing numerically the time-integral of equation 2.24 for each strand of the coil, for different values of filament twist-pitch and capacitance of the capacitor bank.

The results of such calculation are presented in figure 2.12. The inter-filament coupling loss deposited during the first 50 ms after triggering CLIQ, averaged over

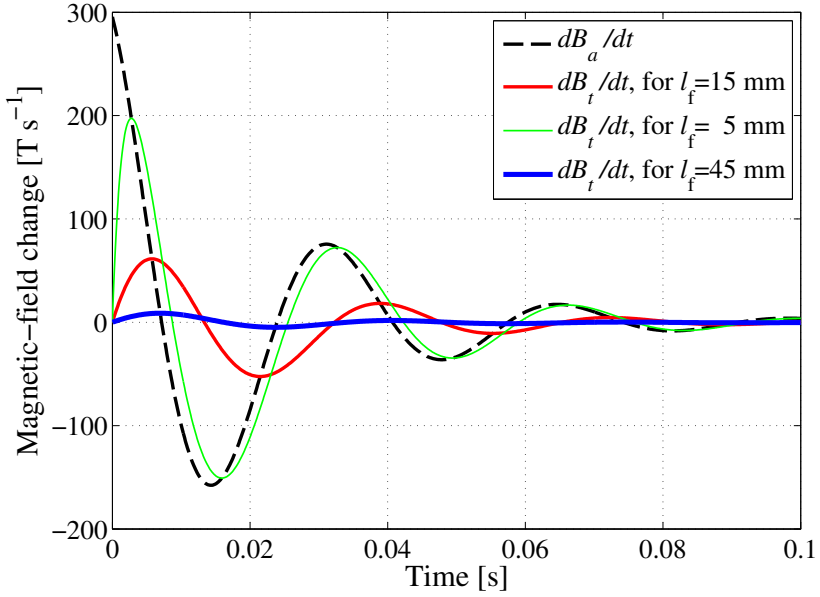


Figure 2.10. Calculated applied magnetic-field change  $dB_{a,x}/dt$  and resulting total magnetic-field change  $dB_{t,x}/dt$  in a selected strand, versus time, for three values of filament twist-pitch  $l_f$  ( $I_0=12.6$  kA,  $U_0=500$  V,  $C=50$  mF).

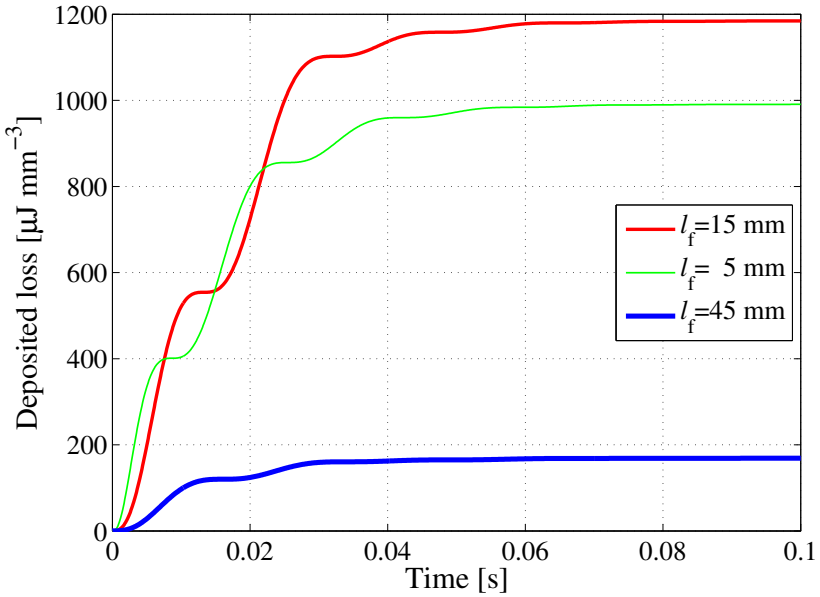


Figure 2.11. Calculated inter-filament coupling loss per unit volume  $W_{if}'''$  deposited by CLIQ in a selected strand, versus time, for three values of filament twist-pitch  $l_f$  ( $I_0=12.6$  kA,  $U_0=500$  V,  $C=50$  mF).

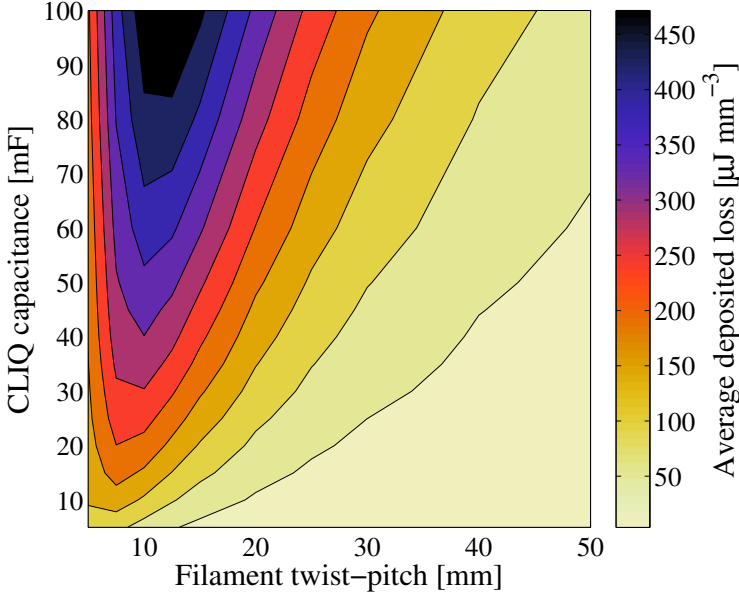


Figure 2.12. Calculated inter-filament coupling loss per unit volume  $W'''_{if}$  deposited during the first 50 ms after triggering CLIQ, averaged over the entire magnet volume, for varying filament twist-pitch  $l_f$  and capacitance  $C$  ( $I_0=12.6$  kA,  $U_0=500$  V).

the entire magnet volume, is calculated for filament twist-pitch and capacitance of the capacitor bank in the range 5 to 50 mm and 5 to 100 mF, respectively.

The average deposited loss monotonously increases with the capacitance of the capacitor bank. This is easily explained considering that the total energy stored in the capacitor bank is proportional to its capacitance. The system oscillation period is proportional to  $\sqrt{C}$ ; hence, for larger capacitance the peak loss deposition is maintained for a longer time.

An optimum value of the filament twist-pitch exists for maximizing the deposited inter-filament coupling loss for given values of capacitance and charging voltage, equivalent inductance and resistance of the discharge circuit, and effective transverse resistivity. The optimum value of the filament twist-pitch is in the range 5 to 30 mm for a wide variety of magnets. It increases for CLIQ systems oscillating at lower frequency, hence with higher equivalent inductance and capacitance of the capacitor bank.

The process presented in this section is useful to estimate the performance of a CLIQ-based protection system with small computation effort. However, analytical calculations are often not sufficiently precise due to the presence of non-linear dynamic effects such as the dependence of the magnet differential self-inductance on the frequency [84, 111, 112, 115, 117–120] and residual magnetization in the superconductor [116]. In fact, the CLIQ working frequency is typically in the range 5 to 100 Hz where these effects have a significant impact on the behavior of a superconducting magnet. Thus, the process of designing a CLIQ-based protection

system must include a detailed electro-magnetic simulation of its behavior. In chapter 4, a new modelling technique aimed at reproducing the dynamic effects in a superconducting magnet due to the presence of coupling-current effects is presented [95].

## 2.6 Conclusion

A complete description of the electro-magnetic and thermal transient occurring in a superconducting coil during and after a CLIQ discharge is presented, to be used as a reference for the future implementation of this technology. The electrical circuit of a CLIQ system connected to a coil can be represented by an equivalent RLC circuit.

The charging voltage and the capacitance of the CLIQ capacitor bank, together with the equivalent self-inductance of the discharge circuit, determine the oscillation frequency and the maximum value reached by the introduced oscillating current.

CLIQ performance is mostly determined by the generation of inter-filament coupling loss in the superconductor, which is the most reliable and effective mechanism to generate transitory loss during the first tens of millisecond after the triggering. Thus, the strand parameters, namely the filament twist-pitch and the effective transverse resistivity of the matrix, depending on its RRR and magneto-resistivity, are key parameters for CLIQ technology.

A characteristic CLIQ discharge is analyzed in order to describe more in detail the complex interaction between the introduced current-change, the generated magnetic-field changes, and the resulting inter-filament coupling loss. The main observations are:

- CLIQ performance depends strongly on the charging voltage  $U_0$ ; in fact, both the peak power density and the total energy deposited are proportional to  $U_0$ ;
- increasing the capacitance  $C$  improves the performance since the total energy deposited is proportional to  $C$ ; besides, the oscillation period is proportional to  $\sqrt{C}$ , hence for larger capacitance the peak loss deposition is maintained for a longer time;
- an optimum value of the filament twist-pitch  $l_f$  exists for maximizing the deposited inter-filament coupling loss for given values of capacitance and charging voltage, equivalent inductance and resistance of the discharge circuit, and effective transverse resistivity.

A crucial aspect of CLIQ implementation is the design of its discharge circuit, object of the next chapter, which depends on the coil geometry, the electrical order of the coil sections, and the number and positioning of CLIQ units.





## Chapter 3

# Optimization of the CLIQ discharge circuit

*The performance of a CLIQ-based protection system is highly dependent on the configuration of its discharge circuit. The positioning of the CLIQ connections to the coil, the electrical order of the coil sections, and the installation of multiple CLIQ units can effectively reduce the equivalent impedance of the circuit and achieve a more effective distribution of the deposited energy in the coil windings.*

### 3.1 CLIQ effectiveness, $\Psi$

CLIQ limits the temperature reached in the magnet hot-spot after a transition to the normal state by more homogeneously distributing the magnet energy in its coil windings. This is achieved by very quickly transferring to the normal state voluminous regions of the coil. Thus, the overall CLIQ performance is strongly influenced by the power deposition introduced immediately after the quench detection and triggering of CLIQ.

As explained in section 2.2, the most reliable CLIQ energy-deposition mechanism is the inter-filament coupling loss, which in accordance with equation 2.25 is proportional to the square of the filament twist pitch,  $l_f$  [m], to the inverse of the effective transverse resistivity of the stabilizer matrix,  $\rho_{\text{eff}}$  [ $\Omega\text{m}$ ], and to the square of the total magnetic-field change introduced by the discharge,  $dB_t/dt$  [ $\text{Ts}^{-1}$ ]. For a given strand, only the latter can be optimized by varying the electrical parameters and the configuration of its discharge circuit. In chapter 7 it is presented how to optimize the magnet design in order to improve CLIQ performance. In many applications the conductor parameters are imposed by design and can only to a certain extent be included in the CLIQ optimization. The design of a CLIQ protection system for an existing magnet obviously cannot include a change of the coil conductor. For this

reason, optimizing the design of the discharge circuit for a given magnet is an essential ingredient of the CLIQ technology.

Following the treatise presented in sections 2.2 and 2.5, one can conclude that in first approximation the peak power density deposited by CLIQ in a wire, or in a strand of a cable, achieved immediately after triggering, is proportional to

$$\begin{aligned} P'''_{\text{if,peak}} &= \left( \frac{l_f}{2\pi} \right)^2 \frac{1}{\rho_{\text{eff}}} \left( \frac{dB_{\text{t,peak}}}{dt} \right)^2 \\ &\propto \left( \frac{dB_{\text{a,peak}}}{dt} \right)^2 \quad [\text{Wm}^{-3}] \quad (3.1) \\ &= \left( f_{\text{CLIQ}} \frac{dI_{\text{C,peak}}}{dt} \right)^2 = \left( f_{\text{CLIQ}} \frac{U_0}{L_{\text{eq}}} \right)^2, \end{aligned}$$

where  $dB_{\text{t,peak}}/dt$  and  $dB_{\text{a,peak}}/dt$  [ $\text{Ts}^{-1}$ ] are the peak total and applied magnetic-field changes in each strand, following equations 2.15 and 2.22, respectively,  $dI_{\text{C,peak}}/dt$  [ $\text{As}^{-1}$ ] is the peak change-rate of the introduced current,  $U_0$  [V] is the charging voltage,  $f_{\text{CLIQ}}$  [ $\text{TA}^{-1}$ ], presented in equation 2.14, is a parameter expressing the magnetic field generated by the CLIQ introduced current, and  $L_{\text{eq}}$  [H] is the equivalent inductance of the discharge circuit, defined in equation 2.4. The relation between  $dB_{\text{t}}/dt$  and  $dB_{\text{a}}/dt$  depends on the strand characteristics, which determine the time constant of the inter-filament coupling currents, and is thoroughly analyzed in section 2.2. Instead, the applied magnetic-field change is independent of the strand and cable parameters. Equation 3.1 can be rewritten as

$$P'''_{\text{if,peak}} \propto \left( \frac{f_{\text{CLIQ}} U_0}{L'_{\text{eq}} l_{\text{m}}} \right)^2, \quad [\text{Wm}^{-3}] \quad (3.2)$$

where  $l_{\text{m}}$  [m] is the magnetic length and  $L'_{\text{eq}}$  [ $\text{Hm}^{-1}$ ] is the equivalent inductance per unit length of the CLIQ discharge circuit. Note that from equation 2.4 it follows

$$L'_{\text{eq}} = \frac{L'_A L'_B - M'^2_{\text{AB}}}{L'_A + L'_B + M'_{\text{AB}}}, \quad [\text{Hm}^{-1}] \quad (3.3)$$

where  $L'_A$  and  $L'_B$  [ $\text{Hm}^{-1}$ ] are the self-inductances of the two coil sections of the discharge circuit,  $L_A$  and  $L_B$ , per unit length, and  $M'_{\text{AB}}$  [ $\text{Hm}^{-1}$ ] their mutual inductance, per unit length.

The power deposited during a CLIQ discharge is proportional to the square of the capacitor charging voltage, which is usually limited for risk limiting reasons, and inversely proportional to the square of the magnet length, which is defined by magnet design. However, methods exist for minimizing  $L'_{\text{eq}}$  and optimizing the distribution of  $f_{\text{CLIQ}}$  in the coil cross-section by varying the CLIQ discharge circuit. The primary figure of merit for assessing the performance of a CLIQ discharge circuit is the CLIQ effectiveness, here defined as

$$\Psi \equiv \frac{f_{\text{CLIQ}}}{L'_{\text{eq}}}. \quad [\text{m}^{-1}] \quad (3.4)$$

The effectiveness is a measure for the distribution of the peak applied magnetic-field change obtainable in the various strands, per volt of capacitor

charging voltage and per meter of magnetic length. It is independent of the cable, strand parameters, and operating conditions of the CLIQ system, and is purely geometric apart from second-order non-linear effects such as iron-yoke saturation and dynamic inductive effects related to the coupling-loss time-constants. Thus, in first approximation the square of  $\Psi$  is proportional to the peak coupling loss per unit volume developed by the current-change introduced by CLIQ. Interestingly, the CLIQ effectiveness has no effect on the total energy delivered to the coil, which only depends on the operating parameters of the CLIQ system, but only on the rate of transfer of such energy to the strands, i.e. the power generated per unit volume.

Whilst the CLIQ effectiveness does not provide quantitative information about the actual coupling loss generated in the strands, it is a convenient means to compare the relative performance of different configurations of the CLIQ discharge circuit. The distribution of  $\Psi$  in the magnet cross-section and its maximum and average value have to be assessed. High magnetic-field, high energy-density coils can be protected by inducing a fast and homogeneous transition to the normal state in the coil windings, which can be achieved only by a rapid and uniform energy deposition in the coil strands; hence, for these coils the average  $\Psi$  is the quantity of highest interest. Coils operating at lower magnetic field have lower energy density and can be protected by transferring to the normal state a more limited amount of conductor, but a higher energy per unit volume is required to initiate the transition due to the higher margin to quench; thus, for these coils the quantity of highest interest is the maximum  $\Psi$  in the strands.

The distribution of the high- $\Psi$  regions in the coil has a significant impact on CLIQ performance. In fact, an optimal distribution can result in the development and propagation of multiple normal zones, and hence in a fast and uniform transition to the normal state. Configurations generating high coupling loss in regions comprising many turns are higher performing than configurations depositing high loss in many layers, due to the more numerous insulation barriers between turns rather than between layers. For instance, from sections 3.3.5 and 3.3.6 it will become clear that CLIQ is more effective on solenoids than on pancake coils.

The next sections include methods for optimizing the CLIQ effectiveness and their application to various magnet geometries.

### 3.2 Multi-CLIQ

A quench protection system composed of multiple CLIQ units (Multi-CLIQ) can offer considerable advantages. In fact, the equivalent inductance of the discharge circuit can be effectively reduced by connecting  $N_C$  CLIQ units across  $2N_C$  different branches of the magnet, which are therefore connected in parallel. The electrical transient following the simultaneous discharge of multiple units can be analyzed with the same method described in section 2.2 for a 1-CLIQ system. The dynamics of a 2-CLIQ system, like the one shown in figure 3.1, is described by a set of equations analogous to the set 2.1,

$$\left\{ \begin{array}{ll}
 (L_A + M_{AB} + M_{AD} + M_{AE})\dot{I}_A + (M_{AB} + L_B + M_{BD} + M_{BE})\dot{I}_B \\
 + (M_{AD} + M_{BD} + L_D + M_{DE})\dot{I}_D + (M_{AE} + M_{BE} + M_{DE} + L_E)\dot{I}_E \\
 + R_{C,A}I_A + R_{C,B}I_B + R_{C,D}I_D + R_{C,E}I_E + U_D = 0 & [V] \\
 U_{C1} = L_A\dot{I}_A + M_{AB}\dot{I}_B + M_{AD}\dot{I}_D + M_{AE}\dot{I}_E + R_{C,A}I_A + R_{eq,C1}I_{C1} & [V] \\
 U_{C2} = M_{AD}\dot{I}_A + M_{BD}\dot{I}_B + L_D\dot{I}_D + M_{DE}\dot{I}_E + R_{C,D}I_D + R_{eq,C2}I_{C2} & [V] \\
 I_A = I_B + I_{C1} & [A] \\
 I_D = I_E + I_{C2} & [A] \\
 I_B = I_E & [A] \\
 I_{C1} = -C_{C1}\dot{U}_{C1} & [A] \\
 I_{C2} = -C_{C2}\dot{U}_{C2} & [A]
 \end{array} \right. \quad (3.5)$$

with the following initial conditions:

$$\left\{ \begin{array}{ll}
 I_A(0) = I_B(0) = I_D(0) = I_E(0) = I_0 & [A] \\
 I_{C1}(0) = \dot{U}_{C1}(0) = 0 & [A] \\
 I_{C2}(0) = \dot{U}_{C2}(0) = 0 & [A] \\
 U_{C1}(0) = U_{0,1} & [V] \\
 U_{C2}(0) = U_{0,2}, & [V]
 \end{array} \right. \quad (3.6)$$

where  $I_A$ - $I_E$  [A] are the currents flowing in coil sections  $L_A$ - $L_E$ ,  $I_{C1}$  and  $I_{C2}$  [A] the current introduced by the two units C1 and C2,  $U_{C1}$  and  $U_{C2}$  [V] the voltage across C1 and C2,  $L_A$ - $L_E$  [H] the self-inductances of  $L_A$ - $L_E$ ,  $M_{AB}$ - $M_{DE}$  [H] their mutual inductances,  $R_{C,A}$ - $R_{C,E}$  [ $\Omega$ ] the electrical resistances of the normal-zones developed in  $L_A$ - $L_E$ ,  $C_{C1}$  and  $C_{C2}$  [F] the capacitances of the capacitor banks of C1 and C2,  $R_{eq,C1}$  and  $R_{eq,C2}$  [ $\Omega$ ] the equivalent resistances of the discharge circuits of C1 and C2, as defined in equation 2.3,  $U_D$  [V] the voltage drop across the diode  $D_{PC}$ ,  $I_0$  [A]

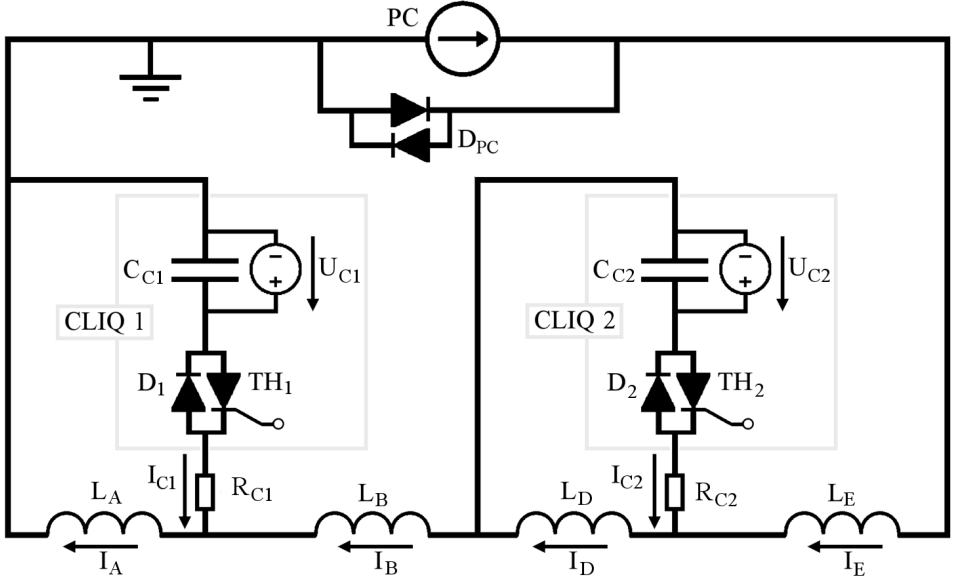


Figure 3.1. Example of a 2-CLIQ configuration connected to a coil composed of four sections  $L_A$ ,  $L_B$ ,  $L_D$ , and  $L_E$ .

the initial magnet transport current, and  $U_{0,1}$  and  $U_{0,2}$  [V] the initial charging voltage across C1 and C2.

The analytical solution, even for this relatively simple example, is ponderous and not practical. Nowadays, network-solver software exists that can efficiently simulate the electrical transient described by equations 3.5 and even more complex circuits.

The presence of symmetry in the geometry of a magnet circuit drastically simplifies the analysis of the system dynamics. If the CLIQ units have the same charging voltage and capacitance of the capacitor banks, and are connected symmetrically across coil sections with the same self- and mutual inductances, equations 3.5 reduce to a series RLC circuit described by

$$\ddot{I}_C + \frac{R_{eq2}}{L_{eq2}} \dot{I}_C + \frac{1}{L_{eq2} C_{tot}} I_C = 0, \quad [\text{As}^{-2}] \quad (3.7)$$

identical to equation 2.3 derived for a 1-CLIQ system, where  $I_C = I_{C1} + I_{C2}$  [A] is the total current discharged by the two units,  $C_{tot} = C_{C1} + C_{C2}$  [F] is the total capacitance of the system, and  $R_{eq2} = R_{eq1}/2$  [ $\Omega$ ] and  $L_{eq2} = L_{eq1}/4$  [H] are the equivalent resistance and inductance of the discharge circuit, respectively, calculated as fractions of the equivalent resistance and inductance of a 1-CLIQ system,  $R_{eq1}$  [ $\Omega$ ] and  $L_{eq1}$  [H]. Note that in this symmetric discharge circuit the current introduced by each of the two units is the same ( $I_{C1} = I_{C2} = I_C/2$ ).

Furthermore, in the case of  $N_C$  identical CLIQ units connected symmetrically across  $2N_C$  coil sections with the same self- and mutual inductances, the equivalent inductance per unit length is decreased proportionally to  $N_C^2$  [106, 121]. The total

capacitance of the system is increased by a factor  $N_C$ , and its equivalent resistance reduced by a factor  $N_C$ , since the units are also in parallel. Finally, since the total current introduced by all units is divided among symmetric branches, the current changes introduced in the various sections are  $\pm I_C/(2N_C)$ . Thus, in the case of a Multi-CLIQ system equation 3.2 becomes

$$P'''_{\text{if,peak}} \propto \left( f_{\text{CLIQ}} \frac{1}{N_C} \frac{dI_{C,\text{peak}}}{dt} \right)^2 = \left( N_C \frac{f_{\text{CLIQ}}}{L'_{\text{eq1}}} \frac{U_0}{l_m} \right)^2, \quad [\text{Wm}^{-3}] \quad (3.8)$$

where  $L'_{\text{eq1}}$  [ $\text{Hm}^{-1}$ ] is the equivalent inductance per unit length of a discharge circuit with a single unit. In the case of a Multi-CLIQ system the definition of CLIQ effectiveness is extended to

$$\Psi \equiv N_C \frac{f_{\text{CLIQ}}}{L'_{\text{eq1}}} = N_C \Psi_1, \quad [\text{m}^{-1}] \quad (3.9)$$

with  $\Psi_1 = f_{\text{CLIQ}}/L'_{\text{eq1}}$  the effectiveness of a system with a single unit. For a 1-CLIQ system, this definition reduces to equation 3.4.

In table 3.1 the main equations used to calculate the behavior of Multi-CLIQ systems are summarized [106]. For instance, the peak power deposition of a single unit can be increased by a factor four by either doubling the charging voltage of the unit or installing a second unit. However, the total energy stored in the entire system,  $E_{\text{CLIQ}}$ , is twice larger in one unit charged with double voltage than in two units. The reduction of the circuit equivalent impedance causes a quicker damping of the oscillations introduced in the magnet current. For this reason, the performance of a 1-CLIQ system charged with double voltage is higher than of a 2-CLIQ system, in particular when used for the protection of low energy-density, high-margin magnets. In fact, in this condition the total energy delivered to the coil has larger impact on the quench initiation than the peak power deposition.

The high and fast energy deposition required for protecting full-size accelerator magnets without increasing the charging voltage beyond acceptable limits makes the Multi-CLIQ solution very promising [89]. Note that an  $N_C$ -CLIQ system can achieve a peak power deposition  $N_C^2$  times higher than a 1-CLIQ system due to the reduction of the circuit impedance.

This reduction of  $L'_{\text{eq}}$  and related increase of power deposition is achieved only when the discharge circuit can be subdivided in a number of distinct coil sections  $N_S$  equal to or higher than  $2N_C$ . The net effect of installing more than  $N_S/2$  units is an increase of the total capacitance of the system. The  $N_S$  sections can be poles or layers in a single magnet, or even full magnets in a chain of magnets. By-pass elements such as a pair of anti-parallel connected diodes are required across the series of coil sections for allowing a path for the introduced oscillating current and avoiding propagating the high current change to other elements of the circuit, such as other magnets or the main power supply. Figure 3.2a shows an example of a 4-CLIQ system including back-to-back by-pass diodes.

In addition, it is possible to design a system capable of selectively initiating a transition to the normal state in individual coil sections. As shown in figure 3.2b, it is sufficient to install by-pass elements, such as passive resistors or a pair of

Table 3.1. Main equations used to assess the behavior of a 1-CLIQ protection system and correction coefficients for symmetric Multi-CLIQ systems with two units (2-C), four units (4-C), or a generic number of units ( $N_C$ -C). For comparison, also the coefficients for a 1-CLIQ charged with a voltage two times larger are shown (1-C,  $2U_0$ ). All symbols used in the table are defined in chapter 2.

Parameter	1-CLIQ	1-C, $2U_0$	2-C	4-C	$N_C$ -C
Parallel sections, $N_S$	2	=	$\times 2$	$\times 4$	$\times N_C$
$L'_{eq}$ [Hm $^{-1}$ ]	$L'_{eq1}$	=	$\times \frac{1}{4}$	$\times \frac{1}{16}$	$\times \frac{1}{N_C^2}$
$R_{eq}$ [ $\Omega$ ]	$R_{eq1}$	=	$\times \frac{1}{2}$	$\times \frac{1}{4}$	$\times \frac{1}{N_C}$
Total capacitance, $C_{tot}$ [F]	$C$	=	$\times 2$	$\times 4$	$\times N_C$
Charging voltage [V]	$U_0$	$\times 2$	=	=	=
$E_{CLIQ}$ [J]	$\frac{1}{2}CU_0^2$	$\times 4$	$\times 2$	$\times 4$	$\times N_C$
$\frac{dI_{A,peak}}{dt}, \frac{dI_{B,peak}}{dt}$ [As $^{-1}$ ]	$\pm \frac{U_0}{N_S L'_{eq1} l_m}$	$\times 2$	$\times 2$	$\times 4$	$\times N_C$
$P'''_{if,peak}$ [Wm $^{-3}$ ]	$\propto \left( \frac{U_0}{N_S L'_{eq1} l_m} \right)^2$	$\times 4$	$\times 4$	$\times 16$	$\times N_C^2$
$\Psi$ [m $^{-1}$ ]	$\frac{f_{CLIQ}}{L'_{eq1}}$	=	$\times 2$	$\times 4$	$\times N_C$
$I_{A,peak} - I_0$ [A]	$\propto \frac{U_0}{N_S} \sqrt{\frac{C_{tot}}{L'_{eq1} l_m}}$	$\times 2$	$\times \sqrt{2}$	$\times 2$	$\times \sqrt{N_C}$
$\omega$ [rad s $^{-1}$ ]	$\frac{1}{\sqrt{L'_{eq1} l_m C_{tot}}}$	=	$\times \sqrt{2}$	$\times 2$	$\times \sqrt{N_C}$
$\alpha$ [rad s $^{-1}$ ]	$\frac{R_{eq1}}{2L'_{eq1} l_m}$	=	$\times 2$	$\times 4$	$\times N_C$
$\zeta$	$\alpha/\omega$	=	$\times \sqrt{2}$	$\times 2$	$\times \sqrt{N_C}$

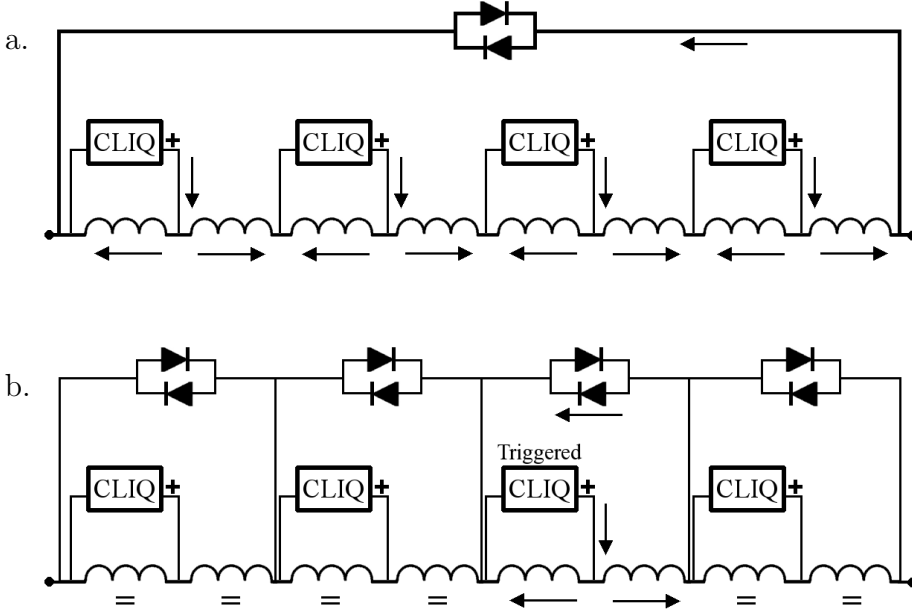


Figure 3.2. Examples of CLIQ-based protection of a multi-section coil. Arrows indicate the direction of the introduced current changes just after simultaneously triggering CLIQ; symbols "=" indicate no introduced current change. a. One 4-CLIQ module. b. Four 1-CLIQ modules. Only the unit protecting one coil section is triggered.

anti-parallel diodes, across each coil section. In the presented example, the CLIQ system is composed of four 1-CLIQ modules, each connected to the middle of a coil section. Upon detection of a quench in one section, the protection system can selectively initiate a fast transition to the normal state of the section where the quench is detected by triggering the respective CLIQ unit. The presence of the by-pass diodes effectively subdivides the coil and provides a return path for the current introduced by the triggered CLIQ unit. Thus, only a very limited current change is introduced in the other coil sections, not sufficient to initiate a transition to the normal state. The electrical resistance of the conductor in the normal state transfers the magnet transport current from the quenched coil to the by-pass element, while the transport current flows through the other coil sections still in the superconducting state.

As further discussed in chapter 8, this solution is also well suited for the protection of chains of superconducting magnets, such as the circuits of the main dipole and quadrupole magnets used in particle accelerators [23, 52, 122–125].



Table 3.2. Geometry, self-inductance per unit of magnetic length,  $L'_0$ , and nominal current,  $I_0$ , of the magnets analyzed as examples in this chapter.

Magnet geometry	$L'_0$ [Hm <sup>-1</sup> ]	$I_0$ [A]	References
One-layer cos- $\theta$ dipole	5.8 10 <sup>-3</sup>	12000	[126]
Two-layer cos- $\theta$ dipole	7.1 10 <sup>-3</sup>	11850	[80, 81, 127–130]
Two-layer cos- $\theta$ quadrupole	10.3 10 <sup>-3</sup>	17300	[131–134]
Block-coil dipole	5.9 10 <sup>-3</sup>	18600	[135–144]
Solenoid	185	350	
Pancake	185	350	
Chain of uncoupled magnets	-	-	-

### 3.3 Optimum discharge circuit for various magnet geometries

The CLIQ effectiveness depends on the magnet geometry, the positioning of the CLIQ terminals, and the electrical order of the coil elements such as magnet poles, layers, or blocks of turns. Common geometries adopted for superconducting magnets in particle accelerators, magnetic resonance imaging, and particle detectors are analyzed in order to identify the most effective configuration for each type of magnet. The self-inductance per unit of magnetic length  $L'_0$  [Hm<sup>-1</sup>] and nominal current  $I_0$  [A] of the magnets analyzed as examples for each geometry are summarized in table 3.2.

#### 3.3.1 One-layer cos- $\theta$ dipole

The simplest example of a CLIQ discharge circuit consists of a single unit connected to the middle of a one-layer, cos- $\theta$  dipole magnet. As a case study, the geometry of the beam separation dipole for the high-luminosity LHC is considered [126]. Figures 3.3a-b show the geometry of this magnet and the distribution of magnetic-field in its cross-section at nominal current.

If no terminals connected at the joint between individual stacks of cables are available, only two distinct coil sections are present, namely the two magnet poles. Hence, the maximum number of branches in the discharge circuit is two and only one unit can be installed ( $N_C=1$ ). Furthermore, only one configuration is available, where each of the two coil sections  $L_A$  and  $L_B$  (figure 2.1) is a pole of the magnet. Note that the two adimensional geometric parameters  $f_{g,A}$  and  $f_{g,B}$  occurring in equations 2.8 and 2.9 are simply  $\pm 1/2$  in this symmetric configuration. Thus, the current  $I_C$  discharged by CLIQ is equally divided between the two coil sections, and the absolute rates of change introduced are also equal,  $|dI_A/dt|=|dI_B/dt|=0.5|dI_C/dt|$ .

Figures 3.4a-b show the polarity of the current changes introduced in the coil windings by this Pole-Pole CLIQ configuration, together with the resulting CLIQ effectiveness in the strands. Note that in the mid-plane region two zones are developed where the effectiveness is highest, due to the superposition of the magnetic field generated by the two poles. Table 3.3 shows the equivalent inductance per unit

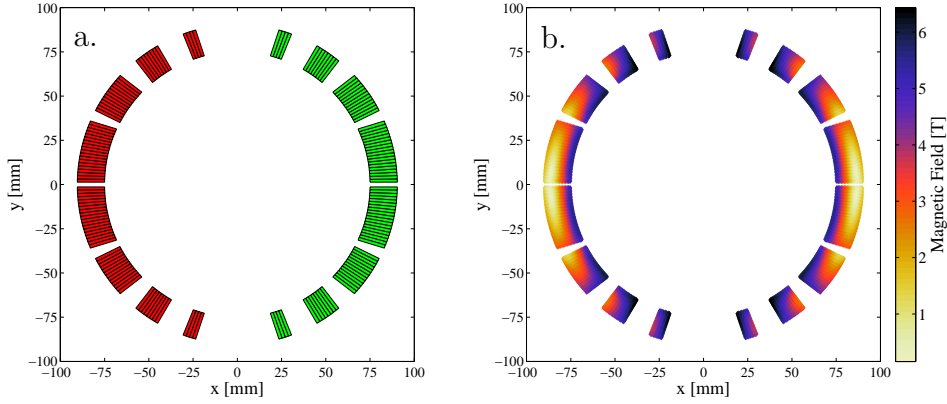


Figure 3.3. Stationary magnetic-field map in the analyzed one-layer dipole magnet. a. Polarity of the transport current. b. Magnetic field distribution ( $I_0=12$  kA).

Table 3.3. Equivalent inductance per unit length and CLIQ effectiveness of the analyzed CLIQ configuration for a one-layer dipole magnet.

Configuration	$L'_{eq1}$ [ $\mu\text{Hm}^{-1}$ ]	Max $\Psi$ [ $\text{m}^{-1}$ ]	Mean $\Psi$ [ $\text{m}^{-1}$ ]
Pole-Pole	556	0.56	0.21

length of the discharge circuit and the average and peak effectiveness in the strands.

For a one-layer dipole magnet with only one available CLIQ terminal between the two poles, no further optimization of the discharge circuit is possible (figure 3.4c). The performance of the system can only be improved by increasing the capacitance of the capacitor bank  $C$  [F] or its charging voltage. As mentioned in section 2.5, increasing  $C$  linearly enhances the total energy deposited during the entire discharge; however, the peak power deposition is unaffected by this modification.

For such a single-layer dipole magnet, the only other option to modify the CLIQ configuration is to include additional terminals attached to the cable sections between distinct stacks of cables. These terminals need a cross-section of a few square millimetres, because they only carry a pulsed current with an amplitude of a few kiloamperes for hundreds of milliseconds. Hence, it is relatively easy to include them in the magnet design, especially when positioning them in the coil heads where space is available.

### 3.3.2 Two-layer $\cos\theta$ dipole

In figures 3.5a-b the magnetic-field map of the 11 T dipole magnet for the high luminosity LHC is shown [80,81,127–130]. Coils with the same two-layer  $\cos\theta$  dipole geometry are composed of four distinct sections, namely the four layers. Hence, up to two CLIQ units can be connected to their coils, if terminals are made available at the two joints between two layers ( $1 \leq N_C \leq 2$ ). Table 3.4 summarizes the three possible CLIQ configurations that can be adopted for this geometry:

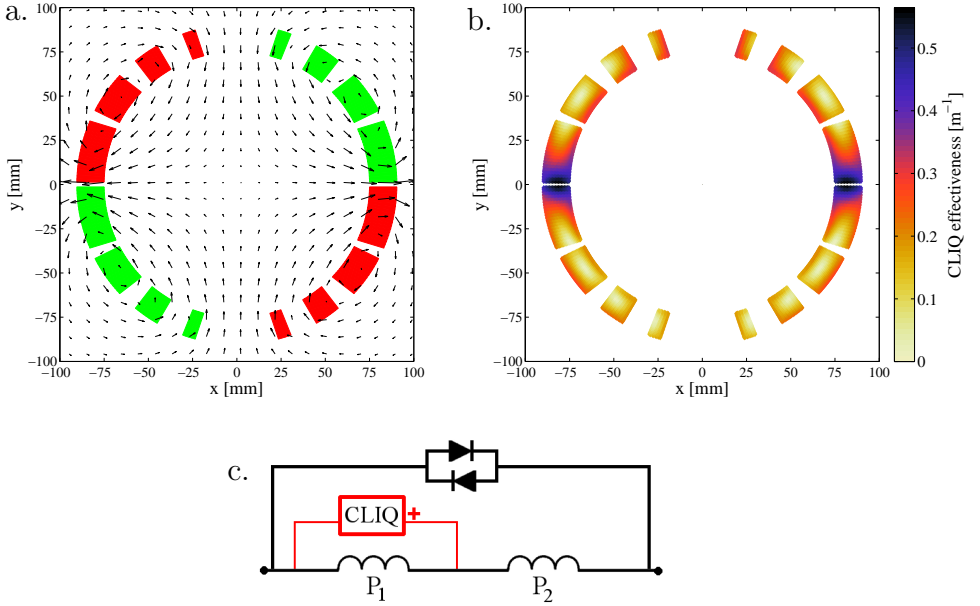


Figure 3.4. Example of the Pole-Pole CLIQ configuration applied to a 1-layer dipole magnet. a. Polarity of the current changes and direction of the magnetic-field changes introduced by CLIQ. b. CLIQ effectiveness,  $\Psi$ . c. Connection of CLIQ to a dipole magnet with electrical order  $P_1$ - $P_2$ .

- Pole-Pole, analogous to the configuration shown in the previous section, by which opposite current changes are introduced in the windings of the two poles (figures 3.6a-b);
- Layer-Layer, by which opposite current changes are introduced in the inner and outer layers (figures 3.6c-d);
- Cross-Layers, by which opposite current changes are introduced in all adjacent layers (figures 3.6e-f).

Note that the choice of configuration does not affect the magnet performance during stationary operation and is independent by the number of CLIQ units installed in the system. However, depending on the electrical order of the magnet layers, not all configurations can be easily implemented on existing magnets.

The impact of choosing for a certain CLIQ configuration is twofold: firstly, the equivalent inductance of the circuit can be greatly reduced; secondly, the CLIQ effectiveness peak value and its distribution in the magnet cross-section can be optimized. These advantages are both achieved when the discharge circuit is designed so as to introduce opposite current changes in coil sections which are physically adjacent. In fact, sections which are closer are more strongly magnetically coupled. As shown in equation 3.3, the equivalent inductance of the discharge circuit can be greatly reduced if the mutual inductance between the coil sections  $L_A$  and  $L_B$  is enhanced. Furthermore, each coil section generates magnetic fields with opposite

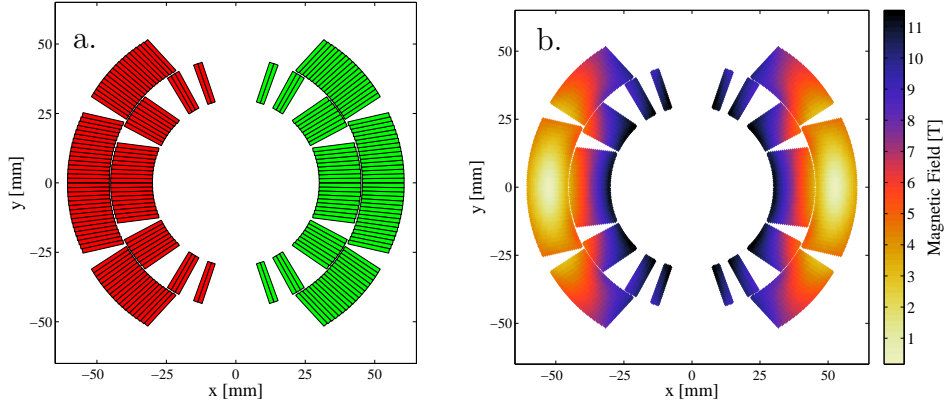


Figure 3.5. Stationary magnetic-field map in the analyzed two-layer dipole magnet. a. Polarity of the transport current. b. Magnetic field distribution ( $I_0=11.85$  kA).

Table 3.4. Equivalent inductance per unit length and CLIQ effectiveness of the analyzed CLIQ configurations for a two-layer dipole magnet.

Configuration	$L'_{eq1}$ [ $\mu\text{Hm}^{-1}$ ]	Max $\Psi$ [ $\text{m}^{-1}$ ]	Mean $\Psi$ [ $\text{m}^{-1}$ ]
Pole-Pole	581	0.78	0.32
Layer-Layer	186	1.77	0.69
Crossed-Layers	186	1.49	0.62

polarities in its turns and in the turns of the adjacent sections. Thus, opposite current changes discharged in adjacent coil sections effectively result in regions where the magnetic-fields generated by different sections superpose and a high coupling loss is developed.

This result becomes evident when comparing figures 3.6a-b, 3.6c-d, and 3.6e-f. As explained in section 2.5, the relevant quantity to consider when studying the initiation of a coupling-loss induced normal zone is the average loss deposition in the strands composing each cable, whose temperature in first approximation is uniform given the very fast intra-strand heat diffusion [113,114]. The choice of the Pole-Pole configuration results in two mid-plane zones with relatively high CLIQ effectiveness (figure 3.6b). However, both the Layer-Layer and the Crossed-Layers configurations allow reaching roughly twice higher CLIQ effectiveness and developing more extensive high- $\Psi$  regions which encompass the entire arc of the magnet. In these cases, the uniform distribution of strands characterized by high CLIQ effectiveness in the coil turns results in a highly homogeneous temperature increase in the entire winding pack.

Figures 3.7a-c show examples of implementation of the three above-mentioned CLIQ configurations. The order of the four coil sections ( $P_{1o}$ ,  $P_{1i}$ ,  $P_{2o}$ ,  $P_{2i}$ ), namely the outer and inner layers of the two poles, and the position of the CLIQ terminals are modified to obtain the desired discharge circuit. The discharge circuit is symmetric for the Pole-Pole and the Crossed-Layers configurations, because the coil sections  $L_A$

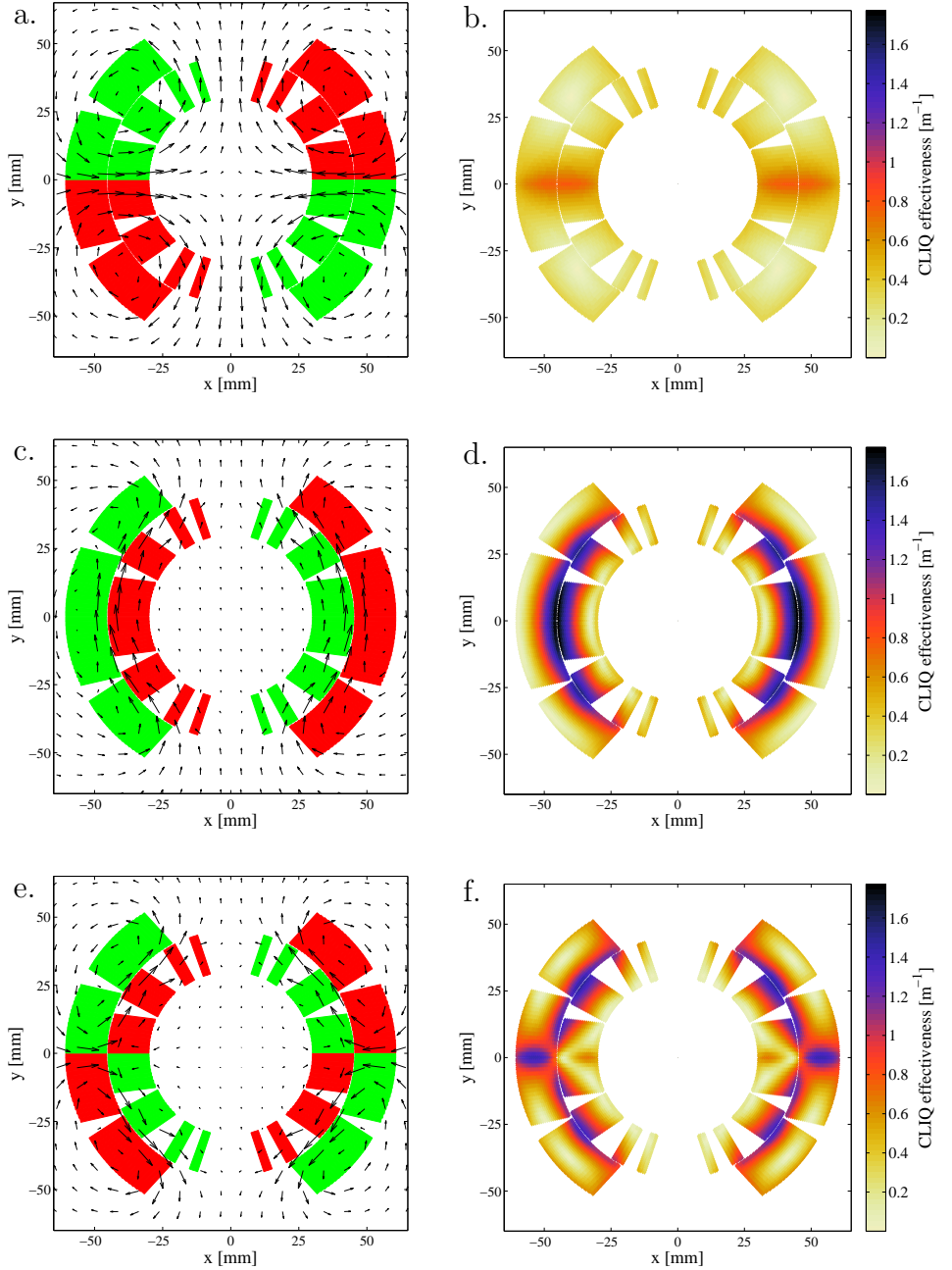


Figure 3.6. Example of CLIQ configurations applied to a two-layer dipole magnet. Polarity of the introduced current changes, direction of the introduced magnetic-field changes, and calculated CLIQ effectiveness,  $\Psi$ . a-b. Pole-Pole. c-d. Layer-Layer. e-f. Crossed-Layers.

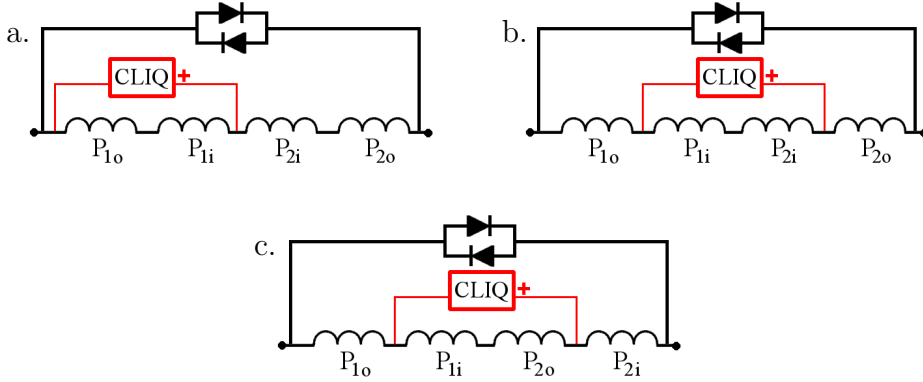


Figure 3.7. Examples of implementation of three different CLIQ configurations applied to a two-layer dipole magnet. a. Pole-Pole. b. Layer-Layer. c. Crossed-Layers.

and  $L_B$ , each composed of an outer and an inner layer, have the same impedance, i.e.  $f_{g,A} = -f_{g,B} = 1/2$ ; whereas in the Layer-Layer configuration the coil section composed by the two outer layers has a higher impedance and the resulting absolute current-changes introduced in  $L_A$  and  $L_B$  differ. The presence of an asymmetric discharge does not impede CLIQ operation. However, the voltages developed across the two sections, i.e. across the two pairs of layers, are inherently unbalanced and require to be carefully studied. In fact, the inner, high-magnetic field layer of the coil is transferred to the normal state more quickly due to the lower margin, its normal zone has higher electrical resistance due to the magneto-resistivity, and the inductive voltage across it is lower due to its smaller self-inductance.

### 3.3.3 Two-layer $\cos\theta$ quadrupole

Figures 3.8a-b show as example the geometry and field-map of a two-layer quadrupole magnet, namely the 150 mm aperture quadrupole magnet for the high-luminosity LHC [131–134]. Such a magnet is composed of eight distinct coil sections, namely the two layers in each of its four poles; thus, a CLIQ-based protection system can include up to four units ( $1 \leq N_C \leq 4$ ). Moreover, the magnetic elements and the CLIQ terminals can be arranged so as to form a number of alternative CLIQ discharge circuits. The most interesting configurations analyzed are:

- Upper-Lower-Poles, by introducing opposite current changes in the upper and lower poles of the magnet (figures 3.9a-b);
- Crossed-Poles, by introducing opposite current changes in all adjacent poles (figures 3.9c-d);
- Layer-Layer, by introducing opposite current changes in the inner and outer layers of the magnet (figures 3.10a-b);

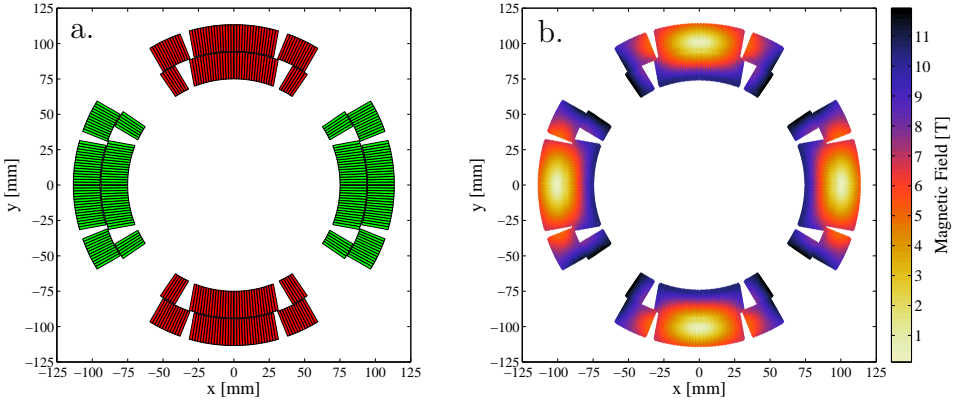


Figure 3.8. Stationary magnetic-field map in the analyzed two-layer quadrupole magnet. a. Polarity of the transport current. b. Magnetic field distribution ( $I_0=17.3$  kA).

Table 3.5. Equivalent inductance per unit length and CLIQ effectiveness of the analyzed CLIQ configurations for a two-layer quadrupole magnet.

Configuration	$L'_{eq1}$ [ $\mu\text{Hm}^{-1}$ ]	Max $\Psi$ [ $\text{m}^{-1}$ ]	Mean $\Psi$ [ $\text{m}^{-1}$ ]
Upper-Lower-Poles	2045	0.17	0.09
Crossed-Poles	827	0.43	0.17
Layer-Layer	347	0.86	0.40
Crossed-Layers	255	0.81	0.35

- Crossed-Layers, by introducing opposite current changes in all adjacent layers (figures 3.10c-d).

Table 3.5 summarizes the equivalent inductance and the performance of each analyzed configuration. As observed in the previous section, the highest performing configurations are those resulting in the introduction of opposite current changes in adjacent coil sections. Thus, analogously to the case of the dipole geometry, the Layer-Layer and the Crossed-Layers configurations are most effective.

Nevertheless, the majority of the existing magnets do not include accessible conductor sections between layers to which CLIQ terminals can be connected. In this case, only the Upper-Lower-Poles and the Crossed-Poles configurations can be implemented. Note that the magnet stationary performance is not affected by the chosen configuration, but the Crossed-Poles configuration significantly enhances the CLIQ effectiveness and shows an optimized distribution of the high- $\Psi$  regions in the coil windings.

This improvement in CLIQ effectiveness is a consequence of the reduction of the equivalent inductance of the discharge circuit, which can be explained by considering the self- and mutual inductances of the four poles. Let us define  $L'_s$  [ $\text{Hm}^{-1}$ ] as the self-inductance of one pole, per unit length;  $M'_a > 0$  [ $\text{Hm}^{-1}$ ] as the mutual inductance between adjacent poles, per unit length; and  $M'_o < 0$  [ $\text{Hm}^{-1}$ ] as the mutual

inductance between opposite poles, per unit length. Depending on the selected configuration, each of the two sections  $L_A$  and  $L_B$  of the discharge circuit can be either composed of two opposite poles (in the Crossed-Poles configuration), or of two adjacent poles (in the Upper-Lower-Poles configuration). For the latter configuration  $L'_A=L'_B=2L'_s+2M'_a$  and  $M'_{AB}=2M'_a+2M'_o$  and by substituting in equation 3.3 one obtains  $L'_{eq1}=L'_s-M'_o>L'_s$ . On the contrary, for the Crossed-Poles configuration one finds  $L'_A=L'_B=2L'_s+2M'_o$ ,  $M'_{AB}=4M'_a$ , and  $L'_{eq1}=L'_s-2M'_a+M'_o<L'_s$ . To sum up, selecting the Crossed-Poles typically allows reducing  $L'_{eq1}$  by a factor 2.5 to 3 due to the increased coupling between the two branches  $M'_{AB}$  [106].

Note that, depending on the electrical order of the four poles of the magnet, the CLIQ terminals must be connected differently in order to obtain the selected configuration. Let us define  $P_1$  as the pole in the first electrical position;  $P_o$  as the pole physically opposite to  $P_1$ ; and  $P_a$  either of the two poles adjacent to  $P_1$ . Thus, three possible electrical connection orders are possible:  $P_1$ - $P_a$ - $P_o$ - $P_a$ ,  $P_1$ - $P_o$ - $P_a$ - $P_a$ , and  $P_1$ - $P_a$ - $P_a$ - $P_o$ . The 1-CLIQ and 2-CLIQ connection schemes for an Upper-Lower-Pole configuration or the optimized Crossed-Poles configuration, for the three different electrical orders, are shown in figures 3.11a-f. One can notice that the electrical order  $P_1$ - $P_a$ - $P_a$ - $P_o$  is the only one that allows implementing the optimized Crossed-Poles configuration either in a 1-CLIQ or 2-CLIQ system.

If intra-layer terminals are available, even higher performing CLIQ configurations can be obtained. Two examples of 1-CLIQ configurations, obtained by modifying the electrical order of the coil outer ( $L_{1o}$ ,  $L_{ao}$ ,  $L_{oo}$ ) and inner ( $L_{1i}$ ,  $L_{ai}$ ,  $L_{oi}$ ) layers, are schematized in figures 3.12a-b.



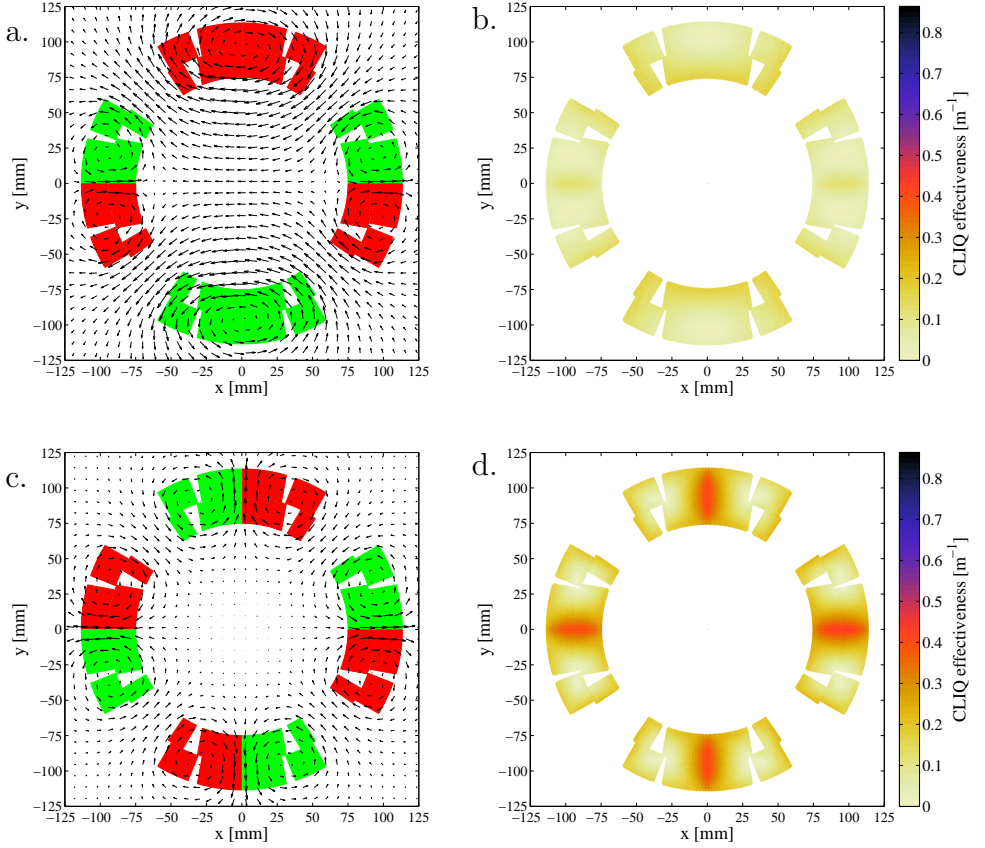


Figure 3.9. Example of CLIQ configurations not requiring intra-layer terminals applied to a two-layer quadrupole magnet. Polarity of the introduced current changes, direction of the introduced magnetic-field changes, and calculated CLIQ effectiveness,  $\Psi$ . a-b. Upper-Lower-Poles. c-d. Crossed-Poles.

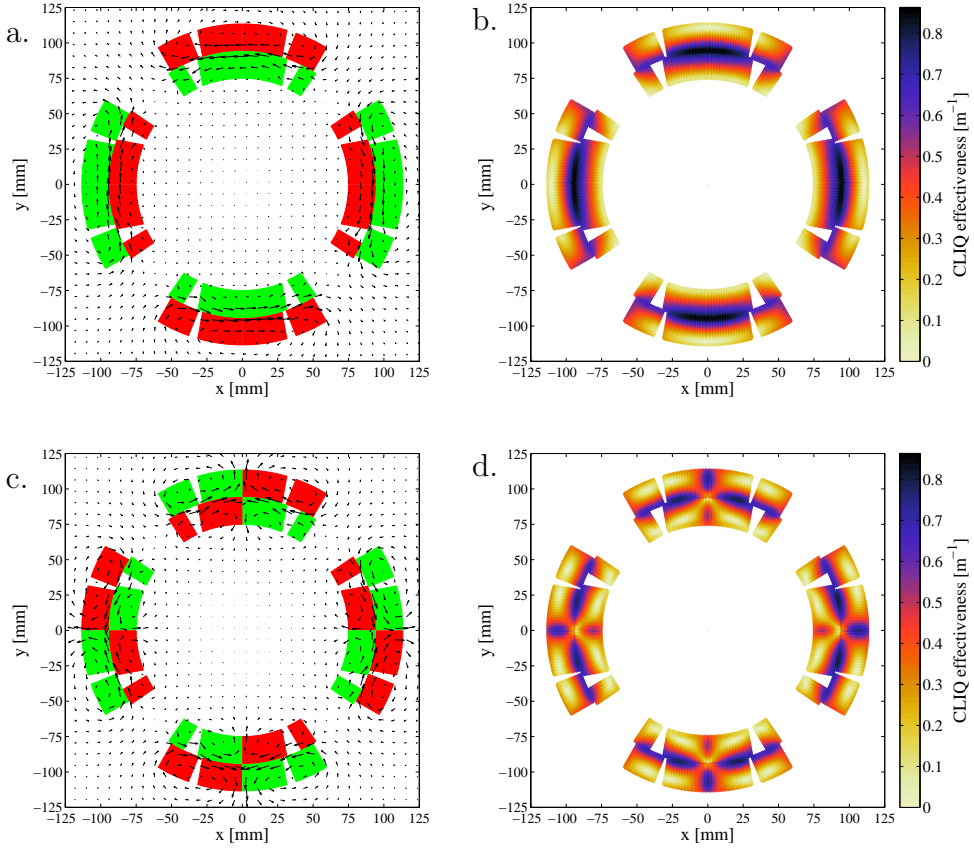


Figure 3.10. Example of CLIQ configurations requiring intra-layer terminals applied to a two-layer quadrupole magnet. Polarity of the introduced current changes, direction of the introduced magnetic-field changes, and calculated CLIQ effectiveness,  $\Psi$ . a-b. Layer-Layer. c-d. Crossed-Layers.

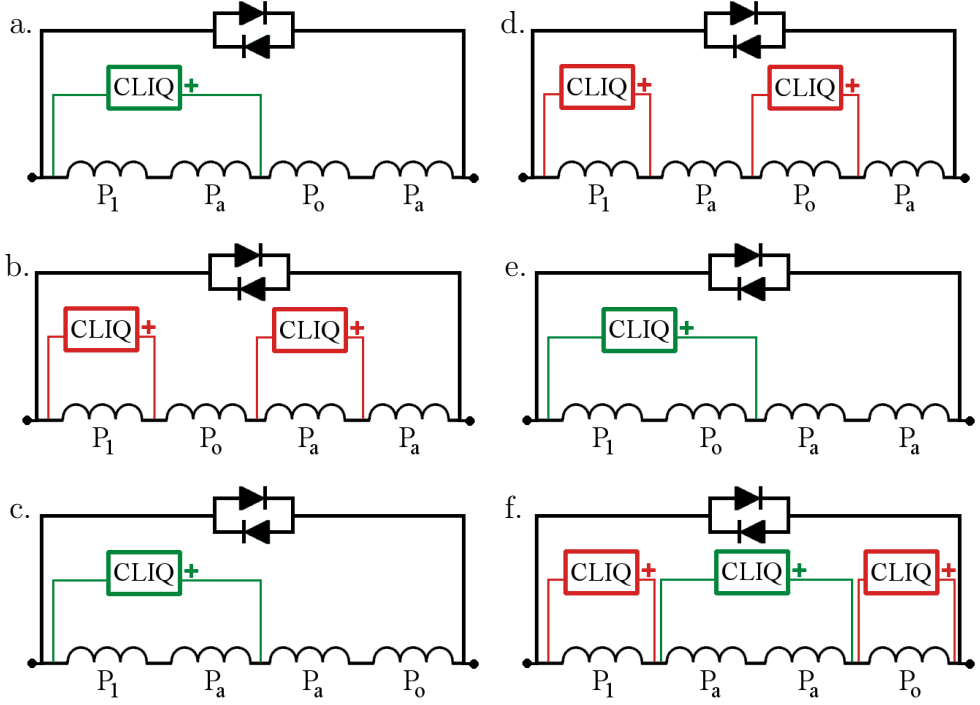


Figure 3.11. Examples of implementation of different 1-CLIQ (shown in green) and 2-CLIQ (in red) configurations not requiring intra-layer terminals applied to a two-layer quadrupole magnet. a,b,c. Upper-Lower-Poles configuration. d,e,f. Crossed-Poles configuration.

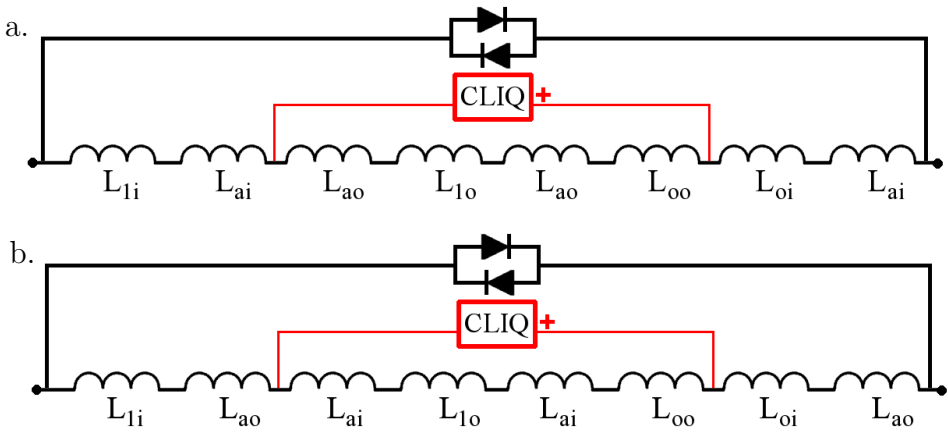


Figure 3.12. Examples of implementation of different CLIQ configurations requiring intra-layer terminals applied to a two-layer quadrupole magnet. a. Layer-Layer. b. Crossed-Layers.

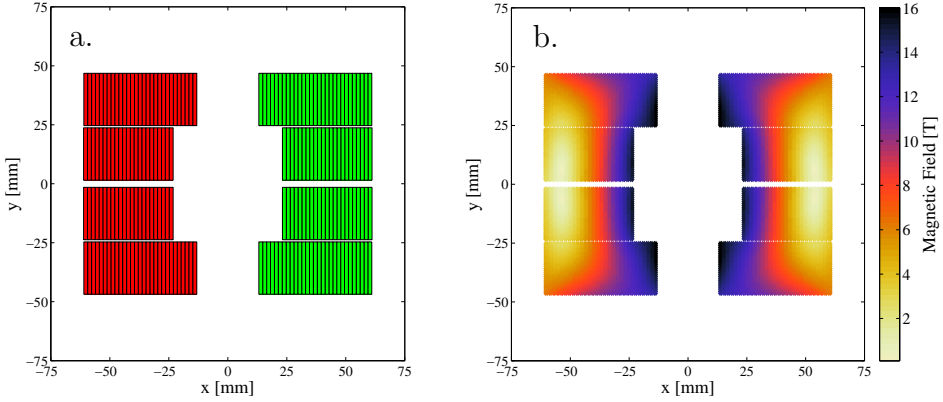


Figure 3.13. Stationary magnetic-field map in the analyzed block-coil dipole magnet. a. Polarity of the transport current. b. Magnetic field distribution ( $I_0=18.6$  kA).

Table 3.6. Equivalent inductance per unit length and CLIQ effectiveness of the analyzed CLIQ configurations for a block-coil dipole magnet.

Configuration	$L'_{eq1}$ [ $\mu\text{Hm}^{-1}$ ]	Max $\Psi$ [ $\text{m}^{-1}$ ]	Mean $\Psi$ [ $\text{m}^{-1}$ ]
Pole-Pole	560	0.62	0.27
Layer-Layer	247	1.11	0.49
Crossed-Layers	198	1.17	0.49

### 3.3.4 Block-coil dipole

The different disposition of the coil turns makes the geometry of block-type coils even better suited for CLIQ applications as compared to  $\cos\theta$  coils [144]. In fact, CLIQ deposits most of its energy in the regions at the edge between distinct coil sections, due to the superposition of the magnetic-fields generated by opposite current changes introduced in adjacent sections. In block-type coils, these regions comprise most coil turns, as will be evident observing the configurations proposed in this section. The selected case is the high-field dipole magnet developed at the Lawrence Berkeley National Laboratory [135–143], whose geometry and magnetic-field map are shown in figures 3.13a-b. The three analyzed CLIQ configurations, presented in table 3.6, follow the same concept introduced for the two-layer  $\cos\theta$  dipole geometry in section 3.3.2.

The Pole-Pole configuration shown in figure 3.14a-b generates high CLIQ-effectiveness zones in the mid-plane region. In the block-coil geometry, all turns of the inner blocks are located in this region; thus, they simultaneously receive roughly the same power deposition. On the contrary, the same Pole-Pole configuration applied to a  $\cos\theta$  magnet geometry achieves high CLIQ-effectiveness in regions comprising both inner and outer layers, but only a limited number of coil turns (figures 3.6a-b).

The CLIQ effectiveness can be significantly enhanced by selecting a Layer-Layer

configuration, where opposite current changes are introduced in the inner and outer blocks (figure 3.14c-d). The peak CLIQ effectiveness roughly doubles with respect to the Pole-Pole configuration, and the high- $\Psi$  regions cover strands located in every turn of the coil.

Alternatively, a Crossed-Layers configuration can be selected (figure 3.14e-f). This solution further reduces the circuit equivalent inductance due to the increased coupling between the two CLIQ coil sections and causes a more optimized distribution of CLIQ effectiveness. In fact, six extensive regions are developed where the magnetic fields are superposed and high coupling loss is generated, resulting in an even more uniform quench initiation in the coil windings.

For this particular geometry, all three CLIQ configurations are symmetric. In fact, even in the case of the Layer-Layer configuration  $L_A \approx L_B$ , because the lower number of turns in the inner layer is compensated by the larger layer aperture, and the current changes introduced in the two sections are very similar.

### 3.3.5 Solenoid

CLIQ is often very well-suited for the protection of a solenoid composed of multiple series-connected layers. In fact, the magnetic-field changes generated by opposite current-changes introduced in adjacent layers of a solenoid effectively superpose. The resulting coupling loss generated in the magnet is highly uniform along the longitudinal direction as well as along the direction of the conductor. Furthermore, the strong magnetic coupling between the resulting CLIQ coil sections  $L_A$  and  $L_B$ , composed of concentric solenoidal layers, makes the equivalent inductance of the CLIQ discharge circuit but a fraction of the stationary magnet self-inductance, typically less than 1%. Finally, many existing solenoids already include terminals between different multi-layer sections of the coil, often used for connecting protection by-pass elements. Thus, it is relatively simple to connect one or more CLIQ units to a solenoid.

The presence of multiple terminals allows a broad choice of configurations. The impedances of the two branches of the CLIQ discharge circuit are inherently asymmetric as outer layers of the solenoid have larger inductance than the inner ones. The identification of the highest performing CLIQ configuration requires careful analyses to be carried out on a case-by-case basis. This section provides general guidelines which are qualitatively valid for any solenoid.

As a case study, a solenoid with an inner diameter of 954 mm and a length of 910 mm, composed of 44 layers of 350 turns, is considered. This coil has a self-inductance of about 169 H and generates a magnetic field of about 5 T at its axis, at a nominal current of 350 A. Figures 3.15a-b show the coil geometry and field-map; note that the radial and longitudinal directions  $r$  and  $z$  are not represented in the same scale in order to properly capture the magnetic-field radial gradient. The coil is subdivided in 11 coil sections of 4 layers, each powered in series; at the joint between each two coil sections, a terminal is present to which CLIQ terminals can be connected. Thus, the CLIQ discharge circuit can comprise up to eleven branches and up to five CLIQ units can be included in the protection system ( $1 \leq N_C \leq 5$ ). Table 3.7 summarizes the equivalent inductance and CLIQ effectiveness of six different configurations applied to the solenoid geometry.

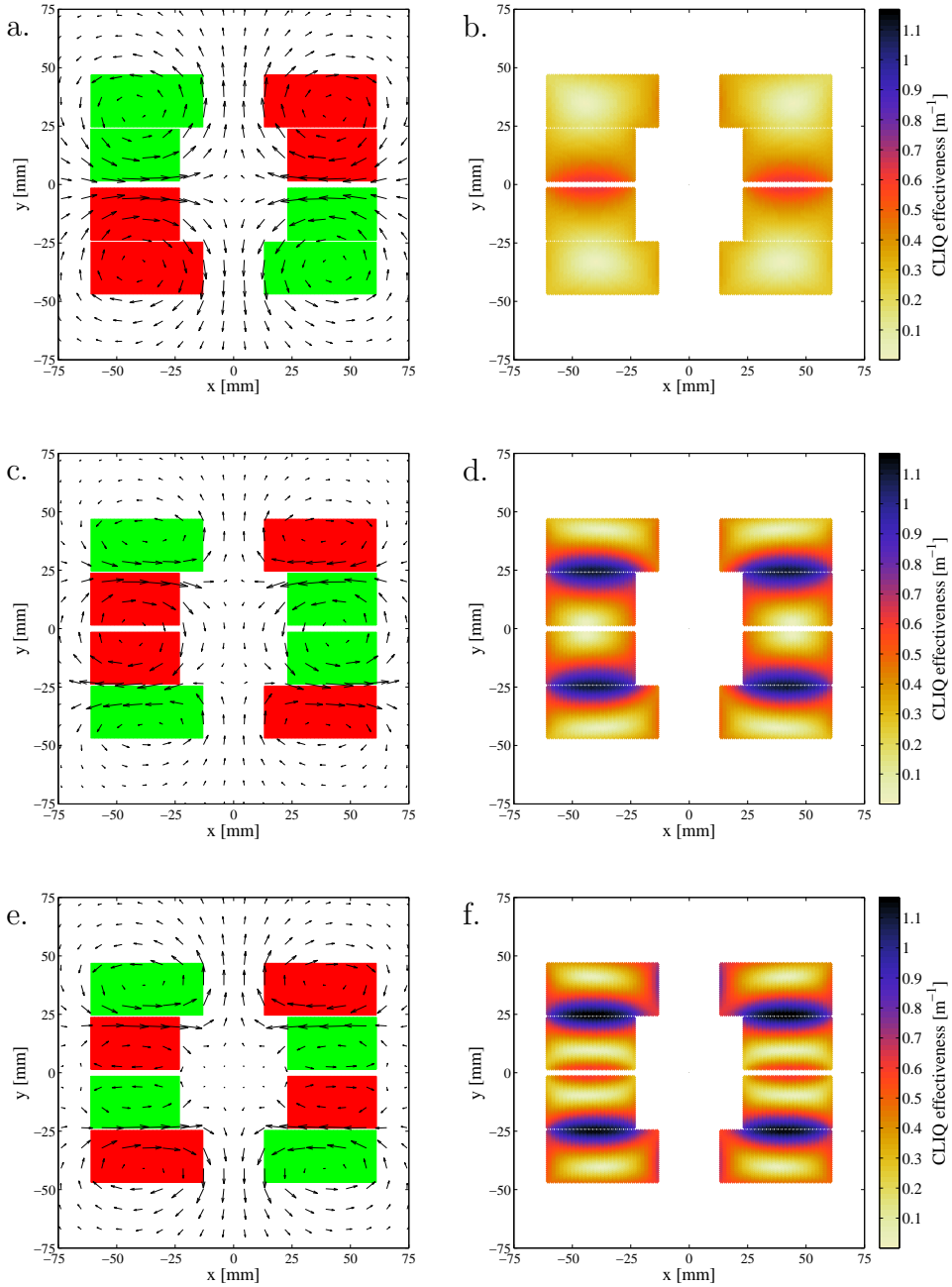


Figure 3.14. Example of CLIQ configurations applied to a block-coil dipole magnet. Polarity of the introduced current changes, direction of the introduced magnetic-field changes, and calculated CLIQ effectiveness,  $\Psi$ . a-b. Pole-Pole. c-d. Layer-Layer. e-f. Crossed-Layers.

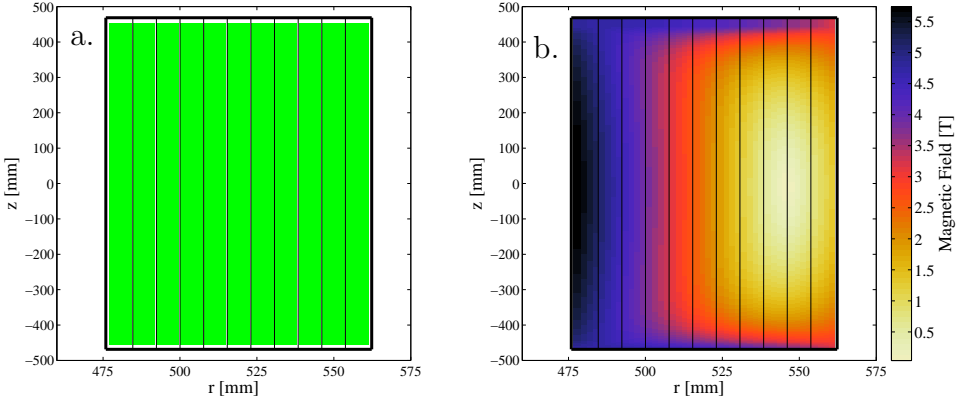


Figure 3.15. Stationary magnetic-field map in the analyzed 11-section solenoid. a. Polarity of the transport current. b. Magnetic field distribution ( $I_0=350$  A). Note that the radial dimension is intentionally inflated.

Table 3.7. Equivalent inductance per unit length and CLIQ effectiveness of the analyzed CLIQ configurations for a solenoid.

Configuration	$L'_{eq1}$ [Hm <sup>-1</sup> ]	$f_{g,A}$	$f_{g,B}$	Max $\Psi$ [mm <sup>-1</sup> ]	Mean $\Psi$ [mm <sup>-1</sup> ]
Sc1	1.80	0.47	-0.53	2.7	1.3
Sc2	0.61	0.83	-0.17	4.7	2.2
Sc3	0.49	0.46	-0.54	5.1	2.6
Sc4	0.35	0.46	-0.54	6.9	2.9
Sc5	0.12	0.46	-0.54	12.5	4.8
Sc6	0.04	0.46	-0.54	21.8	8.8

Configuration Sc1 is obtained by discharging opposite current changes in the innermost six coil sections and in the the outer five sections (figure 3.16a-b). Thus, the CLIQ discharge circuit is composed of two concentric solenoids, electrically in parallel, strongly magnetically coupled, and subject to opposite current-changes. The equivalent inductance of such a circuit is less than 1% of the magnet stationary self-inductance due to the strong magnetic coupling between the solenoid coil sections. Note that the coil subdivision of configuration Sc1 results in similar impedances of the two branches of the CLIQ discharge circuit; hence, current changes with similar amplitude are introduced in the two coil sections. This result is confirmed by the values of the geometric parameters  $f_{g,A}$  and  $f_{g,B}$ , defined in equations 2.8 and 2.9 and reported in table 3.7, which approach  $\pm 1/2$ , corresponding to a perfectly symmetric discharge circuit.

A current change in either of the two solenoid sections generates a very uniform longitudinal magnetic-field change in the closest layers of the neighbouring section, which superposes to the longitudinal self-field generated by the section itself. Thus, high coupling loss is homogeneously developed in the coil windings located in the few

layers at the edge between the two coil sections. It is expected that the energy deposited in this high-loss region is sufficient to initiate a fast transition to the normal state. The ohmic loss generated in the normal zone causes its propagation along the radial direction through the wire insulation between layers. Note that the well-centered location of the region where the transition to the normal state is initiated improves the performance of the protection system. In fact, the normal zone can propagate radially both outwardly and inwardly.

On the contrary, a highly asymmetric CLIQ configuration like Sc2 (figure 3.16c-d) can prove less effective. In this configuration, one CLIQ terminal is connected between the second and the third innermost sections of the coil. Thus, the high magnetic-field change, high coupling-loss generation region is off-center and located far from the outer layers of the coil. As a result, the normal zone is expected to propagate more slowly and a longer time is required to quench the entire coil.

If all coil sections are connected electrically in series following the order of their radial position in the coil, the highest performing CLIQ configuration includes two CLIQ connections to the coil, thus effectively subdividing the coil into three concentric solenoids where opposite current changes are introduced. As a result, two separate regions are developed where high coupling loss is generated and a transition to the normal state is provoked. The equivalent inductance of the discharge system can still be calculated using equation 2.4, where  $L_A$  and  $L_B$  are the self-inductances of the layers between and outside the two CLIQ terminals, respectively. In fact, the two ends of the solenoid are connected through two diodes in antiparallel configuration, and in first approximation the two portions of the coil outside the CLIQ terminals can be considered electrically in series.

Configurations similar to Sc3, shown in figure 3.16e-f, obtained by introducing opposite current changes in the layers located in the central half of the solenoid and in its innermost and outermost quarters, achieve the highest CLIQ effectiveness and the most optimized distribution of deposited loss. In fact, the resulting regions which are quickly transferred to the normal state are well distributed in the solenoid cross-section, thus allowing an optimal radial normal zone propagation. The high mutual inductance between the central half of the solenoid and the remaining coil layers further reduces the equivalent inductance of the discharge circuit, and a higher current change can be introduced in the coil sections. Similar CLIQ configurations were extensively tested during a measurement campaign on a small-scale test solenoid at the CERN cryogenic laboratory [84].

If the electrical order of the solenoid sections can be modified, a further significant improvement of CLIQ performance can be achieved. Let us name S1-S11 the eleven coil sections composing the analyzed solenoid, ordered from the innermost (S1) to the outermost (S11). In conventional connection schemes, their electrical order is either S1-S11 or S11-S1, obtained by connecting in series adjacent layers. However, the solenoid stationary performance are unchanged if this order is modified.

For example, sections S1-S3 and S7-S9 can be connected in series, then S4-S6 and S10-S11. When a CLIQ unit is connected to the terminal in the middle of the solenoid, between S9 and S4, a configuration Sc4 is obtained, represented in figures 3.17a-b. As shown in table 3.7, the equivalent inductance of the discharge circuit is reduced and the CLIQ effectiveness improved with respect to the previous configurations.



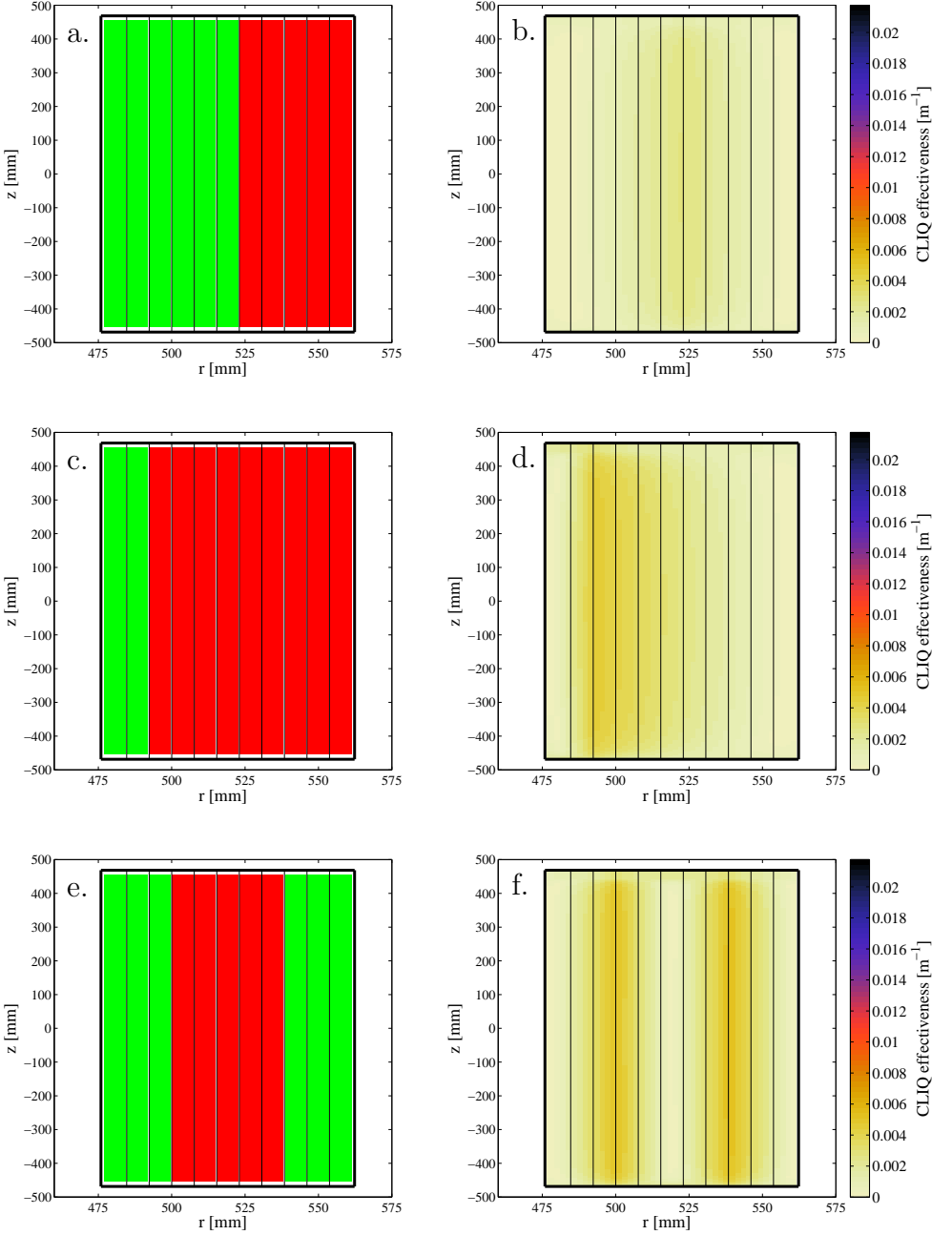


Figure 3.16. Examples of CLIQ configurations applied to a solenoid coil. Polarity of the introduced current change and calculated CLIQ effectiveness,  $\Psi$ . a-b. Configuration Sc1. c-d. Configuration Sc2. e-f. Configuration Sc3.

This is achieved due to the stronger coupling between the two CLIQ coil sections (S1-S3)+(S7-S9) and (S4-S6)+(S10-S11).

By connecting in series every pair of solenoid sections, configuration Sc5 is obtained (figures 3.17c-d). A CLIQ unit connected to the middle of the solenoid effectively subdivides it in two series (S1-S2)+(S5-S6)+(S9-S10) and (S3-S4)+(S7-S8)+(S11). Multiple high- $\Psi$  regions are developed, resulting from the superposition of the magnetic-field changes generated by the tightly-coupled CLIQ coil sections.

Finally, a top-performance configuration Sc6 is obtained by connecting in series one every two solenoid sections, as shown in figures 3.17e-f. The CLIQ effectiveness achieved with such a configuration is about four times higher than Sc3, the most optimized configuration if the electrical order of the solenoid sections can not be modified, and the peak power deposition is about sixteen times higher. This power is generated in ten well-distributed areas and deposited very uniformly in the longitudinal and azimuthal directions. More generally, for a solenoid composed of  $N_S$  sections,  $N_S-1$  high coupling-loss regions are achieved with this type of configuration.

Alternatively, multiple CLIQ units can be connected to the same solenoid, thus profiting both from the enhancement of CLIQ effectiveness due to the more optimized discharge circuit and from the advantages of a Multi-CLIQ system described in section 3.2. Given the inherently asymmetry of the discharge circuit in the case of a solenoid, the presence of by-pass elements across various solenoid layers, and the high number of different configurations to consider, the design of a Multi-CLIQ system protecting a solenoid has to be addressed on a case-by-case basis.

### 3.3.6 Pancake coil

In this section the performance of a CLIQ system protecting a pancake coil is presented. The same coil studied in the previous section, whose field-map is shown in figure 3.15b, is used as an example; however, it is now considered that the coil is composed of  $N_P=7$  stacked pancake sections, each including  $50 \times 44$  turns. Whilst the self-inductance and stationary performance of the coil are similar, the performance of the CLIQ system is highly affected by the change in the geometry.

Table 3.8 lists the three different analyzed configurations, obtained by subdividing the discharge circuit into 2, 3, or  $N_P=7$  sections, respectively. Note that the calculated equivalent inductance of the discharge circuit is one to two orders of magnitude higher than the values obtained for the solenoid geometry. This result can be easily explained considering that the mutual coupling between the different sections of the circuit is significantly lower in the case of the pancake geometry; hence, following equation 2.4, the equivalent inductance of a CLIQ system composed of weakly-coupled magnetic elements is higher.

The simple CLIQ configuration shown in figures 3.18a-b consists in subdividing the coil into two sections composed of 3 and 4 pancakes, hence with similar self-inductance. CLIQ effectively generates a uniform magnetic-field change in the turns which are in the region at the edge between the two coil sections. However, the other pancake coils are distant from the zone where high magnetic-field is generated and thus little coupling loss is developed there. Consequently, a fast transition to the normal state is expected only in a rather small region, followed by a slower

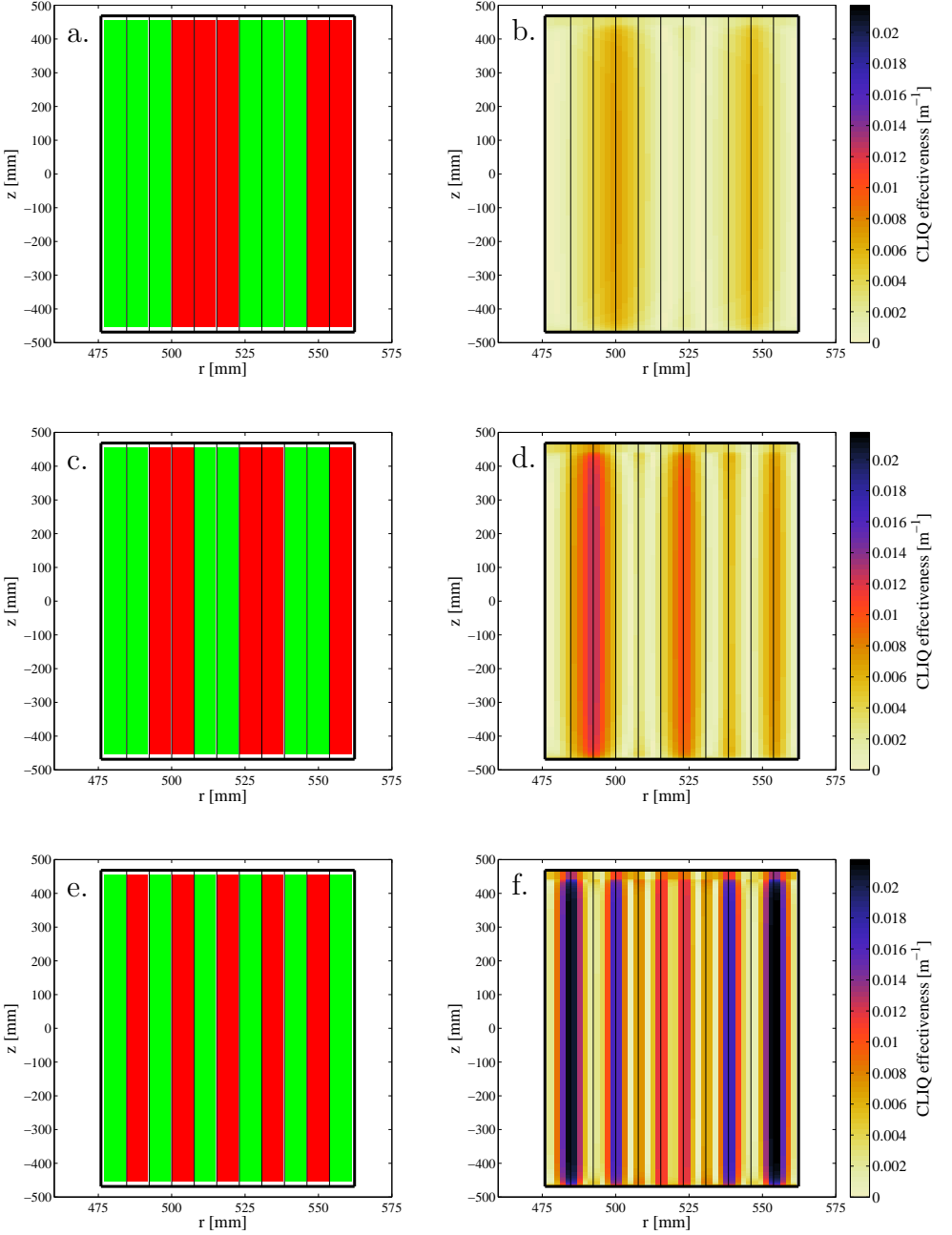


Figure 3.17. Examples of CLIQ configurations applied to a solenoid coil. Polarity of the introduced current change and calculated CLIQ effectiveness,  $\Psi$ . a-b. Configuration Sc4. c-d. Configuration Sc5. e-f. Configuration Sc6.

Table 3.8. Equivalent inductance per unit length and CLIQ effectiveness of the analyzed CLIQ configurations for a pancake coil.

Configuration	$L'_{\text{eq1}}$ [Hm <sup>-1</sup> ]	$f_{g,A}$	$f_{g,B}$	Max $\Psi$ [mm <sup>-1</sup> ]	Mean $\Psi$ [mm <sup>-1</sup> ]
Pc1	20.8	0.42	-0.58	0.50	0.19
Pc2	12.8	0.47	-0.53	0.74	0.31
Pc3	3.5	0.45	-0.55	1.81	0.77

propagation of the normal zone in the longitudinal direction. The heat diffusion along this direction is usually much slower than in the radial direction due to the presence of more numerous insulation barriers. In the selected geometry, for example, there are in total  $2 \times 350$  insulation layers in the longitudinal direction and  $2 \times 44$  in the radial direction. As compared to the CLIQ configurations applied to a simple-layer wound solenoid, this configuration is less performing. Nonetheless, this localized normal zone initiation may be sufficient to protect the entire pancake coil.

A CLIQ configuration as shown in figures 3.18c-d offers improved performance due to the more effective subdivision of the pancakes in the two coil sections. The stronger coupling between the two branches greatly reduces the equivalent inductance of the discharge circuit, thus allowing the introduction of higher current changes in the coil sections. Two separate regions are produced where the magnetic fields generated by the two coil sections superpose. Thus, it is expected that two normal zones are developed, each propagating the normal zone in the longitudinal direction. Finally, note that this configuration can be implemented either as a 1-CLIQ or 2-CLIQ system.

If CLIQ terminals are available only between individual pancakes, the highest performing CLIQ configuration is obtained by introducing opposite current changes in all adjacent pancakes, as shown in figures 3.18e-f. This solution effectively exploits the presence of  $N_P$  individual pancake sections to maximize the inductance reduction and optimize the coupling loss deposition. In the selected example, the maximum number of branches in the discharge circuit is  $N_P=7$ , hence up to 4 CLIQ units can be connected ( $1 \leq N_C \leq 4$ ). Such a solution develops  $N_P-1$  regions at the edges between each two pancake coils where high coupling loss is generated. If no further subdivision of the coil is possible, this configuration represents the highest performing configuration for a pancake geometry.

### 3.3.7 Chain of uncoupled magnets

A CLIQ system can be implemented for the protection of a chain of superconducting magnets not magnetically coupled. This solution presents significantly lower performance with respect to the protection of single magnets. In fact, such a CLIQ system introduces the same current changes in the coil turns of the same magnet, thus not exploiting any effective superposition of the magnetic field produced by individual coil sections. Also, the equivalent inductance of the discharge circuit is not reduced by the presence of coupling between the coil sections; hence, the introduced current change is very limited as compared to single-magnet CLIQ configurations. Nevertheless, this solution has the great advantage of requiring no CLIQ terminals

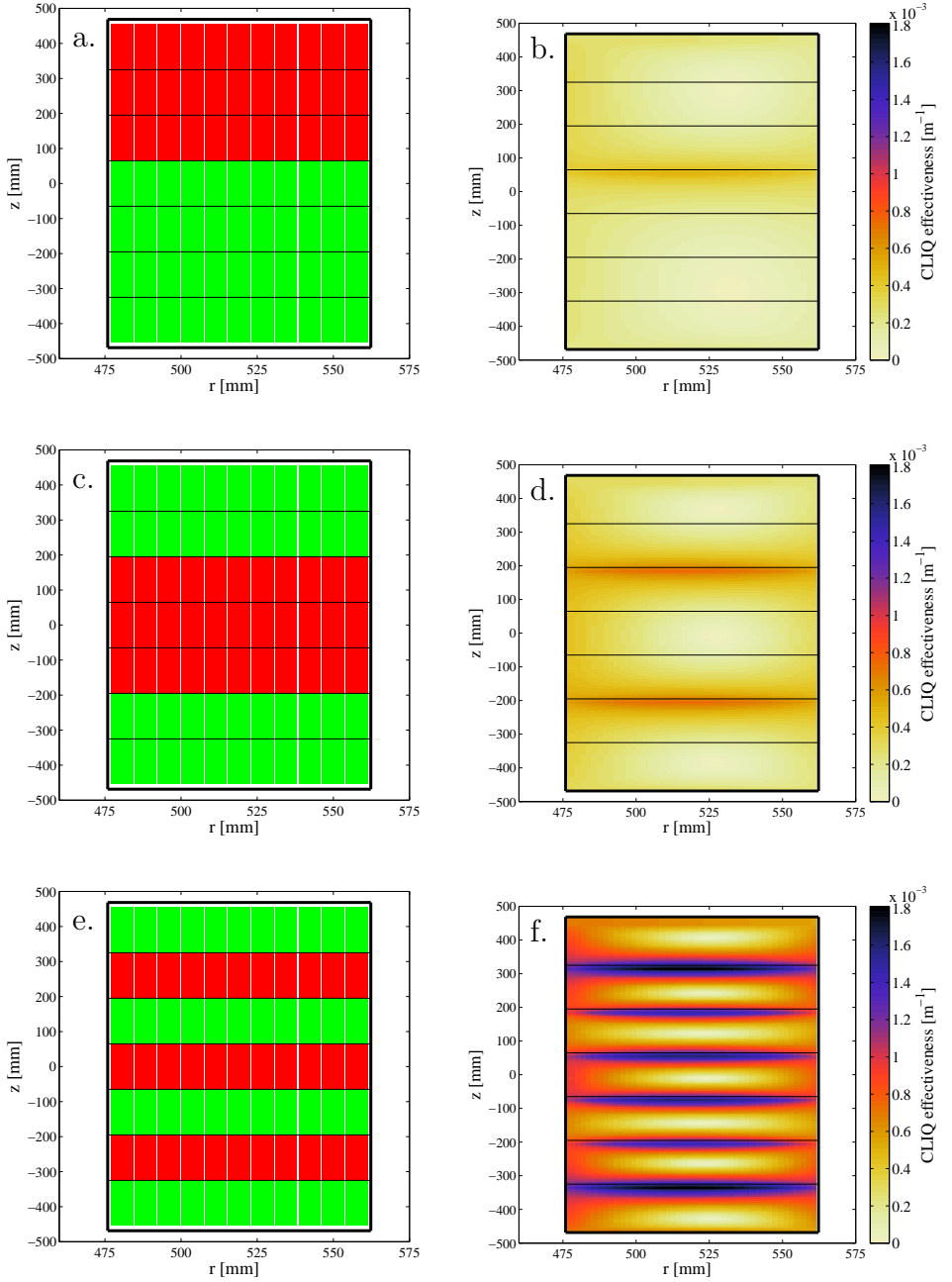


Figure 3.18. Examples of CLIQ configurations applied to a pancake coil. Polarity of the introduced current change and calculated CLIQ effectiveness,  $\Psi$ . a-b. Configuration Pc1. c-d. Configuration Pc2. e-f. Configuration Pc3.

internal to the coils. Thus, it can be easily implemented on existing chains of superconducting magnets if terminals at the joints between magnets are present.

Let us consider the case of a chain of  $N_M$  superconducting magnets, each with the same self-inductance  $L_M$  [H], physically distant or shielded by presence of iron elements, sufficiently to be considered magnetically uncoupled; and a CLIQ protection system composed of  $N_C$  units with the same charging voltage and capacitance of the capacitor banks, connected to the circuit so as to form  $N_S=2N_C$  sections, each containing an equal number of magnets. In this simple configuration, the CLIQ discharge circuit has an equivalent inductance of

$$L_{eq} = \frac{N_M L_M}{N_S^2} = \frac{N_M L_M}{4N_C^2}. \quad [H] \quad (3.10)$$

The peak current change introduced in each magnet is

$$\frac{dI_M}{dt} = \pm \frac{1}{N_S} \frac{dI_C}{dt} = \pm \frac{2N_C U_0}{N_M L_M}. \quad [As^{-1}] \quad (3.11)$$

Since the current in the strands of each coil is the same, the parameters  $f_{CLIQ}$  [TA<sup>-1</sup>], defined in equation 2.14, reduce to  $|f_M|/N_S$ , where the magnetic parameters  $f_M$  [TA<sup>-1</sup>] characterize the magnetic field generated in each strand of the magnet by a stationary transport current. The CLIQ effectiveness can therefore be calculated as

$$\Psi = \frac{2N_C |f_M|}{N_M L'_M}, \quad [m^{-1}] \quad (3.12)$$

where  $L'_M$  [Hm<sup>-1</sup>] is the magnet self-inductance per unit length. Note that in this configuration the zones where higher coupling loss is deposited correspond to the high magnetic-field regions in the coil cross-section.

This solution can prove effective for the protection of chains of magnets with relatively low inductance. With respect to the alternative method usually implemented for protecting such circuits, i.e. an energy-extraction system, a CLIQ system is more compact and less expensive.

### 3.4 Conclusion

A general strategy for the design and optimization of a CLIQ-based quench protection system is outlined for the majority of magnet geometries used in particle accelerators, magnetic resonance imaging, and particle detectors.

The peak power per unit volume deposited by CLIQ is proportional to the square of its charging voltage, which is generally limited by the coil winding technology, safety constraints, and risk reduction; and inversely proportional to the square of the magnet length, which is imposed by design. Methods exist to optimize the CLIQ discharge circuit and allow an effective energy deposition also in magnets of large dimensions and high self-inductance.

The main ingredients for CLIQ optimization, valid for any magnet geometry, are the subdivision of the coil into multiple sections and the introduction of current changes with opposite polarity in coil sections which are physically adjacent. In fact,

both measures significantly reduce the equivalent inductance of the CLIQ discharge circuit, hence increasing the introduced current change and therefore the coupling loss developed in the superconductor. A correct choice of the current changes to introduce in the various coil sections allows an effective magnetic-field superposition and an optimized distribution of the coupling loss generated in the coil cross-section.

When CLIQ is included in the magnet design from the start, terminals can be made available at the joints between individual coil sections in order to maximize the coil subdivision and improve the performance. A typical example is the addition of terminals at the joint between the inner and outer layers of a dipole or quadrupole magnet.

A parameter  $\Psi$  called CLIQ effectiveness is defined which can be used to assess the performance of different configurations on a given coil. The discharge circuit can be effectively optimized by changing the electrical order of different coil sections, such as magnet poles or layers, and the positioning of the CLIQ terminals connected to the coil. Examples are shown where two different configurations result in drastically different performance of the quench protection system, resulting in a peak CLIQ power increased by an order of magnitude and in a most optimized distribution of the energy delivered to the coil.

For symmetric discharge circuits, as in the case of dipole or quadrupole magnets, the peak power deposited by CLIQ is proportional to the square of the number of CLIQ units installed across distinct coil sections.

CLIQ is effective on any analyzed magnet geometry. Its performance is highest for magnet configurations including strongly-coupled coil sections, such as solenoids.





## Chapter 4

# Lumped-Element Dynamic Electro-Thermal model

*Modeling accurately the electro-thermal transients occurring in a superconducting magnet is challenging. The behavior of the magnet is the result of complex phenomena occurring in distinct physical domains (electrical, magnetic, thermal) at very different spatial and time scales. Combined multi-domain effects significantly affect the dynamics of the system and are to be taken into account in a coherent and consistent model.*

*A new methodology for developing a Lumped-Element Dynamic Electro-Thermal (LEDET) model of a superconducting magnet is proposed. This innovative model includes non-linear dynamic effects such as the dependence of the magnet differential self-inductance on the presence of inter-filament and inter-strand coupling currents in the conductor. These effects are usually not taken into account in models because superconducting magnets are primarily operated in stationary conditions. However, they have often significant impact on magnet performance, particularly when the magnet is subject to high rates of change of current. Any model to simulate the transient following a CLIQ discharge has to include this essential ingredient.*

### 4.1 Dynamic electro-thermal model

The proposed LEDET method allows simulating the behavior of a superconducting magnet by means of a network of lumped-elements [95]. It includes purely electrical components, a 2D thermal model of the coil-cross section, and a model of the coupling currents in the coil and their influence on the electrical components.

#### 4.1.1 Lumped-element modeling

Finite-element modeling (FEM) is an advanced and powerful computational method of solving boundary-value problems on the basis of domain discretization into a finite number of elements. Non-linear behavior in superconducting cables can be successfully reproduced by means of such software [145, 146]. However, the computational effort required to obtain accurate results is usually high, which makes FEM application inefficient due to the long simulation time.

An alternative approach consists in modeling the dynamic behavior of a superconducting magnet by means of a network of non-linear lumped-elements, which is then solved with an in-house or commercial network solver, such as Simulink, PSpice, or Simplorer. In fact, in many practical cases the electro-magnetic and thermal dynamics of a superconducting magnet can be effectively reproduced with a limited number of differential-algebraic equations. This technique requires a deep understanding of the phenomena occurring in the coil strands and cables, which significantly influence the system dynamics. Once properly implemented it renders a significant reduction in CPU time for solving the model with respect to FEM.

The same simulation environment can simultaneously model macroscopic electrical transients and phenomena occurring at the level of superconducting strands. Thus, the flexibility of the model is greatly improved.

#### 4.1.2 LEDET in a nutshell

Figure 4.1 shows a schematic representation of a purely electrical model and the interaction between its components, subdivided into energy sources, sinks, or storage elements. The energy provided by the power source (PS) is stored in capacitive (C) and inductive (L) elements, and dissipated in resistive components (R), such as resistors, diodes, or switches. The model is a closed system with only two energy-exchange interfaces with the exterior: energy exchanges with an infinite source, representing the main electric network (EN), and energy output to an infinite sink, representing the room-temperature environment (RT).

An electro-thermal model includes an electrical sub-system similar to the previous example interacting with a thermal sub-system [147, 150, 151]. For instance, the thermal network used by the LEDET model is described in section 4.3. Since the transient occurring in one domain influences the other, and vice versa, the two subsystems can be solved simultaneously by the simulation software. A typical example of electro-thermal transient is the generation of ohmic loss, whose occurrence builds a voltage across the conductor, which affects the electrical domain, and enhances its temperature, which affects the thermal domain.

The energy exchanges in a model composed of an electrical and a thermal sub-system are represented in figure 4.2. Within the thermal domain, energy is stored in heat-capacitance elements ( $C_{th}$ ), which can exchange energy with each others ( $P_{ex}$ ). Energy transferred to infinite heat sinks is dissipated and lost to the system. This is the case, for instance, of the heat delivered to a helium bath (HE) surrounding a superconducting coil ( $P_{He}$ ).

The electrical and thermal sub-systems exchange energy through components simulating ohmic loss internal to the conductor ( $R_C \rightarrow P_{ohm}$ ). To satisfy the overall

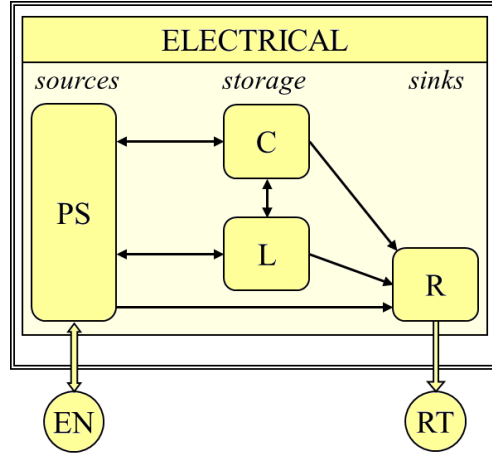


Figure 4.1. Representation of the energy exchanges occurring in a purely electrical model.

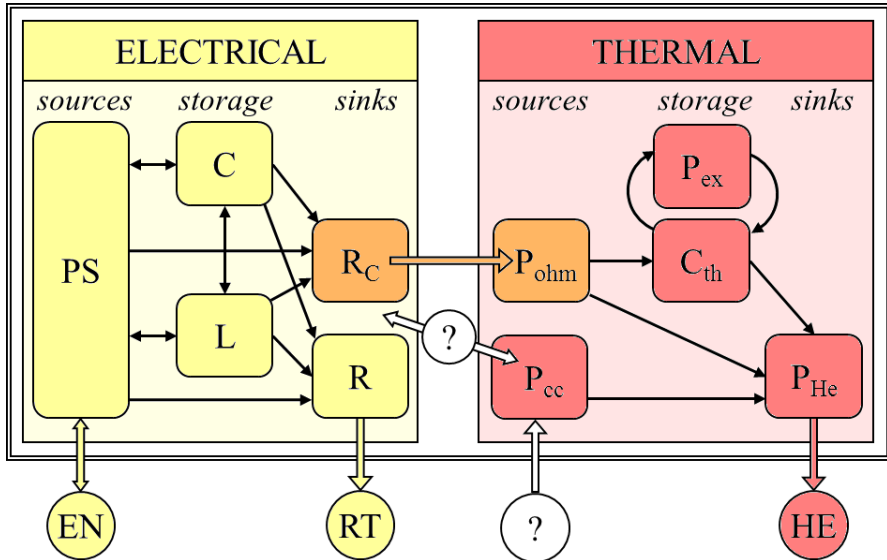


Figure 4.2. Representation of the energy exchanges occurring in a conventional electro-thermal model. The two main shortcomings of this approach are indicated by question marks.

energy balance in the entire electro-thermal system, the energy dissipated in the electrical components  $R_C$  must equal the input energy to the thermal sub-system through the components  $P_{ohm}$ .

Additional energy input can be included in the thermal sub-system to account for other loss sources. These contributions are often added as heat inputs from sources external to the electro-thermal system. This approach is satisfactory only in the case the physical phenomena causing the loss are not related to the magnet system considered, as in the case of radiation or beam loss. Instead, coupling-loss effects cannot be treated as an external, independent heat source since by definition it is generated by an electro-magnetic interaction between the magnet's field and its conductor.

In fact, a variation in the magnet transport current determines a change of the magnetic field applied to its conductor,  $dB_a/dt$  [Ts<sup>-1</sup>], which in turn results in the generation of an induced magnetic field  $B_i$  [T] opposing the applied magnetic-field change [3,18]. Thus, during electro-magnetic transients part of the magnetic energy stored in the superconducting coil does not contribute to the generation of the main coil's magnetic field, but to the development of local induced magnetic fields, that cause currents flowing between superconducting filaments. In a cable with multiple strands, similar currents are also generated between strands. These coupling currents, developed with a characteristic time constant, flow through the strand matrix and through strand-to-strand contact resistances and both result in local ohmic losses, which are called inter-filament and inter-strand coupling loss, respectively.

Many existing electro-thermal models are inadequate to correctly simulate the effect of local coupling currents and consequently coupling loss in the magnet system. Their shortcomings, schematically illustrated in figure 4.2, are twofold. Firstly, they do not correctly reproduce the energy flows in the magnet system. In fact, in reality the energy developed as coupling loss  $P_{cc}$  and appearing as a heat source in the thermal sub-system does not come from an external system, but is subtracted from the magnet stored energy. Ultimately, this loss is provided by the main power source. This is also the physical background allowing the measurement of coupling loss by calculating the time integral of the energy provided by the power source during a current cycle,  $\oint U_{ps} I_M dt$  [J], with  $U_{ps}$  [V] the voltage across the power source and  $I_M$  [A] the magnet transport current. Secondly, the dependence of the magnet differential self-inductance on the coupling currents developed in the coil is disregarded. Since local coupling currents change the local magnetic flux in the conductor  $\Phi$  [Tm<sup>2</sup>], they obviously have an influence on the effective differential self-inductance of the magnet,  $L_d = d\Phi/dI_M$  [H].

With the proposed LEDET approach, represented in figure 4.3, a third coupling-current sub-system is included in the magnet model to describe the energy exchange between the electrical and thermal sub-systems through local coupling currents. The amount of energy subtracted from the magnet and determining a change of its differential self-inductance is the input to the coupling sub-system ( $M_{cc} \leftrightarrow M_{cc}$ ). This is the stored magnetic energy which maintains the coupling currents flowing ( $L_{cc}$ ). Part of this energy is returned to the electrical sub-system, and another part is lost and constitutes the heat generated in the conductor due to coupling loss ( $R_{cc} \rightarrow P_{cc}$ ).

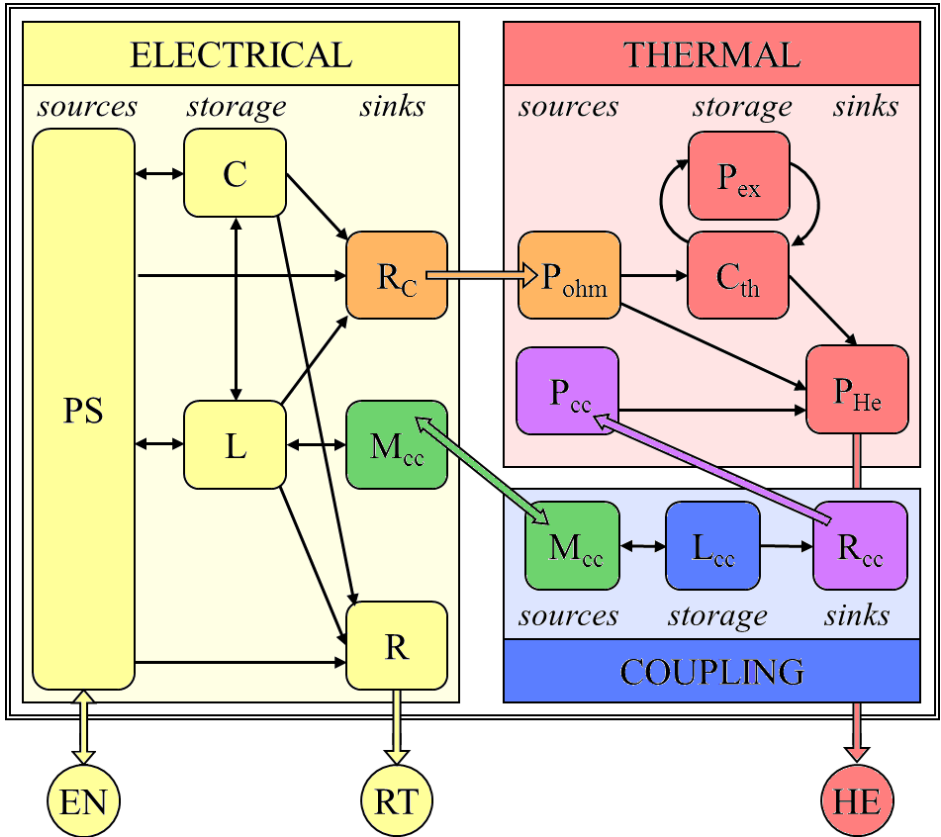


Figure 4.3. Representation of the energy exchanges occurring in a LEDET model. Elements pertaining to one sub-network are represented in yellow (electrical), red (thermal), and blue (coupling). Elements pertaining to two different sub-networks are represented in orange (electrical-thermal), green (electrical-coupling), and purple (coupling-thermal).

Following the LEDET method, the complex interdependence between the electro-magnetic and thermal domains can be represented with three sub-networks of lumped-elements, reproducing the electrical transient in the main magnet circuit, the thermal transient in the coil cross-section, and the electro-magnetic transient of the inter-filament and inter-strand coupling currents in the coil's superconductor, respectively. The software solves the three sub-networks simultaneously treating them as coupled networks.

Figure 4.4 shows a sample implementation of a LEDET model of a superconducting coil. The three sub-networks and their components, described in detail in the following sections, are represented with different colors indicating the domain to which they belong. Various elements pertaining to two different sub-networks are present to describe multi-domain effects such as ohmic loss and coupling loss.

A Quench Simulation Framework was recently developed in order to automatize the process of developing, editing, and running LEDET models in a fast and convenient way [148, 149].

## 4.2 Electrical sub-network

The LEDET electrical sub-network contains conventional electrical lumped-elements such as voltage and current sources, self- and mutual inductances, resistors, capacitors, diodes, thyristors, switches, and ground connections.

The parameters of the electrical elements can vary with temperature, magnetic field, transport current, or other relevant physical properties, such as electrical resistivity, heat capacity, and thermal conductance.

A superconducting magnet is represented as a series connection of  $N_E$  electrical elements. Each element  $e$  is composed of a self-inductance  $L_e$  [H], mutually coupled to the other magnet self-inductances, and a resistor  $R_e$  [ $\Omega$ ], which is non-zero only in the case of a transition to the normal state. If the magnet is surrounded by an iron yoke,  $L_e$  decreases with transport current due to iron yoke saturation.

A reasonable choice for the number of electrical elements  $N_E$  can be the number of poles in a multi-pole magnet, or the number of layers in a solenoid magnet. In conventional applications the same transport current  $I_e$  [A] flows in the coil of each electrical element. However, after a CLIQ discharge different current changes are introduced in the various coil sections.

## 4.3 Thermal sub-network

The method for describing a thermal problem with analogous electrical equations and then solving it in the electrical domain is well known in the literature [147, 150, 151]. A thermal system can be represented as an electrical network where any current flowing in a branch of the circuit is equivalent to a heat flow and the potential of any node is equivalent to a temperature.

The thermal sub-network is composed of  $N_B$  thermal blocks. Each block corresponds to a certain volume of conductor, usually comprising one or a few coil

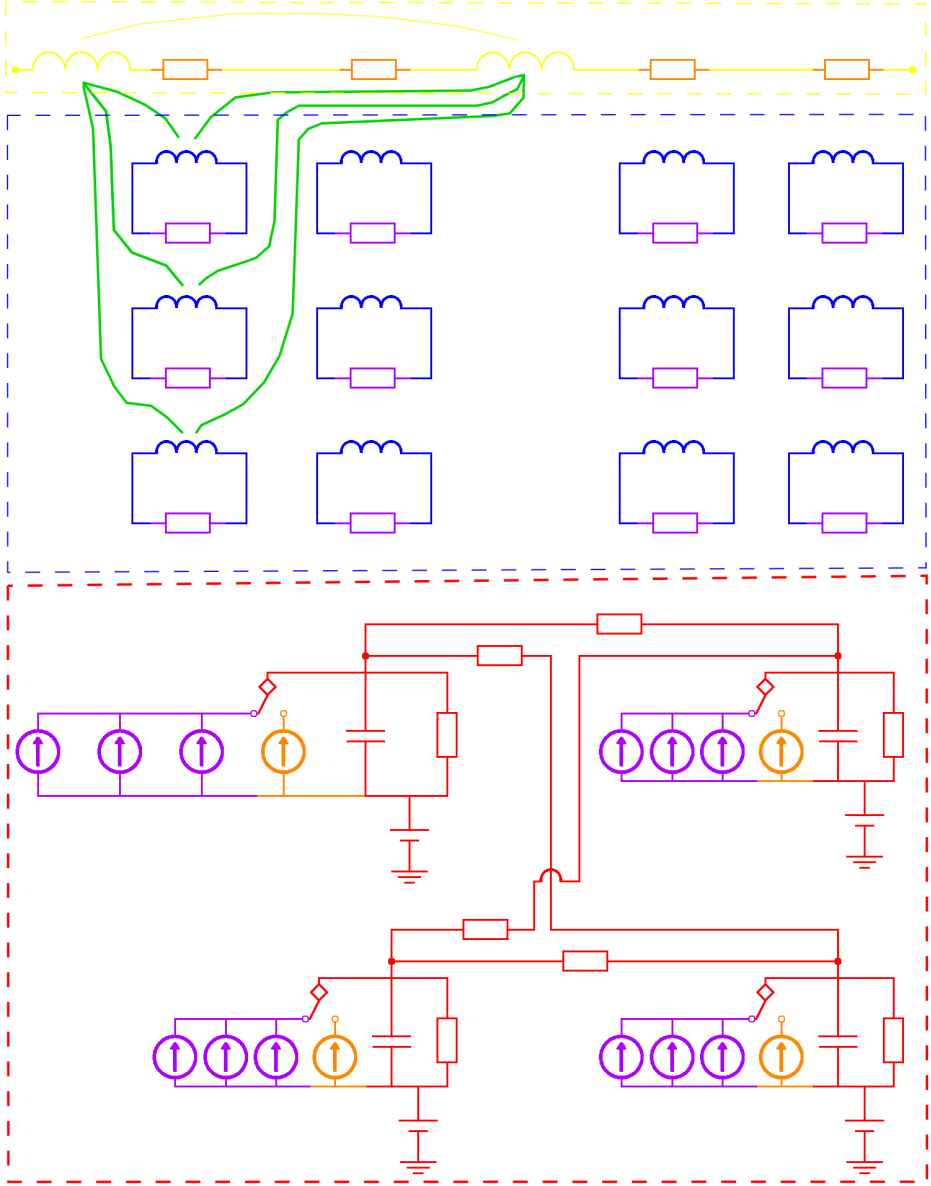


Figure 4.4. Sample implementation of a LEDET model of a superconducting coil, composed of two electrical elements, four thermal blocks, and four coupling blocks. Elements pertaining to one sub-network are represented in yellow (electrical), red (thermal), and blue (coupling). Elements pertaining to two different sub-networks are represented in orange (electrical-thermal), green (electrical-coupling), and purple (coupling-thermal). Note: Only the coupling lines of the first coupling block are shown.

turns. The physical and magnetic properties in each block are assumed homogeneous and are averaged over the block volume. The thermal balance in each block  $b$  reads

$$P_{\text{if},b} + P_{\text{is},b} + P_{\text{ohm},b} + P_{\text{ex},b} + P_{\text{He},b} = C_b(T_b) \frac{d[(T_b - T_{\text{He}})]}{dt}, \quad [\text{W}] \quad (4.1)$$

where  $P_{\text{if},b}$ ,  $P_{\text{is},b}$ , and  $P_{\text{ohm},b}$  [W] are the heat sources corresponding to the inter-filament and inter-strand coupling loss and ohmic loss in block  $b$ , respectively,  $P_{\text{ex},b}$  [W] is the heat exchanged with other blocks,  $P_{\text{He},b}$  [W] is the heat flow to the helium bath,  $C_b$  [JK<sup>-1</sup>] is the thermal capacity of  $b$ ,  $T_b$  [K] its average temperature, and  $T_{\text{He}}$  [K] is the temperature of the helium bath surrounding the magnet, assumed constant. The calculation of  $P_{\text{if},b}$  and  $P_{\text{is},b}$  will be treated in sections 4.4.1 and 4.4.2, respectively.

In a conductor composed of a superconductor and a stabilizer, the ohmic loss can be calculated as

$$P_{\text{ohm},b} = R_b I_{e(b)}^2 = \frac{\rho_b(T_b, B_{t,b}) N_{c,b} l_b}{S_b f_{\text{st},b}} I_{e(b)}^2 q_b, \quad [\text{W}] \quad (4.2)$$

where  $R_b$  [ $\Omega$ ] is the electrical resistance of block  $b$ ,  $I_{e(b)}$  [A] is the current flowing in the electrical element  $e$  where  $b$  is located,  $\rho_b$  [ $\Omega\text{m}$ ] is the average resistivity of the stabilizer in the block strands,  $B_{t,b}$  [T] is the average absolute value of the total magnetic field in block  $b$ , introduced in equation 2.16,  $N_{c,b}$  is the number of conductors (coil turns) in block  $b$ ,  $l_b$  [m] is the conductor length,  $S_b$  [m<sup>2</sup>] is the conductor cross-section, including its insulation and impregnation,  $f_{\text{st},b}$  is the volumetric fraction of stabilizer, and  $q_b$  is either 0 or 1 if block  $b$  is in the superconducting or in the normal state, respectively.

The parameter  $q_b$  in equation 4.2 is set to 1 any time the  $T_b$  is larger than the current-sharing temperature in the strand with the highest magnetic field located in block  $b$ . In fact, due to the transposition of the cable strands, each strand occupies the highest magnetic-field position within the cable cross-section twice every strand twist-pitch length. The transition from the superconducting to the normal state is considered to be instantaneous.

The approach followed for the calculation of the heat diffusion between adjacent blocks is schematized in figure 4.5a. By assuming that the temperature is uniform in the conductor and in its insulation layer, and that heat diffusion occurs only in the direction perpendicular to the insulation layers, the heat exchanged by block  $b$  with other blocks can be approximated as

$$P_{\text{ex},b} = - \sum_{h=1}^{N_{bh}} \frac{k_b(T_b) k_h(T_h)}{s_h k_b(T_b) + s_b k_h(T_h)} A_{b,h} (T_b - T_h), \quad [\text{W}] \quad (4.3)$$

where  $N_{bh}$  is the number of blocks that exchange heat with  $b$ ,  $A_{b,h}$  [m<sup>2</sup>] is the contact area between blocks  $b$  and  $h$ ,  $s_b$  and  $s_h$  [m] are the insulation thicknesses of the conductor in blocks  $b$  and  $h$ ,  $k_b$  and  $k_h$  [Wm<sup>-1</sup>K<sup>-1</sup>] are the thermal conductivities of the insulation material in blocks  $b$  and  $h$ , and  $T_h$  [K] is the average temperature in block  $h$ . Note that the thermal barrier due to the conductor material is neglected because it is much smaller than that due to the insulation layer.



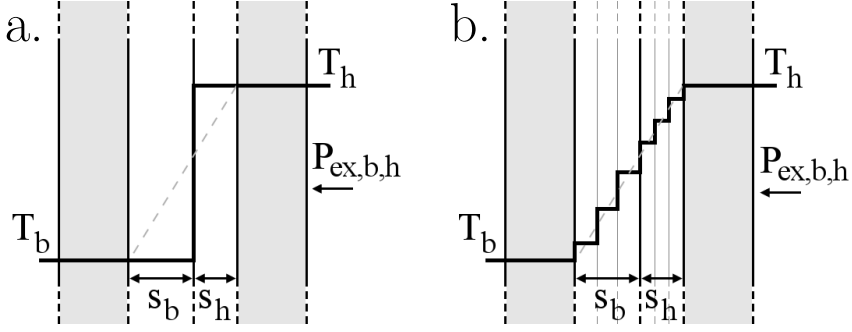


Figure 4.5. Model adopted to calculate the heat diffusion between blocks  $b$  and  $h$ . Temperature profile along the direction perpendicular to the insulation layer. a. Simplified one-layer approach. b. Multi-layer approach.

This simplified one-layer approach is usually satisfactory when simulating electro-thermal transients in superconducting coils since the contribution of thermal diffusion is less than about 10% of the ohmic power generated in the conductor during the magnet discharge. However, if required the model can be improved by considering that the conductor insulation is composed of multiple regions, each with different temperature and hence different thermal conductivity, as shown in figure 4.5b.

The heat dissipated into the helium bath can be calculated as

$$P_{\text{He},b} = -h_{\text{He},b}(T_b, T_{\text{He}})A_{b,\text{He}}(T_b - T_{\text{He}}), \quad [\text{W}] \quad (4.4)$$

where  $h_{\text{He},b}$  [ $\text{Wm}^{-2}\text{K}^{-1}$ ] is the heat transfer coefficient between block  $b$  and the helium bath surrounding the magnet and  $A_{b,\text{He}}$  [ $\text{m}^2$ ] is the contact area between  $b$  and the helium bath.

The total thermal capacity of block  $b$  is the sum of the thermal capacities of the  $N_{m,b}$  materials composing its volume, including superconductor, stabilizer, insulation, and impregnation:

$$C_b = \sum_{m=1}^{N_{m,b}} C_{m,b}(T_b) = V_b \sum_{m=1}^{N_{m,b}} [c_{m,b}(T_b)f_{m,b}], \quad [\text{JK}^{-1}] \quad (4.5)$$

where  $V_b = S_b l_b$  [ $\text{m}^3$ ] is the volume of block  $b$ ,  $C_{m,b}$  [ $\text{JK}^{-1}$ ] the heat capacity of material  $m$ ,  $c_{m,b}$  [ $\text{JK}^{-1}\text{m}^{-3}$ ] the specific heat of material  $m$ , and  $f_{m,b}$  is the volumetric fraction of material  $m$  in block  $b$ .

The thermal system described by equations 4.1-4.4 can be represented by the analogous electrical circuit shown in figure 4.6. The characteristic equations of this electrical circuit correctly reproduce the behavior of the thermal system if the equivalent parameters are defined as shown in table 4.1.

The interaction between the thermal and electrical sub-networks is twofold. Firstly, the ohmic loss  $P_{\text{ohm},b}$  in block  $b$  depends on the current  $I_{e(b)}$  flowing in the electrical element  $e$  where block  $b$  is located. Secondly, the resistance  $R_e$  of each

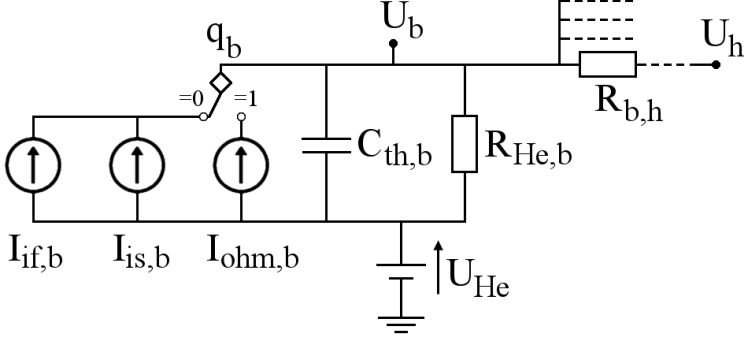


Figure 4.6. Equivalent LEDET sub-network modeling the thermal behavior of block  $b$ .

Table 4.1. Electro-thermal analogy implemented in the LEDET model, for a generic block  $b$ . Symbols pertaining to the electrical domain refer to figure 4.6.

Thermal domain		Electrical domain	
$T_b$	[K]	$U_b$	[V]
$T_h$	[K]	$U_h$	[V]
$T_{He}$	[K]	$U_{He}$	[V]
$P_{if,b}$	[W]	$I_{if,b}$	[A]
$P_{is,b}$	[W]	$I_{is,b}$	[A]
$P_{ohm,b}$	[W]	$I_{ohm,b}$	[A]
$C_b(T_b)$	[JK <sup>-1</sup> ]	$C_{th,b}$	[F]
$\frac{1}{A_{b,h}} \frac{s_h k_b(T_b) + s_b k_h(T_h)}{k_b(T_b) k_h(T_h)}$	[KW <sup>-1</sup> ]	$R_{b,h}$	[Ω]
$\frac{1}{h_{He,b}(T_b, T_{He}) A_{b,He}}$	[KW <sup>-1</sup> ]	$R_{He,b}$	[Ω]

electrical element  $e$  is the sum of the resistances in the  $N_{B,e}$  blocks contained in  $e$ ,

$$R_e = \sum_{b \in e} R_b = \sum_{b \in e} \frac{\rho_b(T_b, B_{t,b}) l_b}{S_b f_{st,b}} q_b. \quad [\Omega] \quad (4.6)$$

## 4.4 Coupling-current sub-networks

The innovative approach proposed here aims at reproducing with a limited number of equations the overall effect on the magnet behavior of local inter-filament and inter-strand coupling currents (section 2.2). The analysis of the electro-magnetic transient follows the equivalent magnetization model described in [3] and refers to the equivalent network model presented in [18].

The LEDET coupling model is composed of three sub-networks simulating the effect of inter-filament coupling currents in the two directions perpendicular to the magnet transport current and of inter-strand coupling currents in the direction perpendicular to the cable broad face, respectively.

Each coupling sub-network is further subdivided into  $N_{CL}$  blocks, each modelling effects occurring in a certain volume of conductor. For the sake of simplicity, it is here assumed that each block  $cl$  of the coupling sub-network corresponds to one block  $b$  of the thermal sub-network presented in the previous section ( $cl \equiv b$ ).

### 4.4.1 Equivalent IFCC loops

Consider the case of a strand, or wire, of circular cross-section and of radius  $r_s$  [m], whose superconducting filaments are homogeneously distributed along its diameter  $d_s$  [m]. This assumption is chosen for the sake of simplicity, but the results of this section can be easily extended to less general cases by modifying the value of the effective transverse resistivity of the strand stabilizer matrix,  $\rho_{eff}$  [ $\Omega m$ ], as explained in section 2.2.

When the strand is subject to a magnetic-field change in a direction  $\vec{e}_{x'}$  perpendicular to the direction  $\vec{e}_{z'}$  of the transport current, a surface current-density arises along the circumference  $r=r_s$ . Following [3, 16, 18, 147], this surface current-density can be expressed as

$$\vec{K}_{if} = - \left( \frac{l_f}{2\pi} \right)^2 \frac{1}{\rho_{eff}} \frac{dB_t}{dt} \cos(\phi) \vec{e}_{z'}, \quad [Am^{-1}] \quad (4.7)$$

where  $l_f$  [m] is the filament twist-pitch,  $dB_t/dt$  [ $Ts^{-1}$ ] is the absolute value of the total magnetic field change, also defined in equation 2.25, and  $\phi = \pi/2 - 2\pi z/l_f$  [rad].

The magnetic moment of a current distribution  $\vec{J}$  is computed as  $\vec{m} = \frac{1}{2} \int_V \vec{r} \times \vec{J} dV$  [Am]. For extruded loops of surface currents  $\vec{K}_{if}$  on the

boundary  $\partial\mathcal{V}$  of  $\mathcal{V}$  we define

$$\begin{aligned}
 \vec{m}' &= \lim_{\ell \rightarrow \infty} \frac{1}{2\ell} \int_{\mathcal{V}} \vec{r}' \times \vec{J} \, dV \\
 &= \lim_{\ell \rightarrow \infty} \frac{1}{2\ell} \int_{\partial\mathcal{V}} \vec{r}' \times \vec{K}_{\text{if}} \, da \\
 &= \int_{\partial\mathcal{A}} \vec{r}' \times \vec{K}_{\text{if}} \, ds,
 \end{aligned} \tag{A m} \quad (4.8)$$

where the surface  $\mathcal{A}$  is the cross-section of  $\mathcal{V}$  in the extruded part and the factor two between the second and third lines is due to the omission of the path closure at  $\pm\ell$ . Hence, by combining equations 4.7 and 4.8, one obtains

$$\begin{aligned}
 \vec{m}'_{\text{if}} &= \int_0^{2\pi} \vec{r}' \times \vec{K}_{\text{if}} r_s d\phi \\
 &= \vec{e}_{y'} \int_0^{\pi/2} r_s \cos(\phi) K_{\text{if}} r_s d\phi \\
 &= -\vec{e}_{y'} \int_0^{\pi/2} \left(\frac{l_f}{2\pi}\right)^2 \frac{1}{\rho_{\text{eff}}} \frac{dB_t}{dt} r_s^2 \cos^2(\phi) d\phi \\
 &= -\left(\frac{l_f}{2\pi}\right)^2 \frac{1}{\rho_{\text{eff}}} \frac{dB_t}{dt} \pi r_s^2 \vec{e}_{y'}.
 \end{aligned} \tag{Am}] \quad (4.9)$$

The equivalent magnetization can be derived from  $\vec{m}'_{\text{if}} = \vec{M}_{\text{if}} \pi r_s^2$ :

$$\vec{M}_{\text{if}} = -\left(\frac{l_f}{2\pi}\right)^2 \frac{1}{\rho_{\text{eff}}} \frac{dB_t}{dt} \vec{e}_{y'}. \tag{Am}^{-1}] \quad (4.10)$$

Note that  $\vec{M}_{\text{if}}$  is homogeneous in the strand within the layer of superconducting filaments ( $r < r_s = d_s/2$ ), which in the present case corresponds to the entire strand volume.

By integrating  $\vec{K}_{\text{if}}$  along the circumference where the filaments are situated, the total current  $I_{\text{if}}$  [A] flowing at either side of the strand can be calculated:

$$I_{\text{if}} = 2 \int_0^{\pi/2} K_{\text{if}} r_s d\phi = \left(\frac{l_f}{2\pi}\right)^2 \frac{1}{\rho_{\text{eff}}} \frac{dB_t}{dt} d_s. \tag{A}] \quad (4.11)$$

By combining equations 4.10 and 4.11, one obtains

$$\vec{M}_{\text{if}} = \frac{\vec{I}_{\text{if}}}{d_s}, \tag{Am}^{-1}] \quad (4.12)$$

where the vectorial  $\vec{I}_{\text{if}}$  is introduced as the pair of currents ( $I_{\text{if},x}$ ,  $I_{\text{if},y}$ ) in the  $x$ - and  $y$ -directed dipoles such that the above equation is fulfilled. Note the distinction between the directions ( $\vec{e}_{x'}$ ;  $\vec{e}_{y'}$ ) parallel and perpendicular to the applied magnetic-field change, respectively; and the directions ( $x$ ;  $y$ ) defined in an external orthogonal frame,

arbitrarily chosen and common to all strands in the magnet. For the sake of simplicity, let  $x$  and  $y$  be the same directions as defined in section 2.2.

The magnetic field induced in the strand by the magnetic-field change can be computed following [147], as

$$\begin{aligned} B_{\text{if}} &= \int_0^{2\pi} \frac{\mu_0 K_{\text{if}}}{2\pi r} \cos(\phi) r d\phi \\ &= - \int_0^{2\pi} \frac{\mu_0}{2\pi} \left( \frac{l_f}{2\pi} \right)^2 \frac{1}{\rho_{\text{eff}}} \frac{dB_t}{dt} \cos^2(\phi) d\phi \quad [\text{T}] \quad (4.13) \\ &= - \frac{\mu_0}{2} \left( \frac{l_f}{2\pi} \right)^2 \frac{1}{\rho_{\text{eff}}} \frac{dB_t}{dt}, \end{aligned}$$

analogous to 2.17. By combining equations 4.10-4.13, one obtains

$$\vec{B}_{\text{if}} = \frac{\mu_0}{2} \vec{M}_{\text{if}} = \frac{\mu_0}{2d_s} \vec{I}_{\text{if}}. \quad [\text{T}] \quad (4.14)$$

Furthermore, with the IFCL time-constant introduced in equation 2.18 and defining a tensorial time constant  $\tau_{\text{if}}$ ,

$$\begin{cases} \tau_{\text{if},x} = \frac{\mu_0}{2} \frac{1}{\rho_{\text{eff},x}} \left( \frac{l_f}{2\pi} \right)^2 = \frac{\mu_0}{2} \beta_{\text{if},x} \\ \tau_{\text{if},y} = \frac{\mu_0}{2} \frac{1}{\rho_{\text{eff},y}} \left( \frac{l_f}{2\pi} \right)^2 = \frac{\mu_0}{2} \beta_{\text{if},y}, \end{cases} \quad [\text{s}] \quad (4.15)$$

it follows that the total magnetic-field change is

$$\frac{d\vec{B}_t}{dt} = -\tau_{\text{if}}^{-1} \vec{B}_{\text{if}} = -\frac{\mu_0}{2} \tau_{\text{if}}^{-1} \vec{M}_{\text{if}} = -\beta_{\text{if}}^{-1} \vec{M}_{\text{if}} = -\beta_{\text{if}}^{-1} \frac{\vec{I}_{\text{if}}}{d_s}. \quad [\text{Ts}^{-1}] \quad (4.16)$$

The tensorial effective transverse resistivity  $\rho_{\text{eff}}=(\rho_{\text{eff},x}, \rho_{\text{eff},y})$  occurring in  $\beta_{\text{if}}$  depends on the absolute magnetic field in the copper matrix due to magneto-resistivity effects, as shown in equation 2.19. Note that in the most general case the effective resistivities in the  $x$  and  $y$  directions may differ ( $\rho_{\text{eff},x} \neq \rho_{\text{eff},y}$ ).

Let  $\mathcal{A}_s$  be the reference strand surface delimited by the outer layer of superconducting filaments; and let  $|\mathcal{A}_s|=a_s=\pi r_s^2$  be its metric measure. The loss per unit length of conductor generated by the inter-filament coupling currents are computed using

$$\begin{aligned} P'_{\text{if}} &= - \int_{\mathcal{A}_s} \vec{M}_{\text{if}} \cdot \frac{d\vec{B}_t}{dt} da \\ &= - \vec{M}_{\text{if}} \cdot \frac{d\vec{B}_t}{dt} a_s \quad [\text{Wm}^{-1}] \quad (4.17) \\ &= \beta_{\text{if}} \left( \frac{dB_t}{dt} \right)^2 a_s. \end{aligned}$$

Note that dividing this equation by the strand surface  $a_s$  yields an expression of the inter-filament coupling loss identical to equation 2.25. Furthermore, by rearranging the equation it is possible to obtain an explicit relation between IFCL and IFCC,

$$\begin{aligned}
 P'_{if} &= P'_{if,x} + P'_{if,y} \\
 &= \frac{a_s}{d_s^2} \left( \frac{I_{if,x}^2}{\beta_{if,x}} + \frac{I_{if,y}^2}{\beta_{if,y}} \right) \quad [\text{Wm}^{-1}] \quad (4.18) \\
 &= R'_{if,x} I_{if,x}^2 + R'_{if,y} I_{if,y}^2 \\
 &= \vec{I}_{if}^T R'_{if} \vec{I}_{if},
 \end{aligned}$$

where a tensorial resistance per unit length  $R'_{if}$  is defined following

$$\begin{cases} R'_{if,x} = \frac{a_s}{d_s^2} \frac{1}{\beta_{if,x}} = \frac{\pi}{4} \frac{1}{\beta_{if,x}} \\ R'_{if,y} = \frac{a_s}{d_s^2} \frac{1}{\beta_{if,y}} = \frac{\pi}{4} \frac{1}{\beta_{if,y}}. \end{cases} \quad [\Omega\text{m}^{-1}] \quad (4.19)$$

These defined parameters can be regarded as the resistances of equivalent inter-filament dissipative loops. The self-inductance per unit length of conductor of such equivalent loops can be computed with the "winding density"  $\vec{k}_{if} = \vec{K}_{if}/I_{if}$  [ $\text{m}^{-1}$ ], from

$$\begin{aligned}
 L'_{if} = L'_{if,x} = L'_{if,y} &= \frac{1}{I_{if}} \int_{\partial\mathcal{A}_s} \vec{k}_{if} \cdot \vec{A}_{if} ds \\
 &= \frac{\mu_0 \pi}{8} = \frac{\mu_0 a_s}{2d_s^2}, \quad [\text{Hm}^{-1}] \quad (4.20)
 \end{aligned}$$

where  $\vec{A}_{if} = \frac{d_s}{2} B_{if} \cos(\phi) \vec{e}'_z$ . Consistently, the resulting RL constant of the introduced equivalent IFCC loops equals the IFCL time-constant defined in equation 2.18,

$$\tau_{if} = \frac{L'_{if}}{R'_{if}} = \frac{\mu_0}{2} \beta_{if}. \quad [\text{s}] \quad (4.21)$$

Moreover, the local IFCC influence the behavior of the elements composing the electrical sub-network presented in section 4.2. A relation describing this interaction can be derived from the equation of local magnetic-field change, analogous to equation 2.16. The total change of magnetic-field density is the result of the applied magnetic-field change  $d\vec{B}_a/dt$  generated by a change in the local currents, and the already defined  $d\vec{B}_{if}/dt$  which opposes to the change [18]:

$$\frac{d\vec{B}_t}{dt} = \frac{d\vec{B}_a}{dt} + \frac{d\vec{B}_{if}}{dt}. \quad [\text{Ts}^{-1}] \quad (4.22)$$

The applied magnetic-field change can be expressed as the superposition of the field change generated by the change in the local currents of the  $N_E$  elements in the

electrical sub-network,

$$\begin{cases} \frac{dB_{a,x}}{dt} = \sum_{e=1}^{N_E} f_{e,x} \frac{dI_e}{dt} \\ \frac{dB_{a,y}}{dt} = \sum_{e=1}^{N_E} f_{e,y} \frac{dI_e}{dt}, \end{cases} \quad [\text{Ts}^{-1}] \quad (4.23)$$

where the parameters  $\vec{f}_e = (f_{e,x}, f_{e,y})$   $[\text{TA}^{-1}]$  can be calculated by means of dedicated software, such as ROXIE [98] or SOLENO [99]. In first approximation, they are purely geometric.

By substituting equations 4.16, 4.23, and 4.14 into 4.22; and multiplying by  $a_s/d_s$ , an equation for induced voltages, i.e. time-derivatives of linked magnetic fluxes, per unit length is derived:

$$-\frac{a_s}{d_s^2} \frac{1}{\beta_{if}} \vec{I}_{if} = \frac{a_s}{d_s} \sum_{e=1}^{N_E} \vec{f}_e \frac{dI_e}{dt} + \frac{\mu_0 a_s}{2d_s^2} \frac{d\vec{I}_{if}}{dt}, \quad [\text{Vm}^{-1}] \quad (4.24)$$

where the parameters  $R'_{if}$  and  $L'_{if}$  introduced with equations 4.19 and 4.20 can be identified, together with tensorial mutual inductances per unit length  $M'_{if,e}$ :

$$\begin{cases} M'_{if,e,x} = \frac{a_s}{d_s} f_{e,x} = \frac{\pi d_s}{4} f_{e,x} & \text{for } e = 1 \dots N_E \\ M'_{if,e,y} = \frac{a_s}{d_s} f_{e,y} = \frac{\pi d_s}{4} f_{e,y} & \text{for } e = 1 \dots N_E. \end{cases} \quad [\text{Hm}^{-1}] \quad (4.25)$$

Thus, equation 4.22 can be rewritten as

$$\begin{cases} -R'_{if,x} I_{if,x} = \sum_{e=1}^{N_E} M'_{if,e,x} \frac{I_e}{dt} + L'_{if,x} \frac{I_{if,x}}{dt} \\ -R'_{if,y} I_{if,y} = \sum_{e=1}^{N_E} M'_{if,e,y} \frac{I_e}{dt} + L'_{if,y} \frac{I_{if,y}}{dt} \end{cases} \quad [\text{Vm}^{-1}] \quad (4.26)$$

This set of equations describes the complex interaction between local IFCC and changes in the currents flowing in the main electrical circuit.

Finally, the overall effect on the system dynamics of the local IFCC in a volume of conductor can be calculated by superposition of effects. Let us consider the case of a model block  $b$ , composed of  $N_{c,b}$  conductors with length  $l_b$  [m], as defined in equation 4.2; each conductor being composed of  $N_{s,b}$  superconducting strands. The volume of its strands is  $V_{s,b} = N_{c,b} N_{s,b} \pi \frac{d_{s,b}^2}{4} l_b$   $[\text{m}^3]$ . By multiplying the equations of system 4.26 by  $N_{c,b} N_{s,b} l_b$ , one obtains

$$\begin{cases} -R_{if,b,x} I_{if,b,x} = \sum_{e=1}^{N_E} M_{if,b,e,x} \frac{I_e}{dt} + L_{if,b,x} \frac{I_{if,b,x}}{dt} \\ -R_{if,b,y} I_{if,b,y} = \sum_{e=1}^{N_E} M_{if,b,e,y} \frac{I_e}{dt} + L_{if,b,y} \frac{I_{if,b,y}}{dt}, \end{cases} \quad [\text{V}] \quad (4.27)$$

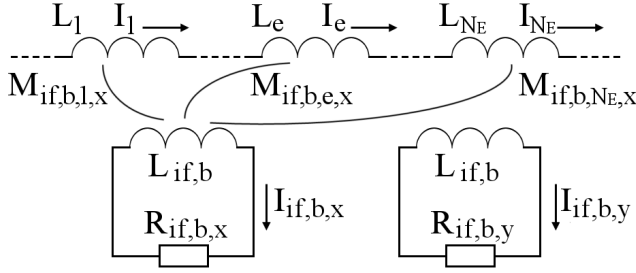


Figure 4.7. Equivalent LEDET sub-network modeling the inter-filament coupling currents in block  $b$  (mutual inductances  $M_{if,b,1,y}$ ,  $M_{if,b,e,y}$ , and  $M_{if,b,NE,y}$  are not shown).

where the tensorial equivalent resistance  $R_{if,b}$ , self-inductance  $L_{if,b}$ , and mutual inductances  $M_{if,b,e}$  of the IFCC loop representing the dynamic behavior of block  $b$  are defined as:

$$\begin{cases} R_{if,b,x} = \frac{V_{s,b}}{d_{s,b}^2} \frac{1}{\beta_{if,b,x}} = \frac{\pi}{4} N_{c,b} N_{s,b} l_b \frac{1}{\beta_{if,b,x}} & [\Omega] \\ R_{if,b,y} = \frac{V_{s,b}}{d_{s,b}^2} \frac{1}{\beta_{if,b,y}} = \frac{\pi}{4} N_{c,b} N_{s,b} l_b \frac{1}{\beta_{if,b,y}} & [\Omega] \\ L_{if,b} = L_{if,b,x} = L_{if,b,y} = \frac{\mu_0}{2} \frac{V_{s,b}}{d_{s,b}^2} = \frac{\mu_0 \pi}{8} N_{c,b} N_{s,b} l_b & [H] \quad (4.28) \\ M_{if,b,e,x} = \frac{V_{s,b}}{d_{s,b}} f_{b,e,x} = \frac{\pi}{4} N_{c,b} N_{s,b} d_{s,b} l_b f_{b,e,x} & \text{for } e = 1 \dots N_E \quad [H] \\ M_{if,b,e,y} = \frac{V_{s,b}}{d_{s,b}} f_{b,e,y} = \frac{\pi}{4} N_{c,b} N_{s,b} d_{s,b} l_b f_{b,e,y} & \text{for } e = 1 \dots N_E. \quad [H] \end{cases}$$

The behavior of the set of equations 4.27 can be modeled with an equivalent lumped-element circuit composed of two closed loops of a resistor and a self-inductance mutually coupled to the  $N_E$  self-inductances  $L_e$  present in the electrical sub-network. Figure 4.7 shows a schematic representation of such a circuit. In order to model the IFCC effects in the  $x$  and  $y$  direction in the  $N_B$  blocks of the coupling sub-network,  $2N_B$  similar equivalent loops are implemented.

In addition to the coupling between local IFCC and system currents, the introduced model provides a calculation of the inter-filament coupling loss in each block. In fact, the ohmic loss dissipated in each equivalent resistor  $R_{if,b}$  corresponds to the IFCL in the stabilizer matrix of the strands of block  $b$ :

$$\begin{aligned} P_{if,b} &= P_{if,b,x} + P_{if,b,y} \\ &= \vec{I}_{if,b}^T R'_{if,b} \vec{I}_{if,b} = R_{if,b,x} I_{if,b,x}^2 + R_{if,b,y} I_{if,b,y}^2. \end{aligned} \quad [W] \quad (4.29)$$

The loss calculated with this equation is used to solve the thermal balance in block  $b$  presented in equation 4.1.

Most of the parameters present in the definitions 4.28 are geometrical or physical quantities. However, the introduced model includes an unknown parameter, namely



$f_{\text{eff,b}}$ , occurring in equation 2.19, which influences the effective transverse resistivity and thus  $\beta_{\text{if,b}}$ . As explained in section 2.2, its value depends on the fraction of superconductor in the strand, on the interface resistance between the filaments and the matrix, and on the position of the filaments in the strand cross-section [101–103]. The value of the effective transverse resistivity for a certain strand, or wire, can be deduced by measuring the transitory loss occurring in a single wire of the same type.

#### 4.4.2 Equivalent ISCC loops

As mentioned in section 2.2, if a conductor is composed of multiple superconducting strands, inter-strand coupling currents develop. The following treatise only considers ISCC through cross-contact resistance and due to a magnetic-field change perpendicular to the cable broad face. These currents typically generate the largest fraction of the ISCL in the cable [18].

The model adopts an approach analogous to that applied in section 4.4.1 for the inter-filament coupling currents. The mutual coupling between local ISCC in a cable and the change of the currents in the main electrical circuit will be described with a limited set of equations and modeled with an equivalent sub-network composed of equivalent ISCC loops.

Consider the case of a flat Rutherford cable, with large aspect ratio  $\alpha_c = w/h$ , with  $w$  [m] and  $h$  [m] the broad and narrow cable dimension, respectively. Its surface  $\mathcal{A}_c$  has metric measure  $|\mathcal{A}_c| = a_c = wh$  [m<sup>2</sup>]. A magnetic-field change in the direction  $\vec{e}_\perp$  perpendicular to the cable broad face induces ISCC through the contact resistance between two crossing strands,  $R_c$  [ $\Omega$ ]. The equivalent magnetization  $\vec{M}_{\text{is}}$  [Am<sup>-1</sup>] generated by these ISCC can be represented as the effect of an equivalent surface current flowing at the surface of the two sides of the cable,

$$\vec{K}_{\text{is}} = \vec{M}_{\text{is}} \times \vec{e}_\parallel = M_{\text{is}} \vec{e}_{z'}, \quad [\text{Am}^{-1}] \quad (4.30)$$

where  $\vec{e}_\parallel$  and  $\vec{e}_{z'}$  are the directions parallel to the cable broad face and to the transport current, respectively. Thus, the equivalent ISCC flowing at either side of the cable is

$$\vec{I}_{\text{is}} = \vec{K}_{\text{is}} h = M_{\text{is}} h \vec{e}_{z'}. \quad [\text{A}] \quad (4.31)$$

The inter-strand coupling loss per unit length of conductor can be calculated as

$$P'_{\text{is}} = - \int_{\mathcal{A}_c} \vec{M}_{\text{is}} \cdot \frac{d\vec{B}_{\text{t},\perp}}{dt} da, \quad [\text{Wm}^{-1}] \quad (4.32)$$

analogous to equation 4.17, where  $dB_{\text{t},\perp}/dt$  [Ts<sup>-1</sup>] is the absolute value of the total magnetic field change in the direction  $\vec{e}_\perp$ . Note that  $\vec{M}_{\text{is}}$  and  $\vec{B}_{\text{t},\perp}$  are not homogeneous along the direction  $\vec{e}_\parallel$ . However, for various applications the assumption of homogeneous equivalent magnetization in the cable cross-section is acceptable. For example, in [3] it is proposed

$$\begin{aligned} \vec{M}'_{\text{is}} &= -\frac{1}{120} \frac{l_s}{R_c} N_s (N_s - 1) \frac{w}{h} \frac{dB_{\text{t},\perp}}{dt} \vec{e}_\perp \\ &= -\beta_{\text{is}} \frac{dB_{\text{t},\perp}}{dt} \vec{e}_\perp, \end{aligned} \quad [\text{Am}^{-1}] \quad (4.33)$$

with  $l_s$  [m] the strand twist-pitch and  $N_s$  the number of strands in the cable. Under this assumption, equations 4.31-4.33 can be combined leading to

$$\begin{aligned} P'_{\text{is}} &= \beta_{\text{is}} \left( \frac{dB_{t,\perp}}{dt} \right)^2 a_c \\ &= \frac{w}{h} \frac{1}{\beta_{\text{is}}} I_{\text{is}}^2 \quad [\text{Wm}^{-1}] \quad (4.34) \\ &= R'_{\text{is}} I_{\text{is}}^2, \end{aligned}$$

where the equivalent resistance per unit length of the equivalent ISCC loop is identified:

$$R'_{\text{is}} = \frac{w}{h} \frac{1}{\beta_{\text{is}}} = \frac{\alpha_c}{\beta_{\text{is}}}. \quad [\Omega\text{m}^{-1}] \quad (4.35)$$

Note the analogy with the definition of  $R'_{\text{if}}$  in equation 4.19. The self-inductance of the ISCC loop can be evaluated by considering the effect of a surface current flowing at the two sides of the cable and generating a magnetic field  $\vec{B}_{\text{is}}$  [T], not homogeneous along the direction  $\vec{e}_{\parallel}$ . The self-inductance per unit length of this system can be approximated as

$$\begin{aligned} L'_{\text{is},c} &= \frac{1}{I_{\text{is}}^2} \int_{\mathcal{A}_c} \vec{M}_{\text{is}} \cdot \vec{B}_{\text{is}} da \\ &\sim \frac{\mu_0}{\pi} \left[ \ln \left( \frac{w}{h} \right) + \frac{3}{2} \right], \quad [\text{Hm}^{-1}] \quad (4.36) \end{aligned}$$

where the approximated formula for the self-inductance per unit length of a pair of infinitely thin strip conductors presented in [152] is used. Thus, the resulting time-constant of the equivalent ISCC loop is

$$\tau_{\text{is},c} = \frac{L'_{\text{is},c}}{R'_{\text{is}}} = \frac{\mu_0}{\pi} \left[ \ln \left( \frac{w}{h} \right) + \frac{3}{2} \right] \frac{h}{w} \beta_{\text{is}} = \frac{\mu_0}{\pi} \left[ \ln(\alpha_c) + \frac{3}{2} \right] \frac{\beta_{\text{is}}}{\alpha_c}. \quad [\text{s}] \quad (4.37)$$

The values of  $\tau_{\text{is},c}$  calculated with this model prove to be a good approximation of the more precise ISCC time-constant obtained with a more detailed equivalent-network model [18]. As an example, the model proposed in [18] predicts an ISCC time-constant of

$$\tau_{\text{is},c,\text{net}} = c_s l_s \frac{N_s^2 - 4N_s}{R_c}, \quad [\text{s}] \quad (4.38)$$

valid for Rutherford cables with  $8 \leq N_s \leq 40$ , where  $c_s$  is a constant with a value between 1.6 and  $1.7 \cdot 10^{-8} \Omega\text{m}^{-1}$  [18]. The comparison between the ISCC time-constant calculated with equation 4.37 and the time constant resulting from equation 4.38, for  $l_s=100$  mm,  $R_c=100 \mu\Omega$ , and  $N_s$  in the range 8 to 40, is shown in figure 4.8.

If  $N_c$  cables are stacked, the total height of the stack  $N_c h$  is comparable or larger than  $w$  and the approximation of infinitely thin strips is not acceptable. Hence, equation 4.36 does not hold and the resulting ISCC time-constant is not correct. When a sufficient number of cables are stacked the approximation of induced magnetic field

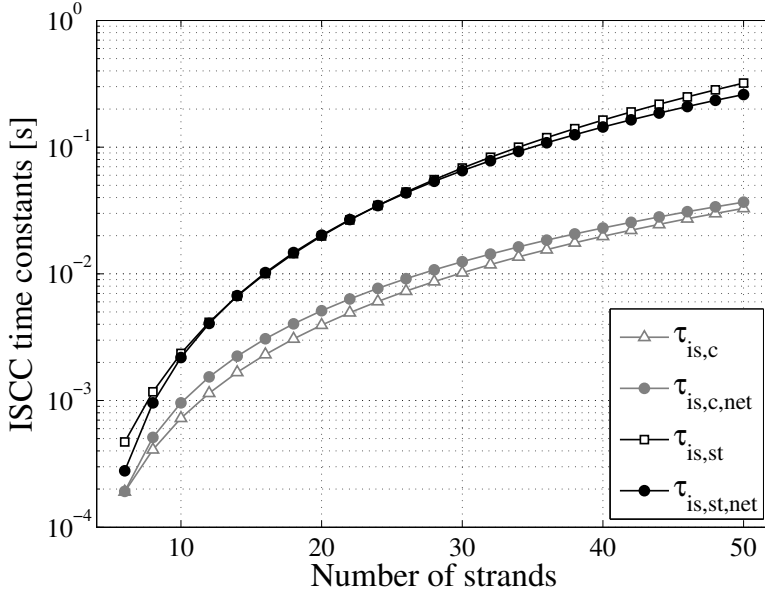


Figure 4.8. Comparison between the ISCC time-constant calculated using equation 4.37; or following the homogeneous-magnetization model presented in [3], see 4.41; or using the formulae derived in [18] with a complete network model for a single cable and for a stack of cables, see 4.38 and 4.42, respectively.

homogeneous in the surface  $\mathcal{A}_c$  and parallel to the magnetization lines is satisfactory:

$$\vec{B}_{is} \sim \mu_0 \vec{M}_{is} = \mu_0 \frac{\vec{I}_{is}}{h}. \quad [\text{T}] \quad (4.39)$$

Thus, the equivalent self-inductance of an ISCC loop modeling a cable which is part of a stack can be approximated as

$$\begin{aligned} L'_{is,st} &= \frac{1}{I_{is}^2} \int_{\mathcal{A}_c} \vec{M}_{is} \cdot \vec{B}_{is} da \\ &\sim \mu_0 \left( \frac{M_{is}}{I_{is}} \right)^2 a_c \quad [\text{Hm}^{-1}] \quad (4.40) \\ &= \mu_0 \frac{w}{h} = \mu_0 \alpha_c, \end{aligned}$$

equivalent to the self-inductance of two parallel sheets carrying current when they are very close [153]. Note the similarity with  $L'_{if}$  introduced in equation 4.20. Thus, the resulting time constant of the equivalent ISCC loop for a cable in a stack is

$$\tau_{is,st} = \frac{L'_{is,st}}{R'_{is}} = \mu_0 \beta_{is}, \quad [\text{s}] \quad (4.41)$$

analogous to  $\tau_{if}$  in equation 4.21. The more detailed equivalent-network model proposed in [18] predicts an overall ISCC time-constant for a stack of cables of

$$\tau_{is,st,net} = \frac{\alpha_c N_c}{\alpha_c + c_{st} (N_c - 1)} \tau_{is,c,net}, \quad [s] \quad (4.42)$$

valid for  $8 \leq N_s \leq 40$ , where  $c_{st}$  is a constant which depends slightly on the number of strands in the cable, increasing from about 1.00 for  $N_s=8$  to 1.15 for  $N_s=40$ . An example calculation of the ISCC time-constant for a stack of cables calculated with equation 4.41, as compared to the time constant resulting from the detailed model [18], see equation 4.42, for  $N_c=15$ ,  $\alpha_c=N_s/4$ ,  $c_{st}=1$ , and  $N_s$  in the range 8 to 40, is shown in figure 4.8. The two calculations show very little difference across the entire range of  $N_s$ .

In conclusion, the time constant of an equivalent ISCC loop resulting from the proposed model with  $L'_{is,c}$  is a good approximation of the time constant for a single cable; and  $L'_{is,st}$  is a good approximation of the time constant for a cable which is part of a stack.

Furthermore, it is of high interest to model the mutual coupling between the local ISCC loops and the current-change in the  $N_E$  self-inductances  $L_e$  present in the electrical sub-network defined in section 4.2. The local balance equation of the magnetic field change reads

$$\frac{dB_{t,\perp}}{dt} = \frac{dB_{a,\perp}}{dt} + \frac{dB_{is}}{dt}, \quad [Ts^{-1}] \quad (4.43)$$

where the applied magnetic-field change  $dB_{a,\perp}/dt$  [ $Ts^{-1}$ ] can be expressed as the superposition of the magnetic-field change in the direction  $\vec{e}_\perp$  generated by variations in the transport currents flowing in the electrical sub-network,

$$\frac{dB_{a,\perp}}{dt} = \sum_{e=1}^{N_E} f_{e,\perp} \frac{dI_e}{dt}, \quad [Ts^{-1}] \quad (4.44)$$

where the parameters  $f_{e,\perp}$  [ $TA^{-1}$ ] can be calculated by means of dedicated software, such as ROXIE [98] or SOLENO [99]. In first approximation, they are purely geometric. The assumption of homogeneous magnetic-field change in the cable cross-section, substituting equations 4.31, 4.33, 4.39, and 4.44 into 4.43 and multiplying by  $w$ , yields:

$$-\frac{w}{h} \frac{1}{\beta_{is}} \vec{I}_{is} = w \sum_{e=1}^{N_E} \vec{f}_{e,\perp} \frac{dI_e}{dt} + \mu_0 \frac{w}{h} \frac{d\vec{I}_{is}}{dt}, \quad [Vm^{-1}] \quad (4.45)$$

where the parameters  $R'_{is}$  and  $L'_{is,st}$  introduced with equations 4.35 and 4.40 can be identified, together with a  $N_E$  mutual inductances per unit length:

$$M'_{is,e,\perp} = w f_{e,\perp}, \quad \text{for } e = 1 \dots N_E, \quad [Hm^{-1}] \quad (4.46)$$

analogous to  $M_{if,e}$  defined in equation 4.25. Thus, equation 4.43 can be rewritten as

$$-R'_{is} I_{is} = \sum_{e=1}^{N_E} M'_{is,e,\perp} \frac{dI_e}{dt} + L'_{is,st} \frac{dI_{is}}{dt}. \quad [Vm^{-1}] \quad (4.47)$$

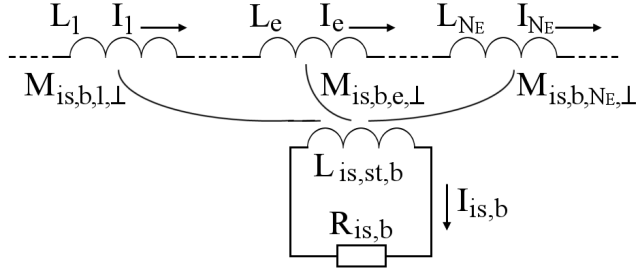


Figure 4.9. Equivalent LEDET sub-network modeling the inter-strand coupling currents in block  $b$ .

Finally, the total effect of local ISCC in a volume of conductor can be calculated. Consider a model block  $b$  composed of  $N_{c,b}$  conductors with length  $l_b$  [m]. Its total volume is  $V_{c,b} = N_{c,b} \text{ wh } l_b$  [m<sup>3</sup>]. By multiplying equation 4.47 by  $N_{c,b} l_b$ , a relation describing the coupling between the ISCC in block  $b$  and the currents in the electrical sub-network is obtained,

$$-R_{is,b} I_{is,b} = \sum_{e=1}^{N_E} M_{is,b,e,\perp} \frac{dI_e}{dt} + L_{is,st,b} \frac{dI_{is,b}}{dt}, \quad [\text{V}] \quad (4.48)$$

where the equivalent resistance  $R_{is,b}$ , self-inductance  $L_{is,b}$ , and mutual inductances  $M_{is,b,e,\perp}$  of the ISCC loop representing the dynamic behavior of block  $b$  are defined as:

$$\begin{cases} R_{is,b} = \frac{V_{c,b}}{h^2} \frac{1}{\beta_{is,b}} = \frac{w}{h} N_{c,b} l_b \frac{1}{\beta_{is,b}} & [\Omega] \\ L_{is,st,b} = \mu_0 \frac{V_{c,b}}{h^2} = \mu_0 \frac{w}{h} N_{c,b} l_b & [\text{H}] \\ M_{is,b,e,\perp} = \frac{V_{c,b}}{h} f_{b,e,\perp} = w N_{c,b} l_b f_{b,e,\perp} & \text{for } e = 1 \dots N_E. \quad [\text{H}] \end{cases} \quad (4.49)$$

Note the analogy between equations 4.48-4.49 and 4.27-4.28, derived for IFCC loops. The behavior of this simple system can be modeled by the equivalent lumped-element circuit shown in figure 4.9, composed of a closed loop of a resistor and a self-inductance coupled to the  $N_E$  self-inductances  $L_e$  present in the electrical sub-network.

In the case of a model block composed of a single non-stacked cable the equivalent inductance  $L_{is,st,b}$  in equation 4.48 is to be replaced by a more appropriate

$$L_{is,c,b} = \frac{\mu_0}{\pi} \left[ \ln \left( \frac{w}{h} \right) + \frac{3}{2} \right] N_{c,b} l_b, \quad [\text{H}] \quad (4.50)$$

obtained multiplying equation 4.36 by  $N_{c,b} l_b$ .

In addition, the inter-strand coupling loss generated in the cable volume of a block  $b$  corresponds to the ohmic loss in the equivalent resistor  $R_{is,b}$ ,

$$P_{is,b} = R_{is,b} I_{is,b}^2, \quad [\text{W}] \quad (4.51)$$

analogous to equation 4.29. This ISCL is used to solve the thermal balance in block  $b$  presented in equation 4.1.

The only unknown parameter in the model of equivalent ISCC loops is the contact resistance between two crossing strands  $R_c$ , inversely proportional to the ISCC time-constant and to the ISCL during transients at constant current-change.

The LEDET model of inter-filament and inter-strand coupling currents neglects the magnetic coupling between individual coupling loops, which could be included in the model with a radically different mathematical approach, based on FEM methods. However, this approximation greatly simplifies the problem and has significantly less influence on the system dynamics than other assumptions, such as uniformity of the physical properties along the direction of the conductor, and unknowns, such as material properties and magneto-resistivity.

#### 4.4.3 Extension to other coupling-current mechanisms

More generally, also other coupling-current mechanisms can be simulated following a methodology analogous to that introduced in sections 4.4.1 and 4.4.2. The total generated loss and the effect of local currents on the magnet differential self-inductance can be reproduced with a sub-network of lumped-elements.

In fact, a generic coupling-current mechanism characterized by a loss  $P_{cc}$  [W] and an equivalent coupling-current  $I_{cc}$  [A] is described by the following two relations:

$$\begin{cases} P_{cc} = \beta_{cc} V_{cc} \left( \frac{dB_{cc}}{dt} \right)^2 & [\text{W}] \\ I_{cc} = -\gamma_{cc} \frac{dB_{cc}}{dt}, & [\text{A}] \end{cases} \quad (4.52)$$

plus a characteristic time constant,  $\tau_{cc}$  [s], where  $V_{cc}$  [m<sup>3</sup>] is the volume where the loss takes place,  $dB_{cc}/dt$  [Ts<sup>-1</sup>] is the resulting total magnetic-field change, and  $\beta_{cc}$  [m $\Omega^{-1}$ ] and  $\gamma_{cc}$  [m<sup>2</sup> $\Omega^{-1}$ ] are characteristic parameters depending on the loss mechanism. The coupling between the local coupling currents and the currents in the main electrical circuit is described by the following equation:

$$-R_{cc}I_{cc} = \sum_{e=1}^{N_E} M_{cc,e} \frac{dI_e}{dt} + L_{cc} \frac{dI_{cc}}{dt}, \quad [\text{V}] \quad (4.53)$$

where the equivalent resistance  $R_{cc}$ , self-inductance  $L_{cc}$ , and mutual inductances  $M_{cc,e}$  of the generic coupling-current loop are defined as:

$$\begin{cases} R_{cc} = \frac{P_{cc}}{I_{cc}^2} = \frac{\beta_{cc} V_{cc}}{\gamma_{cc}^2} & [\Omega] \\ L_{cc} = \tau_{cc} R_{cc} = \frac{\tau_{cc} \beta_{cc} V_{cc}}{\gamma_{cc}^2} & [\text{H}] \\ M_{cc,e} = \frac{\beta_{cc} V_{cc}}{\gamma_{cc}} f_{cc,e} & \text{for } e = 1 \dots N_E, \quad [\text{H}] \end{cases} \quad (4.54)$$

where  $f_{cc,e}$  [TA<sup>-1</sup>] are  $N_E$  magnetic parameters characterizing the applied magnetic field  $B_a$  [T] generated by a current  $I_e$  [A] flowing through electrical element  $e$ . The

definition of the above-mentioned parameters  $M_{cc,e}$  is derived from the consideration that during a transient at constant ramp-rate the induced coupling currents do not vary ( $dI_{cc}/dt=0$ ) and the local magnetic field-change coincides with the applied magnetic-field change ( $dB_{cc}/dt = dB_a/dt$ ); hence, equation 4.53 is reduced to

$$\sum_{e=1}^{N_E} M_{cc,e} \frac{dI_e}{dt} = -R_{cc} I_{cc} = R_{cc} \gamma_{cc} \frac{dB_{cc}}{dt} = \frac{\beta_{cc} V_{cc}}{\gamma_{cc}} \sum_{e=1}^{N_E} f_{cc,e} \frac{dI_e}{dt}, [\text{V}] \quad (4.55)$$

when the definition of  $M_{cc,e}$  is found.

## 4.5 Conclusion

Given the numerous multi-domain, interdependent, non-linear effects occurring in a superconducting magnet during a CLIQ discharge, the development of simulation tools capable of correctly reproducing and predicting coupled electrical, magnetic, and thermal transients is crucial for an effective implementation of the CLIQ technology.

A new technique for modeling the behavior of a superconducting magnet called LEDET (Lumped-Element Dynamic Electro-Thermal) is developed, based on various coupled networks of lumped-elements. The energy-exchanges between different physical domains are correctly accounted for, as well as the influence of local inter-filament and inter-strand coupling currents on the overall magnet differential self-inductance. The same simulation environment can simultaneously model macroscopic electrical transients and phenomena at the level of superconducting strands.

The LEDET model is successful for reproducing experimental results, and hence deepening the understanding of the phenomena occurring in a superconducting magnet. The impact of different operating parameters on CLIQ performance can be assessed by means of complete parametric studies. Finally, new CLIQ configurations can be analyzed to investigate their effectiveness on existing and future magnets of different geometries, sizes, types of superconductor, and strand and cable parameters.





## Chapter 5

# CLIQ-based protection of existing magnets

*The process to follow for designing and implementing a CLIQ system on existing superconducting magnets is outlined. Practical aspects related to the connection of CLIQ units to existing magnets are analyzed. Selected cases among the first implementations of CLIQ-based protection systems are discussed. Experimental results are presented and compared to simulation results carried out with a lumped-element dynamic electro-thermal model (LEDET).*

*A CLIQ system integrated in the magnet design from the start can be fully optimized for maximum effectiveness. Also for the majority of nowadays built superconducting magnets, where CLIQ was not included in the magnet design, it is relatively easy to connect a CLIQ system and obtain satisfactory performance. The option to use CLIQ as an effective back-up system for the protection of existing magnets with broken quench heaters represents a distinct advantage of the CLIQ technology.*

### 5.1 Design

The sequence of actions required for an effective CLIQ design are summarized in the flow diagram presented in figure 5.1. A successful strategy starts with the optimization of the discharge circuit, following the guidelines outlined in chapter 3. This often yields significant improvement of the performance with very limited or no disadvantages. In section 3.1, the parameter  $\Psi$  [ $\text{m}^{-1}$ ], called CLIQ effectiveness, is defined to determine the peak applied magnetic-field change which can be introduced in the strands by a certain CLIQ configuration, per unit of charging voltage and of coil length. Cases were shown where an optimum position of the terminals and electrical order of the coil sections enhances the CLIQ effectiveness by one order of magnitude, corresponding

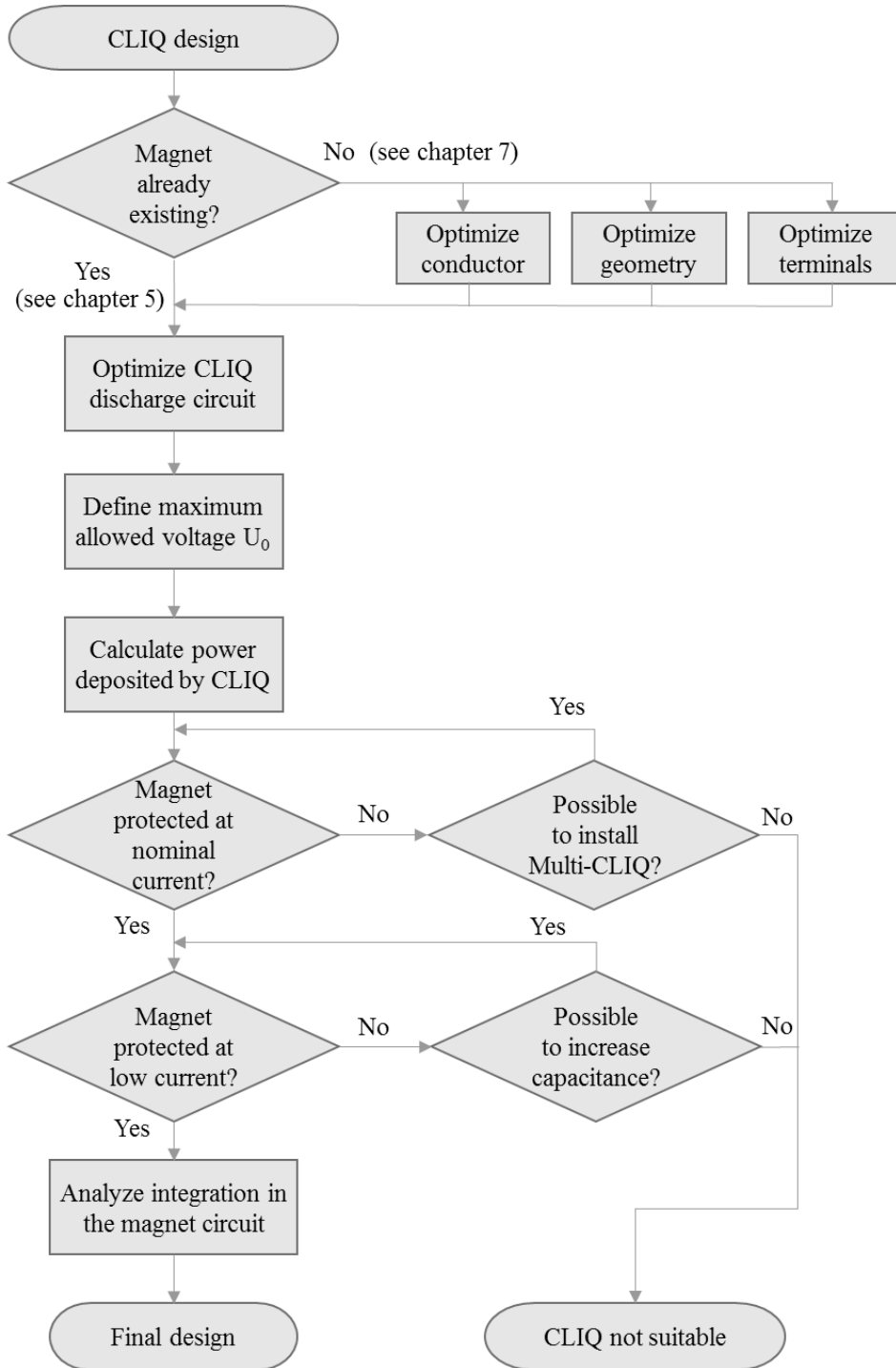


Figure 5.1. Flow diagram of the design of a CLIQ-based protection system.

to a hundredfold increase of the peak coupling loss per unit volume introduced by CLIQ. In the case of existing magnets the options of possible CLIQ configurations applicable with some mechanical work is limited. In fact, depending on the magnet geometry, certain configurations require terminals connected to positions on the coil where terminals are already present, but others require access to positions not easily accessible.

Once the optimum discharge circuit is identified, the designer has to determine whether a 1-CLIQ configuration is sufficient to assure the protection of the magnet at any operating current level, or whether a Multi-CLIQ configuration is required. At higher current, the higher energy density requires introducing a faster transition to the normal state in order to more homogeneously spread the magnet stored energy in the coil windings. Hence, the peak power density deposited immediately after triggering CLIQ is the key parameter. Following the treatise presented in sections 3.1 and 3.2, it can be shown that the CLIQ peak power density is  $P'''_{\text{if,peak}} \propto (N_C U_0 / l_m)^2 \text{ [Wm}^{-3}\text{]}$ , where  $N_C$  is the number of CLIQ units installed across separate coil sections,  $U_0$  [V] the charging voltage of the units, and  $l_m$  [m] the magnet length. For a given magnet geometry and size, and maximum allowed charging voltage, it is therefore possible to calculate the expected peak power density and assess the need to implement a Multi-CLIQ system instead of a 1-CLIQ. Note that the peak power is independent of the capacitance  $C$  [F] of the capacitor bank.

At lower current, the transition to the normal state can be induced more slowly, but the temperature margin is higher. Hence, the CLIQ performance is mainly influenced by the total energy delivered during the entire discharge,  $E_{\text{CLIQ}} = 0.5 N_C C U_0^2$  [J]. The required increase of cost and size of the system due to a higher capacitance has less impact on the protection system than an eventual increase of the charging voltage or of the number of CLIQ units.

The power per unit volume deposited in the strands can be calculated more precisely with equation 2.24 for a given conductor, CLIQ configuration, magnet length, charging voltage, and capacitance. A numerical integration over the time of the CLIQ discharge yields the total deposited energy density. A complete electro-thermal modeling of a CLIQ discharge under various operating conditions is mandatory, as explained in chapter 4.

Finally, the integration of the CLIQ system in the magnet circuit has to be carefully analyzed. With respect to conventional protection systems based on quench heaters, CLIQ is less prone to electrical breakdown due to its more robust design. The introduced current and voltage to ground have to be included in the analysis of the electrical transients in the circuit. The addition of by-pass elements across sections of the circuit is usually required, a subject thoroughly addressed in chapter 8, where it is shown how to connect a CLIQ-based system to a chain of superconducting magnets.

## 5.2 Implementation

One or more CLIQ units and their terminals have to be connected to the coil. In this section the most important aspects of their design and implementation are commented.

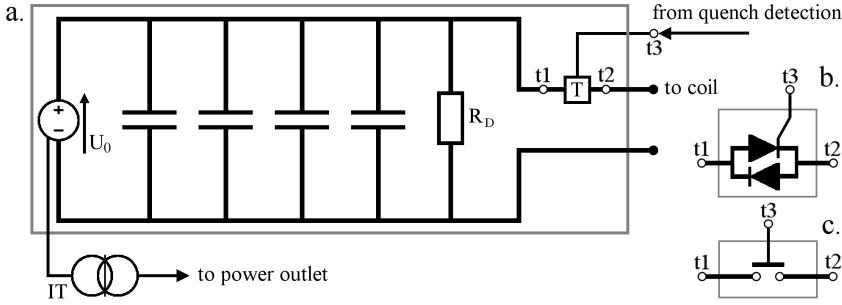


Figure 5.2. a. Electrical scheme of a CLIQ unit. b. Trigger unit T composed of a thyristor and a diode in antiparallel. c. Trigger unit T composed of an electronic switch.

### 5.2.1 Unit

The simplified scheme of a CLIQ unit is shown in figure 5.2a. Its capacitor bank is composed of various capacitors connected in parallel. A discharge resistor  $R_D$  [ $\Omega$ ] is installed across the bank taking up the energy stored in the capacitors when the unit is switched off. The voltage across the capacitors decreases exponentially with time constant  $\tau_D = R_D C$  [s], which is characteristically in the order of a few minutes.

The two main types of capacitors suitable for a CLIQ unit are electrolytic and film capacitors, whose limits for safe and reliable operation are about 500 and 1000 V, respectively. Film capacitors are less compact and more expensive, but they are suited for operation with alternating voltage. On the contrary, electrolytic capacitors do not safely operate when subject to a negative voltage, and when installed in a CLIQ unit they have to be protected by means of by-pass diodes. Capacitors with small equivalent resistance during the discharge are better suited because of the smaller resistance they introduce in the circuit. The corresponding reduction of the damping of the introduced current causes a higher generation of coupling loss in the strands. The picture of one of the first prototype units is shown in figure 5.3.

The trigger unit can be a thyristor and a diode connected in anti-parallel (figure 5.2b), or an electronic switch (figure 5.2c), or another means to allow the current flow in the two directions. The output of a conventional quench detection system is the driver for the trigger unit. Upon quench detection, a signal is sent either to a thyristor or to a switch, and an oscillating current is introduced in the magnet circuit. The components must be rated for operating safely with a peak current at least equal to the peak current  $I_C$  [A] discharged by the CLIQ unit and for sustaining a voltage to ground at least equal to the unit charging voltage. These components only need to carry pulsed currents for a few hundred milliseconds and therefore they generate minimal heat during a discharge.

The use of an isolation transformer (IT in figure 5.2) is advised, to assure galvanic separation between the negative terminal of the floating CLIQ unit and ground. The power supply charging the capacitor bank is powered through such transformers, to avoid unwanted currents to ground after triggering CLIQ.

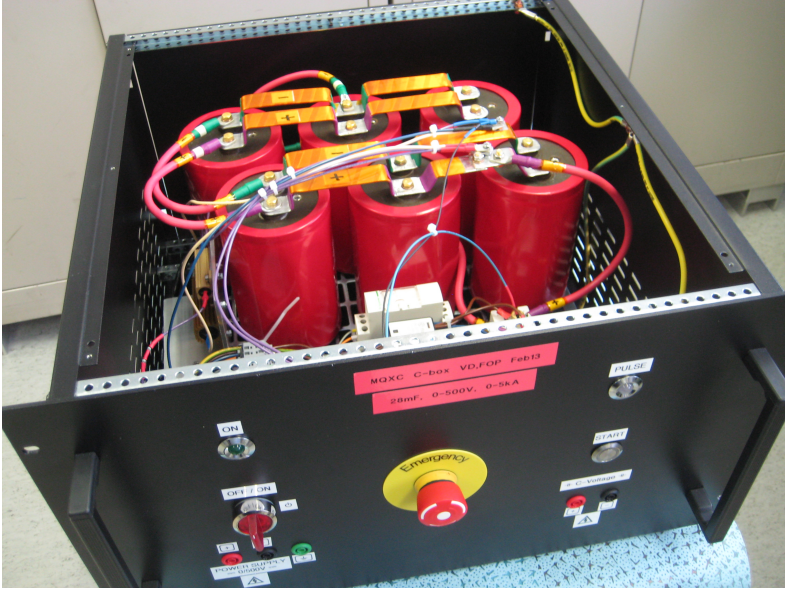


Figure 5.3. Prototype CLIQ unit including a bank of six electrolytic capacitors with a total capacitance of 28.2 mF rated for a charging voltage of 500 V.

### 5.2.2 Terminals

Key ingredients are the leads connecting the unit to the coil. In chapter 3 it is explained how to choose the positioning of the terminals, which subdivides the coil into multiple highly-coupled sections.

The most convenient position for attaching the terminals to the magnet is at the coil end, where more space is available. As an example, figure 5.4 shows the addition of three CLIQ leads to a 14 m long LHC twin-aperture dipole magnet [20–23,108,154]. One terminal is attached at the joint between the two apertures, and two others at the joints between poles. During a CLIQ discharge, a force is exerted on the leads due to the interaction between the current flowing through them and the magnetic field at the magnet end. Thus, it is important to mechanically reinforce the leads and provide proper supports to the coil structure.

In the presented example, the leads are constituted by the same superconducting wire as used for the LHC spool piece bus-bars [23], rated for a stationary current of 600 A. While a superconducting wire for the CLIQ leads is not strictly necessary, it helps reducing the resistance of the discharge circuit  $R_{eq}$  [ $\Omega$ ] defined in equation 2.3. A similar wire of copper would increase  $R_{eq}$  by 2 to 10 m $\Omega$ , hence increasing the damping of the current introduced by CLIQ and reducing the coupling loss generated in the strands. The copper cross-section in the CLIQ leads is 3 mm<sup>2</sup>, which is sufficient to maintain the wire temperature below 50 K even in the case of a transition of the lead to the normal state during the discharge. The wire is properly insulated with polyimide tape.

Of critical importance is the connection between CLIQ lead and coil conductor. In

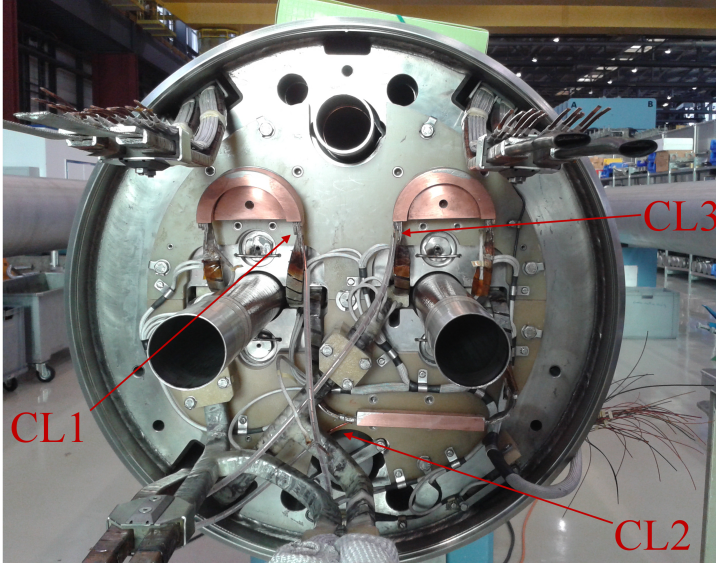


Figure 5.4. Addition of three CLIQ leads to an LHC main dipole magnet, one attached at the joint between the two apertures (CL2), and two at the joints between poles (CL1 and CL3). View from the connection side, before the addition of mechanical supports to the CLIQ leads [108].

order to reduce the local ohmic loss and temperature increase, the cross-section of the leads is increased along a few centimetres, corresponding to the area where CLIQ lead and conductor are in contact. The soldered connections have to be secured by a clamp to avoid disconnection in the case of overheating. The addition of a superconducting CLIQ lead to a  $\text{Nb}_3\text{Sn}$  quadrupole model magnet [90–94], performed according to these guidelines, is shown in figures 5.5a-b.

### 5.2.3 Redundancy

Two measures are required for assuring redundancy. Firstly, in order to enhance the reliability of one CLIQ unit, two trigger units (T in figure 5.2) are installed in parallel, hence assuring the discharge of the capacitor bank and the introduction of the oscillating current in the coil sections even in the case of failure of one of the trigger units. Secondly, by using two CLIQ units in parallel, each including redundant trigger units and connected to the magnet through individual terminals, as shown in the scheme in figure 5.6. Note that this solution does not change the equivalent inductance of the discharge circuit. For instance, the behavior of a redundant 1-CLIQ system composed of two units in parallel, as shown in figure 5.6, is identical to that of a 1-CLIQ system with double capacitance, and different from a 2-CLIQ system. Obviously, each unit has to be dimensioned to assure the protection of the magnet in the case the other unit malfunctions.

The unit charging voltage is constantly monitored to assure the readiness of the

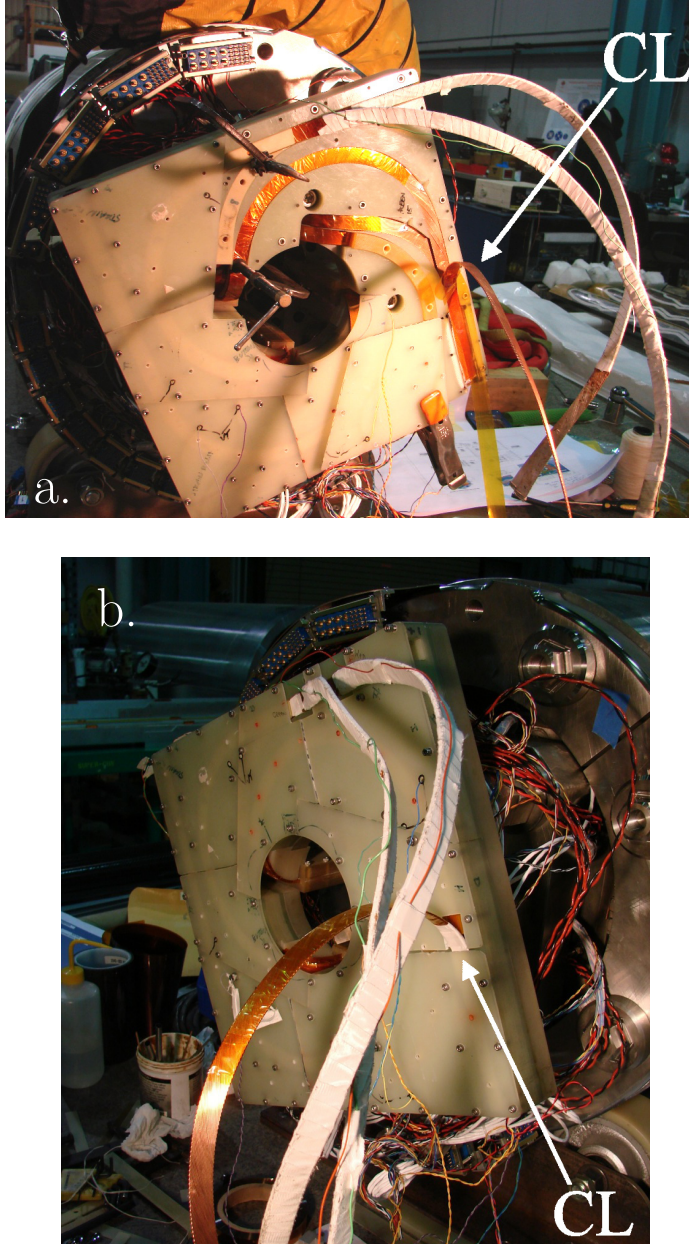


Figure 5.5. Addition of one CLIQ lead to a Nb<sub>3</sub>Sn quadrupole magnet. View from the connection side. a. Connection and insulation of the lead (CL). b. Secure clamping and mechanical support. Courtesy of D.W. Cheng of Lawrence Berkeley National Laboratory.



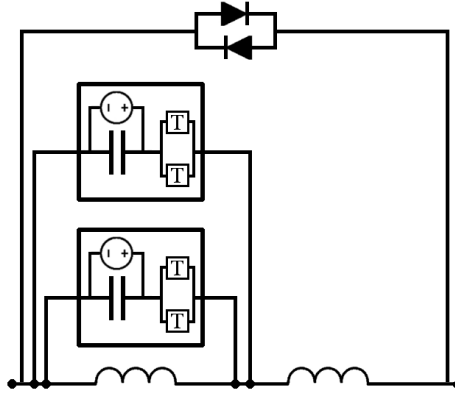


Figure 5.6. Electrical scheme of a redundant 1-CLIQ system composed of two independent units connected in parallel, each with redundant trigger units and each with their own leads and terminals connected to the coil.

system in the case of quench detection. Also, the current introduced after triggering the unit is measured to identify malfunctioning of the unit.

Repairing a CLIQ system is quick and relatively inexpensive as compared to quench-heater based systems, because CLIQ is external to the magnet cryostat and hence easily accessible.

### 5.3 Cases analyzed

An effective CLIQ system can be designed and connected to most existing magnets with relatively low cost. In this section, three cases among the first CLIQ applications tested are presented:

- Case 1: 0.8 meter long, Nb<sub>3</sub>Sn quadrupole model magnet for the LHC upgrade (section 5.3.1) [90–94];
- Case 2: 1.6 meter long, Nb-Ti quadrupole model magnet for the LHC upgrade (section 5.3.2) [83, 106, 109, 110];
- Case 3: small-scale, ten-layer solenoid [157]. The large number of available CLIQ terminals allows a wide choice of configurations, each characterized by high energy deposition in selected regions of the magnet (section 5.3.3).

The main parameters of the three magnets, and their conductors, are listed in tables 5.1 and 5.2, respectively. The examples include magnets of different geometries and types of superconductor, and featuring values of self-inductance, operating current, and strand parameters in a wide range.

Also, the parameters of three magnets that will be tested in the months after the publication of this thesis are included in the tables, notably the 11 T dipole model magnet for the high luminosity LHC (Case 4) [80, 81, 127–130], the 14 m long LHC main dipole magnet (Case 5) [20–23, 108, 154] and the 3.4 m long LHC



Table 5.1. Key parameters of the magnets analyzed in this chapter. Geometry, magnet length  $l_m$ , self-inductance  $L_0$ , nominal current  $I_0$ , and stored energy  $E_0$ .

#	Magnet geometry	$l_m$ [m]	$L_0$ [mH]	$I_0$ [A]	$E_0$ [kJ]	References
1	2-layer quadrupole	0.84	6.4	14600	680	[90–94]
2	2-layer quadrupole	1.65	8.4	12800	670	[83, 106, 109, 110]
3	10-layer solenoid	0.199	462	400	37	[157]
4	2-layer dipole	1.68	12	11850	830	[80, 81, 127–130]
5	2-layer dipole	$2 \times 14.3$	98	11850	6880	[20–23, 108, 154]
6	4-layer quadrupole	$2 \times 3.4$	148	3610	960	[23, 107, 155]

Table 5.2. Key parameters of the conductors used in the magnets analyzed in this chapter. Type of superconductor (SC), number of strands  $N_s$ , strand diameter  $d_s$  or wire dimensions  $w \times h$ , copper to non-copper ratio  $R_{Cu,nCu}$ , filament twist-pitch  $l_f$ , and average RRR of the copper matrix.

#	SC	$N_s$	$d_s$ [mm] or $w \times h$ [mm <sup>2</sup> ]	$R_{Cu,nCu}$	$l_f$ [mm]	RRR
1	Nb <sub>3</sub> Sn	35	0.778	1.23	13.5	80–140
2	Nb-Ti	28, 36	1.065, 0.825	1.65, 1.95	15, 18	209, 228
3	Nb-Ti	1	$0.8 \times 1.25$	4.20	50	91
4	Nb <sub>3</sub> Sn	40	0.700	1.15	14	100
5	Nb-Ti	28, 36	1.065, 0.825	1.65, 1.95	15, 18	150, 150
6	Nb-Ti	22, 34	0.735, 0.480	1.25, 1.75	15, 15	80, 80

matching quadrupole magnet (Case 6) [23, 107, 155]. These tests will constitute the first application of CLIQ to full-scale magnets.

### 5.3.1 Case 1: Nb<sub>3</sub>Sn quadrupole model magnet

One 28.2 mF, 500 V CLIQ unit is connected to the midpoint of the 120 mm aperture, Nb<sub>3</sub>Sn quadrupole model magnet developed for the High Luminosity LHC [90–94]. Given the electrical order of the poles and the presence of only one CLIQ terminal, the only available CLIQ configuration is the 1-CLIQ Pole-Pole configuration shown in figure 3.11a.

The currents in the system measured during and after a CLIQ discharge at the nominal current of  $I_0=14.6$  kA are shown in figure 5.7. At  $t=0$ , an oscillating 2 kA, 26 Hz current  $I_C$  is introduced. As a result, significant current changes occur in the two coil sections, and high coupling loss is generated in the strands. The temperature increase in the superconductor is sufficient to rapidly transfer to the normal state most of the winding pack in less than 10 ms. The high electrical resistance  $R_C$  [ $\Omega$ ] developed in the coil resistive zone causes a quick discharge of the magnet. At  $t=3$  ms, a 10 m $\Omega$  energy-extraction system is triggered as well in order to study the superposition between CLIQ and energy-extraction transients. However, the value

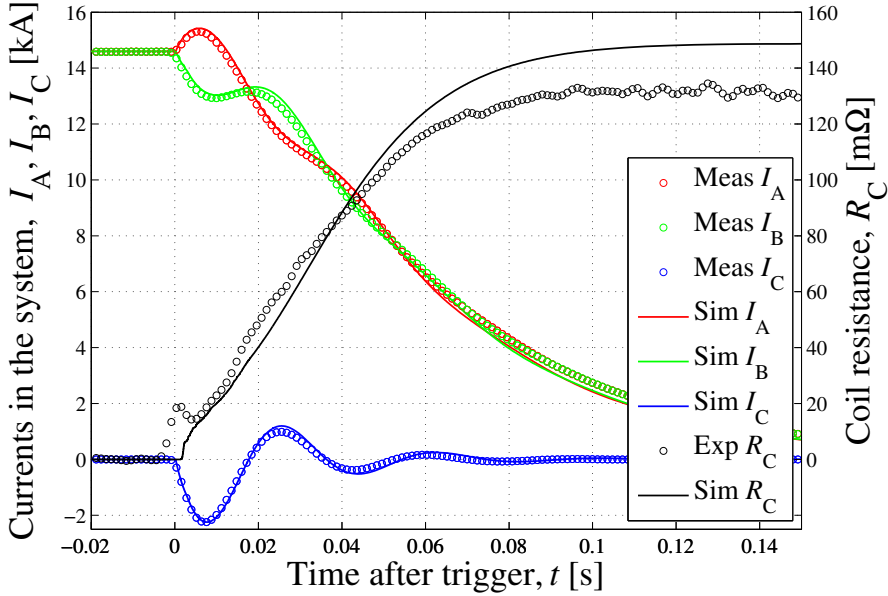


Figure 5.7. Protection of the Nb<sub>3</sub>Sn quadrupole model magnet for the LHC upgrade. Measured currents  $I_C$  and  $I_B$ , calculated current  $I_A = I_B - I_C$  versus time, after triggering CLIQ at  $t=0$ . Experimental effective coil resistance  $R_C$ , versus time. Simulated  $I_A$ ,  $I_B$ ,  $I_C$ , and  $R_C$ .

of the extraction resistor is significantly lower than the coil resistance. This can be observed in figure 5.7, where the effective coil resistance, calculated by subtracting the inductive component from the measured voltage across the magnet, is shown.

The transient is successfully reproduced by the LEDET model presented in chapter 4. The simulated currents and coil resistance, also shown in figure 5.7, are in very good agreement with the experimental results.

Similar tests are performed at different initial currents ranging from 3 to 14.6 kA, triggering CLIQ at  $t=0$  and the energy extraction system at  $t=3$  ms. The magnet currents measured are shown in figure 5.8, and compared to discharges obtained by triggering conventional quench heaters attached to the outer layer of the coil (OL QH) [79], or both to its inner and outer layers (IL+OL QH). One can conclude that this 0.8 m long magnet can be discharged significantly faster by CLIQ.

As shown in chapter 3, the peak power density generated by CLIQ in the strands is roughly proportional to the ratio between the CLIQ charging voltage and the magnet length. Hence, it is of high interest to test CLIQ performance with reduced charging voltage in order to assess its performance when the ratio  $U_0/l_m$  is closer to the value in the case of the protection of a full-length magnet. The quench loads  $\int I^2 dt$  [A<sup>2</sup>s] obtained after triggering quench heaters, a 500 V CLIQ unit, or a 250 V CLIQ unit are shown in figure 5.9. In the current range of 3 to 7.5 kA, the quench load obtained after triggering a CLIQ unit charged with  $U_0=250$  V is larger than with quench heaters. For initial currents higher than 9 kA the performance of a CLIQ unit charged at

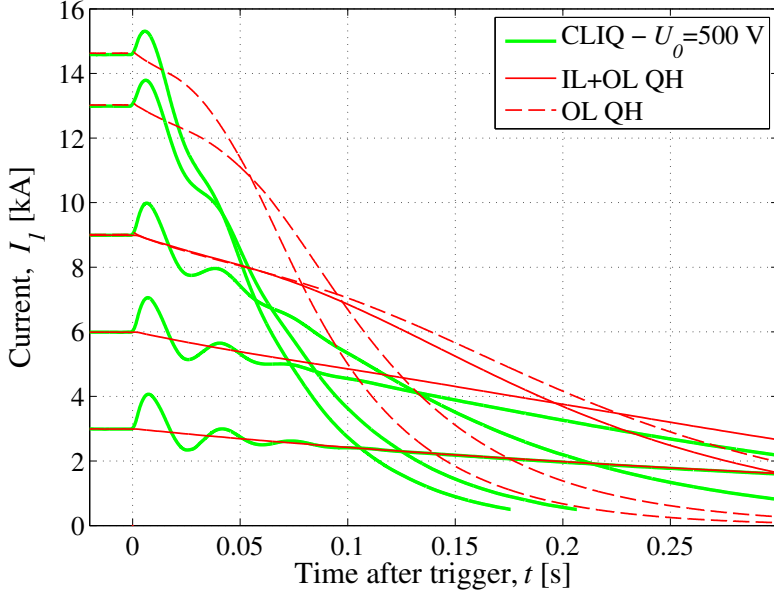


Figure 5.8. Protection of the Nb<sub>3</sub>Sn quadrupole model magnet for the LHC upgrade. Measured magnet current versus time, after triggering CLIQ or quench heaters at  $t=0$ .

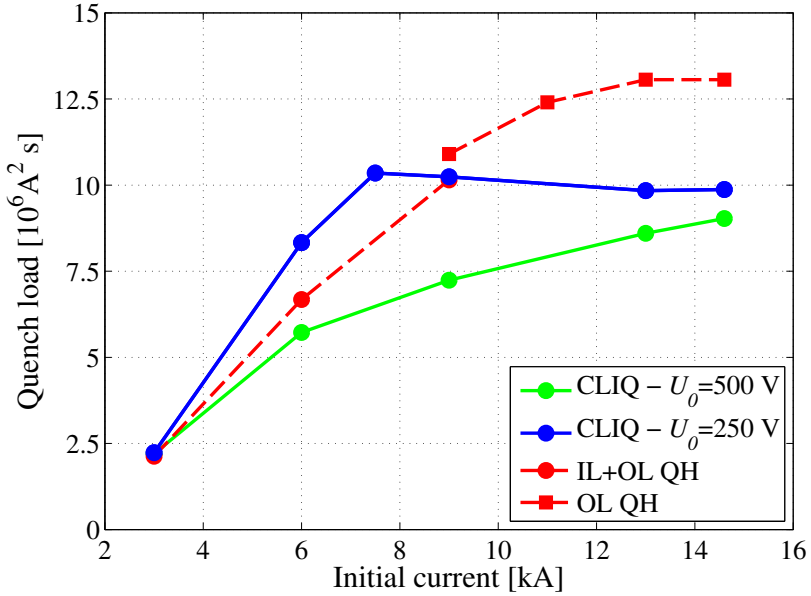


Figure 5.9. Protection of the Nb<sub>3</sub>Sn quadrupole model magnet for the LHC upgrade. Calculated quench load versus initial current, after triggering CLIQ or quench heaters.

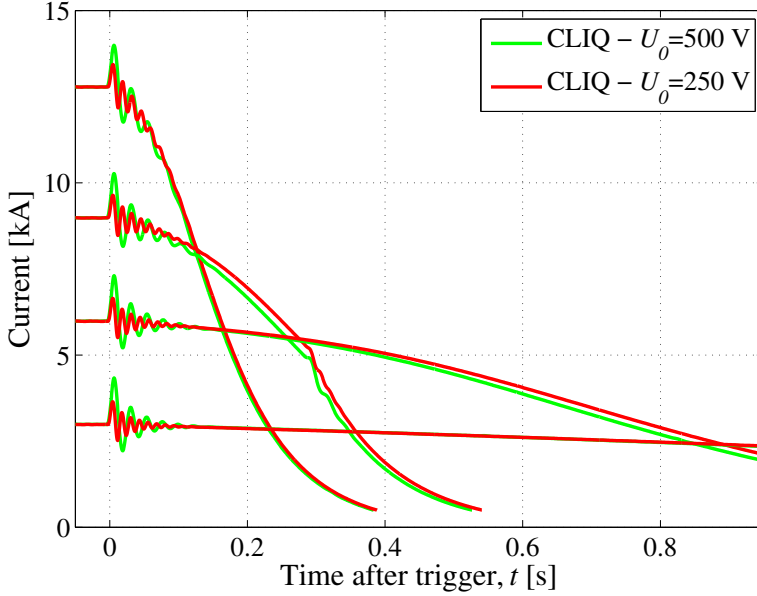


Figure 5.10. Protection of the Nb-Ti quadrupole model magnet for the LHC upgrade. Comparison between the measured magnet current versus time, obtained by triggering a CLIQ unit with  $U_0=500$  V and  $C=28.2$  mF, or with  $U_0=700$  V and  $C=8.8$  mF. Note: A  $40$  m $\Omega$  energy-extraction system was triggered with a delay of 950, 950 and 285 ms during the tests at 3, 6 and 9 kA, respectively.

half voltage is similar to a full voltage CLIQ. This result shows that CLIQ's fast and effective energy transfer mechanism achieves a peak power deposition significantly higher than with quench heaters. At high current, this results in a faster and more homogeneous transition to the normal state, and hence in a faster magnet discharge, even when CLIQ is charged at half voltage. At lower current, where the margin to quench is higher, the total energy stored in the CLIQ capacitor bank is not sufficient to start a voluminous transition to the normal state in the coil. This could be easily overcome by increasing the capacitance, with a relatively small increase of the system size and cost.

### 5.3.2 Case 2: Nb-Ti quadrupole model magnet

CLIQ is tested on the 1.6 m long, 8.4 mH, Nb-Ti quadrupole model magnet for the LHC upgrade [83, 106, 109, 110], whose cross-section and magnetic field distribution are presented in figure 2.4. Given the electrical order of the poles, an optimized 1-CLIQ Crossed-Pole configuration, like the one shown in figure 3.11e, is applied with a single CLIQ terminal connected to the midpoint of the coil.

Two CLIQ units are tested separately, one with  $U_0=500$  V and  $C=28.2$  mF, and another one with  $U_0=700$  V and  $C=8.8$  mF. In figure 5.10, the measured current discharges for initial currents between 3 and 12.8 kA are shown. The peak

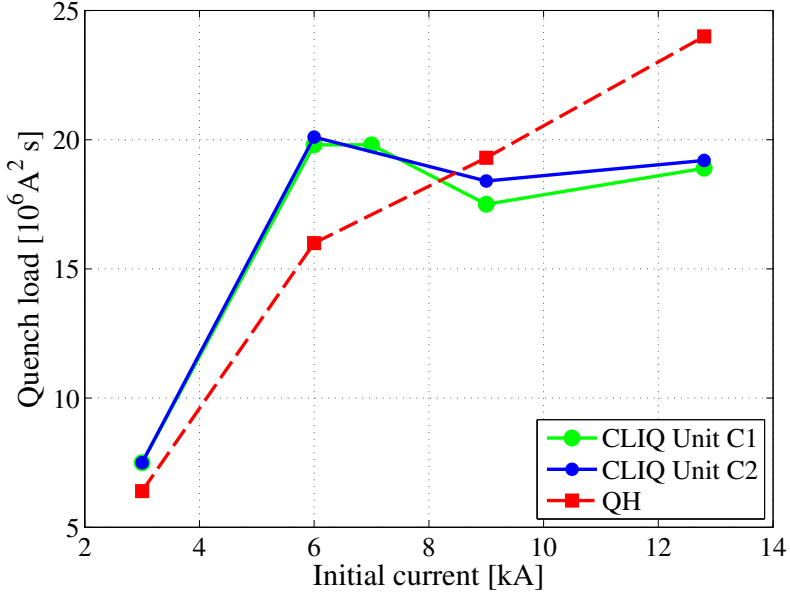


Figure 5.11. Protection of the Nb-Ti quadrupole model magnet for the LHC upgrade. Calculated quench load versus initial current, after triggering CLIQ or quench heaters.

value and the oscillation frequency of the current introduced are a function of the unit parameters. The unit with lower capacitance introduces oscillations at higher frequency. Hence, the direction of the introduced current change varies more often, and less time is given to the coupling loss to fully develop. Besides, about 40% less energy is stored in the unit with lower capacitance. Nevertheless, the performance of the two units in terms of discharge velocity is very similar. This result shows that the energy deposited by CLIQ is largely sufficient to effectively protect this 1.6 meter long magnet.

Conventional quench heaters are tested on the same magnet in order to compare the performance of the two methods. The quench loads for both methods, as a function of the initial current, are shown in figure 5.11. Interestingly, during CLIQ tests the maximum quench load is observed at a current of 6 to 7 kA, corresponding to about 50% of the magnet nominal current. In fact, at higher currents the margin to normal state is less and the magnet can be discharged more quickly by CLIQ due to a much faster quench initiation and propagation. The CLIQ performance is significantly better at nominal current, with a quench load about 20% lower, corresponding to a reduction of the hot-spot temperature of more than 60 K. Again, detailed analyses need to be carried out in order to extend this result to the case of full-scale coils [106].

### 5.3.3 Case 3: ten-layer solenoid

The results of an extensive test campaign carried out on a 462 mH, Nb-Ti, single-wire, solenoid [84, 157] at 4.2 K are reported. About one thousand discharges have been

performed in order to study in great detail the CLIQ performance under different operating conditions, investigate the effect of various system parameters, and optimize its performance. The key parameters under study are the initial current  $I_0$  [A], the capacitance  $C$  [F], the charging voltage  $U_0$  [V], and the positioning of the terminals.

The capacitor bank has 8 film capacitors, each with a capacitance of 1.1 mF; the capacitance of the bank can be varied between 1.1 and 8.8 mF.

Terminals (T1-T9) are available between each of the ten layers of the solenoid (L1-L10), and an additional terminal (T0) is present at one solenoid end. Various 1-CLIQ configurations are presented, each denominated following the terminals to which the CLIQ unit is connected. For instance, configuration T0-T5 is obtained by connecting the positive and negative terminals to terminals T0 and T5, respectively. As explained in section 3.3.5, in the case of a solenoid the discharge circuit of a 1-CLIQ system is composed of two coil sections  $L_A$  and  $L_B$ , effectively in parallel and strongly mutually coupled. The introduced variations of their currents  $I_A$  and  $I_B$  [A] are asymmetric, since the inductance of the outer layers of the solenoid is larger than the inner, and the impedances of the two coil sections are not equal even if CLIQ is connected to the central terminal T5.

A copper bandage is wrapped around the solenoid forming a secondary coil. This resistive coil used as mechanical reinforcement of the superconducting coil is also used to measure the inductive component of the voltage across the solenoid  $U_{\text{ind}}$  [V], which is proportional to the voltage over the bandage coil  $U_{\text{band}}$  [V], if  $I_A = I_B$ . Subtracting the inductive component from the total voltage across the solenoid provides a simple method for calculating the effective electrical resistance developed in the coil,

$$R_C = \frac{U_{\text{tot}} - U_{\text{ind}}}{I_A} = \frac{U_{\text{tot}} - f_{\text{band}} U_{\text{band}}}{I_A}. \quad [\Omega] \quad (5.1)$$

The value of  $f_{\text{band}} \approx 5$  can be calculated with dedicated software [99] or simply deduced as the ratio  $U_{\text{ind}}/U_{\text{band}}$  measured during a transient with constant ramp rate. Note that this equation is not valid during the first tens of milliseconds after a CLIQ discharge because  $I_A \neq I_B$ . Observing the behaviour of  $R_C$  during magnet discharges lasting 1 to 2 second provides useful information about the thermal dynamics of the system and the time required to transfer the coil to the normal state.

The effective electrical resistance developed in each layer  $l$  is similarly calculated by subtracting from the measured voltage across the layer its inductive component, proportional to the voltage over the bandage coil,

$$R_l = \frac{U_l - U_{\text{ind},l}}{I_l} = \frac{U_l - f_{\text{band},l} U_{\text{band}}}{I_l}. \quad [\Omega] \quad (5.2)$$

Again, the linear factors of proportionality  $f_{\text{band},l}$  can be calculated [99] or defined as the ratio  $U_l/U_{\text{band}}$  measured during a transient with steady ramp rate. During the first tens of milliseconds following the CLIQ triggering the dynamic effects are relatively strong and the use of these constant parameters may lead to significant errors in the calculation of  $R_l$ . However, calculating the layer resistance is an effective means to assess which layers are the first to switch to the normal state and how fast the normal zone propagation between layers is.

The evolution with time of the currents in the two coil sections after triggering a CLIQ unit connected between terminals T0 and T5 is shown in figure 5.12. The fast current change introduces enough coupling loss to initiate a transition to the normal state in the solenoid, and the developed coil resistance forces the discharge of the transport current. Three distinct phases are visible in the evolution of the effective coil resistance. Immediately after triggering CLIQ, a sharp increase is observed while the coil transfers from the superconducting to the resistive state. After about 75 ms the entire coil is in the normal state, and its electrical resistance roughly corresponds to the resistance of the coil just above the critical temperature,  $R_C \approx R_{C,10K} \approx 350 \text{ m}\Omega$ . The subsequent rise of the coil resistance is due to the increase in coil temperature through ohmic loss. Finally, the coil resistance decreases because the temperature in the coil reduces due to the helium cooling.

The layer-by-layer coil resistances developed during a discharge are shown in figure 5.13. The first layers that transfer to the normal state are the layers L5 and L6. This result is consistent with the theory presented in section 3.3.5. In fact, the two layers are at the edge between the two coil sections, where the magnetic-field changes generated by the introduced current-changes superpose, and hence the highest coupling loss is developed. Note that the margin to normal state and the coupling-loss generation within each layer are very uniform both in the longitudinal direction and in the direction of the transport current. As a consequence, most of the turns of each layer are transferred to the normal state simultaneously, resulting in a highly homogeneous energy distribution during the magnet discharge.

The normal zone then propagates in radial direction to neighbouring layers. Layers L8, L9, and L10 are more difficult to transfer to the normal state because the local magnetic field is lower and hence the current sharing temperature is higher. Furthermore, the resistances of layers L1 and L10 start decreasing sooner than the other layers as they are nearest to the helium bath. The middle layers take longer to recover as less heat is extracted by the helium cooling.

In first approximation, the current  $I_C$  discharged by CLIQ and the impedance of the two sections  $L_A$  and  $L_B$  do not depend on the initial current flowing in the solenoid. However, being proportional to the initial magnetic field, the initial current has a twofold impact on the system dynamics. Firstly, it determines the energy required to initiate a transition to the normal state. Secondly, it influences the resistivity of the copper matrix of the strands, as shown in equation 2.19. In turn, both the inter-filament coupling loss and its time-constant are inversely proportional to the strand resistivity, see equations 2.18 and 2.25. Thus, at higher magnetic field less coupling loss is generated, but in a shorter time.

The measured currents  $I_A$  after triggering a 4.7 mF, 150 V, CLIQ unit at various current levels are shown in figure 5.14. As expected, the oscillating component of the current is almost independent of  $I_0$ , but at higher current the solenoid is discharged more quickly because the coil resistance increases faster. This is clearly observed in figure 5.15 where the coil resistances for the same set of tests are shown. For higher initial current the fraction of coil transferred by CLIQ increases, and the ohmic loss developed in the coil, proportional to the fraction of the coil in the normal state and to the square of the transport current, causes a faster rise of the coil resistance. Below a certain current, the ohmic loss in the coil becomes smaller than the heat

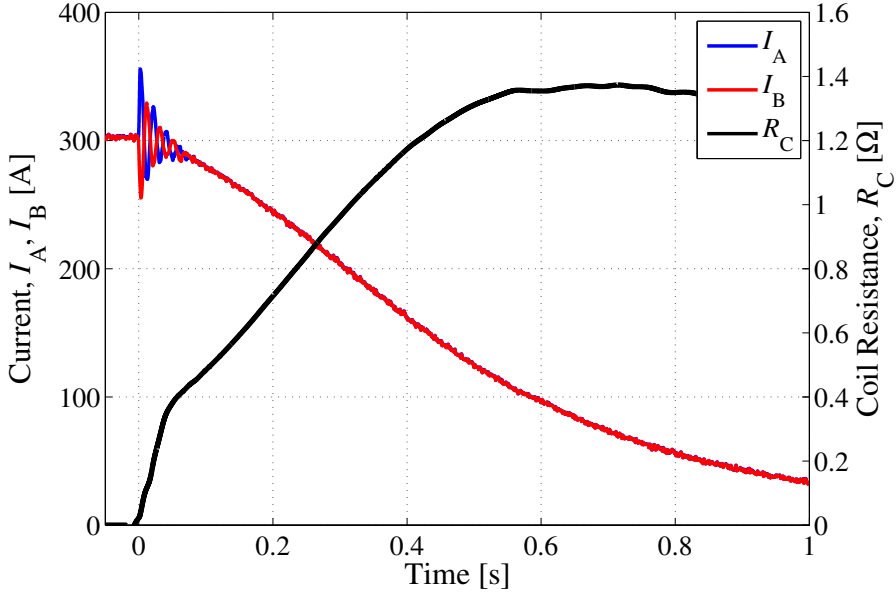


Figure 5.12. CLIQ discharge event on the ten-layer solenoid. Measured currents  $I_A$  and  $I_B$  versus time and calculated effective coil resistance  $R_C$  versus time after triggering CLIQ at  $I_0=300$  A (Configuration T0-T5,  $U_0=75$  V,  $C=4.4$  mF).

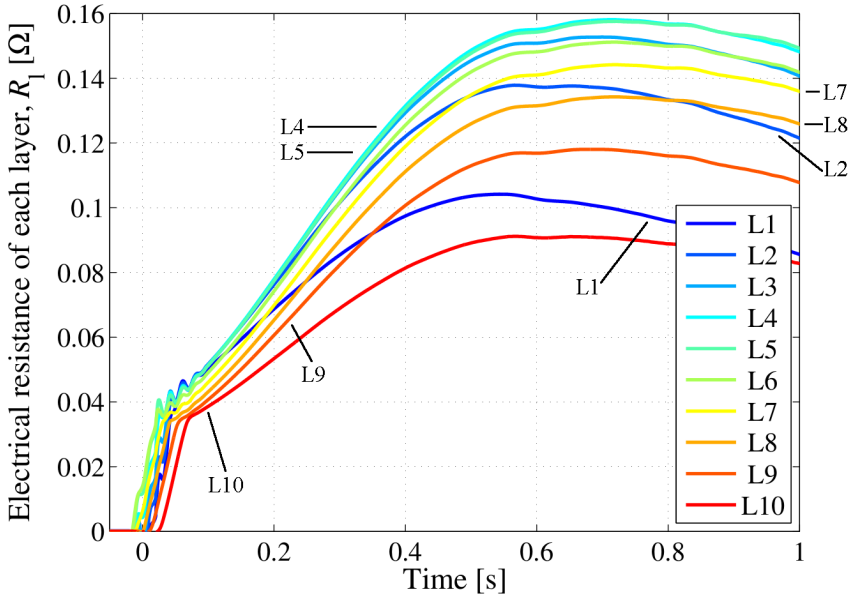


Figure 5.13. CLIQ discharge event on the ten-layer solenoid. Calculated effective coil resistance in each layer  $R_i$  versus time after triggering CLIQ at  $I_0=300$  A (Configuration T0-T5,  $U_0=75$  V,  $C=4.4$  mF).



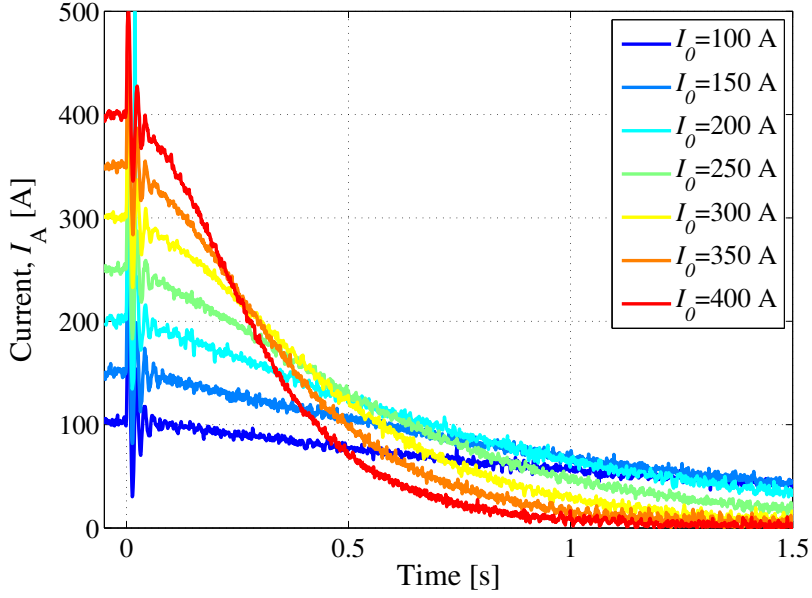


Figure 5.14. CLIQ discharge events on the ten-layer solenoid. Measured current  $I_A$  versus time after triggering CLIQ at various initial currents  $I_0$  (Configuration T6-T0,  $C=4.7$  mF,  $U_0=150$  V).

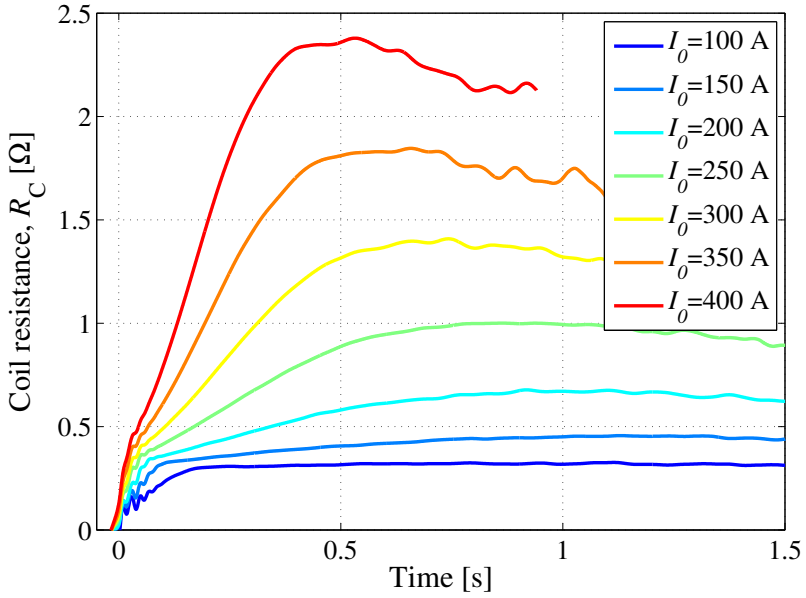


Figure 5.15. CLIQ discharge events on the ten-layer solenoid. Calculated effective coil resistance  $R_C$  versus time after triggering CLIQ at various initial currents  $I_0$  (Configuration T6-T0,  $C=4.7$  mF,  $U_0=150$  V).

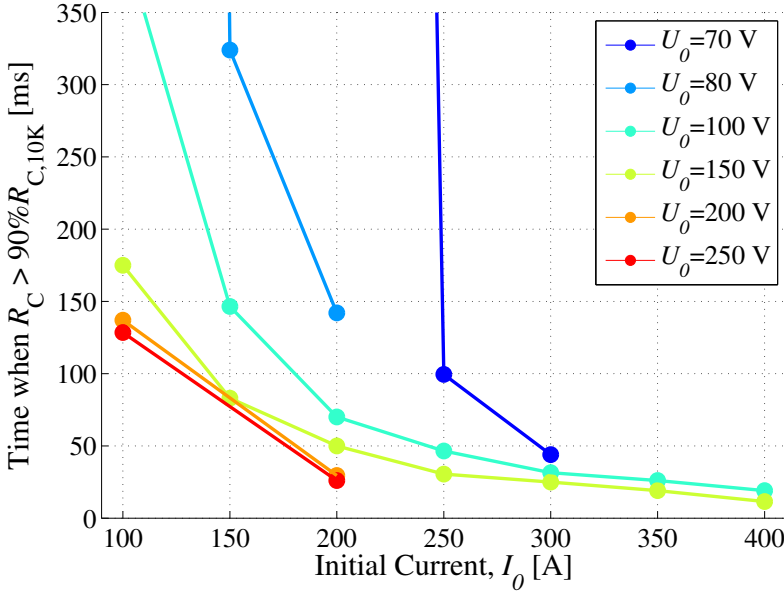


Figure 5.16. CLIQ discharge events on the ten-layer solenoid. Calculated time required to develop a coil resistance higher than  $90\%R_{C,10K}$ , versus initial current, for various charging voltages  $U_0$  (Configuration T6-T0,  $C=4.7$  mF).

removed by the helium surrounding the solenoid, and thus the coil temperature and the coil resistance decrease. In the case of  $I_0=100$  A, the coil reaches an equilibrium state between ohmic loss and helium cooling, and the coil resistance remains almost constant throughout the current discharge.

As observed in the previous chapters, the coupling loss generated in the strands after triggering a CLIQ unit is mainly proportional to the square of its charging voltage. Experimental results clearly confirm this. Let us define  $t_{Q90\%}$  [s] as the time required to develop a normal-zone resistance higher than 90% of the coil resistance just above the critical temperature, i.e. the time when  $R_C > 90\%R_{C,10K}$ . Since the temperature in most of the coil does not raise much during the short transients,  $t_{Q90\%}$  is a good approximation of the time required to turn to the normal state 90% of the entire winding pack. In figure 5.16, the calculated  $t_{Q90\%}$  is plotted for various currents and CLIQ charging voltages. At each current level a certain minimum charging voltage is needed to initiate a transition to the normal state in the magnet.

The positioning of the CLIQ terminals strongly affects the system behaviour and performance. By connecting CLIQ to different terminals the impedance of the coil sections and the overall equivalent inductance of the discharge circuit  $L_{eq}$  significantly change. The peak current introduced and the oscillation frequency of the system, both proportional to  $\sqrt{1/L_{eq}}$ , can be increased by connecting a terminal closer to one side of the coil, thus reducing the impedance of one coil section, and hence  $L_{eq}$ . Enhancing the frequency increases the current change, and thus the coupling loss in the coil section with smaller impedance. However, less symmetric configurations also

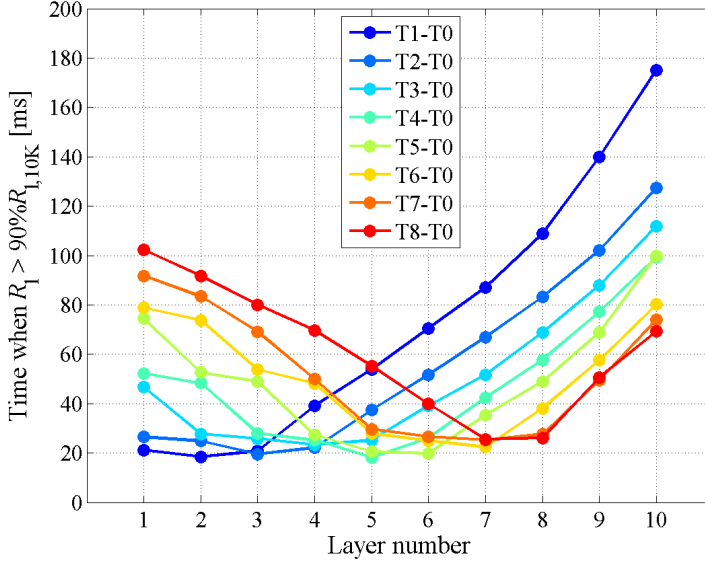


Figure 5.17. CLIQ discharge events on the ten-layer solenoid. Calculated time required to develop a layer resistance higher than  $90\%R_{l,10K}$  after triggering CLIQ for various configurations (T1-T0,...T8-T0,  $I_0=200$  A,  $U_0=75$  V, and  $C=8.8$  mF).

produce inhomogeneous heat deposition in the coil due to the different current changes in the coil sections, which is hardly an optimum result. The regions where most of the energy is deposited can be selected with a correct positioning of the terminals. In fact, even if the same current change is introduced in an entire coil section, the introduced magnetic-field change is concentrated at the edge between the two coil sections where their border effects superpose.

This result, already discussed in section 3.3.5, is evident when observing the time required to turn to the normal state each of the ten layers of the solenoid. The time  $t_{l90\%}$  [s] when the resistance of layer  $l$  is higher than 90% of its resistance just above the critical temperature, i.e. when  $R_l > 90\%R_{l,10K}$ , is shown in figure 5.17, for a range of CLIQ configurations based on a 75 V, 8.8 mF unit. As expected, a transition to the normal state is initiated first in those layers which are adjacent to the CLIQ terminals. Furthermore, the layers located in the inner region of the solenoid are easier to transfer due to the higher magnetic field and hence smaller temperature margin. Configuration T9-T0, not shown in the plot, deposits most of the heat in the two outermost layers (L9 and L10) which are the hardest to quench. As a result, no normal zone is initiated in the coil before several hundred millisecond.

In all configurations shown, once a transition to the normal state is initiated the ohmic heat generated in the portion of coil already in the normal state diffuses to adjacent layers and the normal zone propagates radially. At a current of  $I_0=200$  A, a normal zone fully propagates to a neighbouring layer in 10 to 20 ms. However, the heat propagation is slower in the outer, low magnetic-field region of the solenoid. For this

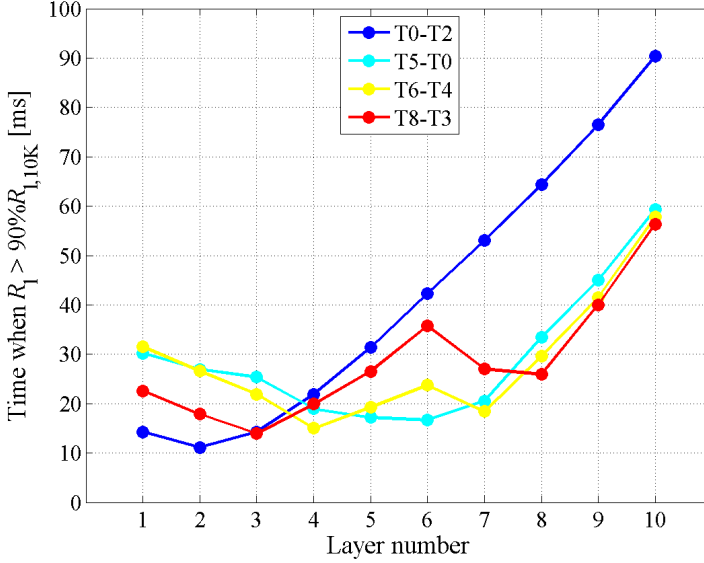


Figure 5.18. CLIQ discharge events on the ten-layer solenoid. Calculated time required to develop a layer resistance higher than  $90\%R_{l,10K}$  after triggering CLIQ for various configurations ( $I_0=300$  A,  $U_0=75$  V, and  $C=8.8$  mF).

reason Configuration T1-T0, which initiates a normal zone in L1 and L2, requires the longest time to transfer the entire coil because the heat needs to propagate through the layers with the highest margin. On the contrary, Configurations T5-T0 and T6-T0 are particularly effective in transferring the entire coil, because a normal zone is initiated right at the centre of the solenoid and the ohmic heat can therefore radially propagate in both directions toward inner and outer layers. These more symmetric configurations reduce the mechanical stress on the peripheral layers.

A further improvement can be achieved by initiating two normal zones due to high coupling loss in two separate regions of the coil. This is obtained by connecting both CLIQ leads to terminals internal to the magnet coil (from T1 to T9). The performance of two configurations, designed following this principle, T8-T3 and T6-T4, as compared to two configurations presented before, T0-T2 and T5-T0, is shown in figure 5.18. The CLIQ configurations discharging through two internal terminals effectively develop two distinct normal zones and are faster to turn to the normal state the entire winding pack. Configuration T8-T3 starts the quench in layers L3 and L8, whereas Configuration T6-T4 in L4 and L7.

Note that relying on the radial normal zone propagation starting only in a few layers may not be acceptable for the protection of solenoids composed of a larger number of layers, or including thicker insulation layers. In such cases, systems can be designed that initiate normal zones more quickly and in more locations. Multi-CLIQ systems composed of  $N_C$  units whose terminals are both connected to points internal to the magnet effectively generate  $2N_C$  separate normal regions, each propagating

radially in the inward and outward directions. This solution seems the most effective for the protection of medium to large scale solenoids.

## 5.4 Conclusion

A general procedure for the design of a CLIQ system for protecting existing magnets is outlined. A successful strategy starts with selecting the optimum configuration of the discharge circuit. The CLIQ performance strongly depends on the charging voltage of the capacitor bank, which is limited by the maximum voltage to ground allowed in the system. If the performance in terms of peak power generation or total energy deposition is unsatisfactory, multiple units can be installed across distinct coil sections, or the capacitance of the units can be increased.

The key issues while implementing a CLIQ system are addressed:

- choice of the capacitor type;
- options for the trigger units used for discharging the capacitor bank;
- attachment of the CLIQ leads to the coil terminals, secure clamping, and mechanical support.

Also, the design of a fully redundant CLIQ system is discussed. The proposed solution is based on parallel units, each comprising two parallel trigger branches capable to discharge the capacitor bank.

Various examples of CLIQ systems for protecting existing magnets have been presented. The first experimental CLIQ campaign, performed on a small solenoid and including about a thousand CLIQ discharges, allowed an extensive study of the CLIQ method and provided a wealth of data to validate the theoretical background and simulation model.

The CLIQ system was further characterized during the test campaigns on Nb-Ti and Nb<sub>3</sub>Sn quadrupole model magnets for the High Luminosity LHC. This experience decisively showed the maturity of CLIQ technology and its applicability to large-scale coils. Full-scale LHC dipole and quadrupole magnets are presently equipped with CLIQ terminals, to be tested in the immediate future.

The performance proved to be very good for a variety of coils of different geometry, size, type of superconductor, cable, and strand parameters. CLIQ technology is mature and ready to be applied to existing superconducting magnets requiring limited mechanical work.



## Chapter 6

# CLIQ using an external excitation coil

*An alternative CLIQ-based quench protection system can be realized by connecting a CLIQ unit to an external excitation coil. This additional coil is magnetically coupled to the main coil to protect, but galvanically separated. The oscillation of the current in the excitation coil generates an oscillating magnetic-field change in the coil windings and thus introduces coupling loss in the superconductor.*

*In particular cases, resistive coils are already present around existing magnets, for instance for providing mechanical reinforcement. If coil terminals are available, this variant of the CLIQ method can be implemented with limited effort and cost. However, when included in the magnet design from the start, the excitation coil can be designed for optimum performance and integration in the magnet system. The advantages and disadvantages of various designs of the excitation coil are discussed. Results of the first experience are presented and compared to similar discharges obtained with a standard CLIQ system. Whilst the excitation coil used in the tests is not optimized for CLIQ technology, the applicability of the method is successfully demonstrated.*

*Finally, the conceptual design of a CLIQ excitation coil capable to protect a full-scale 11 T dipole magnet is presented. The design could be extended to other multipole or solenoid magnets, even when made of high-temperature superconductor.*

### 6.1 Design of the excitation coil

The utilisation of transitory loss to initiate a transition to the normal state in the superconductor and hence protecting the coil against overheating after a quench was studied in the past [48, 158–160]. The proposed methods featured coils with close to zero mutual inductance with the main coil, and mainly relied on introducing hysteresis

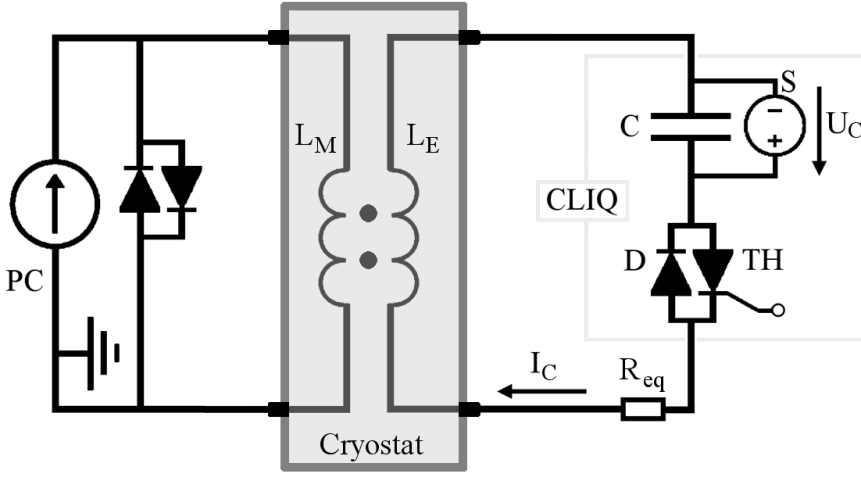


Figure 6.1. Electrical scheme of a CLIQ system based on an external excitation coil  $L_E$  magnetically coupled to the main coil  $L_M$  to be protected.

and eddy-current loss in the stabilizer of the conductor by introducing magnetic-field changes with relatively high oscillation frequency.

Here, a new method is proposed, mostly relying on the development of inter-filament coupling loss and requiring strong magnetic coupling between the external excitation and the main coils [84, 86]. This is achieved with an excitation coil coaxial to the main coil. The electrical scheme of a system using an external excitation coil is shown in figure 6.1. The unit presented in section 2.1 is connected to the terminals of a coil  $L_E$  electrically separated from the main coil  $L_M$  but strongly magnetically coupled. During normal operation, the electrical circuit of the excitation coil is open and no current flows ( $I_C=0$ ). Thus, the magnet performance during normal operation is unchanged. The excitation coil can be either resistive or superconducting. The first version is less expensive and easier to manufacture, whereas the second one yields higher performance due to the smaller electrical resistance of the discharge circuit  $R_{eq}$  [ $\Omega$ ].

The main design features of a CLIQ excitation coil, discussed in the rest of the chapter, are:

- position of the excitation coil with respect to the coil to protect;
- geometry of the excitation coil;
- length and number of separate sections of the excitation coil.

### 6.1.1 Position

The excitation coil can be located at the exterior of the coil to protect, at its interior, or in between certain layers. Figures 6.2a and 6.2b show the implementation of two different designs on a solenoid. In the first solution, the coil has to be reinforced



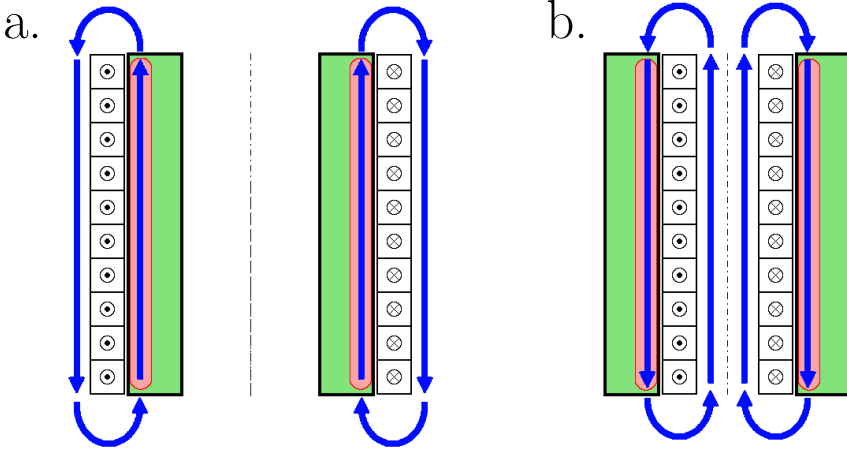


Figure 6.2. The positions of the CLIQ excitation coil with respect to the main coil to protect. a. At the exterior of the coil. b. At the interior of the coil. Magnetic-field lines generated by the excitation coils are in blue, regions where high coupling loss is deposited in pink. Note that the radial dimensions and the size of the excitation coils are intentionally inflated.

to sustain the mechanical stress during magnet operations. If the coil is collared, the excitation coil is placed between the main coil and the collar. In the latter solution, the region around the magnet axis is partly reduced due to the presence of the excitation coil and the magnetic design is affected. Also, when placed inside the magnet, the excitation coil is subject to significantly higher magnetic field, resulting in considerable Lorentz force.

Naturally, higher coupling loss is generated in the regions physically closer to the excitation coil, which are subject to higher magnetic-field change. Since the effectiveness of the helium cooling may be reduced by the presence of the excitation coil in close contact with the main coil, the excitation coil can even be mechanically separated from the main coil. However, higher performance is achieved by reducing as much as possible the distance between the excitation and the main coil in order to maximize magnetic coupling. If placed between layers, the excitation coil simultaneously introduces high coupling loss in larger areas of the coil. This coil needs to be integrated in the magnet design from the start.

### 6.1.2 Geometry

The choice of the excitation-coil geometry is critical for an effective CLIQ system. In fact, as explained in section 2.2, CLIQ's main energy-deposition mechanism is the generation of inter-filament coupling loss, which is proportional to the square of the local magnetic-field changes in the two directions perpendicular to the orientation of the superconducting filaments. As a result, coil configurations prevalently introducing magnetic-field change in the same direction as the main coil conductor are ineffective since they do not generate significant inter-filament coupling loss in the conductor.

Two alternative designs of a CLIQ excitation coil are considered here, based on a solenoid or a multipole coil coaxial to the main coil to protect. A solenoid is easier to manufacture and more robust. As shown in figures 6.2a and 6.2b, the magnetic-field change introduced with such a coil has a dominant longitudinal component. Thus, a CLIQ solenoidal excitation coil is effective in introducing inter-filament coupling loss in the superconductor of another solenoid, but not of a multipole magnet. As an example, consider the solenoidal excitation coil shown in figure 6.3a. The direction of the introduced magnetic-field change is parallel to the multipole-magnet conductor and ineffective in developing coupling loss.

On the contrary, a multipole coil can be effectively used to generate inter-filament coupling loss in the conductor of another multipole coil, as shown in figure 6.3b. In fact, not only is the direction of the introduced magnetic-field change perpendicular to the main coil conductor, but this coil type can be designed such that its turns are placed only in correspondence with the coil turns. As a result, a high magnetic-field change is generated only where it is desired, in the region occupied by the coil turns. Also, given the direction of the introduced magnetic-field change, this type of CLIQ excitation coil allows developing high local coupling loss in the superconductor of a solenoid as well.

### 6.1.3 Subdivision

The CLIQ excitation coil can be designed as a single coil covering the entire coil length, as in the examples shown in figures 6.2a and 6.2b. Such a coil deposits roughly the same energy along the longitudinal direction.

Alternatively, the excitation coil can be composed of a series of identical sections covering only certain parts of the coil length. The reduction of the length of the coil decreases the self-inductance of the excitation coil with a beneficial effect on the overall CLIQ performance. Furthermore, the energy delivered to the superconductor is concentrated at multiple inductive heating stations corresponding to the two ends of each section of the excitation coil. Once the high-loss regions of the winding pack are transferred to the normal state, the resulting ohmic loss causes propagation of the normal zone in the longitudinal direction. In the case of a series of solenoid sections, the magnetic-field change introduced by the CLIQ current has a high radial component at the edges of each section. This magnetic-field change perpendicular to the direction of the coil's superconductor is well-suited for developing high coupling loss in the main coil superconductor.

A further improvement can be achieved with minor manufacture complications by winding the turns of consecutive coil sections with opposite directions. The advantage of this solution is twofold. Firstly, the total self-inductance of the series of excitation-coil sections is reduced since a significant part of the magnetic flux generated by consecutive sections compensates. For instance, consider two sections of a solenoidal excitation coil with self-inductance  $L_{E,s}$  [H] and mutual inductance  $M_{E,m}$  [H], wound with the same current direction or with opposite current direction, as shown in figures 6.4a and 6.4b, respectively. The self-inductances in these two cases are

$$L_E = 2L_{E,s} + 2M_{E,m}, \quad [H] \quad (6.1)$$

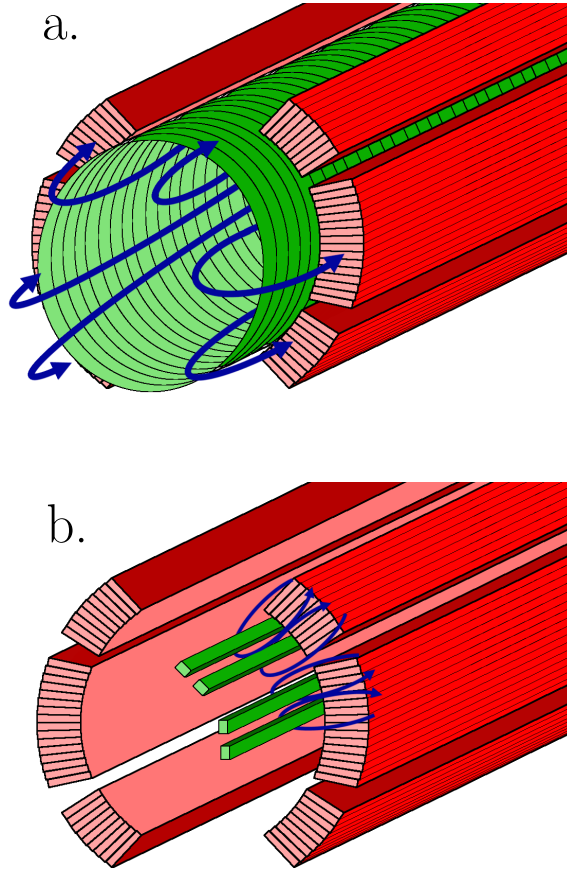


Figure 6.3. Geometry of a CLIQ excitation coil protecting a dipole magnet. a. Solenoidal excitation coil positioned in the bore of the dipole magnet. b. Multipole excitation coil (only two sections out of eight, protecting half a pole, are represented).

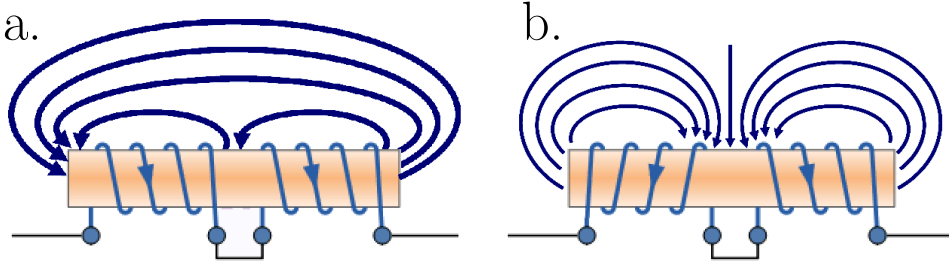


Figure 6.4. Two consecutive sections of a CLIQ solenoidal excitation coil. a. Turns of different sections wound with the same current direction. b. Turns of different sections wound with opposite current direction.

and

$$L_E = 2L_{E,s} - 2M_{E,m}, \quad [H] \quad (6.2)$$

respectively. Secondly, when introducing opposite current changes in adjacent coaxial solenoids, the radial component of the magnetic-field changes generated by the two coil sections effectively superposes in the gap between them (figure 6.4b). The radial component is perpendicular to the direction of the main coil superconductor, both in the case of a solenoid or multipole magnet. Thus, this type of CLIQ excitation coil allows developing high local coupling loss on either magnet geometry.

In conclusion, this last configuration is easy to manufacture, robust, flexible, and effective on both solenoid and multipole magnets. An example of the design of such a coil is presented in section 6.4.

## 6.2 Advantages and disadvantages

With respect to a standard CLIQ, a system based on driving an external excitation coil has a twofold advantage. Firstly, the excitation coil through which the oscillating current is introduced is galvanically separated from the main coil. Hence, since the method does not rely on thermal diffusion for the normal zone propagation process, the thickness of the insulation between the main conductor and the excitation coil can be increased without significant reduction of the propagation performance. Secondly, the introduced oscillating current is not injected directly in the main coil, and thus the variation of the coil transport current is limited. Hence, the current introduced by CLIQ does not interfere with the main electrical circuit to which the coil is connected. Also, local changes in the mechanical stress due to unbalance in the currents of different coil sections are reduced. As a result of this dual advantage, the maximum operating voltage and current of a CLIQ system using an excitation coil can be increased with less impact on the safety and operation of the system.

Nevertheless, one key advantage of the conventional CLIQ technology, namely being a system in physical contact with the coil to protect only in a few restricted spots, is lost. In order to introduce a significant change in the magnetic field of the main coil conductor using an external excitation coil, either a coil composed of a number of turns comparable to the main coil turns is required, or a large oscillating

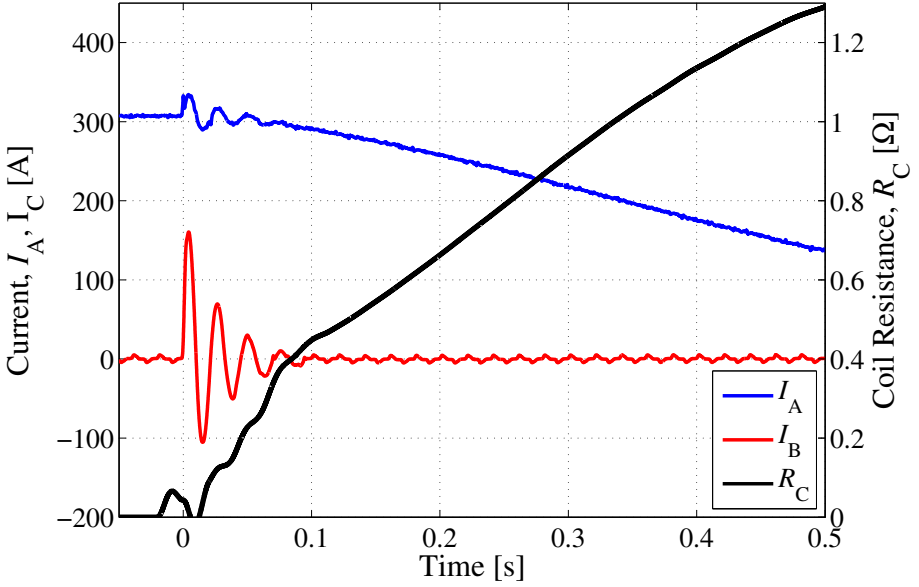


Figure 6.5. Measured currents  $I_A$  and  $I_C$  versus time and calculated effective coil resistance  $R_C$  versus time after triggering a CLIQ system using an excitation coil surrounding the main coil ( $I_0=300$  A,  $U_0=75$  V,  $C=8.8$  mF).

current has to be injected. This short-come can be partially solved by designing an excitation coil composed of multiple separated sections.

### 6.3 First experience using an external excitation coil

A series of tests were performed to assess the performance of this method [84]. One CLIQ unit was connected to an excitation coil surrounding the 462 mH, 10-layer solenoid presented in section 5.3.3. The excitation coil is composed of two layers of copper wire with the same number of turns and cross-section as of the superconducting single wire composing the solenoid.

Figure 6.5 shows the measured current  $I_C$  introduced in the excitation coil after triggering an 8.8 mF, 75 V CLIQ unit connected to its terminals, at an initial transport current  $I_0$  of 300 A. As a result of the strong coupling between the solenoid and the excitation coil, the solenoid transport current  $I_A$  [A] oscillates with the same frequency as the current introduced by CLIQ. The amplitude of the oscillations introduced in the solenoid transport current is about 15% of the amplitude of the oscillating current introduced by CLIQ. This is the result of the smaller self-inductance of the excitation coil with respect to the solenoid, which is composed of about five times more turns.

The coupling loss generated in the wires by effect of the introduced magnetic-field change is sufficient to initiate a transition to the normal state of large areas of the

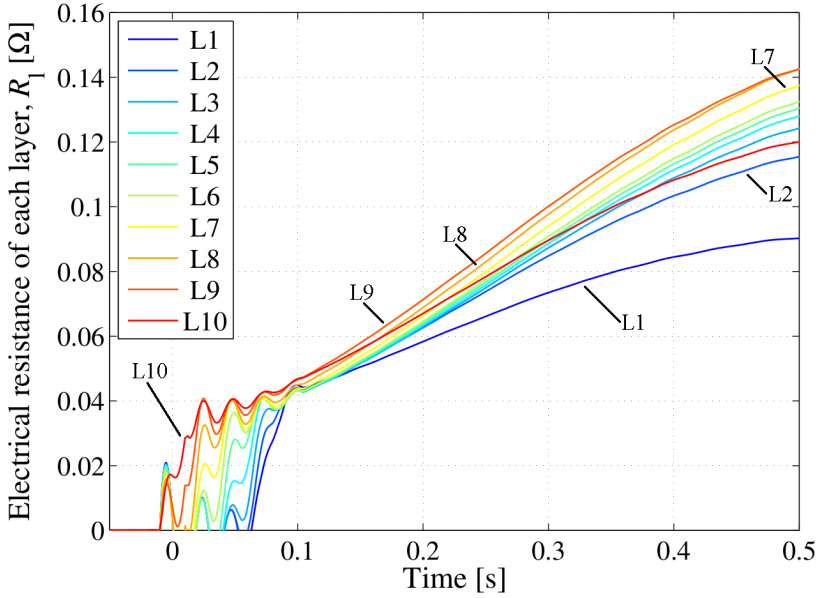


Figure 6.6. Calculated effective coil resistance in each layer  $R_l$  versus time after triggering a CLIQ system using an excitation coil surrounding the main coil ( $I_0=300$  A,  $U_0=75$  V,  $C=8.8$  mF).

winding pack, as observed in figure 6.5 where the coil resistance  $R_C$  [ $\Omega$ ], calculated, as explained in section 5.3.3, is shown.

Used in this configuration, CLIQ generates higher coupling loss in the outer layers of the solenoid, which are closer and more strongly coupled to the surrounding excitation coil, and thus are exposed to a higher change of the magnetic field. This result can be observed in figure 6.6, where the calculated electrical resistances of all layers of the solenoid (L1-L10) are shown. The outermost layer (L10) is the first to be transferred to the normal state, and the heat then orderly propagates to the inner layers. After a few hundred millisecond the rate of increase of the resistance of the outermost and innermost (L1) layers reduces due to the cooling of the helium bath surrounding the coil.

For given charging voltage and capacitance of the capacitor bank of the unit, this alternative method introduces less coupling loss in the main coil than a standard CLIQ system, if the excitation coil is composed of a single solenoid with less turns than the main coil itself. As an example, figure 6.7 shows the comparison between the quench performance at 200 A of a standard CLIQ (Configuration T6-T0, see section 5.3.3) and a CLIQ using an excitation coil. One can observe that an 8.8 mF CLIQ using the excitation coil requires 20 to 30 ms more to transfer to the normal state the solenoid coil than a 4.7 mF standard CLIQ. This performance is achieved using a resistive excitation coil present for providing mechanical reinforcement, hence not optimized for a CLIQ discharge.

A first obvious improvement is the increase of the insulation layer between the

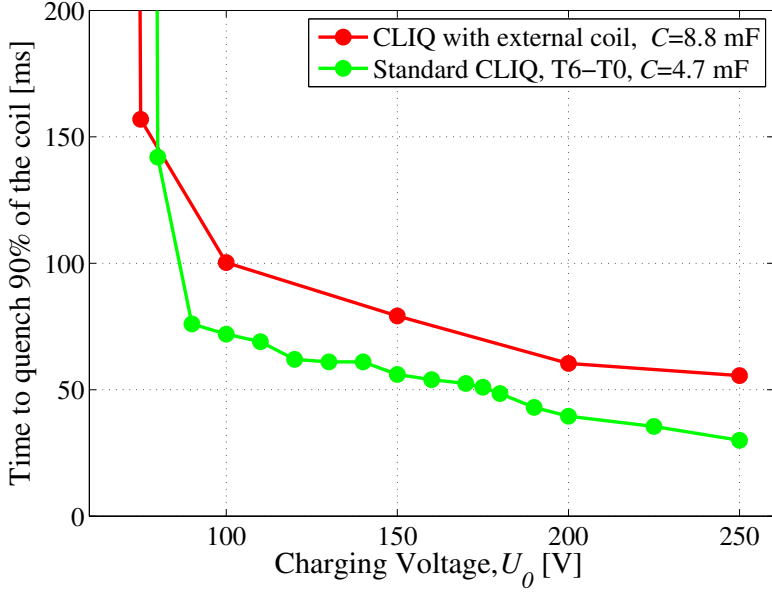


Figure 6.7. Comparison between standard CLIQ (Configuration T6-T0,  $C=4.7$  mF) and CLIQ using an excitation coil surrounding the main coil ( $C=8.8$  mF). Calculated time required to transfer to the normal state 90% of the main coil after triggering CLIQ at  $I_0=200$  A, versus charging voltage.

excitation coil and the main coil, thus allowing a larger charging voltage. In fact, as explained in chapter 2, the coupling loss per unit volume introduced by CLIQ is proportional to the square of the CLIQ charging voltage. Thus, a simultaneous tenfold increase of the CLIQ charging voltage and of the excitation-coil insulation layer results in a 100 times higher energy deposition without changing the voltage per unit of insulation thickness. This is a definite advantage of the method as compared to alternative protection systems based on standard CLIQ or on quench heaters.

Although in the case of using an excitation coil the voltages across the main-coil sections are only a fraction of the charging voltage, they are still linearly proportional to the CLIQ voltage. Hence, the maximum allowed voltage between the main coil and ground ultimately sets a limit to the maximum charging voltage.

## 6.4 Excitation coil for a full-scale 11 T dipole magnet

The conceptual design of a CLIQ excitation coil to protect the 11 T, 6 m long,  $\text{Nb}_3\text{Sn}$  dipole magnet introduced in section 3.3.2 [80, 81, 127–130] is presented. Its inner and outer layers are located at a radius of  $30 \leq r \leq 45$  mm and  $45 \leq r \leq 60$  mm, respectively. The results can be easily applied to other multipole or solenoid magnets, and to excitation coils located around the coil to protect, or between coil layers.

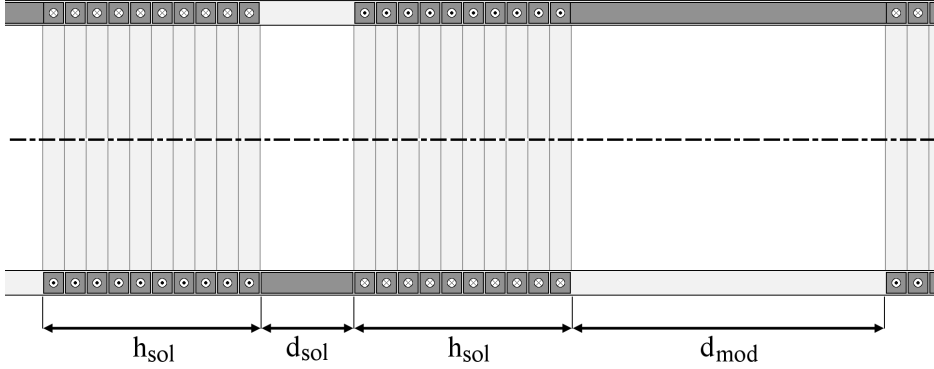


Figure 6.8. Cross-section of one module of the CLIQ excitation coil to protect the 11 T, 6 m long, Nb<sub>3</sub>Sn dipole magnet.

Table 6.1. Main parameters of the CLIQ excitation coil to protect the 11 T, 6 m long, Nb<sub>3</sub>Sn dipole magnet. Values for the baseline design and range of variation considered in the analysis.

Parameter	Unit	Baseline	Range
Outer radius, $R_{\text{out}}$	mm	25	-
Turns per solenoid, $N_{\text{T,sol}}$	-	10	1-200
Layers, $N_{\text{L,sol}}$	-	1	1-2
Distance between solenoids, $d_{\text{sol}}$	mm	5	5-50
Distance between modules, $d_{\text{mod}}$	mm	100	5-300
Wire width, $w_{\text{w}}$	mm	1.0	-
Wire height, $h_{\text{w}}$	mm	1.0	-
Insulation layer, $s_{\text{ins}}$	mm	0.1	-

A schematic representation of the excitation coil is shown in figure 6.8. It has an outer radius  $R_{\text{out}}$  of 25 mm and is small enough to be inserted in the bore of one magnet aperture. The coil comprises  $N_{\text{mod}}$  modules, distributed along the magnet length at a distance  $d_{\text{mod}}$  [m], each composed of two solenoids whose turns are wound in opposite directions. The two solenoids in each module are separated by a distance  $d_{\text{sol}}$  [m], and are composed of  $N_{\text{T,sol}}$  turns and  $N_{\text{L,sol}}$  layers. The coil is made of a square copper wire with a cross-section of  $w_{\text{w}}h_{\text{w}}=1 \text{ mm}^2$ , surrounded by an insulation layer with thickness  $s_{\text{ins}}=0.1 \text{ mm}$ . The length of each module is

$$l_{\text{mod}} = 2N_{\text{T,sol}}(h_{\text{w}} + 2s_{\text{ins}}) + d_{\text{sol}} + d_{\text{mod}} = 2h_{\text{sol}} + d_{\text{sol}} + d_{\text{mod}}. \text{ [m]} \quad (6.3)$$

The main parameters are summarized in table 6.1. For each design, the number of modules composing the excitation coil is chosen so as to cover the entire magnet length  $l_{\text{m}}=6 \text{ m}$ , i.e.  $N_{\text{mod}} \approx l_{\text{m}}/l_{\text{mod}}$ . For example, the baseline design includes 46 modules, each 129 mm long. An optimization is carried out in order to maximize



the inter-filament coupling loss generated in the superconductor of the main coil. This is achieved with a compromise between reducing the self-inductance of the excitation coil, calling for a smaller number of turns largely spaced, and increasing the magnetic field generated by the CLIQ-introduced current, expressed by the parameter  $f_{\text{CLIQ}}$  [ $\text{TA}^{-1}$ ] defined in equation 2.14, calling for many tightly-wound turns.

The equivalent inductance of the CLIQ discharge circuit  $L_{\text{eq}}$  [H] is the total self-inductance of the excitation coil. As expressed by equation 6.2, this is reduced by a high mutual coupling between the two solenoids of each module. The mutual inductance between the excitation and the main coil is neglected in the present analysis. However, it will need to be included in the final coil design. The equivalent inductance per unit length, calculated as a function of the number of turns per solenoid and of the distance between modules, is shown in figure 6.9a. As expected, the coil self-inductance increases for higher number of turns and for shorter distance between modules, as in both cases the total number of turns needed to cover the magnet length is higher. As a reference, the experimental results presented in section 6.3 correspond to a zero distance between coil sections and turns covering the entire magnet length, hence featuring a very high self-inductance.

For the same parameters, the generated magnetic field at a distance  $r=30$  mm from the solenoid axis, per ampere of current introduced by CLIQ, is calculated, averaged over the length of a module, and plotted in figure 6.9b. Its value is maximum for a range of turns per solenoid between 20 and 60, and for shortest distances between modules.

As explained in sections 2.2 and 2.5, the power per unit volume generated due to inter-filament coupling loss is proportional to the square of the total magnetic-field change, see equation 2.24, which in first approximation is proportional to the CLIQ effectiveness,  $\Psi=f_{\text{CLIQ}}/L'_{\text{eq}}$  [ $\text{m}^{-1}$ ], defined in section 3.1. However, the coupling currents need a certain time to fully develop, characterized by the time constant defined in equation 2.18. Thus, coil configurations resulting in too high oscillation frequencies are relatively ineffective, since the introduced current-change inverts its polarity too quickly to generate a significant magnetic-field change.

Given the numerous interdependent effects, the energy per unit volume developed due to inter-filament coupling loss,  $W'''_{\text{IFCL}}$  [ $\text{Jm}^{-3}$ ], is to be calculated on a case-by-case basis. As an example, the deposited energy density is here computed for a 500 V, 60 mF CLIQ unit, using the method described in section 2.2. For the cases analyzed, the peak and average energy densities within a module, deposited during the first 50 ms after triggering CLIQ, are shown in figures 6.10a and 6.10b, respectively. Selecting larger distances between modules increases the achieved peak energy deposition due to the reduced coil self-inductance, but also augments the region where very little loss is generated. Vice versa, decreasing the distance between modules results in a more homogeneous energy generation along the magnet length, but reduces the peak deposition. It can be observed that the highest average and peak energy densities can be achieved with configurations featuring 10 to 20 turns per solenoid and largest distance between modules. These configurations feature a good combination of low coil self-inductance and high  $f_{\text{CLIQ}}$ . This remarkable performance is obtained by introducing currents in the order of tens of kiloampere in the excitation coil, which may result in excessive Lorentz force due to the interaction with the background

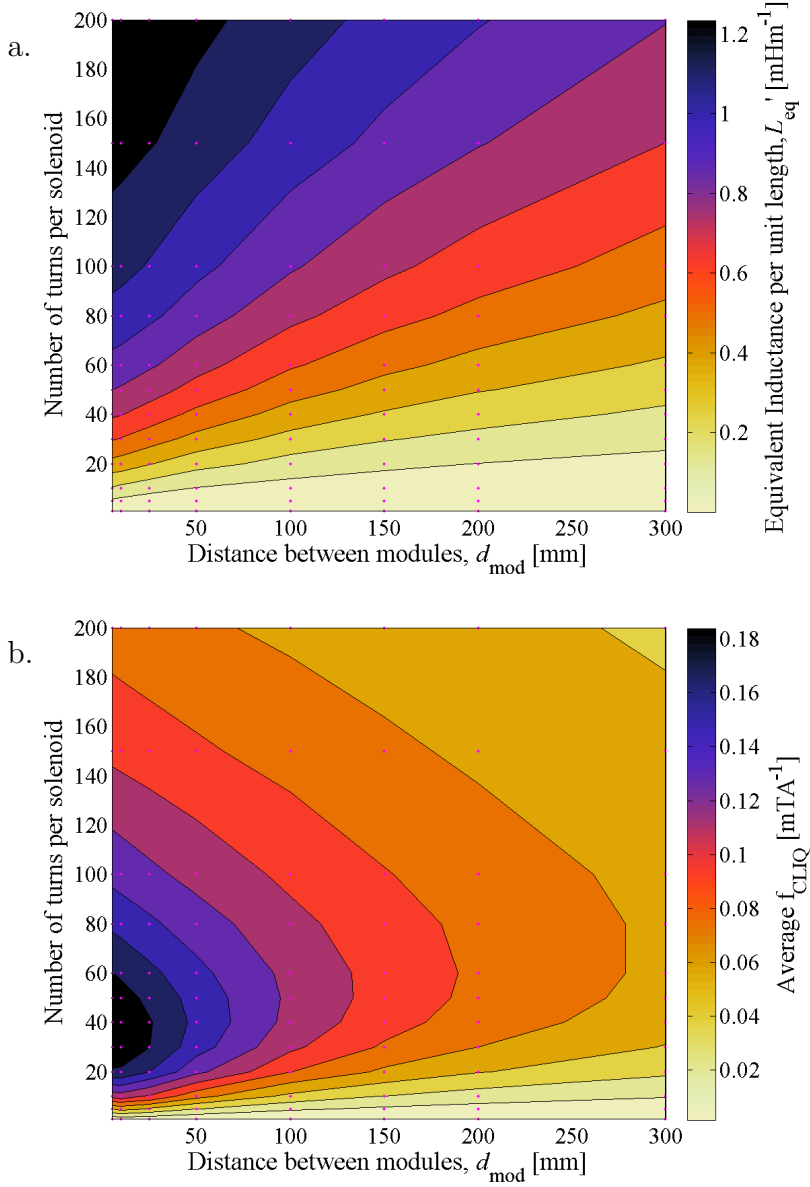


Figure 6.9. Design optimization of a CLIQ excitation coil to protect the 11 T, 6 m long, Nb<sub>3</sub>Sn dipole magnet. Influence of the number of turns per solenoid and distance between modules. a. Equivalent inductance per unit length. b. Average  $f_{\text{CLIQ}}$ .

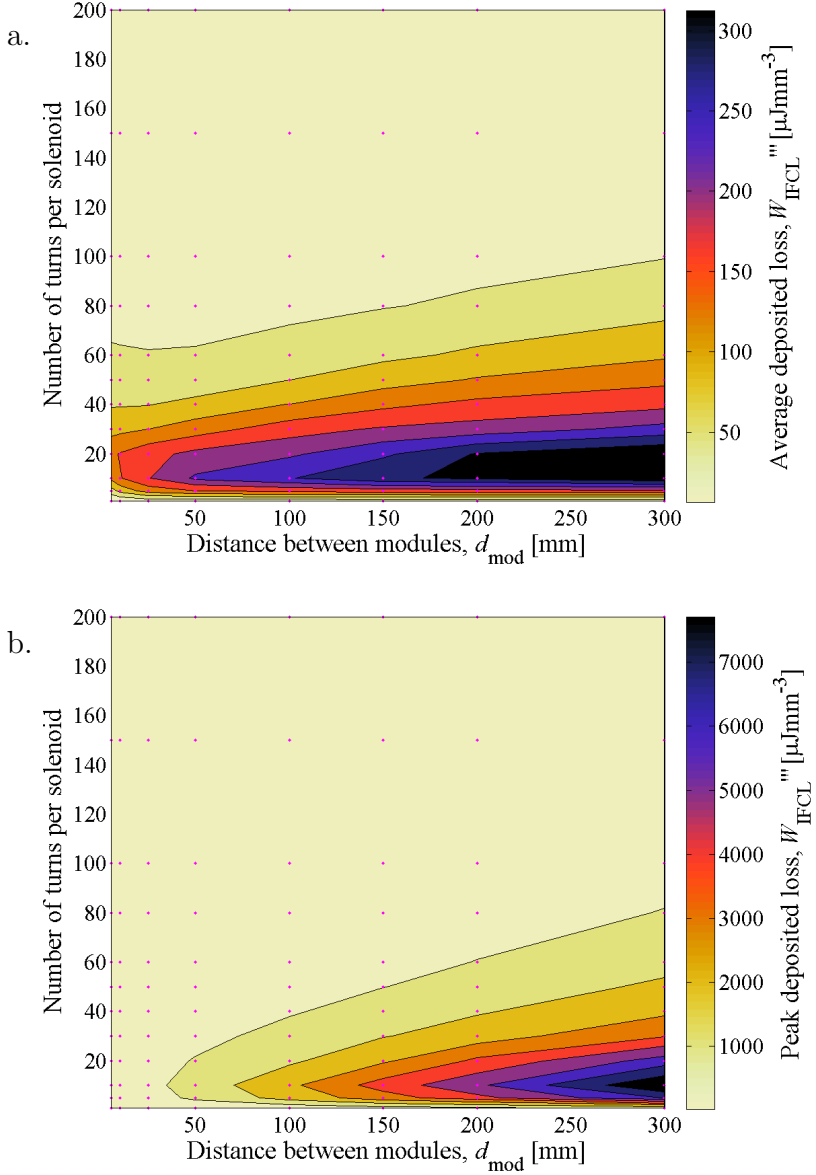


Figure 6.10. Design optimization of a CLIQ excitation coil to protect the 11 T, 6 m long,  $\text{Nb}_3\text{Sn}$  dipole magnet. Influence of the number of turns per solenoid and distance between modules. Deposited energy density 50 ms after triggering CLIQ a. Average over the module length. b. Peak within the module length.

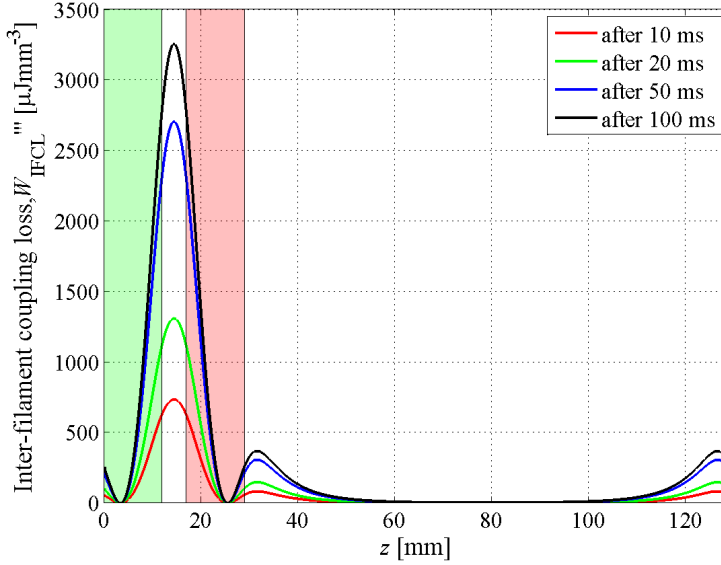


Figure 6.11. Baseline design of a CLIQ excitation coil to protect the 11 T, 6 m long,  $\text{Nb}_3\text{Sn}$  dipole magnet. Generated inter-filament coupling loss per unit volume, versus position along the magnet length. Only the region occupied by one module is shown. Regions occupied by solenoids with opposite current are represented with semi-transparent rectangles.

magnetic field. For this reason, the distance between modules selected in the baseline design is reduced to 100 mm.

The deposited energy density achieved with the baseline design is largely sufficient to initiate a very fast and homogeneous transition to the normal state of the inner layer of the 6 m long magnet. For instance, consider that in this coil the margin to quench is between 20 and  $150 \mu\text{Jmm}^{-3}$  at the nominal current of 11.85 kA, and between 220 and  $300 \mu\text{Jmm}^{-3}$  at 3 kA.

To summarize, the design of this CLIQ excitation coil is optimized by:

- selecting a number of turns per solenoid comprised in the optimum range;
- avoiding an excessively small number of turns per solenoid, to prevent too high oscillation frequencies and to limit the peak introduced current;
- avoiding an excessively large distance between modules, for the same reason.

For the baseline design, the profile of the energy deposition within the length of a module is shown in figure 6.11. The region where significant loss is developed corresponds to about 50% of the module length. The ohmic loss generated in this region causes the normal zone to propagate to the areas between heating stations, which are only a few centimeter apart. The peak deposition is achieved in the 5 mm gap between the two solenoids, where the magnetic-field changes generated by the two solenoids effectively superpose. Depending on the conductor geometry

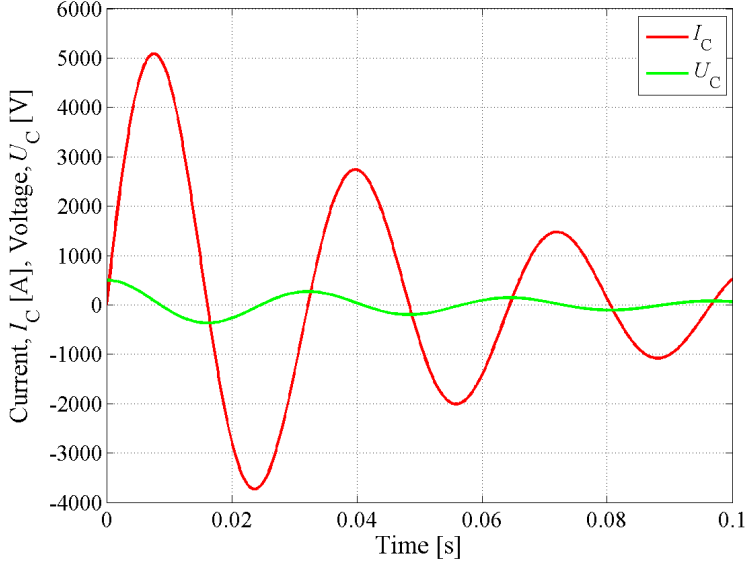


Figure 6.12. Baseline design of a CLIQ excitation coil to protect the 11 T, 6 m long,  $\text{Nb}_3\text{Sn}$  dipole magnet. Introduced oscillating current and voltage, versus time.

and thermal properties, the heat generation may be faster or slower than the heat propagation along the conductor. In the present case, in the high-loss region of the module, the heat is generated so quickly that the heat propagation is negligible as compared to the coupling loss in the superconductor. As a result, the transition to the normal state in the superconductor located close to the gap between two solenoids is nearly instantaneous. A complete 3-D model including electro-magnetic coupling, inter-filament coupling loss, and heat propagation along the conductor is required in order to properly analyze the transient.

The voltage across the excitation coil and the introduced current are shown in figure 6.12. The loss deposited by CLIQ is proportional to the square of its charging voltage. Hence, in first approximation a similar excitation coil could achieve a peak energy deposition higher than  $50 \text{ mJmm}^{-3}$  in 50 ms, if charged with 2 kV. This very high energy is sufficient to transfer to the normal state in a few tens of millisecond most of the winding pack, even if made of high-temperature superconductor. Since CLIQ is not relying on thermal diffusion, the thickness of the insulation layer can be increased as well, to reduce the risk of electrical failure without reduction of the system performance.

The charging voltage is also proportional to the introduced current, hence careful studies of the Lorentz force acting on the excitation coil and of the heat deposition in its wire are required. An alternative design solution consists in a multi-layer excitation coil, which can achieve similar power deposition with reduced peak currents, but has larger dimensions.

In conclusion, a well-insulated, well-supported CLIQ excitation coil seems a

promising solution for a very effective protection of low- and even high-temperature superconductor magnets, and possible to implement in the near future. Various important design features are not addressed here and will need further investigation, including:

- calculating the mutual inductance between the excitation and the main coil;
- calculating the Lorentz force acting on the excitation coil, and designing proper supporting structures;
- implementing a 3-D model simulating the generation of inter-filament coupling loss and heat propagation along the direction of the superconductor;
- assessing the impact of the space taken by the excitation coil on the magnetic properties of the main coil;
- exploring the advantages of a system composed of multiple excitation coils, distributed along the magnet, to assure redundancy and reduce the self-inductance of each coil;
- simulating the thermal transient in the wire used in the excitation coil;
- optimizing the material of the wire, including alloys and its cross-section.

## 6.5 Conclusion

A CLIQ system based on an external coaxial excitation coil strongly coupled to the main coil is an effective method for the protection of superconducting magnets. With respect to the standard CLIQ, this method has the definite advantage of providing galvanic isolation between the protection unit and the magnet to protect. Consequently, the system can operate with higher charging voltage and introduced oscillating current without significantly increasing the risk of electrical breakdown of the conductor insulation.

An existing magnet can be protected with this method with relatively limited effort, provided a suitable coil magnetically coupled to the main coil is present or can be added with simple means. Including this CLIQ variant in the magnet design from the start can significantly improve the system performance and its integration in the magnet circuit. Possible design enhancements include the simultaneous increase of the CLIQ charging voltage and thickness of the insulation layer between excitation and main coil, the choice between an excitation coil surrounding the main coil, internal to it, or located between magnet layers, and the optimization of the excitation-coil geometry to concentrate the power deposition in well-distributed separate regions, resulting in effective inductive heating stations.

A high-voltage CLIQ system based on a well-insulated and well-supported excitation coil is also a promising solution for initiating a transition to the normal state in coils with very large margin to quench, such as high-temperature superconductor coils.

## Chapter 7

# CLIQ-integrated magnet design

*The various aspects in the design of a superconducting magnet can be adapted for improving the performance of a CLIQ-based protection system in terms of lower hot-spot temperature, safer electrical design, and reduced size and cost. The impact of the proposed measures, including modifications of the superconductor, changes of the coil turns, and addition of multiple CLIQ terminals, are analyzed and discussed.*

### 7.1 Design strategy

A number of modifications can be applied to the magnet design in order to improve CLIQ performance. Table 7.1 summarizes the design parameters most affecting CLIQ behavior, ordered by their increasing impact on the magnetic requirements and coil manufacture.

As thoroughly discussed in chapter 3, the order of the coil sections and the positioning and number of CLIQ terminals yield a very significant enhancement of CLIQ effectiveness with no impact on magnetic performance. For most coil geometries, manufacturing a coil with additional CLIQ terminals is relatively easy and inexpensive. The addition of CLIQ terminals between coil layers may require a modification in the coil design, but the improvement of performance is usually very significant.

The optimization of the superconductor for maximum CLIQ performance requires reconsidering strand and cable properties as detailed in section 7.2.

Since CLIQ performance increases if higher current-changes can be introduced in the coil sections, magnet designs with reduced coil self-inductance and equivalent inductance of the CLIQ discharge circuit  $L_{eq}$  [H] offer higher quench protection performance. In the case of a CLIQ-based system the advantages of these measures

Table 7.1. Qualitative impact of possible design modifications on the magnetic requirements, coil manufacture, and quench protection.

Design modification	Magnetic performance	Coil manufacture	Quench protection
Order of coil sections	Nil	Low	High
Positioning of CLIQ terminals	Nil	Medium	High
Number of CLIQ terminals	Nil	Medium	High
Strand/wire parameters	Low	Low	Medium
Cable parameters	Low	Low	Low
Number of coil turns	Low	Medium	Medium
Magnetic length	Medium	Medium	Medium
Coil type	High	High	High

are not limited to those common to all protection systems, namely the reduced voltage to ground and the faster current discharge. In fact, in first approximation the peak power per unit volume delivered by CLIQ is inversely proportional to the square of the CLIQ equivalent inductance. Thus, a decrease of the number of coil turns and/or of the magnetic length can significantly enhance CLIQ performance.

Finally, the impact of a change of the coil geometry on the effectiveness of the CLIQ system has to be considered. As an example, in sections 3.3.2 and 3.3.4 the CLIQ performance in the case of a dipole magnet based on the  $\cos\theta$  or on the block-coil design is analyzed.

## 7.2 Optimization of the superconductor

Since CLIQ technology primarily relies on inter-filament coupling loss developed in the matrix of the superconducting wires, it is possible to optimize the wire parameters in order to enhance the performance without significantly affecting the magnet design. As shown in chapter 2, the key parameters affecting the inter-filament coupling loss are the filament twist-pitch  $l_f$  [m] and the effective resistivity of the stabilizer matrix between the filaments in the wires. These parameters can usually be modified even in the case of coils which are already in the final stage of their design. In fact, their impact on the magnetic-field errors during stationary operation and on the transitory loss while changing the magnet transport current with steady ramp-rates is usually small as compared to the contributions of other non-linear effects, such as inter-strand coupling loss and hysteresis in the superconducting filaments.

### 7.2.1 Filament twist-pitch and resistivity of the matrix

As shown in equations 2.18 and 2.25, both the characteristic time constant of the inter-filament coupling currents and the power per unit volume developed due to inter-filament coupling loss are proportional to the square of the filament twist-pitch



and inversely proportional to the effective transverse resistivity of the matrix material between filaments. Thus, strands with longer filament twist-pitch and with higher RRR generally develop more coupling loss, but more slowly. For this reason, the choice of the optimum filament twist-pitch and matrix resistivity is a compromise between generating enough loss and generating it fast enough. Since different coil geometries and parameters of the CLIQ system result into different CLIQ oscillations frequencies, the choice of strand parameters has to be addressed on a case-by-case basis.

In addition, the presence of local inter-filament coupling currents modifies the overall differential self-inductance of the coil, as explained in section 4.4.1. The higher the filament twist-pitch and the lower the resistivity of the matrix, the more the coil self-inductance decreases and the CLIQ oscillation frequency increases.

These interdependent non-linear effects need to be included in the analysis in order to correctly assess the CLIQ performance and predict the hot-spot temperature. The electro-thermal transient following a CLIQ discharge are simulated with the LEDET model presented in chapter 4.

As an example showing the dependence of the CLIQ performance on the strand parameters, the case of the full-size, 6.8 meter long,  $\text{Nb}_3\text{Sn}$  quadrupole magnet for the high-luminosity LHC is considered [131–134]. In section 3.3.3, it was already shown how to optimize the electrical order of the coil sections and the positioning of the leads in order to improve the CLIQ effectiveness. Given the presently advanced design stage of the magnet, the range of configurations easily implementable is rather limited. Among these, the most optimized is the Crossed-Poles 2-CLIQ configuration shown in figures 3.9c-d, which is now considered as the baseline for a CLIQ-based protection system for this magnet.

The latest design of the superconductor used for this coil is composed of strands with a filament twist-pitch of 19 mm and a copper matrix with  $\text{RRR}=140$  [132–134]. Since no transitory loss measurements of this superconductor are available, it is not possible to precisely determine the value of the effective transverse-resistivity factor  $f_{\text{eff}}$  presented in equation 2.19. Hence, it is here assumed that this parameter, depending on the matrix filling factor and on the position of the filaments in the strand cross-section, is 1.5, the same value as the superconductor with similar characteristics used in the model magnet [89, 91].

In figure 7.1 simulated CLIQ discharges at  $I_0=I_{\text{nom}}=17.3$  kA are shown, for three different values of filament twist-pitch and for a RRR of 140. As expected, there is a relation between the value of the filament twist-pitch and the oscillation frequency, amplitude, and damping of the current  $I_{C1}$  [A] discharged by each of the two CLIQ units. This is a consequence of the above-mentioned reduction of the coil self-inductance due to the presence of inter-filament coupling currents, which is more significant for a longer filament twist-pitch.

More importantly, the different power depositions achieved with the three configurations result in significantly different CLIQ performance. The hot-spot temperature, also shown in figure 7.1, is the primary indicator of the performance of the protection system. At the nominal current of 17.3 kA, the magnetic field in the strands of the coil varies from 0.1 to 11.9 T. For the baseline filament twist-pitch of 19 mm, the characteristic time constants of the inter-filament coupling currents in the

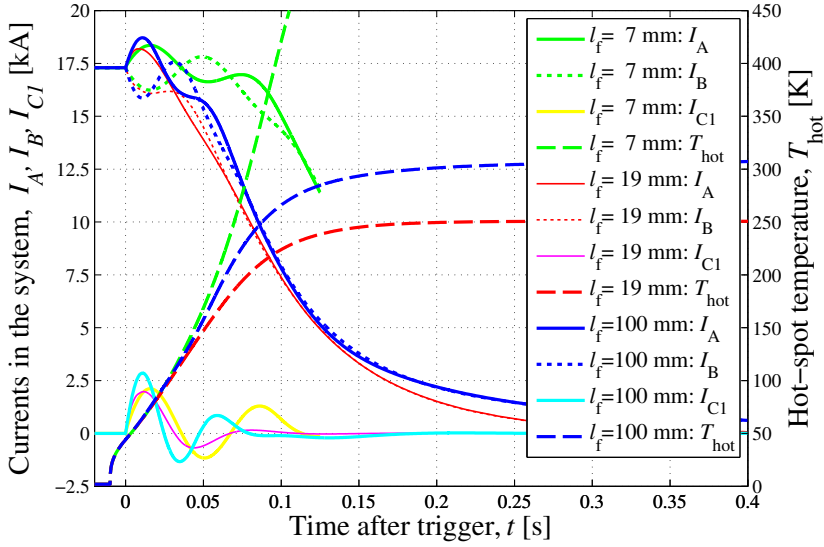


Figure 7.1. Comparison of the CLIQ performance for three values of filament twist-pitch  $l_f$ . Simulated currents  $I_A$ ,  $I_B$ , and  $I_{C1}$  and hot-spot temperature,  $T_{\text{hot}}$ , versus time, after triggering a 500 V, 60 mF, 2-CLIQ system at  $I_0 = I_{\text{nom}} = 17.3$  kA.

various strands, calculated using equation 2.18, are therefore between 5 and 30 ms. Thus, during the first quarter of oscillation period of the current introduced by CLIQ ( $0 < t \leq 12$  ms), and during the following half period ( $12 < t \leq 42$  ms), the inter-filament coupling currents do not have time to fully develop. However, the developed coupling loss is sufficient to turn to the normal state the entire inner layer of the coil in about 10 ms and the outer layer in about 40 ms. This performance limits the hot-spot temperature to about 250 K. Interestingly, the electrical resistance of the normal zone in the coil increases so quickly that it enhances the dampening of the introduced current.

In the case of transients with constant current-changes lasting much longer than the time constant of the inter-filament coupling currents, the generated inter-filament coupling loss per unit volume is directly proportional to the square of the filament twist-pitch. This relation, however, does not hold for the fast transient developed after triggering CLIQ. For instance, increasing the filament twist-pitch to 100 mm deteriorates the performance, clearly shown in figure 7.1. In fact, in this case the energy deposition is less effective due to the large increase of the inter-filament time constant comprised between 150 and 840 ms, which is an order of magnitude higher than the CLIQ oscillation period.

On the other hand, excessively decreasing the filament twist-pitch can also result in a reduction of the CLIQ power deposition, and hence of its performance. For example, figure 7.1 shows the simulated transient for a twist-pitch of 7 mm, corresponding to inter-filament time constants in the range of 1 to 4 ms. In this case the inter-filament coupling loss developed in the strands is insufficient to transfer to the normal state a

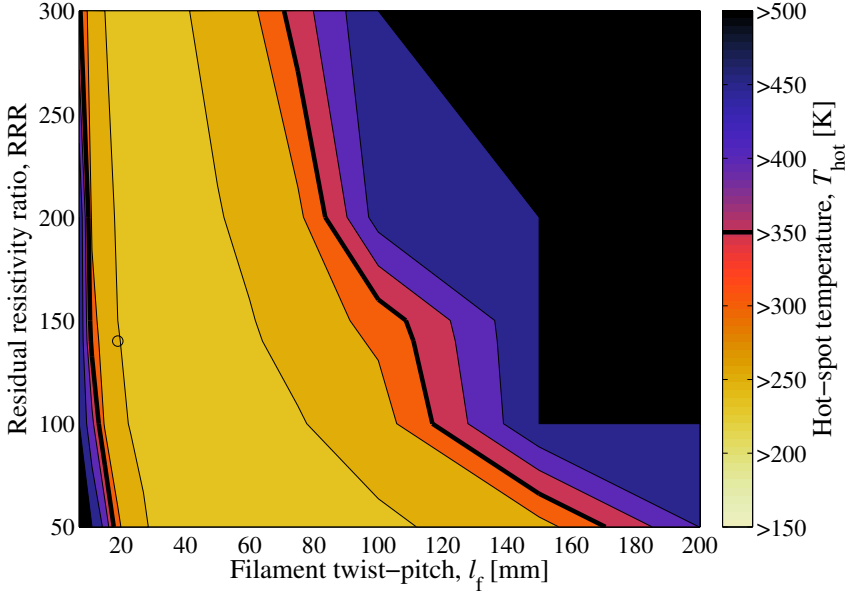


Figure 7.2. Simulated hot-spot temperature,  $T_{\text{hot}}$ , after triggering a 500 V, 60 mF, 2-CLIQ system protecting a 6.8 m long quadrupole magnet at  $I_0=I_{\text{nom}}=17.3$  kA for various filament twist-pitch,  $l_f$ , and matrix RRR. Baseline design indicated by a circle ( $l_f=19$  mm, RRR=140).

large volume of superconductor, and as a result the magnet is not properly protected by CLIQ.

For a given coil, CLIQ system, and initial current level, a range of filament twist-pitches exists that allows an effective generation of inter-filament coupling loss and the protection of the coil. Analogously, for CLIQ to be effective the value of the transverse resistivity of the stabilizer matrix has to be within a certain range of values.

In the case of the coil analyzed in this section, the ranges of filament twist-pitch and RRR allowing the protection of the coil are rather wide. Figure 7.2 shows the simulated hot-spot temperature after triggering CLIQ at  $I_0=I_{\text{nom}}=17.3$  kA for filament twist-pitches in the range of 7 to 200 mm and RRR in the range of 50 to 300. The hot-spot temperature can be kept below the target value of 350 K for a twist-pitch between about 10 and 150 mm and RRR between 50 and 300.

The value of RRR is not as critical for CLIQ performance as the filament twist-pitch, because its impact on the inter-filament coupling loss and characteristic time constant is less important. In addition to the effect on the coupling loss, the influence of RRR has a twofold effect on the hot-spot temperature. When in the normal state strands with higher RRR develop less electrical resistance per unit length, hence the coil transport current is discharged more slowly by effect of the reduced coil resistance. But due to the lower resistivity less ohmic loss per unit length is generated in the coil's hot-spot, hence its temperature increases more slowly for the same current discharge. For the coil and CLIQ system considered in this

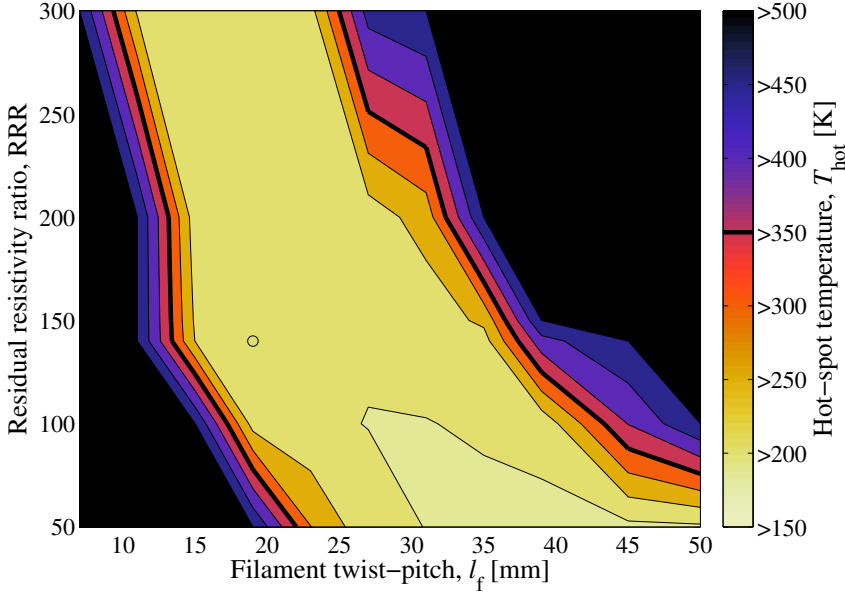


Figure 7.3. Simulated hot-spot temperature,  $T_{\text{hot}}$ , after triggering a 500 V, 60 mF, 2-CLIQ system connected to a 6.8 m long quadrupole magnet at  $I_0=9$  kA for various filament twist-pitch,  $l_f$ , and matrix RRR. Baseline design indicated by a circle ( $l_f=19$  mm, RRR=140).

section, at  $I_0=17.3$  kA these two effects compensate each other almost completely and the effect on the hot-spot temperature is very limited.

A similar analysis can be performed for a different initial current level. Due to the presence of non-linear effects such as magneto-resistivity and saturation of the iron yoke surrounding the magnet, a complete electro-thermal simulation is required to assess the CLIQ performance in full. The results of a series of simulations at an intermediate current of  $I_0=9$  kA are shown in figure 7.3.

At lower current, if a sufficient volume of the coil is transferred to the normal state, the hot-spot temperature can be kept lower than in the case of  $I_0=17.3$  kA due to the reduced energy density. However, more energy per unit volume is required to initiate a transition to the normal state due to the lower magnetic field. Hence, the ranges of filament twist-pitch and RRR that allow an effective protection of the coil are reduced. A simultaneous decrease of the filament twist-pitch and of the RRR can cause an excessive reduction of the coupling loss developed in the strands. But a simultaneous increase of the filament twist-pitch and of the RRR can result in too high time constants of the inter-filament coupling currents and an ineffective power deposition in the strands. Both cases result in a heat generation insufficient to initiate a transition to the normal state in voluminous regions of the coil, a slow discharge of the magnet current, and thus an unacceptably high hot-spot temperature at the end of the transient. If required, the ranges of acceptable strand parameters can be extended by increasing the capacitance of the CLIQ capacitor banks  $C$  [F] or its charging voltage. In the present example, for both studied current levels the filament

twist-pitch and RRR of the baseline superconductor are well within the range of values resulting in acceptable performance.

The performance of the protection system has to be studied in the entire range of operating current to assess its performance and identify worst-case scenarios. The simulated hot-spot temperature obtained for initial current levels between 1 and 20 kA are shown in figure 7.4. Values of filament twist-pitch in the range 15 to 35 mm allow maintaining the hot-spot temperature below 350 K for an initial current higher than about 3 kA. For lower initial currents, the energy delivered by the CLIQ system is insufficient to initiate a transition to the normal state in the coil. Note that the adopted model does not take into account the electrical resistance developed in the hot-spot region, but only the electrical resistance of the turns transferred by the protection system. In various practical cases, the hot-spot electrical resistance is sufficient to safely discharge the magnet and avoid damage due to overheating. For this reason, the presented results are too pessimistic in particular in the range of an initial current lower than 4 kA.

Even with this conservative assumption, it is possible to assure the coil protection at low current by increasing the CLIQ capacitance. Alternatively, a 1-CLIQ configuration charged with double voltage can be implemented. The energy stored in a 1 kV, 60 mF, 1-CLIQ system is twice of a 500 V, 60 mF, 2-CLIQ one. If the unit is connected to the coil with two intra-pole terminals, as shown in figure 3.11f, the peak voltage to ground after triggering CLIQ is half of the unit charging voltage, the same as for the 2-CLIQ case analyzed in this section.

The simulated hot-spot temperature with this configuration is shown in figure 7.5. The performance at high current levels remains the same with respect to the 500 V 2-CLIQ case, since both systems achieve the same peak power density. On the contrary, the increased total energy delivered to the coil allows protecting the coil even at current levels as low as 1 kA.

In conclusion, the baseline filament twist-pitch and RRR of the matrix are well within the range of values assuring high CLIQ performance, and a modification of their values would only yield marginal performance improvement.

## 7.2.2 Performance of a multi-pitch cable

Since the strands of a cable effectively see different magnetic fields and are subjected to different magnetic-field changes during the CLIQ discharge, the inter-filament coupling loss and its characteristic time constant are not homogeneous over the cable cross-section. However, given the very efficient heat diffusion between adjacent strands of the same cable, occurring on a time scale shorter than 1 ms [113,114], the strands of a cable are transferred to the normal state almost simultaneously. This transition occurs once the total energy deposited in all strands of a cable is higher than the total enthalpy to quench all strands, even if the power deposition is not uniform in the cable cross-section.

Thus, one can envisage to manufacture a superconducting cable composed of strands with different filament twist-pitches, hence optimized to maximize the energy deposition at different current levels and/or CLIQ oscillation frequencies. Such a multi-pitch cable can be composed of a few groups of strands with different

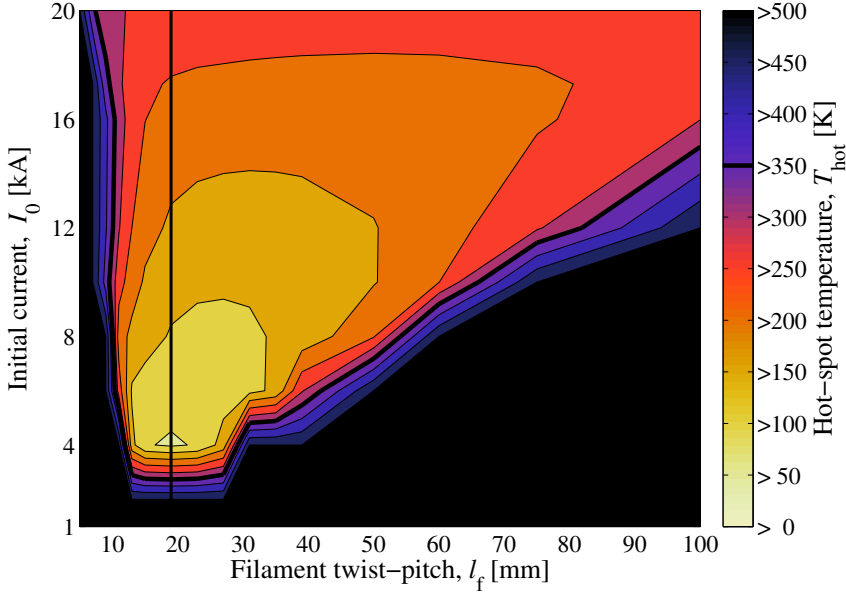


Figure 7.4. Simulated hot-spot temperature,  $T_{\text{hot}}$ , after triggering a 500 V, 60 mF, 2-CLIQ system connected to a 6.8 m long quadrupole magnet, for various initial currents,  $I_0$ , and filament twist-pitch,  $l_f$ . Baseline design indicated by a straight line ( $l_f=19$  mm).

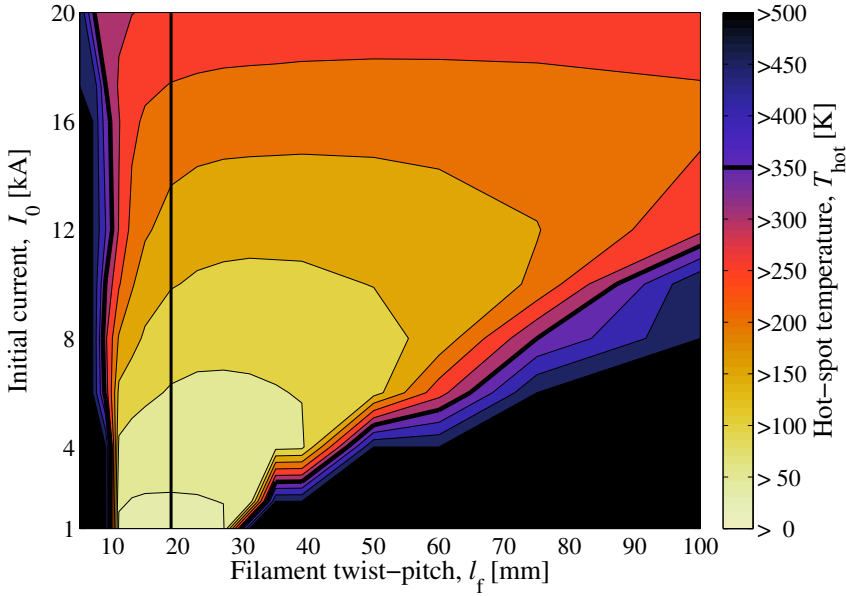


Figure 7.5. Simulated hot-spot temperature,  $T_{\text{hot}}$ , after triggering a 1 kV, 60 mF, 1-CLIQ system connected to a 6.8 m long quadrupole magnet, for various initial currents,  $I_0$ , and filament twist-pitch,  $l_f$ . Baseline design indicated by a straight line ( $l_f=19$  mm).

twist-pitches. The variation of the magnetic field in time and location can be compensated by the difference in the filament twist-pitches of the various strands. As a result, the distribution of the inter-filament coupling loss and its time constant in the cable cross-section are not uniform along the cable direction. The inhomogeneous energy deposition in the cable cross-section and along the cable direction may result in a superconductor optimized for CLIQ over a wider range of operating currents.

This performance improvement is achieved only if the generation of inter-filament coupling loss is highly dependent on the initial current level. This is not the case for many magnet systems. As an example, the same coil and CLIQ system presented in the previous section are considered. The calculated energy per unit volume deposited by CLIQ, averaged over all strands of the coil, is shown in figures 7.6 and 7.7, for a conventional cable composed of strands with the same filament twist-pitch and for a multi-pitch cable whose strands have a filament twist-pitch distribution with  $\pm 5$  mm variation, respectively.

One can observe that the dependence of the generated inter-filament coupling loss on the current level is rather limited. Thus, a single value of filament twist-pitch for all strands already achieves a very high performance at all operating currents. This result is confirmed by the simulated hot-spot temperature previously shown in figure 7.5, which shows little variation for values of the filament twist-pitch between 10 and 35 mm. The performance of a multi-pitch cable in terms of CLIQ deposited energy is very similar and actually slightly lower than a conventional cable.

In order to properly assess the performance of a multi-pitch cable, a full three-dimensional electro-magnetic analysis has to be performed. However, this solution does not seem too promising and additional efforts are not justified.

### 7.2.3 Strand twist-pitch and cross-contact resistance

During transients with constant current-change lasting much longer than the characteristic time constant of the inter-strand coupling currents, the inter-strand coupling loss developed in Rutherford cables is proportional to the strand twist-pitch and inversely proportional to the cross-contact resistance between strands, as shown in equation 4.34. As mentioned in section 2.2, inter-strand coupling loss usually has only a marginal effect on CLIQ performance. In fact, for typical strand and cable parameters the characteristic inter-strand time constants, calculated with equations 4.38 and 4.42, are one order of magnitude higher than the inter-filament time constants. Indeed, cables with very short strand twist-pitch and with very high cross-contact resistance can have lower inter-strand coupling-currents time constants, but the actual loss generated in these particular cables is very limited.

As a result, the CLIQ performance is effectively independent on the strand twist-pitch and cross-contact resistance. For instance, the same case presented in section 7.2.1 is studied for base strand parameters ( $l_f=19$  mm,  $RRR=140$ ) and a variation of the strand twist-pitch and cross-contact resistance in the range of 20 to 500 mm and 1 to 1000  $\mu\Omega$ , respectively. This wide variation of cable parameters yields less than 1% difference in the amplitude and frequency of the current introduced by CLIQ, and in the coil's hot-spot temperature.

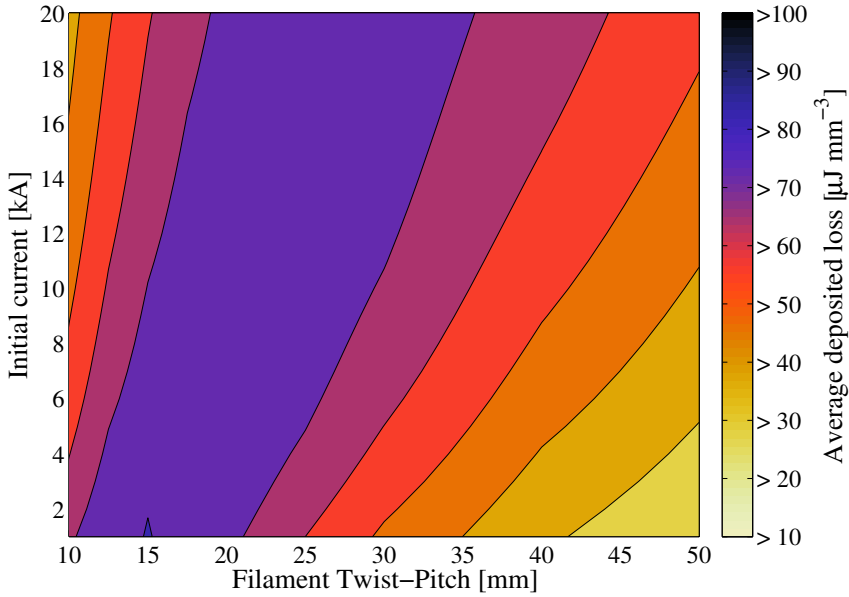


Figure 7.6. Performance of a conventional cable. Calculated deposited energy per unit volume, averaged over the strands of a 6.8 m long quadrupole magnet, during the first 100 ms after triggering a 500 V, 60 mF, 2-CLIQ system.

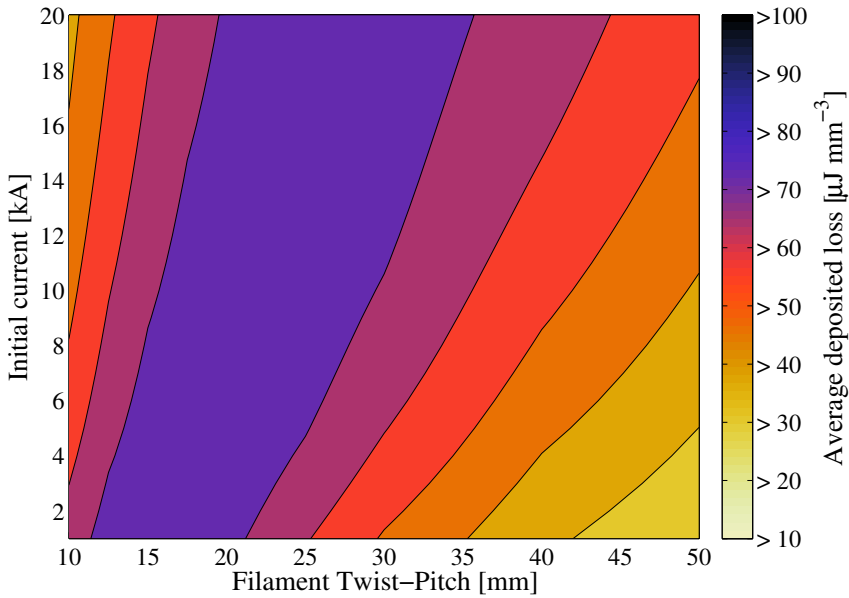


Figure 7.7. Performance of a multi-pitch cable (random distribution,  $\pm 5$  mm variation). Calculated deposited energy per unit volume, averaged over the strands of a 6.8 m long quadrupole magnet, during the first 100 ms after triggering a 500 V, 60 mF, 2-CLIQ system.



### 7.2.4 Fraction of superconductor and stabilizer

Increasing the superconductor fraction  $f_{sc}$  is desirable to achieve a higher engineering current-density in the conductor, hence improving the magnetic performance or leading to manufacture more compact and less expensive coils. However, the fraction of stabilizer and superconductor in the strands has a twofold negative influence on the magnet protection.

Firstly, decreasing the fraction of stabilizer causes a reduction of the strand cross-section capable of transporting current after the superconductor is transferred to the normal state. The corresponding increase of the ohmic loss per unit length makes it more challenging to effectively protect the coil against overheating after a quench.

Secondly, the variation of the strand composition modifies the relative contribution of superconductor and stabilizer to the strand specific heat. Both Nb-Ti and Nb<sub>3</sub>Sn have a higher specific heat than copper and aluminium at low temperature ( $1.9\text{ K} \leq T \leq 20\text{ K}$ ), but lower specific heat than copper at higher temperature ( $50\text{ K} \leq T \leq 300\text{ K}$ ). Thus, strands with higher superconductor fraction are more difficult to transfer to the normal state and their temperature increases more quickly after they are in the normal state due to the reduced overall specific heat in the medium to high temperature range. As a result, coils composed of strands with higher superconductor fraction have a higher temperature margin, but are more challenging to protect against overheating after a quench, in particular using systems based on active heating of the conductor, such as CLIQ or quench heaters.

In addition, the fraction of superconductor affects the value of the effective transverse resistivity of the matrix  $\rho_{\text{eff}}$  [ $\Omega\text{m}$ ], defined in equation 2.19, which is inversely proportional to the inter-filament coupling loss and its characteristic time constant. The effect of an increase of the effective transverse resistivity is similar to a reduction of the RRR described in section 7.2.1.

In the early stage of the design of a coil, the fractions of superconductor and stabilizer are selected as a careful compromise between effectiveness of the quench protection system against magnetic performance and coil compactness. By relying on CLIQ's more effective and faster energy deposition mechanism, it is now possible to protect coils made with superconductor with smaller fraction of stabilizer.

The cases of two Nb<sub>3</sub>Sn cos- $\theta$  magnets for the high-luminosity LHC are discussed here, namely the 6.8 m long, 12 T quadrupole coil presented in section 3.3.3 [131–134] and one aperture of the 6 m long, 11 T dipole coil presented in section 3.3.2 [80, 81, 127–130], with fractions of superconductor of 0.47 and 0.44, respectively [91, 134].

The simulated hot-spot temperatures in the two coils, at nominal current and at about half nominal current, are shown in figure 7.8 as a function of the fraction of superconductor. In both cases, the hot-spot temperatures are well below the maximum allowed value of 350 K [35].

Thus, an increase of the fraction of superconductor can be envisaged in order to improve the magnet performance while still assuring proper coil protection. For instance, the critical surface at a temperature of 1.9 K and the load line of the quadrupole magnet are shown in figure 7.9 for three different values of the fraction of superconductor. In the baseline design, this coil is operated at a nominal current

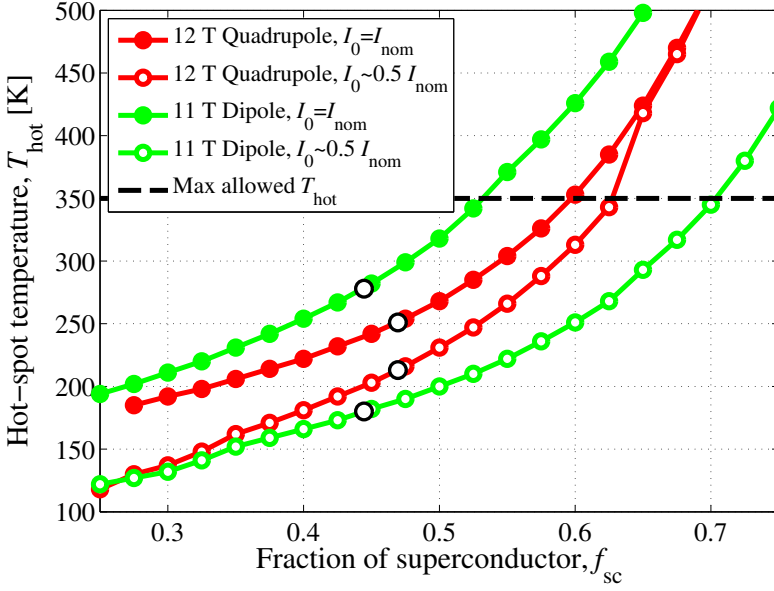


Figure 7.8. Simulated hot-spot temperature,  $T_{\text{hot}}$ , after triggering CLIQ on two different magnets (sections 3.3.3 and 3.3.2) for various values of the superconductor fraction,  $f_{\text{sc}}$ . Baseline design values indicated by black circles ( $f_{\text{sc}}=0.47$  and  $0.44$ ).

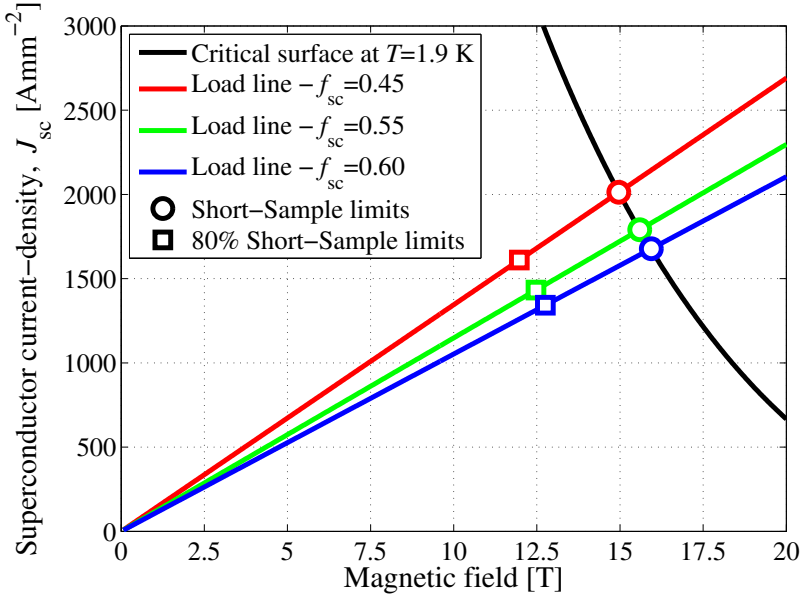


Figure 7.9. Critical surface at  $T=1.9$  K and load line of the superconductor used for the analyzed 12.2 T quadrupole magnet, for three values of the fraction of superconductor,  $f_{\text{sc}}$ .

of 17.3 kA, reaching a magnetic field of 12.2 T and a superconductor current-density of  $1622 \text{ Amm}^{-2}$ , corresponding to 80% of its short-sample limit. By allowing an increase of the hot-spot temperature from 250 K to 300 K, the same coil could be manufactured with strands with a superconductor fraction of 0.55, hence decreasing the superconductor current-density by 17%. In this case, the operating current of 17.3 kA would correspond to 77.5% of the short-sample limit, resulting in a higher stability margin; or else, the magnet could be operated at a magnetic field of 12.5 T without increasing the stability margin. An increase of the fraction of superconductor to 0.60 would push the operating magnetic field to 12.7 T, and the hot-spot temperature to about 350 K.

## 7.3 Optimization of the magnet design

The potential of CLIQ technology can be fully exploited when CLIQ is included in the magnet design from the beginning. A coil can be redesigned to better adapt its characteristics to CLIQ, thus improving the quench performance, the system safety, and the coil compactness without significantly affecting the magnetic requirements and the stationary operations. Proposed measures include modifying the number of turns of the magnet, its operating current, the fraction of superconductor and stabilizer of its strands, its cable dimensions, and the thickness of its pole-to-pole insulation layer.

### 7.3.1 Number of coil turns

The optimization of the number of coil turns is a usual process during the magnet design. A similar peak magnetic field can be generated by coils characterized by the same product  $N_T I_{\text{nom}}$  of their number of turns  $N_T$  and their operating current  $I_{\text{nom}}$  [A], without changing the current density in the strand superconductor  $J_{\text{sc}}$  [ $\text{Am}^{-2}$ ] and stabilizer  $J_{\text{st}}$  [ $\text{Am}^{-2}$ ]. For instance, a coil can be redesigned by replacing each turn with a pair of turns in the same geometric position, each carrying twice less transport current and with twice smaller cross-section  $a_c$  [ $\text{m}^2$ ]. The resulting coil meets similar magnetic requirements, but its operation and protection change significantly.

On the one hand, increasing the number of turns reduces the coil operating current, thus decreasing the rated current of the other electrical components in the circuit, such as power supplies and current leads. Furthermore, the positioning of the coil turns can be optimized with more flexibility if their number is larger, hence reducing the magnetic-field errors. On the other hand, the self-inductance  $L_M$  [H] of a coil is roughly proportional to the square of the number of turns. As a result, a coil with more turns requires higher operating voltages or longer charging time.

Coils with higher self-inductance are protected less effectively by an energy-extraction system. In fact, a higher operating voltage is required to obtain the same discharge time constant and hot-spot temperature at the end of the discharge. For example, a coil with twice more turns requires an energy-extraction system with a voltage four times higher to maintain the hot-spot temperature at the same level.

On the contrary, if a coil is protected by a quench-heaters based system, the quench performance is less significantly affected by the number of coil turns. In fact, since the same heat per unit of heater-strip surface diffuses from the heater strips to the turns, and since the volume of conductor to heat up is unchanged, a similar volume of the winding pack is transferred to the normal state in the case of coils with different number of turns protected by similar quench heaters. Besides, once in the normal state the electrical resistance of a coil with twice more turns and twice smaller cross-section is four times higher, and hence the discharge time-constant of its transport current is unchanged, even if its self-inductance is also four times higher. The only ingredient in a quench-heaters based protection system that depends on the number of turns is the turn-to-turn quench propagation. In fact, the heat generated by ohmic loss in coils composed of more turns with smaller cross-section needs to diffuse through more insulation layers in order to reach the entire winding pack, but the heat required to initiate a transition to the normal state of each individual turn is smaller. These opposite effects usually compensate each other and are not critical for the coil protection.

The performance of a CLIQ-based protection system can be greatly enhanced by reducing the number of coil turns. In fact, the self- and mutual inductances per unit meter of the coil sections, and hence the equivalent inductance per unit meter of the CLIQ discharge circuit  $L'_{eq}$  [ $\text{Hm}^{-1}$ ], are roughly proportional to the square of the number of turns; whereas the parameters  $f_{\text{CLIQ}}$  [ $\text{TA}^{-1}$ ], defined in equation 2.14, characterizing the magnetic-field change generated by the current-change introduced by CLIQ, are roughly proportional to the number of turns. As a results, the CLIQ effectiveness  $\Psi$  [ $\text{m}^{-1}$ ], defined in equation 3.4, is inversely proportional to the number of coil turns.

The case of the 11 T,  $\text{Nb}_3\text{Sn}$ , dipole magnet presented in section 3.3.2 [80, 81, 127–130], is analyzed here. Table 7.2 shows the main parameters of its coil for the standard design (ST) and for two alternative designs featuring half (HT) or double (DT) number of turns.

In order to meet similar magnetic requirements, the operating current in the alternative design is multiplied or divided by a factor two, respectively. Note that the total magnetic energy stored in the coil is independent on the chosen design,  $E_M = 0.5 L_M I_{\text{nom}}^2$  [J]. The CLIQ parameters and equivalent inductance per unit length

Table 7.2. Key coil parameters for the three alternative designs for an 11 T  $\text{Nb}_3\text{Sn}$  dipole magnet: standard design (ST) and designs featuring half (HT) or double (DT) number of turns. Number of turns  $N_T$ , nominal current  $I_{\text{nom}}$ , equivalent inductance per unit length of the CLIQ discharge circuit  $L'_{eq}$ , average value of the parameters  $f_{\text{CLIQ}}$ , defined in equation 2.14, and average CLIQ effectiveness  $\Psi$ .

Design	$N_T$	$I_{\text{nom}}$ [A]	$L'_{eq}$ [ $\mu\text{Hm}^{-1}$ ]	$\overline{f_{\text{CLIQ}}}$ [ $\mu\text{TA}^{-1}$ ]	$\overline{\Psi}$ [ $\text{m}^{-1}$ ]
ST	$4 \times 56$	11850	581	185	0.32
HT	$4 \times 28$	23700	141	95	0.67
DT	$4 \times 112$	5925	2402	368	0.15

are calculated based on the Pole-Pole CLIQ configuration shown in figure 3.6a-b. As expected, the average CLIQ effectiveness  $\bar{\Psi}$  [ $\text{m}^{-1}$ ] is roughly proportional to the inverse of the number of coil turns. This result indicates that the maximum power deposition achievable in the strands with a certain CLIQ charging voltage, proportional to  $\Psi^2$ , is increased by a factor four by halving the number of turns. However, as explained in the rest of the section, this enhancement of the CLIQ effectiveness is only achieved if the oscillation periods of the current introduced by CLIQ are sufficiently long, as compared to the time constant of the inter-filament coupling currents. Hence, each modification to the magnet design has to be analyzed in more detail.

In order to maintain the same cable width, stabilizer to superconductor ratio, and superconductor and stabilizer current-density in the three designs, the conductor parameters are also modified, as shown in table 7.3.

Note that since the superconductor current-density and the magnetic field in the various positions of the coil cross-section do not vary in the three designs, the energy per unit volume required to initiate a transition to the normal state is unchanged. Furthermore, the two key strand parameters affecting the inter-filament coupling loss developed in the strands, namely the filament twist-pitch and the RRR of the matrix, are also the same in each configuration. As a result, the overall CLIQ performance is primarily influenced by the number of coil turns, which determines the oscillation frequency, peak amplitude, and damping factor of the current introduced, and the CLIQ effectiveness.

Figure 7.10 shows a comparison of the simulated electro-thermal transient after triggering a 500 V, 60 mF, Pole-Pole, 1-CLIQ system connected to one aperture of the full-scale, 6 meter long, 11 T dipole magnet at the nominal operating current.

To provide a convenient comparison of the three designs, the simulated currents in the two coil sections, each corresponding to one pole,  $I_A$  [A] and  $I_B$  [A], and the current introduced by CLIQ,  $I_C$  [A], are normalized to the operating current of each design. The CLIQ oscillation frequency is strongly dependent on the number of coil turns. In fact, neglecting non-linear effects, this frequency is solely determined by the equivalent inductance of the CLIQ discharge circuit and the capacitance of the CLIQ capacitor bank,  $f = \omega / (2\pi) \approx 1 / (2\pi \sqrt{L_{\text{eq}} C})$  [Hz], as detailed in section 2.2. Thus, for configuration HT, whose coil has an equivalent inductance of the CLIQ discharge circuit four and sixteen times lower than the ST and DT configurations, respectively,

Table 7.3. Key conductor parameters for the three alternative designs for an 11 T Nb<sub>3</sub>Sn dipole magnet. Number of strands  $N_s$ , strand diameter  $d_s$ , cable width  $w$ , average cable height  $h$ , fraction of superconductor  $f_{\text{sc}}$ , and cross-section of superconductor in the cable  $a_{\text{sc}}$ , and current density in the superconductor  $J_{\text{sc}}$ .

Design	$N_s$	$d_s$ [mm]	$w$ [mm]	$h$ [mm]	$f_{\text{sc}}$	$a_{\text{sc}}$ [ $\text{mm}^{-2}$ ]	$J_{\text{sc}}$ [ $\text{Amm}^{-2}$ ]
ST	40	0.70	14.85	1.31	0.44	6.8	1730
HT	22	1.32	14.85	2.44	0.44	13.4	1770
DT	90	0.33	14.85	0.61	0.44	3.4	1730

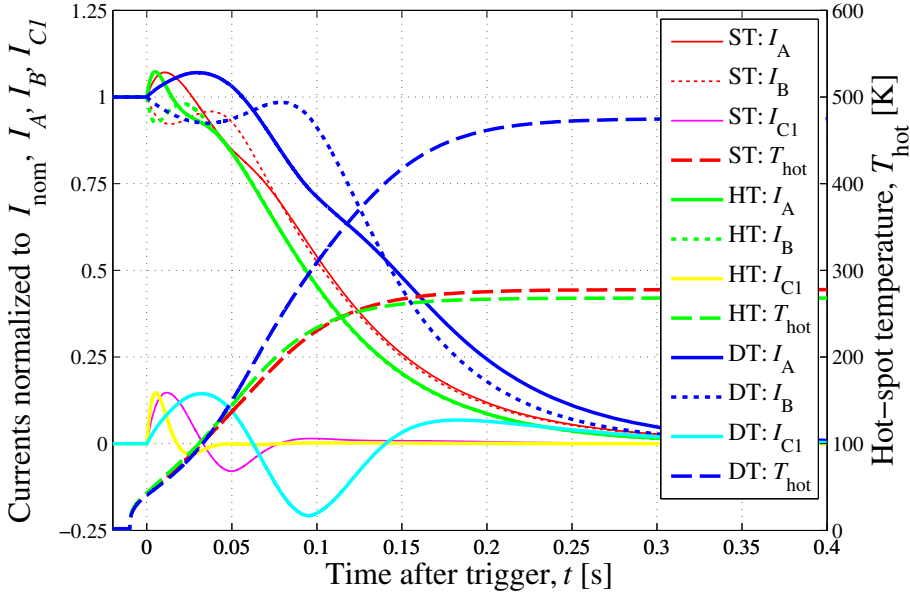


Figure 7.10. Comparison of CLIQ performance for three different designs of a 6 m long 11 T dipole magnet, after triggering a 500 V, 60 mF, 1-CLIQ system. Simulated currents  $I_A$ ,  $I_B$ , and  $I_{C1}$ , normalized to  $I_{nom}$ , and hot-spot temperature,  $T_{hot}$ , versus time.

an oscillation frequency two and four times higher is obtained, respectively. On the contrary, the normalized amplitude of the introduced current is independent of the designs. In first approximation, as shown in equation 2.32,  $I_{C,peak} \approx U_0 \sqrt{C/L_{eq}}$ , hence the ratio between  $I_{C,peak}$  and  $I_{nom}$  remains unchanged in the three designs and corresponding to about 0.14.

The higher CLIQ power deposition achieved for a lower number of coil turns results in a faster transition to the normal state of the winding pack and a lower temperature obtained in the coil hot-spot at the end of the discharge. Figure 7.11 shows the performance of the three different designs for the entire range of operating currents.

The performance of the DT design is not high enough to maintain the hot-spot temperature below 350 K and assure the coil protection for operating currents higher than 50% of  $I_{nom}$ . The calculated fourfold enhancement of the CLIQ effectiveness, achieved by selecting the HT design instead of the standard ST design, only yields a marginal performance improvement, with a reduction of the hot-spot temperature of only 10 to 20 K. This result can be explained by considering that the predicted increase of power deposition is fully achieved only if the oscillation period of the current introduced by CLIQ is long compared to the characteristic time constants of the inter-filament coupling currents developed in the strands. Otherwise, the generation of inter-filament coupling loss is less effective and the overall CLIQ performance is not much improved.

The improvement of CLIQ performance achieved by reducing the number of coil

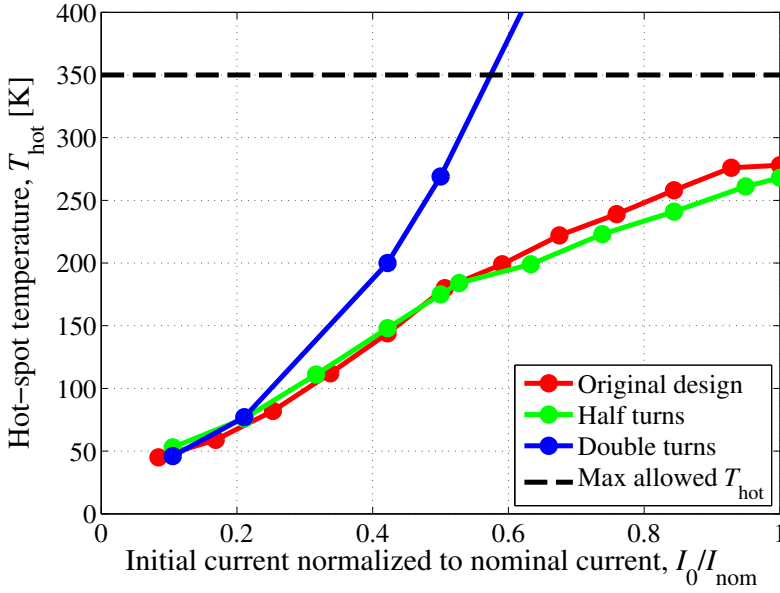


Figure 7.11. Comparison of CLIQ performance for three different designs of a 6 m long 11 T dipole magnet. Simulated hot-spot temperature,  $T_{\text{hot}}$ , after triggering a 500 V, 60 mF, 1-CLIQ system for various initial currents,  $I_0$ .

turns is larger in the case of coils with a higher equivalent inductance and/or protected by CLIQ units with higher capacitance. In fact, in both cases the duration of the CLIQ oscillation period is increased.

As an example, a 12 meter long version of the same 11 T dipole magnet is considered, characterized by twice higher self-inductance and CLIQ equivalent inductance with respect to the previous case. In order to maintain the same ratio between the energy stored in the coil and in the CLIQ system, the capacitance of the capacitor bank is doubled to 120 mF. Thus, the CLIQ oscillation period for each of the three designs is roughly twice longer than in the previous examples. The simulated normalized currents and hot-spot temperature for the three designs are shown in figure 7.12. Selecting a design with twice less coil turns yields higher power deposition and faster transition to the normal state of the winding pack, resulting in a hot-spot temperature about 50 K lower than the standard design. On the contrary, in the case of the double-turn design the power delivered by CLIQ is not sufficient to initiate a transition to the normal state in the coil, which therefore is not properly protected.

The performance of the standard design and of the half-turns design, for the entire range of operating currents, can be observed in figure 7.13. The coil is not protected at any current level in the case of the double-turns design, which is not shown in the figure. Halving the number of turns achieves a reduction of the hot-spot temperature of 50 to 100 K and maintains the hot-spot temperature below the maximum allowed value of 350 K [35].

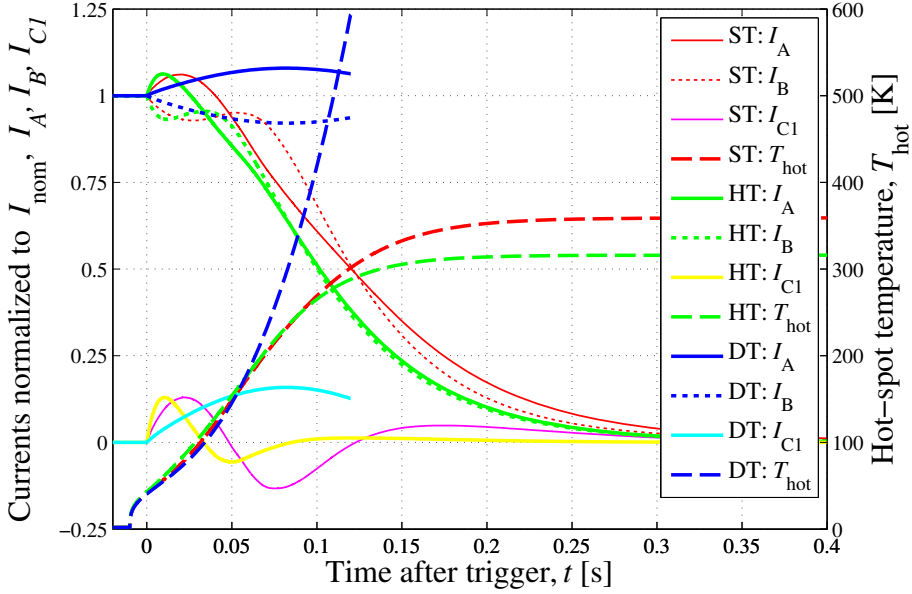


Figure 7.12. Comparison of CLIQ performance for three different designs of a 12 m long 11 T dipole magnet, after triggering a 500 V, 120 mF, 1-CLIQ system. Simulated currents  $I_A$ ,  $I_B$ , and  $I_{C1}$ , normalized to  $I_{\text{nom}}$ , and hot-spot temperature,  $T_{\text{hot}}$ , versus time.

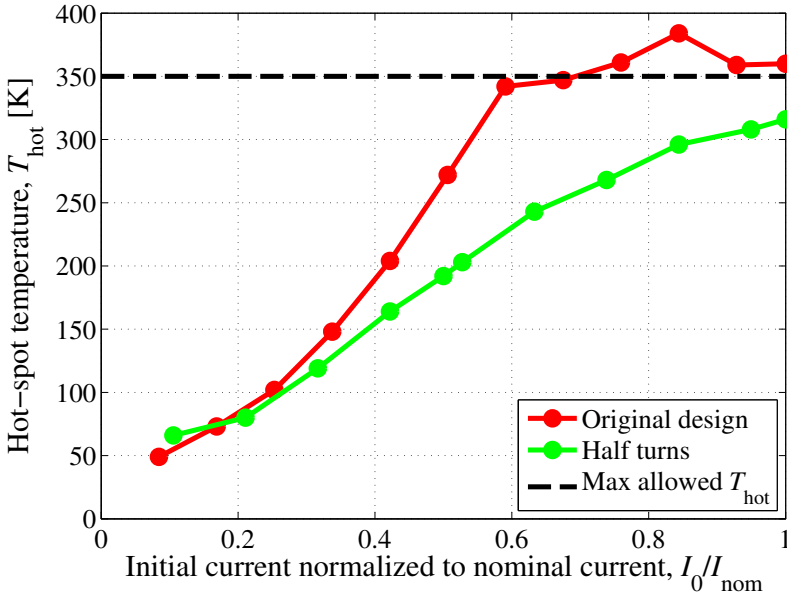


Figure 7.13. Comparison of CLIQ performance for two different designs of a 12 m long 11 T dipole magnet. Simulated hot-spot temperature,  $T_{\text{hot}}$ , after triggering a 500 V, 120 mF, 1-CLIQ system for various initial currents,  $I_0$ .



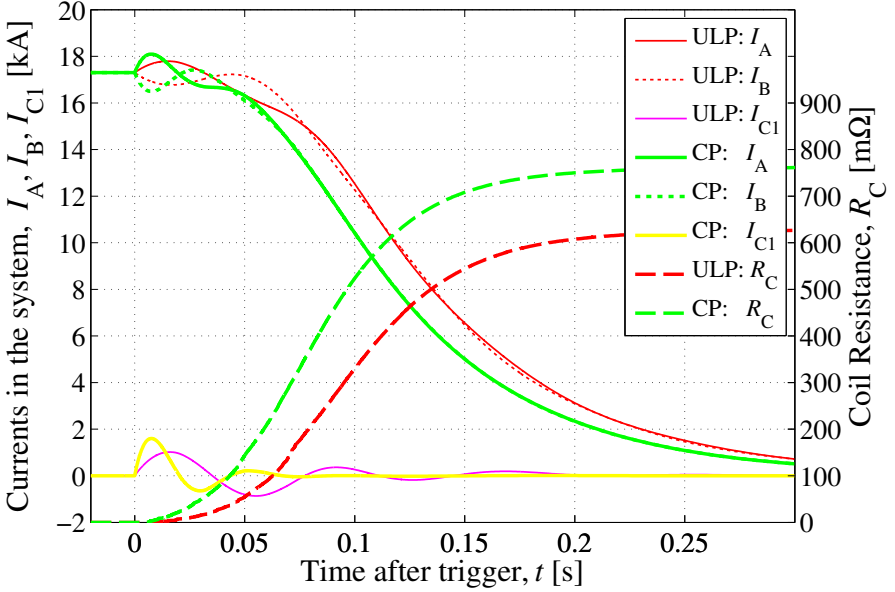


Figure 7.14. Quench protection of a 6.8 m long 12.2 T quadrupole magnet. Simulated currents and coil resistance versus time, for two different 2-CLIQ, 60 mF, 500 V configurations: Upper-Lower-Poles (ULP) and the Crossed-Poles (CP).

### 7.3.2 Electrical order of coil sections

In chapter 3, it was shown how the CLIQ effectiveness can be greatly enhanced by modifying the electrical order of coil sections, thus reducing the equivalent inductance of the discharge circuit and optimizing the generation of coupling loss in the coil cross-section. If implemented in the design phase, this significant improvement of CLIQ performance has usually very little impact on the coil manufacturing process nor on the magnet operational performance.

As an example, the comparison between the Upper-Lower-Poles and Crossed-Pole CLIQ configuration applied to a quadrupole magnet is presented here. Both configurations can be obtained by means of CLIQ terminals located between poles, as shown in figures 3.11a-f.

The simulated electro-thermal transients after triggering a 2-CLIQ system connected to the 12.2 T quadrupole magnet are shown in figure 7.14. As observed in table 3.5, the CLIQ equivalent inductance of the Crossed-Poles configuration is about 60% lower than the Upper-Lower-Poles. Accordingly, the frequency and the amplitude of the current introduced by the Crossed-Poles CLIQ system, roughly proportional to  $1/\sqrt{L'_{eq1}}$ , increase by about 60%. Furthermore, the CLIQ effectiveness of the Crossed-Poles configuration is two to three times higher than in the alternative design. Consequently, the temperature increase due to local coupling loss is faster and the coil is transferred to the normal state more quickly. The development of electrical resistance in the coil and hence the discharge of the magnet transport current occur

more rapidly. The energy stored in the magnet is distributed more uniformly in the coil turns due to the more homogeneous transition to the normal state. In conclusion, if no terminals are available between individual layers, the Crossed-Poles configuration is the best solution for the protection of high magnetic-field, high energy-density quadrupole magnets [89, 156].

### 7.3.3 Intra-layer terminals

Subdividing the coil into multiple sections and introducing opposite current-changes in coil sections physically adjacent are very effective methods to maximize performance. Increasing the number of sections reduces the equivalent CLIQ inductance and allows the implementation of Multi-CLIQ systems, increasing the peak deposited power per unit volume with the square of the number of coil sections, as described in 3.2. Moreover, additional flexibility in selecting the direction of the current-changes to introduce in multiple coil sections allows maximizing the CLIQ effectiveness, as detailed in section 3.3.

In particular, the addition of CLIQ terminals positioned between magnet layers is especially beneficial. This is very easily achieved in solenoids, but it usually requires some modification to the coil design in the case of multi-pole magnets. For instance, in figures 3.7b-c and 3.12a-b it is explained how to obtain high-performance Crossed-Layer and Layer-Layer CLIQ configurations on dipole and quadrupole magnets, respectively.

The comparison of the performance of the standard Pole-Pole configuration, relying only on one intra-pole CLIQ terminal, and of the optimized configurations relying on intra-layer terminals, in the case of the 11 T dipole magnet, is shown in figure 7.15. Due to the decreased inductance of the CLIQ discharge system, the current change introduced with the more optimized configurations roughly doubles with respect to the simpler Pole-Pole configuration. The faster development of coupling loss allows transferring the entire inner and outer layer to the normal state in about 10 and 40 ms, respectively. As a result, the hot-spot temperature can be significantly decreased from 260 K, obtained with the Pole-Pole configuration, to 210 and even 170 K with the Crossed-Layer and Layer-Layer configurations.

The performance of conventional quench heaters attached to the outer layer of this coil is much lower. Values in the range 10 to 30 ms for the transition of the first coil regions to the normal state were recently measured on the model magnet [80, 81], in good agreement with simulation predictions [71, 72]. The quench propagation from the outer to the inner layer of the coil required additional 30 to 50 ms [81].

### 7.3.4 Electrical and mechanical improvements

Secure and reliable installation of CLIQ terminals, as described in section 5.2.2, is one of the most effective improvements to the coil design and a key ingredient for a successful implementation of the CLIQ technology.

After triggering CLIQ and during the magnet discharge, high voltages are imposed across coil sections and fast development of electrical resistance in the normal zone occurs. Thus, an increase of the thickness of the insulation layers between coil sections

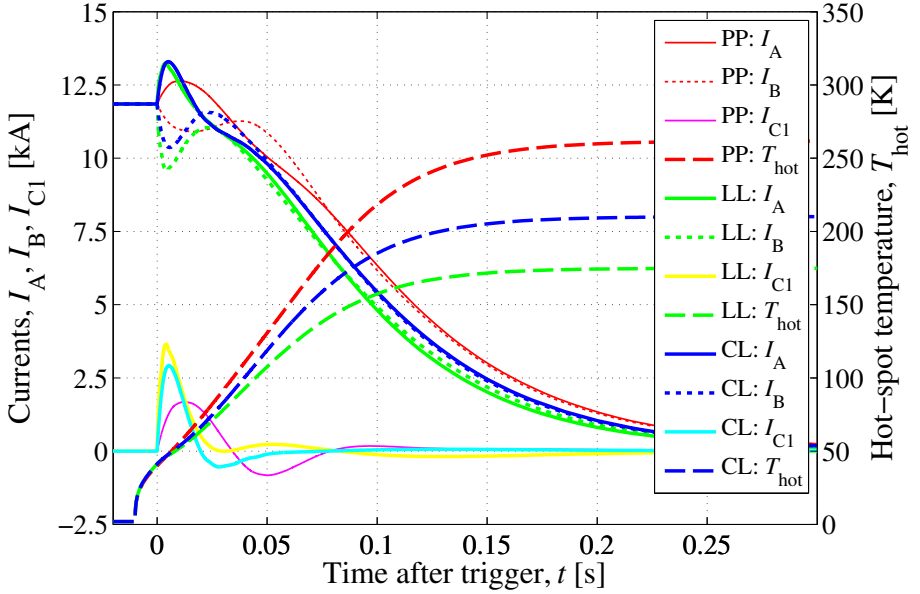


Figure 7.15. Quench protection of a 6 m long 11 T dipole magnet. Simulated currents and hot-spot temperature versus time, for three different 1-CLIQ, 60 mF, 500 V configurations: Pole-Pole (PP), Crossed-Layers (CL), and Layer-Layer (LL).

can be considered to reduce the risk of electrical breakdown and burn-throughs. Since CLIQ transient is mainly independent of the turn-to-turn normal zone propagation, this increase does not influence CLIQ's performance.

Complete electro-thermal simulations are mandatory to assess the voltage across turns, between poles, between layers, and from coil to ground [156]. Particular care is required when designing asymmetric CLIQ configurations, such as the Layer-Layer configuration, due to the delay in the transition to the normal state of the different coil sections, which can cause unbalanced distribution of the resistive and inductive voltage components.

## 7.4 High-temperature superconducting magnets

The possibility of protecting coils made of high-temperature superconductors with CLIQ is briefly mentioned here. Such coils are significantly more challenging to protect than when low-temperature superconductors, due to the very low normal-zone propagation velocity and high enthalpy margin to quench. In fact, when operated at temperatures in the range 1.9 to 4.5 K, high-temperature superconductors have a normal zone propagation velocity in the order of a centimeter per second, and an energy margin to quench one to two orders of magnitude higher than low-temperature superconductors. Thus, detecting the start of the quench with conventional voltage-based methods, and activating an effective quench protection

system, is particularly difficult.

An energy-extraction system can be implemented to quickly discharge the coil. However, due to the very slow normal-zone propagation velocity, the inhomogeneous distribution of inductive and resistive components over the conductor length can result in a highly non-uniform profile of the internal voltages and stress.

An active protection system based on heating of the conductor can homogeneously distribute the energy stored in the coil, hence avoiding hot-spot overheating and excessive internal voltages, but only if it quickly transfers a large fraction of the winding pack to the normal state, for which very high heating power is required.

High-temperature superconductors are characterized by quench margins in the range of a few to a few tens of  $\text{mJmm}^{-3}$ . Preliminary studies indicate that a CLIQ system could be designed to generate this amount of energy in a few tens of millisecond. The required increase of the power delivered to the coil, with respect to the case of low-temperature superconductors, can be achieved by applying multiple CLIQ units and increasing their charging voltage. Alternatively, a protection system based on one or various external excitation coils, as proposed in section 6.1.3, can be considered. However, thorough electro-thermal simulation and experimental qualification are required to draw a conclusion.

Various high-temperature superconductors are characterized by anisotropic critical current density when subject to magnetic field with direction perpendicular or parallel to the transport current. Magnet designs may be optimized to reduce the perpendicular component of the magnetic field on the high-temperature superconductor. However, CLIQ can utilize this anisotropy to reduce the critical current density, while simultaneously increasing the superconductor temperature due to the high coupling loss.

Also, the protection of hybrid coils composed of both low- and high-temperature superconductors [57, 58] is particularly challenging due to the magnetic interaction between coil sections and the presence of regions with very different margins to quench. These coils feature winding blocks powered in series but operating at different current densities. The addition of CLIQ terminals located between winding blocks is feasible, and allows a high flexibility in selecting optimized directions of the current changes introduced in the various blocks in order to maximize the developed coupling loss.

In conclusion, CLIQ-based systems protecting high-temperature superconductors are not out of reach, provided reliable quench detection systems are implemented. However, experimental results are required to confirm this statement.

## 7.5 Conclusion

Integrating CLIQ in the magnet design from the start can lead to better performing, safer, more compact, and more cost-effective magnets. Such CLIQ-optimized magnets will fully exploit the potential of CLIQ technology by implementing various modifications in the magnet design. Key design features of the coil geometry, superconductor, and CLIQ terminals are examined, and their impact on the magnetic performance and on the coil manufacturing process is assessed.

Including additional terminals, in particular between magnet layers, is the most

effective means to improve CLIQ performance, while causing hardly any influence on magnet stationary performance. Various examples are presented where the implementation of more optimized configurations, obtained by changing the electrical order of the coil sections or the positioning of the terminals, results in a very significant reduction of the hot-spot temperature.

The possibility of enhancing CLIQ performance by reducing the number of coil turns is also analyzed. Higher power deposition and faster transition to the normal state can be achieved due to the reduced equivalent inductance of the discharge circuit.

The filament twist-pitch and the RRR of the strand matrix are the most important conductor parameters affecting CLIQ behavior. The optimum ranges of these parameters have to be determined case by case. However, evidence shows that CLIQ performance is satisfactory over a wide range of strand/wire parameters.

CLIQ's faster energy-deposition mechanism allows designing magnets that can safely operate in a wider range of energy per unit volume than magnets protected by quench heaters. This can result in conductor designs featuring high fractions of superconductor, hence more compact and cost-effective magnets.

In summary, CLIQ provides future magnet designers a solution for a very effective, yet electrically robust, quench protection system, resulting in better magnet performance and lower electrical risk than possible with traditional magnet protection.



## Chapter 8

# CLIQ integrated in a chain of superconducting magnets

*The protection of a chain of superconducting magnets usually is considerably more challenging than the protection of stand-alone magnets. The increased energy stored in the circuit makes it more difficult to safely remove the circuit transport current. The electro-dynamics of a chain of superconducting magnets requires particular consideration due to the presence of distributed coil-to-ground parasitic capacitance, frequency-dependant impedance of the superconducting magnets, and the very low electrical resistance of the circuit.*

*It is demonstrated that CLIQ technology can be successfully applied to magnets, which are part of a chain, provided suitable by-pass elements are installed across each magnet.*

### 8.1 Protection of a chain of magnets

A collider like LHC relies on superconducting multi-pole magnets to bend and focus the particle beam in its trajectory. Magnets are often connected in series, hence forming a chain, to feed the same current to all magnets and to reduce the number of power converters and current leads required for operation. As the particle collision energy is proportional to the magnetic field generated by the collider's main dipole magnets, the case of a circuit composed of series-connected, high-field superconducting magnets is of significant interest.

The quench protection is particularly challenging due to the very high magnetic energy stored in the coils. A common design for the protection of a chain of  $N_M$  magnets is shown in figure 8.1. It includes active quench heaters (QH), by-pass diodes ( $D_1$ - $D_N$ ), and an energy-extraction system (EE). As shown in section 1.3.5, to assure protection against overheating of the coil's hot-spot, high energy-density

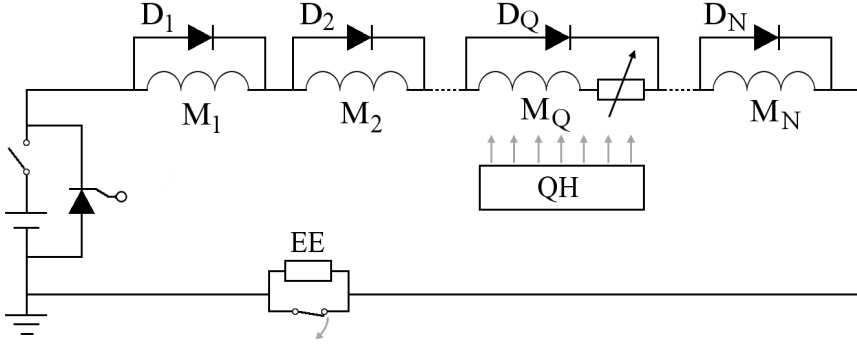


Figure 8.1. Electrical scheme of a chain of  $N_M$  superconducting magnets ( $M_1$ - $M_N$ ) protected by active quench heaters (QH), by-pass diodes ( $D_1$ - $D_N$ ), and an energy-extraction system (EE). In this example, only the active protection system of magnet  $M_Q$  is activated.

coils require systems capable of quickly detecting a quench and actively forcing a fast transition of a large coil fraction to the normal state. Upon the detection of a quench in a magnet  $M_Q$ , its protection system, conventionally based on quench heaters, is activated. In the case of a chain of superconducting magnets, additional by-pass diodes connected across each magnet are also required (section 1.3.2). They provide an alternative path for the circuit current after a coil is transferred to the normal state, thus avoiding the deposition of the stored magnetic energy of the entire chain in the quenched coil. Furthermore, to avoid overheating of the by-pass diode across the quenched magnet, an energy-extraction system is triggered for discharging the stored energy in an external resistor.

The electro-dynamics of a chain of superconducting magnets requires particular consideration due to the presence of distributed coil-to-ground parasitic capacitance, frequency-dependant impedance of the superconducting magnets, and the very low electrical resistance of the circuit. Any voltage transient occurring in a point of the circuit propagates along the chain as an electrical wave, as further explained in section 8.3.3.

Non-linear effects of wave reflection and superposition need to be considered. The impact of voltage transients routinely expected during normal operation, such as power supply switching-off and energy-extraction activation, has to be carefully studied to avoid excessive voltage peaks arising in any position along the chain. Also, the impact of travelling waves on the behavior of quench detection systems based on monitoring the voltage differences between coils, or between coil sections, has to be assessed, as propagating waves cause voltage differences between two coils or coil sections [111, 115].

## 8.2 Integration of CLIQ in the chain

The proposed scheme is shown in figure 8.2. The only modification to the quench protection design presented in the previous section is the implementation



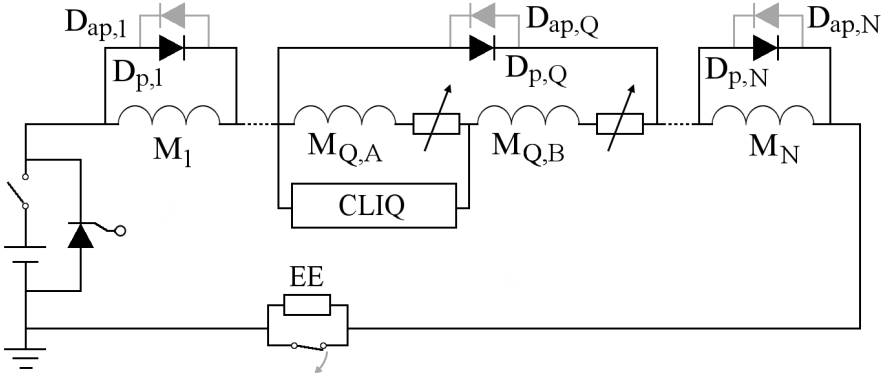


Figure 8.2. Schematic of a chain of  $N_M$  superconducting magnets ( $M_1$ - $M_N$ ) protected by CLIQ, by-pass diodes in parallel ( $D_{p,1}$ - $D_{p,N}$ ) and antiparallel ( $D_{ap,1}$ - $D_{ap,N}$ ), and an energy-extraction system (EE). Only the CLIQ system connected to magnet  $M_Q$  is shown.

of CLIQ instead of quench heaters and the presence of additional anti-parallel diodes ( $D_{ap,1}$ - $D_{ap,N}$ ) across each magnet protected by a CLIQ system. As later explained in section 8.3.5, the antiparallel diodes are required to provide a return path for the current introduced by CLIQ, hence avoiding the introduction of significant current changes in the other magnets of the chain. Since they only carry a short pulsed current, limited heat deposition is expected in these components.

In order to avoid conduction after activating the energy-extraction system, the opening voltage of the antiparallel diodes has to be sufficiently high. Consider a chain of  $N_M$  identical magnets operating at current  $I_0$  [A], connected in series to an energy-extraction system with resistance  $R_{EE}$  [ $\Omega$ ]. After activating the extraction system, a voltage  $-R_{EE}I_0/N_M$ , usually in the order of a few volt or tens of volt, develops across each magnet of the chain. An antiparallel-diode opening voltage higher than this value has to be selected to avoid damage. Alternatively, various diodes can be connected in series to obtain the required opening voltage.

## 8.3 CLIQ in the LHC chain of dipole magnets

The design of a CLIQ system protecting one magnet of an LHC chain of 154 dipole magnets is presented and discussed [108, 161].

### 8.3.1 LHC chain of dipole magnets

The LHC comprises eight octants, each featuring a chain of  $N_M=154$  superconducting twin-aperture dipole magnets [20–23, 108, 115, 154]. Each dipole magnet has a self-inductance  $L_M$  of 98 mH at nominal field, making the total self-inductance of each circuit 15.1 H with a total stored energy of 1.1 GJ at a nominal current of 11850 A.

The electrical scheme of one LHC chain of dipole magnets is shown in figure 8.3.

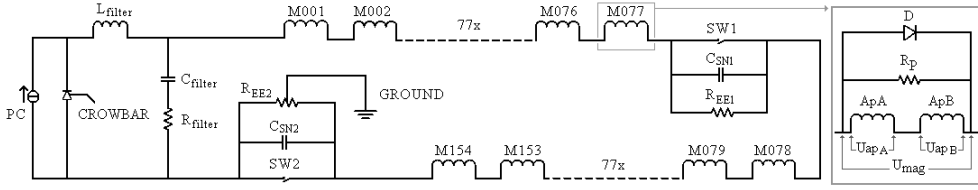


Figure 8.3. Electricla scheme of an LHC main dipole circuit comprising a chain of 154 magnets. Detailed schematic of one magnet of the chain.

The circuit is powered by a 13 kA power converter (PC), by-passed by a crowbar, which conducts the current when the power converter is switched off. At the output of the power converter an LC filter is present with nominal self-inductance  $L_{\text{filter}}=250 \mu\text{H}$  and capacitance  $C_{\text{filter}}=100 \text{ mF}$ , hence having a theoretical resonance frequency of  $f_{\text{filter}}=1/(2\pi\sqrt{L_{\text{filter}}C_{\text{filter}}})\approx 31.8 \text{ Hz}$ . After having measured a frequency of 28.5 Hz in each of the eight chains, the reference values of the filter self-inductance and capacitance are set to  $285 \mu\text{H}$  and  $110 \text{ mF}$ , respectively. The resistance of the capacitive branches of the filter  $R_{\text{filter}} [\Omega]$ , initially set to  $3.4 \text{ m}\Omega$ , was changed to  $10.1 \text{ m}\Omega$  in 2011 [115]. The protection of each magnet (M001-M154) in the case of a quench [52, 53] is ensured by two individual quench detection systems [162–164], cold by-pass diodes, and quench heaters [23, 66–69]. Two separate energy extraction units are present in order to quickly discharge the circuit and thus protect the by-pass diodes and the busbars [60–62]. Each unit is composed of redundant electro-mechanical switches (SW), a  $74 \text{ m}\Omega$  extraction resistor ( $R_{\text{EE}}$ ), and  $53 \text{ mF}$  snubber capacitors ( $C_{\text{SN}}$ ) in parallel [165]. In parallel to each dipole magnet, a  $100 \Omega$  resistor ( $R_{\text{P}}$ ) is present for smoothing transient voltage oscillations.

In the case of a quench detection or in the case of problems related to the power converter, the power converter is switched off and the two energy-extraction switches are opened. The current of the circuit is then forced to flow through the two extraction resistors and decays with a time constant of  $\tau_{\text{EE}}\approx N_{\text{M}}L_{\text{M}}/(2R_{\text{EE}})\approx 102 \text{ s}$ .

### 8.3.2 Electro-dynamic model of an LHC dipole magnet

Linear models are not sufficient for accurately analyzing and predicting the voltage transients occurring in a chain of superconducting magnets due to the presence of magnetization effects, coupling currents, eddy currents, and coil-to-ground parasitic capacitances, which make the magnet behavior not ideally inductive. The problem of modeling the frequency-dependent behavior of a superconducting magnet has been frequently faced in the past [111, 112, 117–119]. An equivalent lumped-element circuit, shown in figure 8.4, is developed in order to model the behavior of an LHC dipole magnet at different frequencies [111, 112, 118]. The model is composed of two coil

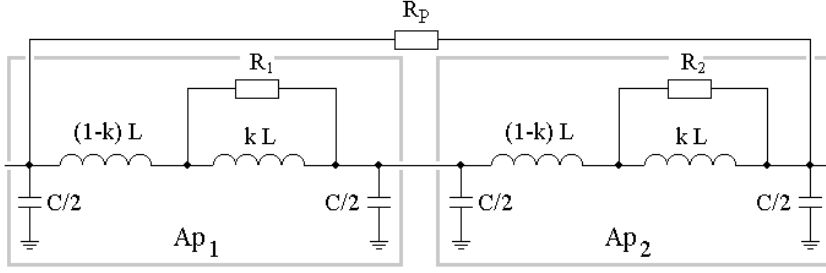


Figure 8.4. Electro-magnetic model of an LHC main dipole magnet.

apertures connected in series, whose equivalent impedance is

$$Z_a(s) = \frac{sL \left\{ 1 + \frac{s}{R_a/[k(1-k)L]} \right\}}{\left[ 1 + \frac{s}{R_a/(kL)} \right] \left[ 1 + R_a \frac{C}{4}s + (1-k)L \frac{C}{4}s^2 \right]}, \quad [\Omega] \quad (8.1)$$

for  $a=1,2$ , where  $s=\sigma+j\omega$  [ $s^{-1}$ ],  $L=49$  mH and  $C=150$  nF are physical properties representing the self-inductance of an aperture and its coil-to-ground parasitic capacitance, respectively, and  $k$  and  $R_a$  [ $\Omega$ ] are two parameters which model the effect of coupling currents induced in its superconductor. For most LHC main dipole magnets, a good correlation between experimental data and simulations is obtained for  $k=0.75$  and  $R_{1,2}=10$   $\Omega$ . However, the two apertures of about half of the LHC main dipole magnets have a different dynamic behavior. In this case the parameter  $R_a$  of one of the apertures is modified to a value in the range 7 to 10  $\Omega$ .

### 8.3.3 Electrical transients in the chain of dipole magnets

The chain of dipole magnets behaves as a transmission line composed of  $N_{ap}=2N_M$  elements representing the magnet apertures and their distributed coil-to-ground parasitic capacitances. The propagation of a wave along the chain, in time and space, is described by

$$U(t, n) = A \exp(-t/\tau) \cos \left( \omega_{chain} t - \sum_{i=1}^n \theta_i \right), \quad [V] \quad (8.2)$$

where  $A$  [V] is the wave amplitude,  $\tau$  [s] its decay time constant,  $\omega_{chain}$  [ $\text{rads}^{-1}$ ] its angular frequency,  $\theta_i$  [rad] the phase shift introduced by element  $i$ , and  $n$  its position along the chain. Each aperture introduces a different phase shift on the incoming wave. The wave phase velocity  $v_i=\omega_{chain}/\theta_i$  [ $s^{-1}$ ] is thus changing along the chain. Given the low resistance of the chain, any incoming voltage wave is slowly damped. When the oscillation period of the wave is comparable to the time needed to make a complete loop along the chain,  $t_{chain}=\sum_{i=1}^{N_{ap}} (\theta_i/\omega_{chain})$  [s], additional phenomena of reflection and superposition occur.

In order to analyze and reproduce these complex electrical transients, the electro-dynamic model presented in the previous section was developed. After validation under various operating conditions, it is now adopted as the standard tool for the simulation of electro-dynamic transients occurring in the eight LHC chains of dipole magnets [111, 112]. As an example, the electrical transient following a fast power abort occurring at a current of 2 kA and current-change of  $10 \text{ As}^{-1}$  is analyzed here. Note that the results shown in this section refer to the circuit configuration adopted during the first LHC run (2010-2013), when the resistances of both energy-extraction resistors were increased to  $148 \text{ m}\Omega$  [166].

The circuit dynamics following a fast power abort is characterized by three separate voltage transients, occurring at the switching-off of the power converter ( $t=0$ ), at the opening of the extraction switch SW1 in the middle of the chain ( $t=350 \text{ ms}$ ), and at the opening of the switch SW2 at the end of the chain ( $t=600 \text{ ms}$ ). The voltage waves generated at the output of the power converter and across the extraction switches propagate through the magnet chain and, as a consequence, the voltage across each magnet  $U_{\text{mag}}$  [V] undergoes three distinct transients.

When the power converter is switched off, the voltage at its output  $U_{\text{PC}}$  [V] starts oscillating with the filter resonance frequency. The amplitude of the oscillations is governed by the initial voltage  $U_{\text{PC}}(0) = R_{\text{circuit}} I_0 + N_{\text{M}} L_{\text{M}} dI/dt$ , with  $R_{\text{circuit}} \approx 1 \text{ m}\Omega$ , the resistance of the non-superconducting components of the circuit. This initial voltage strongly depends on the circuit current-change, and is about  $153 \text{ V}$  at  $2 \text{ kA}$  and  $10 \text{ As}^{-1}$ . The damping of the generated wave depends on the self-inductance and resistance of the branches of the power converter and its filter, and not on the characteristics of the dipole chain.

A comparison between the measured and simulated voltages across one selected magnet is shown in figure 8.5. For  $t < 0$ , the voltage drop across the magnet is purely inductive,  $U_{\text{mag}} = L_{\text{M}} dI/dt \approx 1 \text{ V}$ . At  $t=0$  the power converter is switched off and the magnet voltage oscillates with frequency  $f_{\text{filter}}$ .

The electrical transients following each switch opening are relatively smooth due to the presence of snubber capacitors across the extraction switches. After the opening of the first switch, the voltage over each magnet equals  $U_{\text{mag}} = -R_{\text{EE}} I_0 / N_{\text{M}} \approx -1.9 \text{ V}$ , since the voltage drop across the extraction resistor is divided equally across each magnet. Similarly, after the opening of the second switch,  $U_{\text{mag}} = -2R_{\text{EE}} I_0 / N_{\text{M}} \approx -3.8 \text{ V}$ . Comparison between the curves shown in figure 8.5 shows that measured and simulated transients are in good agreement.

The voltage wave generated at the output of the power converter influences each magnet differently, depending on its position and on its electro-dynamic behavior. The peak values of  $U_{\text{mag}}$  during the transient following the power converter switching-off ( $20 < t < 350 \text{ ms}$ ) are illustrated in figure 8.6. The asymmetric distribution of the peak values of the voltage across each magnet in the chain are caused by the propagation of the voltage wave during its first oscillation. Neglecting coupling-current effects in the coils, i.e.  $R_{\text{a}} \gg 1000 \text{ }\Omega$  in figure 8.4, the time needed for propagating through any magnet aperture is  $t_{\text{ap}} \approx \sqrt{LC} \approx 85 \text{ }\mu\text{s}$  [120]. Hence, the wave length, representing the number of apertures crossed in a wave period, is  $\lambda = 2\pi/\theta = 1/(f_{\text{filter}} t_{\text{ap}}) \approx 409$  apertures. Thus, the first  $\lambda - N_{\text{ap}} \approx 101$  apertures of the chain (M001-M050) experience a superposition of the wave and reach higher peak values of  $U_{\text{mag}}$ . Furthermore, the

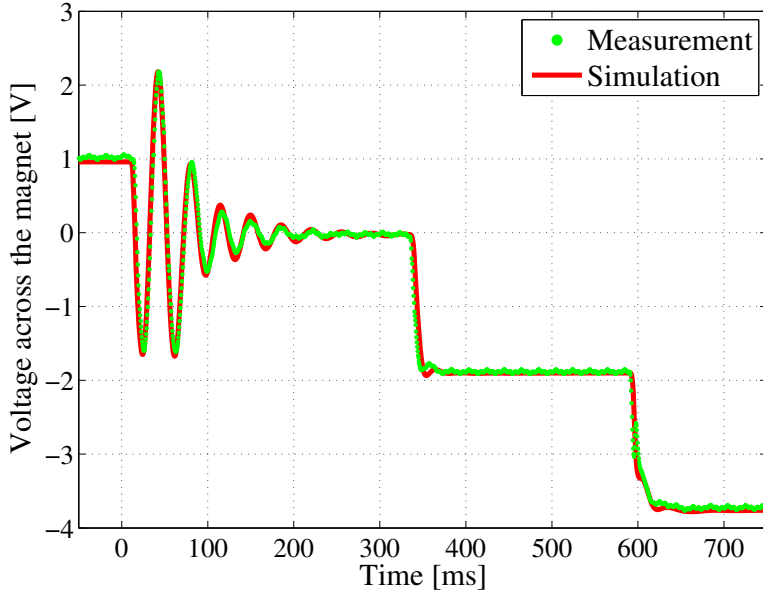


Figure 8.5. Fast power abort in the LHC chain of dipole magnets. Comparison between the measured and simulated voltages across magnet M026 versus time during the analyzed transient.

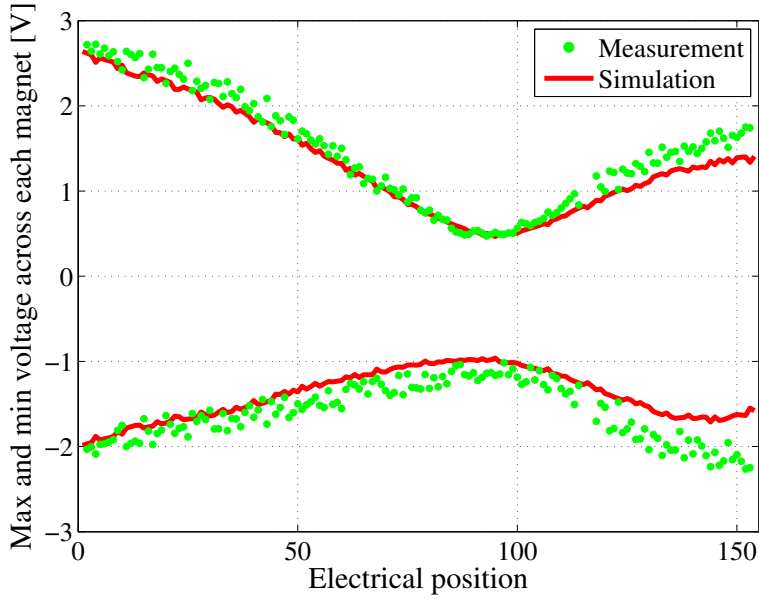


Figure 8.6. Comparison between the measured and simulated minimum and maximum voltages across each magnet versus electrical position during the transient following the power converter switching-off ( $20 < t < 350$  ms).

wave reaches its minimum after a semi-period, when it crosses the aperture numbered  $\lambda/2 \approx 204$  (M102).

Any wave propagating through the magnet chain is shifted by a different phase angle  $\theta_i$  [rad] by each aperture, depending on the frequency of the incoming wave and on the dynamic behavior of the aperture. The wave generated after the power converter switching-off is characterized by a fixed angular frequency  $\omega_{\text{filter}} = 2\pi f_{\text{filter}} \approx 179 \text{ rads}^{-1}$ . If the two apertures of a magnet have a similar impedance at the frequency  $\omega_{\text{filter}}$ , their voltage drops are similar. In this case, after a fast power abort, the voltage difference between apertures,  $\Delta U_{\text{ap}}$  [V], remains in the order of a few tens of millivolt due to the limited phase shift introduced on the incoming wave. On the contrary, in magnets with very different dynamic behavior in one aperture, the aperture voltage difference undergoes large oscillations. The behavior of such magnets is successfully simulated by setting  $R_1 \neq R_2$  in the model of their apertures [111]. The peak-peak values  $\Delta U_{\text{ap,max}} - \Delta U_{\text{ap,min}}$  [V] reached during the transient following the power converter switching-off ( $0 < t < 350 \text{ ms}$ ) are shown in figure 8.7. The distribution of magnets with  $R_1 \neq R_2$  is in very good agreement with the measured voltages using  $R_a$  of each aperture as a free parameter.

The model presented in this section can be used to reproduce unexpected events occurring during the operation of the LHC chain of dipole magnets and assess their impact on quench detection systems based on monitoring the voltage difference between two electrically adjacent magnets ( $\Delta U_{\text{mag}}$ ) or between two apertures of a magnet ( $\Delta U_{\text{ap}}$ ).

### 8.3.4 CLIQ configuration for the LHC main dipole magnet

The LHC main dipole magnet is composed of two identical 14 meter long, two-layer,  $\cos\theta$  dipole apertures, assembled in a common iron yoke structure and electrically connected in series [20–23, 108, 154]. Its coil cross-section and nominal magnetic field are shown in figure 8.8a. Since the joints between the poles and apertures are easily accessible at one coil end, three CLIQ leads can be attached to the coil conductor (figure 5.4), thus subdividing the coil into four sections. The electrical order of the poles of the two apertures, P1u, P1l, P2u, P2l, and of the CLIQ terminals T0, T1, T2, and T3 are schematically shown in figure 8.8b.

The presence of the iron yoke surrounding the apertures shields the magnetic effect of one aperture on the other and makes them weakly magnetically coupled. Thus, a system composed of a single CLIQ unit connected to terminals T0 at the side of the magnet and T2 between its apertures can be analyzed as a CLIQ system protecting a chain of two uncoupled magnets. As explained in section 3.3.7, this configuration is significantly less effective than alternative solutions which exploit the magnetic coupling between tightly-coupled coil sections. In fact, introducing opposite current changes in coil sections which are strongly coupled effectively reduces the equivalent inductance of the CLIQ discharge circuit,  $L_{\text{eq}}$  [H], and allows the development of regions where the magnetic-field changes generated by different coil sections superpose, and high coupling loss is developed.

An alternative design is a Pole-Pole configuration analogous to the one proposed in section 3.3.2. A 2-CLIQ Pole-Pole configuration can be obtained by connecting

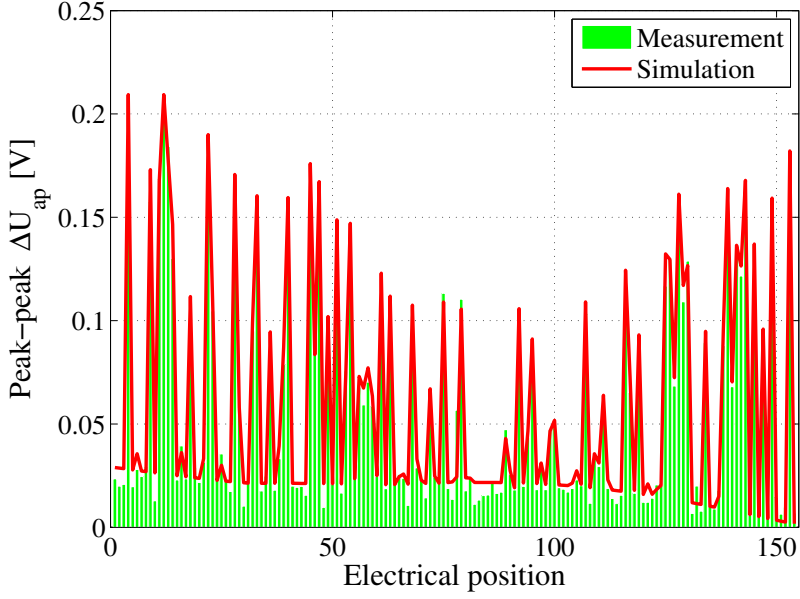


Figure 8.7. Comparison between the measured and simulated peak-peak values  $\Delta U_{\text{ap,max}} - \Delta U_{\text{ap,min}}$  for each magnet in the chain versus electrical position during the transient following the power converter switching-off ( $0 < t < 350$  ms).

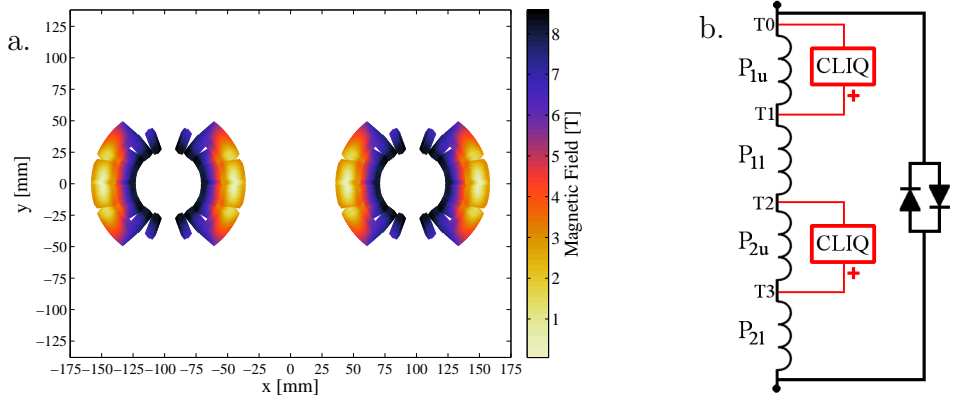


Figure 8.8. CLIQ connected to an LHC main dipole magnet. a. Magnetic field distribution ( $I_0=11.85$  kA). b. Electrical connection to obtain a 2-CLIQ Pole-Pole configuration.

two CLIQ units to the coil terminals as shown in figure 8.8b.

The selected opening voltages of the parallel and antiparallel by-pass diodes are 6 and 20 V, respectively. The former is identical to the value of the parallel diodes presently installed in the LHC chain of dipole magnets. The latter is safely above the limit  $|2R_{EE}I_0/N_M| \approx 11$  V indicated in section 8.2.

### 8.3.5 Simulation of a CLIQ in the LHC chain of dipole magnets

The electro-magnetic and thermal transients occurring in one magnet and the electro-dynamic transients occurring in the entire circuit during and after a CLIQ discharge are simulated with a model that couples the equivalent lumped-element network of a magnet, developed with the LEDET method described in chapter 4, with the transmission line model presented in section 8.3.2 [111]. The interaction between the voltage transient introduced after triggering CLIQ and the voltage waves generated at the output of the power supply or across the energy-extraction system is studied under various operating conditions.

The case is presented of a CLIQ discharge triggered on magnet M039, roughly equidistant from the power supply and the energy-extraction unit in the middle of the chain. In order to assess the impact of the transient caused by CLIQ on the magnets of the chain, it is considered here that CLIQ is activated well after the power converter switching off and triggering of the energy extraction switches.

The simulated currents flowing in the system are shown in figure 8.9. At  $t=0$ , a 2-CLIQ, 60 mF, 600 V system is activated and a 2.4 kA, 13 Hz current  $I_{C1}$  [A] is introduced by each of the two CLIQ units connected to the coil. During the first current pulse, about half of the current introduced, corresponding to  $I_{Dap}=I_A-I_0$ , flows through the antiparallel diode. The oscillations of the currents flowing in the coil sections  $I_A$  [A] and  $I_B$  [A] are sufficient to generate high inter-filament coupling loss in the superconductor and transfer to the normal state a large fraction of the winding pack in a few tens of millisecond. The electrical resistance of the coil's normal zone develops a high resistive voltage. As the voltage across the magnet cannot increase above the parallel-diode opening voltage of 6 V, a high negative inductive voltage is generated in the magnet, i.e. its current is rapidly discharged. The current flowing in the rest of the chain  $I_{chain}$  [A] is discharged with a much longer time constant,  $\tau_{EE} \approx 102$  s, as explained in section 8.3.1. Thus, an increasing fraction of current is diverted to the parallel diode. About one second after triggering CLIQ, the current flowing through the quenched magnet is roughly zero, and the circuit current is completely transferred to the parallel diode, i.e.  $I_{Dp} \approx I_{chain}$ .

The simulated hot-spot temperature as a function of the initial transport current is reported in figure 8.10 for values of a CLIQ charging voltage in the range 400 to 1000 V. A CLIQ system charged at 400 V is clearly not suitable to protect this full-scale coil, and a system charged at 500 V can barely maintain the hot-spot temperature around the risky value of 350 K. A significant improvement is achieved, though, for a charging voltage of 600 V, which assures a maximum hot-spot temperature of about 250 K over the entire range of operating current. An increase of the CLIQ charging voltage up to 1 kV allows a further reduction of the hot-spot temperature to some 180 K.



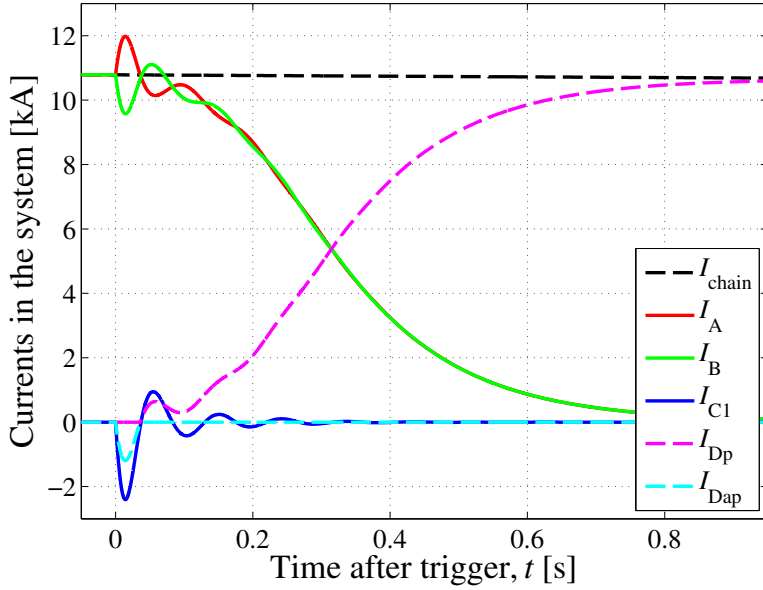


Figure 8.9. Quench protection of an LHC main dipole magnet when part of a chain of 154 magnets. Simulated currents in the main circuit, in the two coil sections, in the CLIQ leads, and in the by-pass diodes, versus time, after triggering a 2-CLIQ, 60 mF, 600 V system.

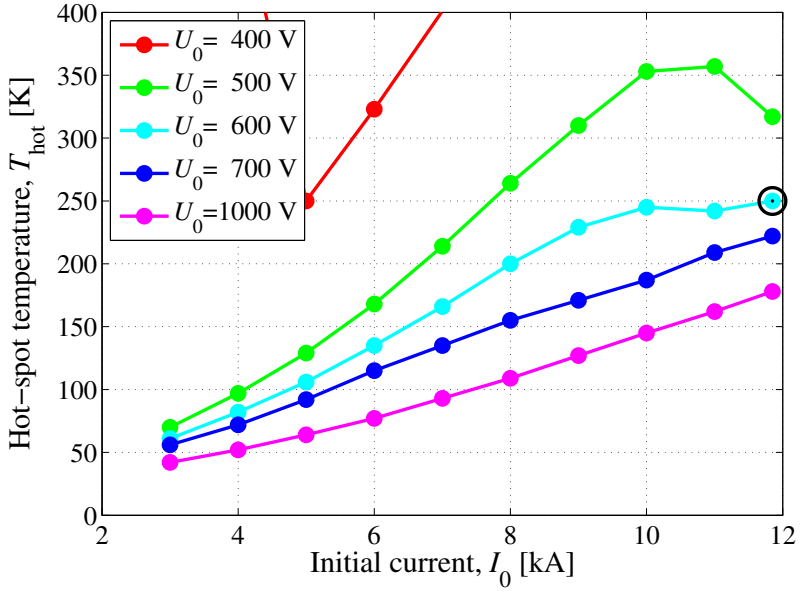


Figure 8.10. Simulated temperature reached in the coil hot-spot versus initial current, for varying CLIQ initial charging voltage  $U_0$ , after triggering a 2-CLIQ 60 mF system. The point circled in black refers to the same simulation shown in figure 8.9.

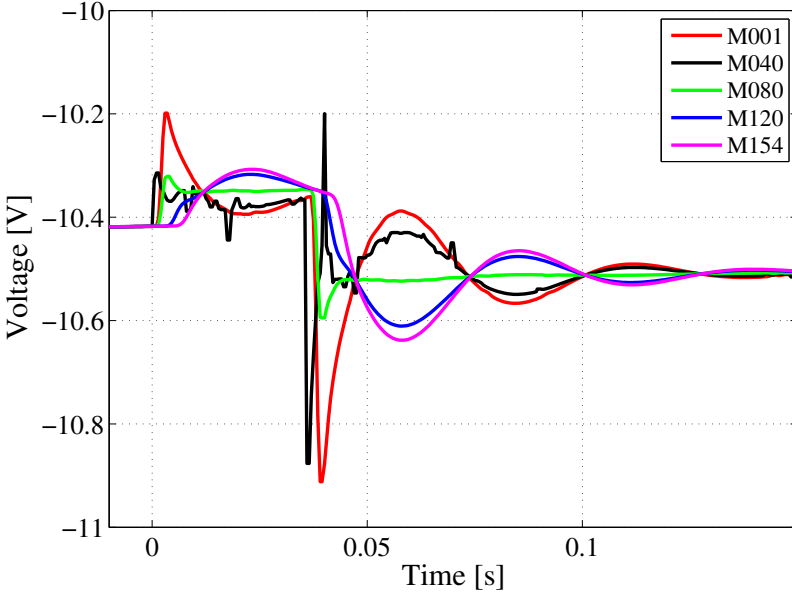


Figure 8.11. Quench protection of an LHC main dipole magnet when part of a chain of 154 magnets. Simulated voltage across five selected magnets just after triggering the CLIQ unit connected to magnet M039.

Triggering a CLIQ system connected to one magnet of the chain develops a voltage wave which propagates through the circuit. Assessing the impact of this wave on the circuit behavior and on the quench detection system is mandatory. The simulated voltages across five selected magnets in different positions of the chain after triggering CLIQ, for the case analyzed in this section, are shown in figure 8.11. The electrical perturbations introduced across the magnets of the chain have a maximum peak of a few hundred millivolt, significantly lower than the transients caused by switching-off the power converter or opening an energy-extraction switch. The voltage difference between apertures are thus small as compared to the quench detection threshold of 100 mV.

This result can be easily understood when realizing that the amplitude of any electrical wave generated across a magnet is limited by the presence of the back-to-back by-pass diodes. In the present example, according to the diode opening voltages indicated in section 8.3.4,  $-20 \text{ V} \leq U_{\text{mag}} \leq 6 \text{ V}$ , and hence the maximum amplitude of a wave generated across a magnet is 26 V. This value is significantly smaller than the initial voltage across the power converter of up to 165 V, or across an extraction switch, up to 800 V. Accordingly, the perturbations generated after a CLIQ discharge are about one order of magnitude smaller than after the power converter switching-off and the switch openings.

In conclusion, the integration of a CLIQ-based protection system in the LHC chain of dipole magnets shows good performance in terms of maximum hot-spot temperature reached in the coil after a quench, and not significantly interferes with the quench

detection system.

## 8.4 CLIQ in a chain of 16 T dipole magnets

Various studies have been carried out aimed at designing particle accelerators achieving collision energies significantly beyond the LHC [167–171]. In particular, CERN launched a Future Circular Collider (FCC) study aiming at a 100 TeV collision energy using 16 T dipole magnets [56–58, 172].

Nb<sub>3</sub>Sn magnets are currently selected as the baseline technology, and one of the proposed designs features the block-coil geometry presented in section 3.3.4 [135–144, 173]. This coil generates a dipole magnetic field  $B_d=16$  T with a transport current of about 18.6 kA.

Coil protection is crucial while designing this new generation of superconducting magnets [143]. A CLIQ-based quench protection system, integrated in the circuit as described in section 8.2, is an excellent choice for protecting these coils. Its performance is here analyzed in the case of a 14 meter long magnet. Note that the performance of a 1-CLIQ system on one magnet aperture can be extended to a 2-CLIQ system protecting two identical apertures, with a design analogous to that shown in the previous section. In all presented simulations, it is assumed that CLIQ is triggered 10 ms after the start of the quench. The same superconductor as used in the series of short model magnets at LBNL is considered [143, 174]. The superconducting cable is composed of 51 Ta-alloyed 54/61 Nb<sub>3</sub>Sn strands with a diameter of 0.8 mm and a copper fraction of 45%. Its filament twist-pitch is 14 mm and the RRR of the wire is 287.

Among the three CLIQ configurations for the block-coil geometry proposed in section 3.3.4, the easiest one to implement is the Pole-Pole configuration, since it relies only on one CLIQ terminal positioned between the two poles. However, this configuration is not effective enough to assure the protection of this high energy-density large-scale coil. The simulated coil hot-spot temperature, as a function of the initial transport current, is shown in figure 8.12 for three 1-CLIQ Pole-Pole configurations featuring different combinations of capacitance and charging voltage of the CLIQ capacitor bank. The results clearly show that a CLIQ charging voltage of 2 kV is needed to maintain the hot-spot temperature below 350 K at the operating current.

The CLIQ performance can be significantly improved by adopting either the Crossed-Layers or the Layer-Layer configurations introduced in section 3.3.4. The hot-spot temperature can be reduced by 40 to 100 K in the current range 10 to 20 kA, as shown in figure 8.13. Since these CLIQ configurations feature a unit connected to two terminals internal to the coil, the maximum voltage to ground just after triggering is half of the CLIQ charging voltage, instead of the full charging voltage, as in the case of the Pole-Pole configuration (figure 3.7).

The simulated transient during and after the CLIQ discharge at a current of 19 kA, for the three analyzed CLIQ configurations, is shown in figure 8.14. The significant enhancement of the current change introduced by the more optimized Crossed-Layer and Layer-Layer configurations is a result of the decreased equivalent inductance of the

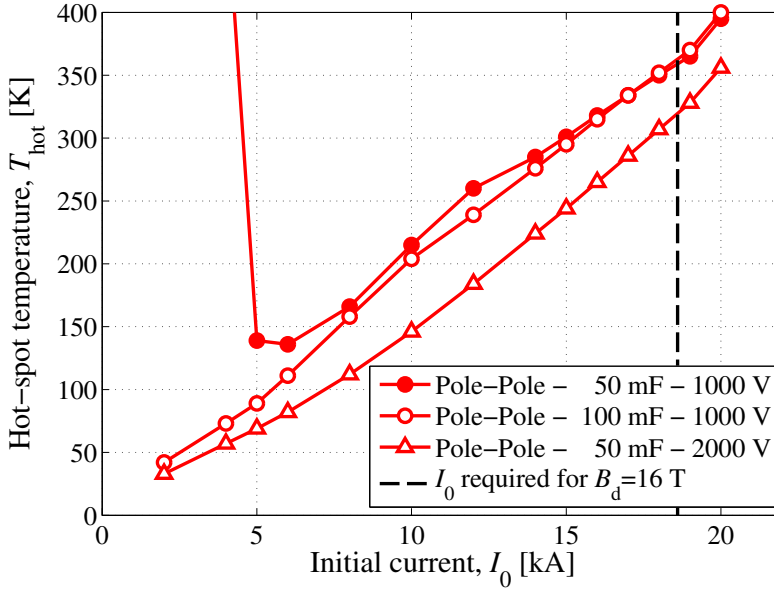


Figure 8.12. Quench protection of a Nb<sub>3</sub>Sn, 16 T block-coil dipole magnet. Simulated temperature reached in the coil hot-spot versus initial current, for a Pole-Pole 1-CLIQ configuration with varying capacitance and charging voltage of its capacitor bank.

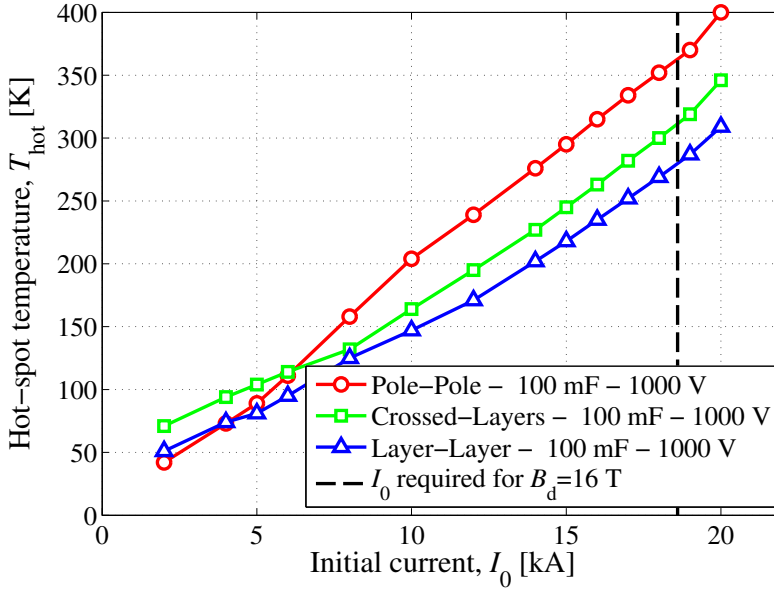


Figure 8.13. Quench protection of a Nb<sub>3</sub>Sn, 16 T block-coil dipole magnet. Simulated temperature reached in the coil hot-spot versus initial current, for three different 1-CLIQ, 100 mF, 1 kV configurations. Nominal current is 18.6 kA.

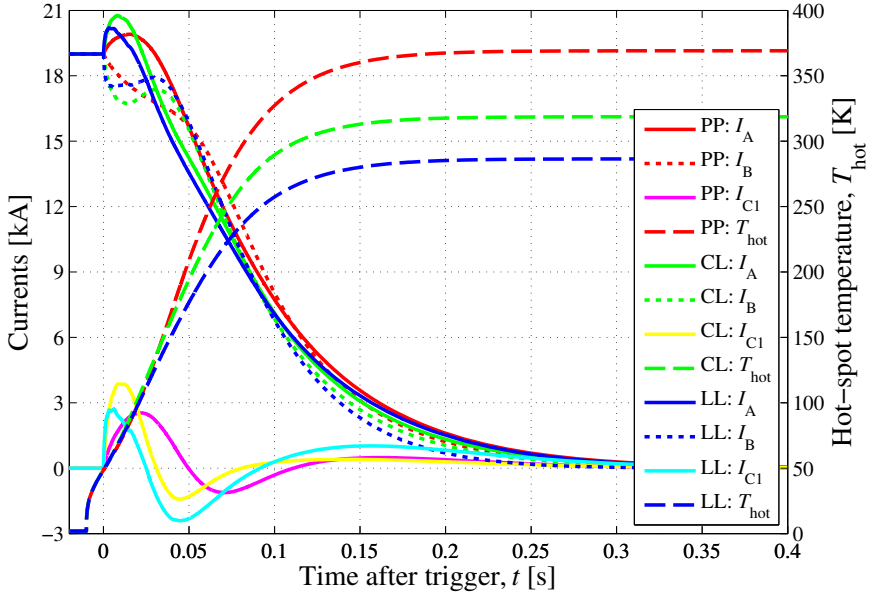


Figure 8.14. Quench protection of a  $\text{Nb}_3\text{Sn}$ , 16 T block-coil dipole magnet. Simulated currents and hot-spot temperature versus time, for three different 1-CLIQ, 100 mF, 1 kV configurations: Pole-Pole (PP), Crossed-Layers (CL), and Layer-Layer (LL). Nominal current is 18.6 kA.

discharge circuit, which was presented in table 3.6. The more optimized distribution of generated coupling loss in the coil cross-section achieved with the Layer-Layer configuration allows maintaining the hot-spot temperature to some 270 K.

Finally, an alternative design of a 16 T block-coil dipole magnet, based on a graded coil, is preliminarily considered [143]. Following this approach, a non-uniform current density is obtained in the coil cross-section by modifying the strand and cable design in various series-connected coil sections. The resulting non-uniform current density is optimized as a function of the magnetic field to achieve a more homogeneous critical current density, and therefore enhance the peak magnetic field generated by the coil at a given current.

One of the difficulties related to the implementation of this advanced design is the coil quench protection, due to the increased coil self-inductance and higher current density in the outer, lower magnetic-field region of the coil. Nevertheless, the very implementation of this design can result in a major improvement of the performance of a CLIQ-based protection system. In fact, the subdivision of the coil into multiple sections and the easy addition of various CLIQ terminals between them can be exploited to design highly effective CLIQ configurations, which reduce the CLIQ equivalent inductance and optimize the power deposition in the strands [144].

## 8.5 Conclusion

A CLIQ-based quench protection system can be applied not only on a stand-alone magnet, but also in a chain of superconducting magnets. This requires the installation of back-to-back by-pass diodes across each magnet. CLIQ can be implemented either on all magnets of the chain, as the main quench protection system; or on one or more magnets of the chain, as a cost- and time-effective repair solution for coils with failing quench heaters.

The analysis of the voltage wave generated after triggering CLIQ and propagating along the circuit has to be included in the design studies. This study can be efficiently carried out by means of an equivalent electro-dynamic model of the chain, provided information about the frequency transfer function of the magnets is available.

As a case study, the integration of CLIQ in the LHC chain of dipole magnets is presented. The proposed CLIQ design keeps the coil hot-spot temperature below safe limits over the entire range of operating currents, and is compatible with the present quench detection system. In fact, the perturbations introduced across the other magnets of the chain by triggering a CLIQ unit connected to one LHC main dipole magnet show a peak of a few hundred millivolt, which is about an order of magnitude lower than the transients following the power converter switching-off or the switch openings.

To summarize, a CLIQ-based solution for the quench protection system of the LHC chain of dipole magnets is analyzed, and is ready to be implemented. The advantages in terms of electrical robustness and energy-deposition velocity make CLIQ the first choice as the quench protection system of the next generation of high magnetic-field accelerator magnet chains.

## Chapter 9

# Conclusion

*In this thesis CLIQ, the Coupling-Loss Induced Quench protection system, is characterized and its effectiveness in protecting existing and future superconducting magnets is demonstrated. The CLIQ technology provides the superconducting magnet community with a new solution for an effective and reliable coil protection in the case of a quench. The first experimental campaigns allowed an extensive study of the CLIQ method and convincingly showed its applicability to large-scale magnets. Clear strategies to optimize its performance for various magnet geometries, operating conditions, and system parameters are outlined.*

## CLIQ

The constant pursuit of higher magnetic performance reaching higher magnetic field and higher current density calls for an equivalent effort in developing effective protection systems capable of quickly and reliably discharging the energy stored in the magnet. This can be obtained by forcing a fast and homogeneous transition to the normal state of the coil, thus distributing more uniformly the energy in the winding pack and developing a high electrical resistance in the normal zone, which rapidly discharges the magnet transport current.

CLIQ's mechanism to transfer the coil to the normal state relies on actively heating the superconductor by means of coupling loss generated in the conductor itself, hence inside its insulation layer. This intra-wire heating process is by principle much faster than the thermal diffusion across insulation layers upon which the alternative quench-heater technology relies. Furthermore, a CLIQ system is built with simple and robust electrical elements operating at room temperature and is only connected to the coil in a limited number of positions. This makes CLIQ inherently less prone to electrical breakdown with respect to conventional quench heaters, and virtually not interfering with the coil manufacturing process. In addition, its relatively easy implementation and wide range of applicability make it possible to install CLIQ as a cost- and time-effective back-up device for magnets with failing protection systems.

CLIQ generates transitory loss in the superconductor by generating an oscillating magnetic field in the strands. This is achieved by discharging the energy stored in a

capacitor bank through multiple terminals connected to different points of the coil, hence introducing oscillating currents in the different coil sections.

The introduced current oscillates at a frequency depending on the self- and mutual inductances of the coil sections, the positioning of the CLIQ terminals, and the capacitance of the capacitor bank; in most cases, this frequency is in the range of 10 to 100 Hz. Inter-filament coupling loss is the most reliable and effective mechanism to generate transitory loss in most practical superconductors by introducing a magnetic-field change in this frequency range. Superconducting magnets designed for AC applications, hence made of a superconductor with high resistivity of the strand matrix, are more challenging to protect with CLIQ.

The study of the electro-magnetic and thermal transient during and after a CLIQ discharge allows identifying the key ingredients determining the performance, subdivided into conductor properties, magnet operating conditions, CLIQ parameters, and configuration of the CLIQ discharge circuit. Since CLIQ primarily relies on inter-filament coupling loss, its performance is virtually independent of the cable properties, but influenced by the wire or strand characteristics, namely the filament twist-pitch and the effective transverse resistivity of the matrix, depending on its RRR and magneto-resistivity. For a given magnet and CLIQ system, ranges of filament twist-pitch and RRR can be identified, resulting in a good performance. For a typical superconductor with copper matrix, a filament twist-pitch of 10 to 30 mm and a RRR higher than 50 give good results; however, even wider ranges are acceptable if other system parameters are modified.

A reliable protection system has to assure the magnet's protection under any operating condition. At high current levels, the energy density in the conductor is high, hence a fast and homogeneous transition to the normal state has to be achieved in order to maintain the temperature of the conductor hot-spot below a safe limit. In this condition, the peak deposited power density is of the essence. At low current levels, the velocity of the heating process is less important, but the energy required to initiate a transition to the normal state is significantly higher, hence the total energy delivered to the coil is the most important parameter. These considerations lead to two main requirements for a CLIQ system composed of  $N_C$  units with capacitor banks of capacitance  $C$  [F] charged at a voltage of  $U_0$  [V], and connected to a given coil with length  $l_m$  [m]:

- to assure protection at high current, the peak power density delivered by CLIQ,  $P'''_{\text{if,peak}} \propto (N_C U_0 / l_m)^2$  [Wm<sup>-3</sup>], needs to be sufficient;
- to assure protection at low current, the total deposited energy per unit volume of conductor,  $E'''_{\text{CLIQ}} \propto N_C C U_0^2 / l_m$  [Jm<sup>-3</sup>], needs to be sufficient.

Both, the total energy and the power per unit volume delivered by a CLIQ system, are proportional to the square of its charging voltage, which is limited for safety and risk-reducing reasons, and on the square of the number of units that are installed across separate coil sections. The capacitance of the CLIQ capacitor bank does not influence the peak power density, but the total delivered energy is proportional to it. In some cases increasing the CLIQ capacitance can improve the system performance without the need of increasing the maximum voltage to ground.



---

The installation and operation of a CLIQ-based protection system present various aspects which need to be carefully considered during its design. Firstly, the oscillations of the magnet transport current provoked by CLIQ propagate to the main circuit, hence appropriate protection elements have to be installed across circuit elements. Secondly, relatively high voltages to ground and between coil sections are introduced in locations where they are otherwise not present, hence an increase of the thickness of the insulation or an improvement of its quality may be needed. Finally, pulsed mechanical stresses caused by the unbalanced oscillating currents in the different coil sections have to be analyzed case by case. However, they usually are of limited entity as compared to the overall mechanical stress due to the magnetic field of the coil.

## CLIQ effectiveness, $\Psi$

For a given coil and superconductor, and for fixed capacitance and charging voltage of the CLIQ capacitor bank, the positioning of the CLIQ terminals and the electrical order of the coil sections can be optimized in order to achieve a significant improvement of the system performance in terms of peak deposited power density.

A parameter  $\Psi$  [ $\text{m}^{-1}$ ], called CLIQ effectiveness, is defined to determine the peak applied magnetic-field change that can be introduced in the strands by a certain CLIQ configuration, per unit of charging voltage and of coil length. Since the inter-filament coupling loss generated in the strands is proportional to the square of the introduced magnetic-field change, the peak power density deposited by CLIQ is proportional to the square of the CLIQ effectiveness,  $P'''_{\text{if,peak}} \propto (\Psi U_0 / l_m)^2$ .

For all magnets, two golden rules are to be followed while designing a CLIQ-based protection system:

- subdivide the coil into multiple sections;
- introduce current changes with opposite polarities in coil sections which are physically adjacent.

In fact, both measures have a threefold beneficial effect on the CLIQ performance. Firstly, they increase the mutual coupling between coil sections, which leads to a significant reduction of the equivalent inductance of the CLIQ discharge system, thus allowing a higher current-change to be introduced in the coil sections. Secondly, they achieve an effective superposition of the magnetic-field changes generated by different coil sections. Finally, they optimize the power distribution in the coil cross-section.

## LEDET model

Given the numerous multi-domain, interdependent, non-linear effects occurring in a superconducting magnet during a CLIQ discharge, a simulation tool capable of correctly reproducing and predicting coupled electro-magnetic and thermal transients is essential in order to implement a CLIQ protection system on a magnet.

Thus, a new technique for modeling the behavior of a superconducting magnet, called LEDET (Lumped-Element Dynamic Electro-Thermal), has been developed,

based on various coupled networks of lumped-elements. The LEDET model includes non-linear dynamic effects such as the dependence of the magnet differential self-inductance on the presence of inter-filament and inter-strand coupling currents in the conductor. This effect is usually not taken into account in existing models because superconducting magnets are primarily operated in quasi-stationary or low ramp-rate conditions. However, it has often significant impact on the magnet performance, particularly when the magnet is subject to fast current changes.

## Protection of existing magnets

CLIQ can be successfully implemented for the protection of superconducting magnets of different geometry (quadrupole, dipole, solenoid), type of superconductor (Nb-Ti, Nb<sub>3</sub>Sn), and size (from small laboratory magnets to full-scale magnets). Experimental results convincingly demonstrated the effectiveness of the method and validated the behavior predicted by the LEDET model.

Simulations show that CLIQ can be applied to most existing magnets, provided one or multiple terminals can be connected somewhere in between the main current leads. CLIQ allows energy depositions as fast as or even faster than conventional quench heaters, but offers a significantly more robust electrical design and easier installation and repair.

Preliminary analyses, including studies of system redundancy and integration of CLIQ in chains of superconducting magnets, are carried out for the design of CLIQ-based repair solutions for various LHC magnets. The aim of the analyses is to assure the availability of a back-up option for repair of quench-heater based protection systems in the case of quench-heater failure. A CLIQ-based solution is less expensive and faster than magnet repair or replacement.

## CLIQ using an external excitation coil

A CLIQ variant based on using an external excitation coil strongly coupled with the main coil is another effective solution for the protection of superconducting magnets. Although less effective than a standard CLIQ, this system has the definite advantage of being galvanically separated from the coil to protect. As a result, the protection system can operate with higher charging voltage, and introducing larger oscillating currents, without the risk of electrical breakdown of the conductor insulation.

First experiments conducted on a small-scale solenoid show the validity of this method. Various improvements to the design of an optimized CLIQ excitation-coil are proposed, including the simultaneous increase of the CLIQ charging voltage and thickness of the insulation layer between excitation and main coil, and the optimization of the excitation-coil geometry to concentrate the power deposition in well-distributed separate regions, resulting in effective inductive heating stations.

A high-voltage CLIQ system based on applying an excitation coil seems a promising solution for the protection of coils operated with large temperature margin, such as high-temperature superconductor coils.

---

## Protection of future magnets

CLIQ is successfully implemented on various existing magnets, not specifically designed to optimize its performance. However, its integration in the magnet design can result in a significant improvement of the magnet protection in terms of even lower hot-spot temperature and safer electrical design. Furthermore, the enhanced protection offered by CLIQ allows safe magnet operation at higher coil energy densities without the need of decreasing the superconductor current density. In turn, this results in magnets reaching a higher operating magnetic field, or in coils of reduced size and cost.

A list of key magnet design modifications is outlined, together with their corresponding benefit on CLIQ performance and impact on the magnet performance and operation. Proposed measures include increasing the number of CLIQ terminals, modifying the electrical order of coil sections, redesigning the coil windings, and optimizing the filament twist-pitch and effective transverse resistivity of the strand matrix.

## Outlook

CLIQ technology has rapidly reached maturity and may cause a drastic change in the design and protection of superconducting magnets. It offers future magnet designers a means to quickly and homogeneously transfer a superconducting coil to the normal state with very low risk of electrical failures.

Validated simulation tools are available to assess the impact of different system parameters, assist the design of CLIQ-based protection systems, and reliably predict the performance of alternative CLIQ configurations.

Given the novelty of the concept and its potential, many opportunities for R&D activities are present for the near future, including

- studying the application of CLIQ to high-temperature superconducting magnets;
- designing CLIQ-based protection systems for the protection of 20 T class superconducting magnets;
- fully characterizing the variant of the CLIQ method based on an external excitation coil;
- designing low-voltage ( $U_0 < 50$  V) CLIQ-based protection systems for magnetic resonance imaging and laboratory magnets.

Thanks to its advantages, CLIQ has proven to be a very powerful quench protection system for most of the high-field superconducting magnets.



# References

- [1] M.N. Wilson, *Superconductivity and accelerators: the good companions*, IEEE Transactions on Applied Superconductivity, vol. 9, no. 2, June 1999, doi: 10.1109/77.783250.
- [2] L. Rossi, *Superconductivity: its role, its success and its setbacks in the Large Hadron Collider of CERN*, Superconductor Science and Technology, 2014, Vol. 23 (3), 034001, doi: 10.1088/0953-2048/23/3/034001.
- [3] M.N. Wilson, *Superconducting Magnets*, Oxford University Press, Oxford, ISBN 0-019-854805-2, 1983.
- [4] M.S. Lubell, *Empirical scaling formulas for critical current and critical field for commercial NbTi*, IEEE Transactions on Magnetics, vol. 19, no. 3, May 1983, doi: 10.1109/TMAG.1983.1062311.
- [5] M.A. Green, *Calculating the  $J_c$ ,  $B$ ,  $T$  Surface for Commercial Niobium Tin Conductors Using a Reduced State Model*, Advances in Cryogenic Engineering Materials, Vol. 40, Part A, 1994.
- [6] L.T. Summers, M. Guinan, J.R. Miller, and P. Hahn, *A model for the prediction of  $Nb_3Sn$  critical current as a function of field, temperature, strain, and radiation damage*, IEEE Transactions on Magnetics, vol. 27, no. 2, Mar 1991, doi: 10.1109/20.133608.
- [7] M.D. Bird and Z. Gan, *Low resolution NMR magnets in the 23 to 35 T range at the NHMFL*, IEEE Transactions on Applied Superconductivity, vol. 12, no. 1, Marc 2002, doi: 10.1109/TASC.2002.1018440.
- [8] D. Leroy, *Review of the R&D and Supply of the LHC Superconducting Cables*, IEEE Transactions on Applied Superconductivity, vol. 16, no. 2, 2006, doi: 10.1109/TASC.2005.864273.
- [9] J.V. Minervini, *Superconductivity: Squeezing out the current*, Nature Materials, vol. 13, n. 4, 2014, doi: 10.1038/nmat3931.
- [10] D. Larbalestier, A. Gurevich, D.M. Feldmann, and A. Polyanskii, *High- $T_c$  superconducting materials for electric power applications*, Nature, 414, November 2001, doi: 10.1038/35104654.

- [11] S. Myers, *The engineering needed for particle physics*, Philosophical Transactions, Series A: Mathematical, Physical, and Engineering Science, vol. 373, n. 2037, July 2012, doi: 10.1098/rsta.2011.0053.
- [12] H.H.J. ten Kate, *ATLAS superconducting toroids: the largest ever built*, Chapter 11 of *At the Leading Edge: The ATLAS and CMS LHC Experiments*, 2010, doi: 10.1142/9789814277624\_0011.
- [13] W. Goldacker, A. Frank, R. Heller, S.I. Schlachter, B. Ringsdorf, K.-P. Weiss, C. Schmidt, and S. Schuller, *ROEBEL Assembled Coated Conductors (RACC): Preparation, Properties and Progress*, IEEE Transactions on Applied Superconductivity, vol. 17, no. 2, June 2007, doi: 10.1109/TASC.2007.899417.
- [14] G. Moritz, *Rapidly-cycling superconducting accelerator magnets for fair at GSI*, Particle Accelerator Conference, June 2007, doi: 10.1109/PAC.2007.4440118.
- [15] G. Rolando, *Cable-in-conduit superconductors for fusion magnets*, PhD thesis University of Twente, The Netherlands, 2013.
- [16] G.H. Morgan, *Theoretical Behavior of Twisted Multicore Superconducting Wire in a Time Varying Uniform Magnetic Field*, Journal of Applied Physics, vol. 41, no. 9, August 1970, doi: 10.1063/1.1659491.
- [17] W.J. Jr. Carr, *AC loss in a twisted filamentary superconducting wire*, Journal of Applied Physics, vol. 45, no. 2, 1974.
- [18] A.P. Verweij, *Electrodynamics of Superconducting Cables in Accelerator Magnets*, PhD thesis University of Twente, The Netherlands, 1995.
- [19] L. Rossi, *State-of-the-art superconducting accelerator magnets*, IEEE Transactions on Applied Superconductivity, vol. 12, no. 1, 2002, doi: 10.1109/TASC.2002.1018387.
- [20] L. Rossi, *The LHC main dipoles and quadrupoles toward series production*, IEEE Transactions on Applied Superconductivity, vol. 13, no. 2, 2003, doi: 10.1109/TASC.2003.812639.
- [21] L. Rossi, *The LHC superconducting magnets*, Proceedings of the Particle Accelerator Conference, 2003.
- [22] L. Rossi, *Superconducting magnets for the LHC main lattice*, IEEE Transactions on Applied Superconductivity, vol. 14, no. 2, 2004, doi: 10.1109/TASC.2004.829031.
- [23] *LHC design report*, CERN-2004-003, 2004.
- [24] L. Rossi, *The Large Hadron Collider and the Role of Superconductivity in One of the Largest Scientific Enterprises*, IEEE Transactions on Applied Superconductivity, vol. 17, no. 2, 2007, doi: 10.1109/TASC.2007.899260.

- [25] L. Rossi, *Superconducting magnets for accelerators and detectors*, Cryogenics, vol. 43, Issues 3-5, 2013, doi: 10.1016/S0011-2275(03)00045-6.
- [26] Y. Iwasa, *Case Studies in Superconducting Magnets*, Plenum Press, 1994.
- [27] B. Seeber ed., *Handbook of Applied Superconductivity*, IoP, 1998.
- [28] P.J. Lee ed., *Engineering Superconductivity*, J. Wiley & Sons, 2001.
- [29] L. Bottura, *Magnet Quench 101*, CERN Yellow Report CERN-2013-006, 2013, doi: 10.5170/CERN-2013-006.1.
- [30] L. Bottura, *Cable Stability*, CERN Yellow Report CERN-2014-005, pp.401-451, 2014, doi: 10.5170/CERN-2014-005.401.
- [31] L. Imbasciati, *Quench Protection Issues of Nb<sub>3</sub>Sn Superconducting Magnets for Particle Accelerators*, PhD thesis Vienna Technical University, Austria, 2003.
- [32] B.J. Maddock and G.B. James, *Protection and stabilisation of large superconducting coils*, Proceedings of the Institution of Electrical Engineers, vol. 115, no. 4, April 1968, doi: 10.1049/piee.1968.0101.
- [33] H.H.J. ten Kate, *(Multi) Normal Zone Propagation Velocity in high current density high field magnets*, WAMSDO 2013, CERN, January 2013.
- [34] P. Fazilleau, M. Devaux, M. Durante, T. Lecrevisse, and J.-M. Rey, *Protection of the 13 T Nb<sub>3</sub>Sn Fresca II dipole*, CERN Yellow Report CERN-2013-006, pp.65-69, 2013, doi: 10.5170/CERN-2013-006.65.
- [35] G. Ambrosio, *Maximum allowable temperature during quench in Nb<sub>3</sub>Sn accelerator magnets*, CERN Yellow Report CERN-2013-006, pp.43-46, 2013, doi: 10.5170/CERN-2013-006.43.
- [36] J.H. Schultz, *Protection of superconducting magnets*, IEEE Transactions on Applied Superconductivity, vol. 12, no. 1, March 2002, doi: 10.1109/TASC.2002.1018662.
- [37] J.H. Schultz, *Superconducting Magnets, Quench Protection*, Wiley Encyclopedia of Electrical and Electronics Engineering, 1999.
- [38] E. Todesco, *Quench limits in the next generation of magnets*, CERN Yellow Report CERN-2013-006, pp.10-16, 2013.
- [39] K.H. Meß, P. Schmüser, and S. Wolff, *Superconducting Accelerator Magnets*, World Scientific, Singapore, 1996.
- [40] A. Ishiyama, K. Urayama, and M. Kawamura, *A geometric scaling law of quench propagation velocity in epoxy-impregnated superconducting windings*, Proceedings of the 11th International Conference on Magnet Technology, vol. 2, 1990.

- [41] Y. Iwasa and Y.M. Butt, *Normal zone propagation in adiabatic superconducting magnets over the temperature range 4.2-80 K*, Cryogenics, vol. 30, January 1990.
- [42] V.S. Vysotsky, N.A. Chernoplekov, A.A. Konjukhov, G.S. Kurljandtsev, V.R. Karasik, M.V. Sidorov, and V.N. Tsikhon, *Autonomous superconducting magnet systems New conception for applications with special conditions*, Proceedings of the 15th International Conference on Magnet Technology, 1998.
- [43] P.H. Eberhardt, Proceedings of the 6th International Conference on Magnet Technology, Bratislava, ALFA, 1977, p. 654.
- [44] V.S. Vysotsky, A.A. Konjukhov, A.I. Rusinov, and V.R. Karasik, *Design and coil protection of the high current density autonomous superconducting magnets for mine sweeping*, Advances in Cryogenic Engineering, vol. 41, 1996.
- [45] D. Hagedorn, F. Rodriguez-Mateos, and R. Schmidt, *Protection of LHC Superconducting Corrector Magnets*, CERN LHC Project Report 63, 1996.
- [46] R. Schmidt, C. Giloux, A. Hilaire, A. Ijspeert, F. Rodriguez-Mateos, and F. Sonnemann, *Protection of the Superconducting Corrector Magnets for the LHC*, CERN LHC Project Report 419, 2000.
- [47] S. Vincent, L. Walckiers, A. Ijspeert, and F. Sonnemann, *Passive Protection by By-pass Resistor for Corrector Magnets Connected in Large Electrical Series*, CERN-MTA-IN-98-054, 1998.
- [48] R. Agustsson, J. Hartzell, and S. Storms, *Inductively coupled pulsed energy extraction system for 2G wire-based magnets*, Proceedings of PAC2013, Pasadena, CA USA, 2013.
- [49] K. Grawatsch, H. Koefler, P. Komarek, H. Kornmann, and A. Ulbricht, *Investigations for the development of superconducting power switches*, IEEE Transactions on Magnetics, vol. MAG-11, pp. 586589, 1975.
- [50] S.A. March, A. Ballarino, and Y. Yang, *Power Switches Utilizing Superconducting Material for Accelerator Magnets*, IEEE Transactions on Applied Superconductivity, vol. 19, no. 3, June 2009, doi: 10.1109/TASC.2009.2017890.
- [51] A. Ballarino and T. Taylor, *Scaling of Superconducting Switches for Extraction of Magnetic Energy*, IEEE Transactions on Applied Superconductivity, Vol. 20, No. 3, June 2010, doi: 10.1109/TASC.2010.2042044.
- [52] L. Coull, D. Hagedorn, V. Remondino, and F. Rodriguez-Mateos, *LHC magnet quench protection system*, IEEE Transactions on Magnetics, vol. 30, no. 4, July 1994, doi: 10.1109/20.305593.
- [53] K. Dahlerup-Petersen, R. Denz, J.L. Gomez-Costa, D. Hagedorn, P. Proudlock, F. Rodrinuez-Mateos, R. Schmidt, and F. Sonnemann,



*The protection system for the superconducting elements of the Large Hadron Collider at CERN*, Particle Accelerator Conference, 1999. Proceedings of the 1999, vol. 5, 1999, doi: 10.1109/PAC.1999.792249.

- [54] V.E. Keilin and A.V. Gavrilin, *Quench description by the characteristic time constants*, IEEE Transactions on Applied Superconductivity, vol. 7, no. 2, June 1997, doi: 10.1109/77.614456.
- [55] B.J. Maddock and G.B. James, *Protection and stabilisation of large superconducting coils*, Proceedings of the Institution of Electrical Engineers, vol. 115, no. 4, April 1968, doi: 10.1049/piee.1968.0101.
- [56] L. Bottura, G. de Rijk, L. Rossi, and E. Todesco, *Advanced Accelerator Magnets for Upgrading the LHC*, IEEE Transactions on Applied Superconductivity, vol. 22, no. 3, June 2012, doi: 10.1109/TASC.2012.2186109.
- [57] E. Todesco, L. Bottura, G. de Rijk, and L. Rossi, *Dipoles for High-Energy LHC*, IEEE Transactions on Applied Superconductivity, vol. 24, no. 3, June 2014, doi: 10.1109/TASC.2013.2286002.
- [58] L. Rossi and E. Todesco, *Conceptual design of 20 T dipoles for High-Energy LHC*, CERN Yellow Report 2011-003 13-9, 2011.
- [59] E. Todesco and P. Ferracin, *Limits to High Field Magnets for Particle Accelerators*, IEEE Transactions on Applied Superconductivity, vol. 22, no. 3, June 2012, doi: 10.1109/TASC.2011.2181143.
- [60] K. Dahlerup-Petersen, A. Medvedko, A. Erokhin, B. Kazmin, V. Sytchev, and L. Vassiliev, *Energy extraction in the CERN large hadron collider (LHC)*, Pulsed Power Plasma Science, 2001. IEEE Conference Record - Abstracts, 17-22 June 2001, doi: 10.1109/PPPS.2001.961178.
- [61] K. Dahlerup-Petersen, A. Medvedko, A. Erokhin, B. Kazmin, V. Sytchev, and L. Vassiliev, *Energy extraction in the CERN Large Hadron Collider: a project overview*, Pulsed Power Plasma Science, 2001. PPPS-2001. Digest of Technical Papers , vol. 2, 17-22 June 2001, doi: 10.1109/PPPS.2001.1001835.
- [62] K. Dahlerup-Petersen, F. Rodriguez-Mateos, R. Schmidt, and F. Sonnemann, *Energy extraction for the LHC superconducting circuits*, Proceedings of the 2001 Particle Accelerator Conference, vol. 5, doi: 10.1109/PAC.2001.988140.
- [63] M.A. Green, *Quench back in thin superconducting solenoid magnets*, Cryogenics, vol. 24, Issue 1, 1984, doi: 10.1016/0011-2275(84)90049-3.
- [64] M.A. Green, *The role of quench back in quench protection of a superconducting solenoid*, Cryogenics, vol. 24, Issue 12, 1984, doi: 10.1016/0011-2275(84)90034-1.

- [65] K. Takeuchi, Y.K. Kang, H. Hashizume, and Y. Iwasa, *Interfilament coupling loss for protection of superconducting multicoil magnets*, Cryogenics, vol. 38, 1998, doi: 10.1016/s0011-2275(98)00003-4.
- [66] F. Rodriguez-Mateos, R. Schmidt, A. Siemko, and F. Sonnemann, *Quench Process and Protection of LHC Dipole Magnets*, LHC Project Note 184, 1999.
- [67] B. Szeless, F. Calvone, and F. Rodriguez-Mateos, *Development of industrially produced composite quench heaters for the LHC superconducting lattice magnet*, LHC Project Report 48, 1996.
- [68] F. Rodriguez-Mateos, P. Pagnat, S. Sanfilippo, R. Schmidt, A. Siemko, and F. Sonnemann, *Quench heater experiments on the LHC main magnets*, Proceedings of EPAC 2000, Vienna, Austria, 2000.
- [69] F. Rodriguez-Mateos and F. Sonnemann, *Quench heater studies for the LHC magnets*, Particle Accelerator Conference, 2001. PAC 2001. Proceedings of the 2001, vol. 5, 2001, doi: 10.1109/PAC.2001.988141.
- [70] H. Felice, G. Ambrosio, G. Chlachidze, P. Ferracin, R. Hafalia, R.C. Hannaford, J.M. Joseph, A.F. Lietzke, A.D. McInturff, J.F. Muratore, S. Prestemon, G. Sabbi, J. Schmalzle, P. Wanderer, X.R. Wang, *Instrumentation and Quench Protection for LARP Nb<sub>3</sub>Sn Magnets*, IEEE Transactions on Applied Superconductivity, vol. 19, no. 3, June 2009, doi: 10.1109/TASC.2009.2019062.
- [71] T. Salmi, D. Arbelaez, S. Caspi, H. Felice, S. Prestemon, G. Chlachidze, H.H.J. ten Kate, *Modeling heat transfer from quench protection heaters to superconducting cables in Nb<sub>3</sub>Sn magnets*, CERN Yellow Report CERN-2013-006, pp.30-37, 2013.
- [72] T. Salmi, G. Ambrosio, S. Caspi, G. Chlachidze, H. Felice, M. Marchevsky, S. Prestemon, and H.H.J. ten Kate, *Protection Heater Delay Time Optimization for High-Field Nb<sub>3</sub>Sn Accelerator Magnets*, IEEE Transactions on Applied Superconductivity, vol. 24, no. 3, June 2014, doi: 10.1109/TASC.2013.2287634.
- [73] V. Maroussov, S. Sanfilippo, and A. Siemko, *Temperature profiles during quenches in LHC superconducting dipole magnets protected by quench heaters*, IEEE Transactions on Applied Superconductivity, vol. 10, no. 1, March 2000, doi: 10.1109/77.828320.
- [74] G. Rolando, M. Bajko, G. Berard, and G. Molinari, *Report on Quench Heater Failures*, CERN AT-MCS-Technical Note, 2008.
- [75] G. Willering, *MP3 Recommendation on fatigue testing of MB quench heaters using the new LHC monitoring system*, CERN technical note, LHC-MP3-EN-0014, 2014.

- [76] J.Ph.G.L. Tock, F.F. Bertinelli, H.H.J. ten Kate, F. Bordry, P. Fessia, R. Ostojic, A. Perin, H. Prin, F. Savary, C.E. Scheuerlein, A.P. Verweij, and G. Willering, *Consolidation of the LHC superconducting circuits: a major step towards 14 TeV collisions*, Proceedings of the 3rd International Particle Accelerator Conference, 2012.
- [77] A.P. Verweij, *Solved and remaining NCs in the SC circuits*, LHC Performance Workshop, Chamonix, 2014.
- [78] G. Apollinari, O. Brüning, and L. Rossi, *High Luminosity LHC Project Description*, CERN internal project description, CERN-ACC-2014-0321, 2014.
- [79] G. Chlachidze, G. Ambrosio, M. Anerella, F. Borgnolutti, R. Bossert, S. Caspi, D.W. Cheng, D. Dietderich, H. Felice, P. Ferracin, A. Ghosh, A. Godeke, A.R. Hafalia, M. Marchevsky, D. Orris, P.K. Roy, G.L. Sabbi, T. Salmi, J. Schmalzle, C. Sylvester, M. Tartaglia, J. Tompkins, P. Wanderer, X.R. Wang, and A.V. Zlobin, *Performance of HQ02, an Optimized Version of the 120 mm Nb<sub>3</sub>Sn LARP Quadrupole*, IEEE Transactions on Applied Superconductivity, vol. 24, no. 3, June 2014, doi: 10.1109/TASC.2013.2285885.
- [80] G. Chlachidze, I. Novitski, A.V. Zlobin, B. Auchmann, and M. Karppinen, *Experimental results and analysis from 11 T Nb<sub>3</sub>Sn DS dipole*, CERN Yellow Report CERN-2013-006, pp.47-56, 2013.
- [81] A.V. Zlobin, N. Andreev, G. Apollinari, B. Auchmann, E. Barzi, S. Izquierdo Bermudez, R. Bossert, M. Buehler, G. Chlachidze, J. DiMarco, M. Karppinen, F. Nobrega, I. Novitski, L. Rossi, D. Smekens, M. Tartaglia, D. Turrioni, and G. Velev, *11 T Twin-Aperture Nb<sub>3</sub>Sn Dipole Development for LHC Upgrades*, IEEE Transactions on Applied Superconductivity, vol. PP, no. 99, doi: 10.1109/TASC.2014.2367312.
- [82] H. Bajas, G. Ambrosio, M. Anerella, M. Bajko, R. Bossert, S. Caspi, A. Chiuchiolo, G. Chlachidze, D. Dietderich, O. Dunkel, H. Felice, P. Ferracin, J. Feuvrier, L. Fiscarelli, A. Ghosh, C. Giloux, A. Godeke, A.R. Hafalia, M. Marchevsky, S. Russenschuck, G. Sabbi, T. Salmi, J. Schmalzle, E. Todesco, P. Wanderer, X. Wang, and M. Yu, *Cold Test Results of the LARP HQ Nb<sub>3</sub>Sn Quadrupole Magnet at 1.9 K*, IEEE Transactions on Applied Superconductivity, vol. 23, no. 3, June 2013, doi: 10.1109/TASC.2013.2245281.
- [83] E. Ravaioli, V.I. Datskov, C. Giloux, G. Kirby, H.H.J. ten Kate, and A.P. Verweij, *New, Coupling Loss Induced, Quench Protection System for Superconducting Accelerator Magnets*, IEEE Transactions on Applied Superconductivity, vol. 24, no. 3, June 2014, doi: 10.1109/TASC.2013.2281223.
- [84] E. Ravaioli, V.I. Datskov, A.V. Dudarev, G. Kirby, K.A. Sperin, H.H.J. ten Kate, and A.P. Verweij, *First Experience with the New*

*Coupling-Loss Induced Quench System*, Cryogenics, 2014, Vol. 60, pp. 33-43, <http://dx.doi.org/10.1016/j.cryogenics.2014.01.008>.

- [85] E. Ravaioli, V.I. Datskov, G. Kirby, H.H.J. ten Kate, and A.P. Verweij, *A New Hybrid Protection System for High-Field Superconducting Magnets*, Superconductor Science and Technology, 2014, Vol. 27 (4), 044023, doi: 10.1088/0953-2048/27/4/044023.
- [86] V.I. Datskov, G. Kirby, and E. Ravaioli, *AC-Current Induced Quench Protection System*, EP13174323.9, priority date: 28 June 2013.
- [87] J.A. Taylor, M. Alston-Garnjost, P. Eberhard, G. Gibson, M.A. Green, B. Pardoe, M. Pripstein, R.R. Ross, R. Smits, and P. Lecomte, *Quench protection for a 2-MJ magnet*, IEEE Transactions on Magnetics, vol. 15, no. 1, January 1979, doi: 10.1109/TMAG.1979.1060158.
- [88] R.M. Schöttler and H.W. Lorenzen, *Temperature and Pressure Rise in Supercritical Helium during the Quench of Indirectly Cooled SC Coils*, Vol. 41, pp. 325-334, Cryogenic Engineering Conference Publication, 1996.
- [89] E. Ravaioli, H. Bajas, V.I. Datskov, V. Desbiolles, J. Feuvrier, G. Kirby, M. Maciejewski, G. Sabbi, H.H.J. ten Kate, and A.P. Verweij, *Protecting a Full-Scale Nb<sub>3</sub>Sn Magnet with CLIQ, the New Coupling-Loss Induced Quench System*, IEEE Transactions on Applied Superconductivity, vol. 25, no. 3, June 2015, doi: 10.1109/TASC.2014.2364892.
- [90] G. Sabbi, *Nb<sub>3</sub>Sn IR Quadrupoles for the High Luminosity LHC*, IEEE Transactions on Applied Superconductivity, vol. 23, no. 3, pp.4000707, June 2013, doi: 10.1109/TASC.2012.2233844.
- [91] H. Felice, G. Ambrosio, M.D. Anerella, D. Bocian, R. Bossert, S. Caspi, B. Collins, D. Cheng, G. Chlachidze, D.R. Dietderich, P. Ferracin, A. Godeke, A. Ghosh, A.R. Hafalia, J.M. Joseph, J. Krishnan, M. Marchevsky, G. Sabbi, J. Schmalzle, P. Wanderer, X.R. Wang, and A. Zlobin, *Impact of Coil Compaction on Nb<sub>3</sub>Sn LARP HQ Magnet*, IEEE Transactions on Applied Superconductivity, vol. 22, no. 3, June 2012, doi: 10.1109/TASC.2012.2183843.
- [92] F. Borgnolutti, G. Ambrosio, R. Bossert, G. Chlachidze, D.W. Cheng, D.R. Dietderich, H. Felice, A. Godeke, A.R. Hafalia, M. Marchevsky, P.K. Roy, G.L. Sabbi, J. Schmalzle, P. Wanderer, and M. Yu, *Fabrication of a Second-Generation of Nb<sub>3</sub>Sn Coils for the LARP HQ02 Quadrupole Magnet*, IEEE Transactions on Applied Superconductivity, vol. 24, no. 3, June 2014, doi: 10.1109/TASC.2013.2282758.
- [93] A. Godeke, G. Chlachidze, D.R. Dietderich, A.K. Ghosh, M. Marchevsky, M.G.T. Mentink, and G. Sabbi, *A review of conductor performance for the LARP high-gradient quadrupole magnets*, Superconductor Science and Technology, 2013, vol. 26, 095015, doi: 10.1088/0953-2048/26/9/095015.

- [94] H. Bajas, G. Sabbi, M. Marchevsky, G. Ambrosio, L. Bottura, H. Felice, E. Todesco, T. Salmi, E. Ravaoli, M. Bajko, A. Ghosh, and A. Godeke, *Cold Test Results of the LARP HQ02-b magnet at 1.9 K*, IEEE Transactions on Applied Superconductivity, vol. PP, no. 99, doi: 10.1109/TASC.2014.2378375.
- [95] E. Ravaoli, B. Auchmann, M. Maciejewski, H.H.J. ten Kate, and A.P. Verweij, *Lumped-Element Dynamic Electro-Thermal model of a superconducting magnet*, Cryogenics, 2015, to be published.
- [96] J.W. Nilsson and S. Riedel, *Electric Circuits*, Prentice Hall, 2011, ISBN 0136114997.
- [97] A. Agarwal and J.H. Lang, *Foundations of analog and digital electronic circuits*, Morgan Kaufmann, 2005, ISBN 1-55860-735-8.
- [98] S. Russenschuck, *ROXIE: Routine for the Optimization of Magnet X-Sections, Inverse Field Calculation and Coil End Design*, Ed. Geneva, Switzerland: CERN, April 1999.
- [99] SOLENO. A high-precision magnetic field, inductances and forces calculation code for air-core systems of multi-solenoids developed by the applied superconductivity applications group at the University of Twente, Enschede, the Netherlands.
- [100] L. Dresner, *Stability of Superconductors. Selected Topics in Superconductivity*, Springer US, 1995, ISBN 9780306450303.
- [101] W.J. Jr. Carr, M.S. Walker, and J.H. Murphy, *Alternating field loss in a multifilament superconducting wire for weak ac fields superposed on a constant bias*, Journal of Applied Physics, vol. 46, no. 9, September 1975, doi: 10.1063/1.322108.
- [102] M.S. Walker, J.H. Murphy, and W.J. Jr. Carr, *Alternating field losses in mixed matrix multifilament superconductors*, IEEE Transactions on Magnetics, vol. 11, no. 2, March 1975, doi: 10.1109/TMAG.1975.1058568.
- [103] M.S. Walker, W.J. Jr. Carr, and J.H. Murphy, *Loss behavior in twisted filamentary superconductors*, IEEE Transactions on Magnetics, vol. 11, no. 5, September 1975, doi: 10.1109/TMAG.1975.1058849.
- [104] B. Turck, *Effect of the respective positions of filament bundles and stabilizing copper on coupling losses in superconducting composites*, Cryogenics, vol. 22, 1982.
- [105] B. Turck, *Coupling losses in various outer normal layers surrounding the filament bundle of a superconducting composite*, Journal of Applied Physics, vol. 50, no. 8, Aug 1979, doi: 10.1063/1.326641.
- [106] E. Ravaoli, V.I. Datskov, V. Desbiolles, J. Feuvrier, G. Kirby, M. Maciejewski, K.A. Sperin, H.H.J. ten Kate, A.P. Verweij, and G. Willering, *Towards an optimized Coupling-Loss Induced Quench protection system (CLIQ) for quadrupole magnets*, Physics Procedia, to be published.

- [107] E. Ravaioli, H. Bajas, V.I. Datskov, J. Blomberg Ghini, G. Kirby, M. Maciejewski, H.H.J. ten Kate, A.P. Verweij, and G. Willering, *First implementation of the CLIQ quench protection system on a full-scale LHC matching quadrupole magnet*, IEEE Transactions on Applied Superconductivity, 2015, to be published.
- [108] E. Ravaioli, V.I. Datskov, G. Kirby, M. Maciejewski, H.H.J. ten Kate, A.P. Verweij, and G. Willering, *First implementation of the CLIQ quench protection system on a 14 m long full-scale LHC dipole magnet*, IEEE Transactions on Applied Superconductivity, 2015, to be published.
- [109] G.A. Kirby, B. Auchmann, M. Bajko, M. Charrondiere, N. Bourcey, V.I. Datskov, P. Fessia, J. Feuvrier, P. Galbraith, A. Garcia Tabares, J. Garcia-Perez, P. Granieri, P. Hagen, C. Lorin, J.C. Perez, S. Russenschuck, T. Sahner, M. Segreti, E. Todesco, and G. Willering, *Testing Results for Nb-Ti, 120-mm-Aperture, Low-B Quadrupole Models for the LHC High-Luminosity Insertion*, IEEE Transactions on Applied Superconductivity, vol. 23, no. 3, June 2013, doi: 10.1109/TASC.2013.2247453.
- [110] G.A. Kirby, B. Auchmann, M. Bajko, V.I. Datskov, M. Durante, P. Fessia, J. Feuvrier, M. Guinchard, C. Giloux, P.P. Granieri, P. Manil, J.C. Perez, E. Ravaioli, J.M. Rifflet, S. Russenschuck, T. Sahner, M. Segreti, E. Todesco, and G. Willering, *LHC IR Upgrade NbTi, 120-mm Aperture Model Quadrupole Test Results at 1.8 K*, IEEE Transactions on Applied Superconductivity, vol. 24, no. 3, June 2014, doi: 10.1109/TASC.2013.2284962.
- [111] E. Ravaioli, K. Dahlerup-Petersen, F. Formenti, J. Steckert, H. Thiesen, and A.P. Verweij, *Modeling of the Voltage Waves in the LHC Main Dipole Circuits*, IEEE Transactions on Applied Superconductivity, vol. 22, no. 3, June 2012, doi: 10.1109/TASC.2011.2176306.
- [112] E. Ravaioli, A.P. Verweij, and H.H.J. ten Kate, *Unbalanced Impedance of the Aperture Coils of Some LHC Main Dipole Magnets*, IEEE Transactions on Applied Superconductivity, vol. 23, no. 3, June 2013, doi: 10.1109/TASC.2012.2227650.
- [113] G. Willering, *Stability of Superconducting Rutherford Cables for Accelerator Magnets*, PhD thesis University of Twente, The Netherlands, 2009.
- [114] W.M. De Rapper, *Thermal Stability of Nb<sub>3</sub>Sn Rutherford Cables for Accelerator Magnets*, PhD thesis University of Twente, The Netherlands, 2014.
- [115] E. Ravaioli, K. Dahlerup-Petersen, F. Formenti, V. Montabonnet, M. Pojer, R. Schmidt, A. Siemko, M.S. Camillocci, J. Steckert, H. Thiesen, and A.P. Verweij, *Impact of the Voltage Transients After a Fast Power Abort on the Quench Detection System in the LHC Main Dipole Chain*, IEEE Transactions on Applied Superconductivity, vol. 22, no. 3, June 2012, doi: 10.1109/TASC.2012.2183572.

- [116] E. Ravaioli, B. Auchmann, and A.P. Verweij, *Fast method to quantify the collective magnetization in superconducting magnets*, IEEE Transactions on Applied Superconductivity, vol. 23, no. 3, June 2013, doi: 10.1109/TASC.2012.2227649.
- [117] R.E. Shafer, *Eddy currents, dispersion relations, and transient effects in superconducting magnets*, IEEE Transactions on Magnetism, vol. 17, no. 1, January 1981, doi: 10.1109/TMAG.1981.1061171
- [118] K.M. Smedley and R.E. Shafer, *Experimental Determination of Electrical Characteristics and Circuit Models of Superconducting Dipole Magnets*, IEEE Transactions on Magnetism, Vol. 30, no. 5, pp. 2708-2712, 1994.
- [119] K. Dahlerup-Petersen and F. Schmidt, *Impedance Measurements and Modeling of the Ten Meter Prototype LHC Dipole Magnet*, LHC Project Note 11, 1995.
- [120] F. Bourgeois and K. Dahlerup-Petersen, *Methods and results of modelling and transmission line calculations of the superconducting dipole chains of CERNs LHC collider*, LHC project report 497, CERN, 2001.
- [121] G.-Q. Zhou, *The Equivalent Self-Inductance of N Coupled Parallel Coils*, Progress In Electromagnetics Research Letters, 2014.
- [122] R. Hanft, B.C. Brown, W.E. Cooper, D.A. Gross, L. Michelotti, E.E. Schmidt, and F. Turkot, *Magnetic field properties of Fermilab Energy Saver Dipoles*, IEEE Transactions on Nuclear Science, vol. 30, no. 4, August 1983, doi: 10.1109/TNS.1983.4336664.
- [123] S. Wolff, *The superconducting magnet system for HERA*, Proceedings of the 19th International Conference on Magnet Technology, ed. By C. Marinucci and P. Waymuth, 1995.
- [124] W. Henning, *FAIR an international accelerator facility for research with ions and antiprotons*, Proceedings of the European Particle Accelerator Conference, 2004.
- [125] *FAIR Baseline Technical Report*, Vol. 3A, Experiment Proposals on QCD Physics, 3.1 CBM, 2006.
- [126] T. Nakamoto, M. Sugano, Q. Xu, H. Kawamata, S. Enomoto, N. Higashi, A. Idesaki, M. Iio, Y. Ikemoto, R. Iwasaki, N. Kimura, T. Ogitsu, N. Okada, K. Sasaki, M. Yoshida, and E. Todesco, *Model Magnet Development of D1 Beam Separation Dipole for the HL-LHC Upgrade*, IEEE Transactions on Applied Superconductivity, vol. 25, submitted for publication, 2014.
- [127] M. Karppinen, N. Andreev, G. Apollinari, B. Auchmann, E. Barzi, R. Bossert, V.V. Kashikhin, A. Nobrega, I. Novitski, L. Rossi, D. Smekens, and A.V. Zlobin, *Design of 11 T Twin-Aperture Nb<sub>3</sub>Sn Dipole Demonstrator Magnet for LHC Upgrades*, IEEE Transactions on Applied Superconductivity, vol. 22, no. 3, June 2012, doi: 10.1109/TASC.2011.2177625.

- [128] G. Chlachidze, N. Andreev, G. Apollinari, B. Auchmann, E. Barzi, R. Bossert, M. Karppinen, F. Nobrega, I. Novitski, L. Rossi, D. Smekens, M. Tartaglia, R. Yamada, and A.V. Zlobin, *Quench Protection Study of a Single-Aperture 11 T Nb<sub>3</sub>Sn Demonstrator Dipole for LHC Upgrades*, IEEE Transactions on Applied Superconductivity, vol. 23, no. 3, June 2013, doi: 10.1109/TASC.2013.2237871.
- [129] A.V. Zlobin, N. Andreev, G. Apollinari, B. Auchmann, E. Barzi, R. Bossert, G. Chlachidze, M. Karppinen, F. Nobrega, I. Novitski, L. Rossi, D. Smekens, D. Turrioni, and R. Yamada, *Development and Test of a Single-Aperture 11 T Nb<sub>3</sub>Sn Demonstrator Dipole for LHC Upgrades*, IEEE Transactions on Applied Superconductivity, vol. 23, no. 3, June 2013, doi: 10.1109/TASC.2012.2236138.
- [130] F. Savary, N. Andreev, G. Apollinari, B. Auchmann, E. Barzi, R. Bruce, G. Chlachidze, R. De Maria, J. DiMarco, D. Ramos, M. Giovannozzi, B. Holzer, J. Jowet, S. Izquierdo Bermudez, M. Karppinen, G. Kirby, F. Lackner, R. Moron-Ballester, A. Nobrega, I. Novitski, L. Oberli, V. Parma, J. Perez, H. Prin, S. Redaelli, L. Rossi, D. Smekens, H. Thiessen, D. Turrioni, and A.V. Zlobin, *Status of the 11 T Nb<sub>3</sub>Sn Dipole Project for the LHC*, IEEE Transactions on Applied Superconductivity, vol. PP, no. 99, doi: 10.1109/TASC.2014.2375914.
- [131] P. Ferracin, *LARP Nb<sub>3</sub>Sn quadrupole magnets for the LHC luminosity upgrade*, AIP Conference Proceedings, 1218, 2010, doi: 10.1063/1.3422298.
- [132] P. Ferracin, G. Ambrosio, M. Anerella, F. Borgnolutti, R. Bossert, D. Cheng, D.R. Dietderich, H. Felice, A. Ghosh, A. Godeke, S.I. Bermudez, P. Fessia, S. Krave, M. Juchno, J.C. Perez, L. Oberli, G. Sabbi, E. Todesco, and M. Yu, *Magnet Design of the 150 mm Aperture Low- $\beta$  Quadrupoles for the High Luminosity LHC*, IEEE Transactions on Applied Superconductivity, vol.24, no.3, pp.1,6, June 2014, doi: 10.1109/TASC.2013.2284970.
- [133] G. Ambrosio, *Nb<sub>3</sub>Sn High Field Magnets for the High Luminosity LHC Upgrade Project*, IEEE Transactions on Applied Superconductivity, vol. PP, no. 99, doi: 10.1109/TASC.2014.2367024.
- [134] G. Manfreda, G. Ambrosio, V. Marinozzi, T. Salmi, M. Sorbi, and G. Volpini, *Quench Protection Study of the Nb<sub>3</sub>Sn Low- $\beta$  Quadrupole for the LHC Luminosity Upgrade*, IEEE Transactions on Applied Superconductivity, vol. 24, no. 3, June 2014, doi: 10.1109/TASC.2013.2285099.
- [135] G. Sabbi, S.E. Bartlett, S. Caspi, D.R. Dietderich, P. Ferracin, S.A. Gourlay, A.R. Hafalia, C.R. Hannaford, A.F. Lietzke, S. Mattafirri, A.D. McInturff, and R. Scanlan, *Design of HD2: a 15 tesla Nb<sub>3</sub>Sn dipole with a 35 mm bore*, IEEE Transactions on Applied Superconductivity, vol. 15, no. 2, June 2005, doi: 10.1109/TASC.2005.849510.



- [136] P. Ferracin, S.E. Bartlett, S. Caspi, D.R. Dietderich, S.A. Gourlay, A.R. Hafalia, C.R. Hannaford, A.F. Lietzke, S. Mattafirri, A.D. McInturff, and G. Sabbi, *Mechanical Design of HD2, a 15 T Nb<sub>3</sub>Sn Dipole Magnet with a 35 mm Bore*, IEEE Transactions on Applied Superconductivity, vol. 16, no. 2, June 2006, doi: 10.1109/TASC.2006.871323.
- [137] P. Ferracin, S. Caspi, D.W. Cheng, D.R. Dietderich, A.R. Hafalia, C.R. Hannaford, H. Higley, A.F. Lietzke, J. Lizarazo, A.D. McInturff, and G. Sabbi, *Development of the 15 T Nb<sub>3</sub>Sn Dipole HD2*, IEEE Transactions on Applied Superconductivity, vol. 18, no. 2, June 2008, doi: 10.1109/TASC.2008.922303.
- [138] P. Ferracin, B. Bingham, S. Caspi, D.W. Cheng, D.R. Dietderich, H. Felice, A. Godeke, A.R. Hafalia, C.R. Hannaford, J.M. Joseph, A.F. Lietzke, J. Lizarazo, G. Sabbi, F. Trillaud, and X.R. Wang, *Assembly and Test of HD2, a 36 mm Bore High Field Nb<sub>3</sub>Sn Dipole Magnet*, IEEE Transactions on Applied Superconductivity, vol. 19, no. 3, June 2009, doi: 10.1109/TASC.2009.2019248.
- [139] P. Ferracin, B. Bingham, S. Caspi, D.W. Cheng, D.R. Dietderich, H. Felice, A.R. Hafalia, C.R. Hannaford, J. Joseph, A.F. Lietzke, J. Lizarazo, G. Sabbi, and X.R. Wang, X., *Recent Test Results of the High Field Nb<sub>3</sub>Sn Dipole Magnet HD2*, IEEE Transactions on Applied Superconductivity, vol. 20, no. 3, June 2010, doi: 10.1109/TASC.2010.2042046.
- [140] D.W. Cheng, S. Caspi, D.R. Dietderich, H. Felice, P. Ferracin, A.R. Hafalia, M. Marchevsky, S. Prestemon, and G. Sabbi, *Design and Fabrication Experience With Nb<sub>3</sub>Sn Block-Type Coils for High Field Accelerator Dipoles*, IEEE Transactions on Applied Superconductivity, vol. 23, no. 3, June 2013, doi: 10.1109/TASC.2013.2246811.
- [141] H. Felice, F. Borgnolutti, S. Caspi, D.W. Cheng, D.R. Dietderich, P. Ferracin, A. Godeke, A.R. Hafalia, J.M. Joseph, J. Lizarazo, M. Marchevsky, S. Prestemon, G. Sabbi, and X.R. Wang, *Challenges in the Support Structure Design and Assembly of HD3, a Nb<sub>3</sub>Sn Block-Type Dipole Magnet*, IEEE Transactions on Applied Superconductivity, vol. 23, no. 3, June 2013, doi: 10.1109/TASC.2013.2243794.
- [142] M. Marchevsky, S. Caspi, D.W. Cheng, D.R. Dietderich, J. DiMarco, H. Felice, P. Ferracin, A. Godeke, A.R. Hafalia, J. Joseph, J. Lizarazo, P.K. Roy, G. Sabbi, T. Salmi, M. Turqueti, X.R. Wang, and S. Prestemon, *Test of the High-Field Nb<sub>3</sub>Sn Dipole Magnet HD3b*, IEEE Transactions on Applied Superconductivity, vol. 24, no. 3, June 2014, doi: 10.1109/TASC.2013.2285881.
- [143] G. Sabbi, L. Bottura, D. Cheng, D. Dietderich, P. Ferracin, A. Godeke, S. Gourlay, M. Marchevsky, E. Todesco, and X.R. Wang, *Performance characteristics of Nb<sub>3</sub>Sn block-coil dipoles for a 100 TeV hadron collider*,

IEEE Transactions on Applied Superconductivity, vol. 25, no. 3, June 2015, doi: 10.1109/TASC.2014.2365471.

- [144] E. Ravaioli, V.I. Datskov, J. Blomberg Ghini, G. Kirby, M. Maciejewski, G. Sabbi, H.H.J. ten Kate, and A.P. Verweij, *Quench protection of a 16 T block-coil dipole magnet for a 100 TeV Hadron Collider using CLIQ*, IEEE Transactions on Applied Superconductivity, 2015, to be published.
- [145] H. De Gersem, C. Mühle, M. Clemens, G. Moritz, and T. Weiland, *Numerical Simulation of Eddy Currents in the Superconductive Rutherford Cable of a Fast-Pulsed Dipole Magnet*, Proceedings of the 6th European Conference on Applied Superconductivity (EUCAS 2003), September 2003.
- [146] H. De Gersem and T. Weiland, *Finite-element models for superconductive cables with finite interwire resistance*, IEEE Transactions on Magnetics, vol. 40, no. 2, March 2004, doi: 10.1109/TMAG.2004.825454.
- [147] S. Russenschuck, *Field Computation for Accelerator Magnets: Analytical and Numerical Methods for Electromagnetic Design and Optimization*, Hoboken, NJ, USA: Wiley, 2011.
- [148] M. Maciejewski, *Automated, Object Oriented Simulation Framework for Superconducting Magnets Modelling at CERN*, Master's thesis University of Lodz, Poland, 2014.
- [149] M. Maciejewski, E. Ravaioli, B. Auchmann, A.P. Verweij, and A. Bartoszewicz, *Automated Lumped-Element Simulation Framework for Modelling of Transient Effects in Superconducting Magnets*, Proceedings of the 20th International Conference on Methods and Models in Automation and Robotics, 2015, to be published.
- [150] J. Kozak, *DIPOLE model in PSPICE*, CERN internal report, 2009.
- [151] A. Laprade, S. Pearson, S. Benczkowski, G. Dolny, and F. Wheatley, *A New PSPICE Electro-Thermal Subcircuit For Power MOSFETs*, Application Note 7532 Fairchild, 2003.
- [152] K.F. Goddard, A.A. Roy, and J.K. Sykulski, *Inductance and resistance calculations for a pair of rectangular conductors*, IEE Proceedings - Science, Measurement and Technology, vol. 152, no. 2, March 2005, doi: 10.1049/ip-smt:20041058.
- [153] E.B. Rosa, *The Self and Mutual Inductances of Linear Conductors*, Bulletin of the Bureau of Standards 4 (2): 301344, 1908, doi: 10.6028/bulletin.088.
- [154] P. Fessia, D. Perini, S. Russenschuk, C. Voellinger, R. Vuillermet, and C. Wyss, *Selection of the cross-section design for the LHC main dipole*, IEEE Transactions on Applied Superconductivity, vol. 10, no. 1, 2000, doi: 10.1109/77.828177.

- [155] J. Lucas, R. Ostojic, D. Tommasini, W.V. Delsolaro, and D. Landgrebe, *Performance of the final prototype of the 6-kA matching quadrupoles for the LHC insertions and status of the industrialization program*, IEEE Transactions on Applied Superconductivity, vol. 13, no. 2, June 2003, doi: 10.1109/TASC.2003.812657.
- [156] E. Ravaioli, V.I. Datskov, G. Kirby, M. Maciejewski, H.H.J. ten Kate, and A.P. Verweij, *Advanced Quench Protection for the Nb<sub>3</sub>Sn Quadrupoles for the High Luminosity LHC*, IEEE Transactions on Applied Superconductivity, 2015, to be published.
- [157] A. Dudarev, T. Mulder, W. van de Camp, E. Ravaioli, A. Teixeira, and H.H.J. ten Kate, *New Fast Response Thin Film-Based Superconducting Quench Detectors*, IEEE Transactions on Applied Superconductivity, vol. 24, no. 3, June 2014, doi: 10.1109/TASC.2013.2286813.
- [158] L. Bromberg, J.V. Minervini, J.H. Schultz, T. Antaya and L. Myatt, *Use of inductive heating for superconducting magnet protection*, PSFC/JA-11-26, November 2011.
- [159] L. Bromberg, J.V. Minervini, J.H. Schultz, L. Myatt, and T. Antaya, *Internal Quench of Superconducting Magnets by the Use of AC Fields*, IEEE Transactions on Applied Superconductivity, vol. 22, no. 3, June 2012, doi: 10.1109/TASC.2011.2175354.
- [160] Leslie Bromberg, Joseph V Minervini, Leonard Myatt, Timothy Antaya, Joel Henry Schultz, *Inductive quench for magnet protection*, WO 2008030911 A2, US 7701677 B2, EP 2064564 A2, priority date: 7 September 2006.
- [161] E. Ravaioli, V.I. Datskov, G. Kirby, M. Maciejewski, H.H.J. ten Kate, and A.P. Verweij, *CLIQ-based quench protection of a chain of high-field superconducting magnets*, IEEE Transactions on Applied Superconductivity, 2015, to be published.
- [162] R. Denz, *Electronic Systems for the Protection of Superconducting Elements in the LHC*, IEEE Transactions on Applied Superconductivity, vol. 16, no. 2, June 2006, doi: 10.1109/TASC.2005.864258.
- [163] R. Denz, K. Dahlerup-Petersen, F. Formenti, K.H. Meß, A. Siemko, J. Steckert, L. Walckiers, and J. Strait, *Upgrade of the Protection System for Superconducting Circuits in the LHC*, Particle Accelerator Conference, May 2009.
- [164] R. Denz, K. Dahlerup-Petersen, A. Siemko, and J. Steckert, *Upgrade of the Protection System for the Superconducting Elements of the LHC During LS1*, IEEE Transactions on Applied Superconductivity, vol. 24, no. 3, June 2014, doi: 10.1109/TASC.2013.2283101.
- [165] K. Dahlerup-Petersen, F. Formenti, B.I. Panev, H. Pfeffer, and G. Ganetis, *Arc suppression snubbers for the energy extraction switchgear in the*

*superconducting main circuits of the LHC collider: impact on the safety-critical quench protection system*, Pulsed Power Conference, June 2011, doi: 10.1109/PPC.2011.6191499.

- [166] S. Meyers and F. Zimmermann, *Chamonix 2010 Summary*, Proceedings LHC Performance Workshop, Chamonix 2010.
- [167] M.J. Syphers, M.A. Harrison, and S. Peggs, *Beyond the LHC: a conceptual approach to a future high energy hadron collider*, Proceedings of the 1995 Particle Accelerator Conference, vol. 1, May 1995, doi: 10.1109/PAC.1995.504681.
- [168] G. Dugan, P. Limon, and M. Syphers, *Really Large Hadron Collider Working Group Summary*, Proceedings of the 1997 DPF/DPB Summer Study on New Directions for High Energy Physics, Snowmass, 1996, p. 251.
- [169] G. Ambrosio et al., *Design Study for a Staged Very Large Hadron Collider*, Fermilab TM-2149, June 2001.
- [170] R. Assmann, R. Bailey, O. Brüning, O. Dominguez, G. de Rijk, J. Miguel Jimenez, S. Myers, L. Rossi, L. Tavian, E. Todesco, and F. Zimmermann, *First Thoughts on a Higher-Energy LHC*, CERN-ATS-2010-177, 2010.
- [171] O. Brüning, B. Goddard, M. Mangano, S. Myers, L. Rossi, E. Todesco, and F. Zimmerman, *High Energy LHC Document prepared for the European HEP strategy update*, CERN ATS 2012-237, August 2012.
- [172] M. Benedikt, *Future Circular Collider (FCC) Study*, Future Circular Collider Study Kickoff Meeting, 2014.
- [173] L. Rossi and E. Todesco, *Electromagnetic Efficiency of Block Design in Superconducting Dipoles*, IEEE Transactions on Applied Superconductivity, vol. 19, no. 3, June 2009, doi: 10.1109/TASC.2009.2017891.
- [174] A. Godeke, G. Chlachidze, D.R. Dietderich, A.K. Ghosh, M. Marchevsky, M.G.T. Mentink, and G. Sabbi, *A review of conductor performance for the LARP high-gradient quadrupole magnets*, Superconductor Science and Technology, vol. 26, 2013.

# Summary

In this thesis is presented the characterization of CLIQ, the Coupling-Loss Induced Quench system, a new method for protecting superconducting magnets, featuring significant advantages over the conventional technology.

In the case of a quench in a high magnetic-field superconducting magnet, the hot-spot temperature raises quickly due to the high energy-density stored in the coil. To avoid damage due to overheating, such a coil can be protected by reducing rapidly the magnet transport current. Conventional methods to achieve this are energy extraction, which usually relies on extracting part of the magnet's stored energy with an external resistor, and quench heaters attached to the coil surface, which transfer part of the coil to the normal state thereby reducing the current with the electrical resistance developed in the coil itself.

Both methods have drawbacks and limitations. An energy-extraction system can be expensive compared to other protection methods. The value of its extraction resistor, and hence the decay time, is limited by the maximum safe voltage in the circuit. The distributions of temperature and stress in the coil are inhomogeneous due to the non-uniform distribution of areas in the normal state. Quench heaters rely on thermal diffusion across insulation layers, an inherently slow process, which makes the protection of high magnetic-field magnets challenging due to the very fast transition to the normal state required to safely discharge the magnet. Furthermore, heater-based systems are often fragile, prone to electrical breakdown, and difficult to repair in the case of damage as they are fully integrated in the cold mass. Heater-related failures are one of the most common causes for rejection or replacement of high field accelerator magnets.

CLIQ bears significant advantages over the existing technology. Its effective mechanism for heating the superconductor relying on coupling loss by principle is much faster than thermal diffusion, upon which the systems based on external heaters rely. The winding pack is transferred to the normal state more quickly and homogeneously, hence spreading the coil energy over a larger volume of conductor thereby reducing the hot-spot temperature. Furthermore, a CLIQ system is composed of simple and robust electrical components and, being an external system, it hardly interferes with the coil windings. Due to the relatively limited work required to implement it, CLIQ is also a cost- and time-effective back-up solution for the protection of magnets with failing heater protection systems.

CLIQ is comprising a charged capacitor bank connected to the coil to protect through two terminals needed for injecting a current. Upon quench detection, the

capacitor bank is discharged and an oscillating current is introduced in the coil sections. As a result, transitory coupling loss is generated in the strands and the temperature of the superconductor is increased. For superconductors used in most high field magnets, the most effective transitory loss to deposit heat in the strands is the inter-filament coupling loss due to its small characteristic time constant. Thus, the system performance depends on and can be tuned by controlling the strand parameters, namely the filament twist-pitch and the effective transverse resistivity of the matrix, and is virtually independent of the cable parameters, such as the number of strands and the strand twist-pitch.

The analysis of the transients during and after a CLIQ discharge allows identifying the system parameters affecting the system performance. At high currents, when a fast transition to the normal state is required to protect the magnet, the performance mainly relies on the peak deposited power density, which is proportional to the square of the charging voltage of the capacitor bank, and independent of its capacitance. Since the charging voltage is limited for risk limiting reasons, and when the power density is not satisfactory, the system performance can be improved by further subdividing the coil into multiple sections, hence decreasing the impedance of the discharge circuit and increasing the introduced current changes. At low currents, the requirement for a fast transition of the superconductor to the normal state is less strict, but more energy is needed in order to reach the current sharing temperature. Hence, the system performance is mainly influenced by the total deposited energy per unit volume, which is proportional to the capacitance and to the square of the charging voltage.

A complete analysis of the electro-magnetic and thermal transients occurring during a CLIQ discharge is mandatory to warrant optimal performance. Thus, a novel and elegant technique for modeling non-linear dynamic effects in superconducting magnets was developed and validated by experimental results. The Lumped-Element Dynamic Electro-Thermal (LEDET) method is based on three coupled networks of lumped-elements, reproducing the electrical transient in the main magnet circuit, the thermal transient in the coil windings, and the electro-magnetic transient of the inter-filament and inter-strand coupling currents in the coil's superconductor. Applying this technique, it is possible to calculate the reduction of the magnet's differential self-inductance due to the presence of inter-filament and inter-strand coupling losses, which has a significant impact on the magnet behavior when it is subject to fast current ramp rates.

A clear strategy to design an effective CLIQ system is outlined. In many practical cases, configurations can be obtained by varying the electrical order of the coil sections or the positioning of the CLIQ terminals. The most convenient configurations are identified for all geometries adopted in most of the existing magnets used in particle accelerators, detectors, magnetic resonance imaging, and other applications requiring high magnetic field. For any geometry analyzed, two main principles are to be respected. Firstly, the performance is improved by subdividing the coil into multiple sections. Secondly, the optimum configurations allow introducing opposite current changes in coil sections that are physically adjacent. Both measures decrease the equivalent impedance of the discharge system and optimize the distribution of the deposited loss in the coil cross-section.

Most existing superconducting magnets can be protected by CLIQ. In the first experimental campaigns, the system was successfully tested on magnets of different sizes (from small test coils to full-size accelerator magnets), superconductor types (Nb-Ti, Nb<sub>3</sub>Sn), geometries, cables and strand parameters. The test results are in good agreement with the predictions based on simulation, hence showing that the theoretical background of the method is well understood and the modeling tools are reliable.

An alternative variant of the CLIQ method is also proposed, based on an external excitation coil galvanically insulated from the coil to protect, but strongly magnetically coupled to it. Successful tests proved the validity of this concept, even if they were carried out with a coil not at all optimized for this application. The conceptual design of a CLIQ excitation coil for protecting full-size, high energy-density magnets is presented. It includes various modules composed of two solenoids whose turns are wound with opposite direction, in order to achieve an effective superposition of the magnetic-field changes introduced by each solenoid. A well-supported, well-insulated excitation coil is a very promising option for CLIQ-based protection system, and its applications and limitations need to be further explored in the near future.

During the design phase of new high magnetic-field superconducting magnets, CLIQ has to be considered as the first option for the quench protection due to its fast and effective heating mechanism and its robust electrical design. The velocity of the transfer to the normal state offered by CLIQ is unprecedented and can achieve safe magnet operation at energy densities presently incompatible with the performance of heater-based quench protection systems. Including CLIQ in the magnet design from the start allows optimizing its performance and integration in the magnet circuit, and can result in safer, more compact, better performing magnets.

Integrating CLIQ in a circuit composed of multiple magnets poses no problems in terms of magnet operation and impact on the quench detection system. Straightforward solutions for its implementation are presented and modeled under various operating conditions.

CLIQ-based systems protecting high-temperature superconducting magnets, characterized by very low normal-zone propagation velocities and a margin to quench roughly two orders of magnitude higher than low-temperature superconductors, appear to be feasible as well but require careful consideration.

In conclusion, a coherent and detailed treatise of a CLIQ transient is presented, reliable and validated simulation tools are available, and experimental results have convincingly shown the effectiveness of this method. CLIQ technology has rapidly reached maturity and is ready for implementation on particle accelerator magnets.





# Samenvatting

## (Summary in Dutch)

In dit proefschrift worden de eigenschappen van CLIQ, (Coupling-Loss Induced Quench, ofwel Quench geïnduceerd door koppelstroomverliezen) geïntroduceerd. CLIQ is een nieuwe methode voor het beschermen van supergeleidende magneten en heeft significante voordelen ten opzichte van conventionele technologie.

Wanneer een hoog-veld supergeleidende magneet plaatselijk in de normaal-geleidende toestand overgaat, quencht, (een plaatselijke overgang van de supergeleidende naar de normaal geleidende toestand) zal de temperatuur in de magneet snel stijgen door de hoge opgeslagen energiedichtheid in de magneet. Schade door oververhitting in de spoel kan worden voorkomen door de transportstroom in de magneet snel te verminderen. Conventionele methodes maken gebruik van een systeem voor energie-extractie waarbij de opgeslagen magnetische energie wordt gedissipeerd in een externe weerstand, of quench-verwarmingselementen die op het oppervlak van de spoelen zijn aangebracht om een deel van de spoel in de normaal-geleidende toestand te brengen waarbij elektrische weerstand in de magneet zelf wordt ontwikkeld.

Beide methodes hebben nadelen en beperkingen. Een energy-extractiesysteem kan een dure oplossing zijn in vergelijking met andere beschermingsmethodes. De weerstandswaarde van de dumpweerstand, en daarmee de stroomhalfwaardetijd, wordt begrensd door de maximale veilige spanning in het circuit. De temperatuur- en drukverdeling in de magneet zijn inhomogeen door de niet-uniforme verdeling van de normaal-geleidende zones. Quench-verwarmingselementen maken gebruik van warmte diffusie door de isolatielaag, een inherent langzaam proces die de bescherming van hoog-veldmagnetten een uitdaging maken omdat deze een zeer snelle overgang van de supergeleidende naar de normaal-geleidende toestand vereisen. Daarbij zijn op quench-verwarmingselementen gebaseerde systemen vaak fragiel, vatbaar voor elektrische defecten en moeilijk te repareren in geval van schade omdat ze volledig geïntegreerd zijn in de magneet. Verwarmingselementen gerelateerde schade is één van de meest voorkomende redenen voor het afwijzen of vervangen van hoog-veld versneller magneten.

CLIQ heeft belangrijke voordelen boven de bestaande technologie. Het effectieve mechanisme voor het opwarmen van de supergeleider door middel van koppelstroom verliezen is intrinsiek sneller dan thermische diffusie waar de Quench Heater systemen

op gebaseerd zijn. De spoelen komen sneller en uniformer in de normaal geleidende toestand waarmee de opgeslagen energie over een groter deel van de geleider wordt verspreid en de hotspot temperatuur lager wordt. Daarnaast is het CLIQ systeem opgebouwd uit eenvoudige en robuuste elektrische onderdelen en heeft het als extern systeem weinig interferentie met de spoel. Omdat slechts een relatief korte ingreep nodig is om CLIQ aan te brengen, kan CLIQ ook dienen als goedkoop en snel toepasbaar reservesysteem voor magneten met defecte quench-verwarmingselementen.

Het CLIQ systeem bestaat uit in serie geschakelde condensatoren die verbonden zijn met de te beschermen magneet door middel van twee stroomkabels. Als een quench is gedetecteerd worden de condensatoren ontladen en ontstaat er een oscillerende stroom in de spoelsecties. Daarbij worden kortdurende koppelstroomverliezen opgewekt in de geleider waardoor deze opwarmt. Inter-filament koppelstroomverliezen hebben een lage tijdconstante en zijn daardoor het meest effectief in veel supergeleiders. De effectiviteit van het CLIQ systeem hangt daarom af, en kan beïnvloed worden door het controleren van de geleider eigenschappen, voornamelijk de twistlengte van de filamenten en de effectieve transversale weerstand van de matrix. De werking wordt nauwelijks beïnvloed door kabeleigenschappen, zoals het aantal draden in de kabel of de twistlengte van de kabel.

De identificatie van parameters die bepalend zijn voor de werking van het systeem is mogelijk door een analyse van de snelle stroom en spanningsveranderingen tijdens en na de CLIQ ontlading. Bij hoge stromen, waarbij een snelle overgang naar de normaal geleidende toestand nodig is om de magneet te beschermen, wordt de effectiviteit van CLIQ voornamelijk bepaald door het piekvermogen, dat evenredig is met het kwadraat van de condensatorspanning, maar onafhankelijk is van de capaciteit. Vanwege het risico op elektrische doorslag in de magneet is de condensatorspanning gelimiteerd. Om alsnog de prestaties van het systeem te verhogen kan de spoel worden verdeeld in meerdere secties waardoor de impedantie van het circuit wordt verminderd en de geïnduceerde stroom vergroot. Bij lage stromen is een minder snelle overgang naar de normaal geleidende toestand vereist maar is een hogere energie nodig om de stroomhervdelingstemperatuur te bereiken. In dit geval worden de prestaties van het systeem voornamelijk beïnvloed door de totale gedissipeerde energie per volume-eenheid die evenredig is met de capaciteit en het kwadraat van de condensatorspanning.

Een volledige analysis van de elektromagnetische en thermische veranderingen tijdens een CLIQ ontlading is nodig om een optimaal effect te bewerkstelligen. Hiervoor is een nieuwe en elegante methode voor het modeleren van niet-lineaire dynamische effecten in supergeleidende magneten ontwikkeld en gevalideerd met experimentele resultaten. De Lumped-Element Dynamic Electro-Thermal (LEDET, dynamische elektro-thermische model met geclusterde elementen) methode is gebaseerd op drie gekoppelde netwerken van geclusterde elementen, die de elektrische veranderingen in het magneet circuit, de thermische veranderingen in de magneet en de elektromagnetische veranderingen in de koppelstromen tussen filamenten en tussen draden in de supergeleidende kabel in de magneet berekenen. Door het toepassen van deze techniek is het mogelijk om de vermindering van de differentiële zelfinductie van de magneet te berekenen die wordt veroorzaakt door de aanwezige koppelstroomverliezen tussen de filamenten en tussen de draden, die een significant

effect hebben op het gedrag van de magneet tijdens snelle stroomveranderingen.

Een duidelijke strategie om een efficiënt CLIQ systeem te ontwerpen wordt beschreven. In vele praktische gevallen kunnen verschillende configuraties worden verkregen door het variëren van de elektrische volgorde van de magneetsecties of door het variëren van de positie van CLIQ stroominjectiepunten. De meest doelmatige configuraties worden beschreven voor alle geometrieën die worden toegepast in de meest voorkomende magneten in deeltjesversnellers, detectoren, MRI magneten en andere hoog-veld toepassingen. Voor elke geanalyseerde geometrie moet aan twee hoofdprincipes worden voldaan. Ten eerste wordt de effectiviteit verbeterd door het opdelen van de magneet in meerdere secties. Ten tweede kan een optimale configuratie verkregen worden door tegengestelde stromen in naast elkaar liggende spoelsecties toe te passen. Beide maatregelen verminderen de equivalente impedantie van het ontlaadsysteem en leiden tot een optimale verdeling van het gedissipeerde verlies in de dwarsdoorsnede van de magneet.

De meeste bestaande supergeleidende magneten kunnen door CLIQ worden beschermd. In een eerste serie experimenten is het systeem succesvol getest op magneten van verschillende grootte (van kleine testspoelen tot volledige versneller-magnetten), type supergeleider (Nb-Ti, Nb<sub>3</sub>Sn), geometrieën, kabels en draadeigenschappen. De testresultaten zijn in goede overeenstemming met de verwachting gebaseerd op simulaties, waarbij aangetoond is dat de theoretische achtergrond van de methode goed wordt begrepen en dat de modellen betrouwbaar zijn.

Een variant van de CLIQ methode wordt ook voorgesteld, waarbij een excitatiespoel zo wordt gewikkeld dat deze magnetisch sterk gekoppeld is met de magneet, maar galvanisch ervan gescheiden is. Succesvolle tests toonden aan dat het concept werkt, zelfs met een niet daarvoor geoptimaliseerde excitatiespoel. Het conceptuele ontwerp van een CLIQ excitatiespoel voor het beschermen van magneten met hoge energiedichtheid wordt gepresenteerd. Het bestaat uit verschillende modules met twee solenoides waarbij tegengestelde wikkelingen voor een effectieve superpositie van het opgewekte magneetveld zorgen. Een goed bevestigde en goed geïsoleerde excitatiespoel is een veelbelovende variant van op CLIQ gebaseerde beschermingssystemen. Toepassingen en beperkingen van deze techniek moeten in de nabije toekomst verder worden onderzocht.

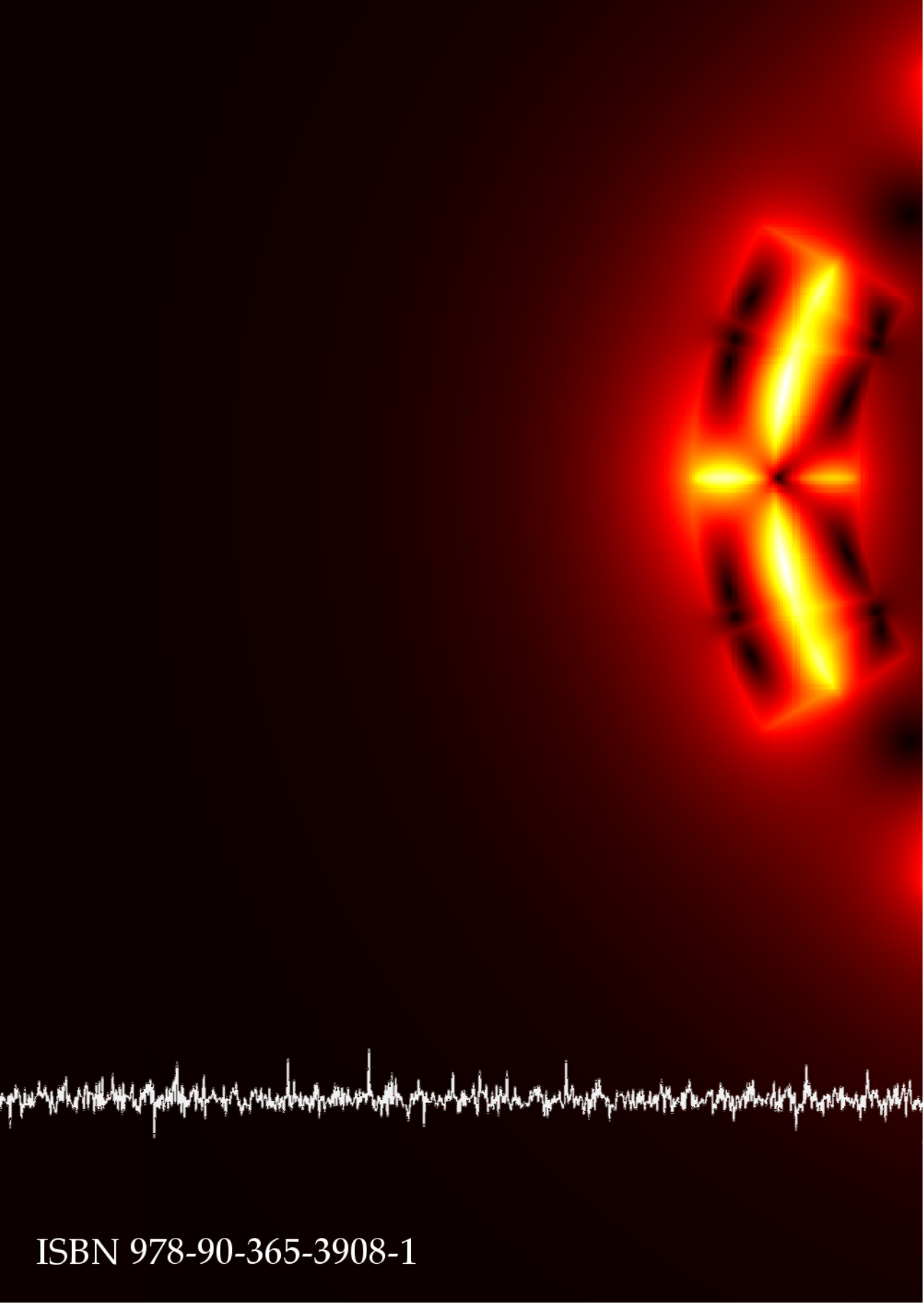
Bij de ontwikkeling van nieuwe hoog-veld supergeleidende magneten dient de CLIQ techniek als de eerste optie voor quench-bescherming te worden overwogen vanwege het snelle en effectieve verwarmingsmechanisme en het robuuste elektrische ontwerp. De overgangssnelheid met CLIQ van de supergeleidende naar de normaal-geleidende toestand is ongeëvenaard en kan garant staan voor een veilig gebruik van een magneet met een energie dichtheid waar de huidige op verwarmings-elementen gebaseerde beschermingssystemen tekort schieten. Door vanaf het begin in het magneetontwerp rekening te houden met de mogelijkheden van CLIQ kan de effectiviteit en integratie in het magneet circuit optimaal gekozen worden hetgeen kan resulteren in een veiliger, compactere en beter presterende magneten.

Het integreren van CLIQ in een circuit van meerdere in serie geschakelde magneten veroorzaakt geen problemen met betrekking tot magneetgebruik en het quench-detectiesysteem. Eenvoudige oplossingen voor de toepassing worden

gepresenteerd en gemodelleerd voor verschillende gebruiksomstandigheden.

Op CLIQ gebaseerde systemen voor het beschermen van hoge-temperatuur supergeleidende magneten, die gekarakteriseerd worden door een erg lage propagatiesnelheid van de normaal geleidende zones en een quench-marge die ruwweg twee orde groottes hoger is dan voor lage temperatuur supergeleiders, lijken toepasbaar maar een zorgvuldige afweging is nodig.

Kort samengevat, wordt er een coherente en gedetailleerde beschrijving van de nieuwe CLIQ technologie gepresenteerd, zijn er betrouwbare en gevalideerde simulatie modellen beschikbaar en hebben experimentele resultaten overtuigend de effectiviteit van deze methode aangetoond. De CLIQ technologie is snel volwassen geworden en is klaar om te worden gebruikt in versneller-magnetten.



ISBN 978-90-365-3908-1